

NORTHWESTERN UNIVERSITY

Processing and Properties of Porous NiTi

A DISSERTATION

SUBMITTED TO THE GRADUATE SCHOOL

IN PARTIAL FULFILMENT OF THE REQUIREMENTS

for the degree

DOCTOR OF PHILOSOPHY

Field of Materials Science and Engineering

By

Ampika Bansiddhi

EVANSTON, ILLINOIS

December 2008

© Copyright by Ampika Bansiddhi 2008

All Rights Reserved

# ABSTRACT

## Processing and Properties of Porous NiTi

Ampika Bansiddhi

Increasing interest in long-life bone implants with reduced mechanical properties reducing the stress-shielding effect and a structure mimicking bone porous architecture has encouraged study and development of fabrication methods for porous NiTi. The main objective of this work was to advance these goals by developing new processing procedures for porous NiTi that offer the following advances over existing technology: (i) controllable pore characteristics (porosity, pore size/shape, connectivity) to stimulate and accommodate a high level of bone ingrowth; (ii) mechanical properties (yield strength, stiffness, recovery strain) matching those of bone, to minimize stress-shielding effects; (iii) dense metal struts and walls, to prevent crack initiation and increase ductility; (iv) simplicity and low cost of production; and (v) capability for either shape-memory or superelasticity.

A new strategy to fabricate porous NiTi with the above characteristics is presented. This strategy is based on densification by hot isostatic pressing (HIP) of a mixture of pre-alloyed NiTi powders and salt space holders, followed by removal of the salt. Using this strategy, the porosity of the NiTi is controllable by varying the volume fraction of the salt, and the pore size and shape

can be tailored in accordance with the geometry of the salt used. The effects of using different space holders, i.e. sodium fluoride (NaF) and sodium chloride (NaCl), on the final porous product are examined. The influence of HIP temperature and further post-HIP sintering on foam properties is also presented.

The high cost associated with HIP processing drove subsequent work towards new strategies to simplify porous NiTi synthesis while maintaining high-quality microstructures and mechanical properties. The strategy followed here involves combining the NaCl space holder technique with in situ transient liquid phase sintering of pre-alloyed NiTi and Nb powders, thereby integrating the densification of NiTi struts and the removal of space holders into a single step. The effect of Nb addition on structural and physical properties of porous NiTi is discussed.

Some extension of the work towards understanding the mechanical behavior and microstructure development of porous NiTi is included.

## Acknowledgement

First and foremost, I would like to express my gratitude to Dr. David Dunand for giving me the opportunity to work on a fascinating topic that inspired passion in me, and for encouraging and advising me throughout the past four years. I have learned tremendously from his example of creative initiative, critical thinking, and self-motivation in researching, as well as innovation and passion in teaching. His trust, understanding, and consideration have been invaluable and are highly appreciated. I will strive to carry these qualities with me in becoming a great advisor for my students in the future.

I would like to thank to my committee members, Dr. Faber, Dr. Brinson, and Dr. Olson (as well as their graduate students) for advice and sharing insight in related field of NiTi and foam materials. I would like to thank Dr. Stupp and T. Sargeant for discussion on bio-related issues, M. Panico for modeling-related aspects, and E. Maddy for her devoted study in Chapter 6. Dr. Stair, M. Seniw, B Meyer, J. Almer, and Thang were fundamental in helping me throughout my research. I am grateful to former and current colleagues in Dr. Dunand's group and NU friends for always filling the work place with fun and happiness, as well as offering great help in every way. It has been such a wonderful journey and great pleasure working/laughing with all of you.

I also would like to acknowledge support in this work from the National Science Foundation Grant DMR-0505772. Financial support from the Royal Thai Government and Kasetsart University throughout my 6 years in the US is also greatly appreciated.

Above all, I would like to give my special thanks to my family: my mom, dad, Opal, and grandmas for giving me this life full with love and happiness, for being such great role models and driving forces in my life, and for positive support in all directions and in all decisions I made in the past years; Alan for helping me correctly express what I want to say in my thesis, for always being there for me and building/sharing/completing another amazing dimension of my life; Annemieke, Mike and Alan's family for comforting me with strength and warmth as in my own family. Now, let's read the following 200 pages or so that your love, patience and support have helped me complete.

# Contents

ABSTRACT	3
Acknowledgements	5
List of Figures	10
List of Tables	19
Chapter 1. Introduction	20
1.1 Bone implants	20
1.1.1 Demand for bone implants	20
1.1.2 Requirements for bone implants	22
1.2 Properties of porous materials	31
1.2.1 Definition of porous characteristics	32
1.2.2 Pore-dependent properties of porous materials	34
1.3 Properties of Nickel Titanium alloy	41
1.3.1 Macroscopic and microscopic structure in NiTi	42
1.3.2 Phase transformation behavior	43
1.3.3 Shape memory effect and superelasticity	45
1.3.4 Variation of standard behavior seem in Ni-rich NiTi	50
1.4 Porous NiTi	53
1.4.1 Processing-related aspects	54

	8
1.4.2 Properties-related aspects	68
1.4.3 Biological-related aspects	72
1.5 Objective of Thesis	77
Chapter 2. General Experimental Procedures	79
2.1 Foam synthesis	79
2.2 Foam characterization	81
Chapter 3. Porous NiTi Produced by Hot Isostatic Pressing (HIP) and Space-Holder Method	88
3.1 Shape-memory NiTi foams produced by replication of NaF space-holders	92
3.1.1 Experiment processing	92
3.1.2 Foam properties	93
3.1.3 Conclusions	109
3.2 Shape-memory NiTi foams produced by replication of NaCl space-holders	111
3.2.1 Experiment processing	112
3.2.2 Foam properties	113
3.2.3 Conclusions	130
Chapter 4. Porous NiTi Produced by Transient Liquid Sintering and Space-Holder Method	132
4.1 Experiment procedures	137
4.2 Foam properties	139
4.3 Conclusions	154

	9
Chapter 5. Processing Development in Sintering of Porous NiTi	156
5.1 Effect of sintering on transformation behavior	156
5.2 Effect of particle size and powder mixing	158
5.3 Effect of sintering time	160
5.4 Effect of cold isostatic pressing (CIP) after sintering	163
5.5 Effect of Ni addition and heat treatment on transformation behavior	165
5.6 Mechanical property evaluation of Ni-rich NiTi foam	170
5.7 Synchrotron x-ray study of phase transformation of porous Ni-rich NiTi	179
Chapter 6. Additional Work on Porous NiTi Produced by Hot Isostatic Pressing	192
6.1 Improvement of interconnectivity in porous NiTi	192
6.1.1 Experimental procedures	197
6.1.2 Results and discussion	199
6.1.3 Properties evaluation of treated foam	212
6.1.4 Conclusions and suggestions	214
6.2 Tomographic analysis and modeling of porous NiTi	216
Chapter 7. Conclusions, Anticipated Benefits and Future Work	223
7.1 Summary	223
7.2 Anticipated benefit	225
7.3 Suggestions for future work	227
References	237

## List of Figures

- |      |                                                                                                                                                                                                                                                                                                                                          |    |
|------|------------------------------------------------------------------------------------------------------------------------------------------------------------------------------------------------------------------------------------------------------------------------------------------------------------------------------------------|----|
| 1.1. | Bone structure in sectioned human femoral head.                                                                                                                                                                                                                                                                                          | 28 |
| 1.2. | Schematic depiction of a closed-cell foam, with the key structural features of foams indicated.                                                                                                                                                                                                                                          | 32 |
| 1.3  | Example of a) closed-cell foam, made by decomposition of $TiH_2$ in molten aluminum, b) low-density open-cell polyurethane foam, c) high-density open-cell NiTi foam, and d) mixed open and closed cells, made by sintering of a bed of hollow stainless steel spheres.                                                                  | 33 |
| 1.4. | Example of a Ti foam with small fenestration size, processed by expansion of entrapped argon gas. Fenestrations between pores are indicated by arrows.                                                                                                                                                                                   | 34 |
| 1.5. | Example of a typical stress-strain curve in a open-cell foam.                                                                                                                                                                                                                                                                            | 38 |
| 1.6. | A unit cell of a foam corresponding to Gibson and Ashby equations.                                                                                                                                                                                                                                                                       | 39 |
| 1.7. | Different pore structures in trabecular bone from different sites: (a) low density, open-cell, rod-like structure in the femoral head, (b) higher density, perforated plate-like structure in the femoral head, and (c) intermediate density, showing an oriented structure with rods normal to parallel plates, in the femoral condyle. | 40 |
| 1.8. | Plots of relative density and (a) relative Young's modulus and (2) relative compressive strength of trabecular bone.                                                                                                                                                                                                                     | 41 |

	11
1.9. The Ni-Ti binary phase diagram.	42
1.10. Stress-temperature phase diagram of NiTi.	45
1.11. Shape memory effect presenting in (a) 3D stress-strain-temperature plot (showing load-unload-heat recovery path) and (b) 2D stress-temperature plot (left upon loading, right upon unloading and heat recovery).	46
1.12. Scheme of superelasticity effect presenting in (a) stress-strain curve and (b) stress-temperature diagram.	49
1.13. Relative density versus (a) relative stiffness, and (b) yield strength of currently produced porous NiTi. Different symbols (in the inset) indicate the processing methods. Open symbols represent open-cell foams; closed symbols represent closed-cell foams.	69
1.14. SEM micrographs of porous NiTi produced by three different methods; (a) SHS process (65±10 % porosity, 100-360 µm), (b) CF-HIP with argon expansion (42% porosity, 50-400 µm), and (c) MIM and sintering with NaCl spaceholder (prealloyed powders, 70 % porosity, 355-500 µm). (d) photograph of commercially-available porous NiTi implant produced by SHS process (Actipore™, Biorthex, Canada), used in a study for intervertebral fusion application.	74
2.1. Representative compressive stress-strain curve for a maximum strain of 5% (from foam H in Chapter 3). Evaluation method for loading and unloading stiffnesses, and for the unloading, shape-memory and plastic strains are illustrated, together with the phases expected (A - austenite, M – martensite, M' – detwinned martensite).	86
3.1. (a-c) SEM micrographs of initial powders: (a) NaF, (b) NaCl and (c) NiTi.	91

	12
3.2. SEM micrographs of 39.5% porosity foam H (densified by HIP and with salt removed): (a, b) resin-filled pores at low and high magnification, (c) unfilled pores.	94
3.3. SEM micrographs of 19.6% porosity foam HS (processed like foam H and additionally vacuum-sintered): (a, b) resin-filled pores at low and high magnification, (c) unfilled pores.	96
3.4. DSC curves of NiTi powder and foams H and HS.	98
3.5. Series of compressive stress-strain curves (load-unload) for increasing maximum strains for: (a) foam H; (b) foam HS. Curves are shifted along the y-axis for clarity. Arrows along the y axis for each curve represent the thermally-recovered shape-memory strain. The stress at which the sample is unloaded is marked with a dot. (c) final compressive stress-strain curve for foam HS up to maximum strain of 15.6%.	101
3.6. Loading and unloading stiffness as a function of maximum compressive strain for foam H and HS.	105
3.7. Unloading, shape-memory and plastic strain as a function of maximum compressive strain for: (a) foam H; (b) foam HS.	107
3.8. SEM micrographs of foam cross-sections with resin-filled pores: (a, b) foam H1 (HIP densified at 950°C, P=36%) and (c, d) foam HS1 (with additional 1250°C sintering, P=35%).	114
3.9. SEM micrographs of foam cross-sections with resin-filled pores: (a, b) foam H2 (HIP densified at 1065°C, P=32%) and (c, d) foam HS2 (with additional 1250°C sintering, P=32%).	115

	13
3.10. SEM micrograph of cross-section of foam HS2' (same process as HS2, except for longer sintering duration at 1250°C, P=32%).	117
3.11. DSC curves of NiTi powder and foams H1, H2, HS1 and HS2.	122
3.12. Compressive stress-strain curves for foams H1 and HS1 upon monotonic loading until onset of stress drop.	124
3.13. Series of compressive stress-strain curves (load-unload-recovery cycles for increasing maximum strains) for: (a) foam H1, including the last stress-strain curve of foam H produced with NaF space-holders (Chapter 3); (b) foam HS1; (c) foam H2. Curves are shifted along the x-axis for clarity. Arrows along the x-axis for each curve represent the thermally-recovered shape-memory strain. The stress at which the foam is unloaded is marked with a dot. Parameters used in evaluation method for loading and unloading stiffnesses, and for the unloading, shape-memory and plastic strains are illustrated, together with the phases expected (A - austenite, M – martensite, M' – detwinned martensite), in the stress-strain curve to 5% maximum strain in Fig. 3.13(a).	125
3.14 Loading and unloading stiffness as a function of maximum compressive strain for all foams.	128
3.15. Unloading, shape-memory, and plastic strain as a function of maximum compressive strain for all foams.	129
4.1. Micrographs of porous NiTi produced by PM combined with space-holder methods: a) MIM with NaCl [80]; b) HIP with NaF (section 3.1); c) HIP with NaCl (section 3.2); d) capsule-free HIP with NH <sub>4</sub> HCO <sub>3</sub> [61].	134

	14
4.2. Quasi-binary NiTi-Nb phase diagram.	136
4.3. Cross-sectional images of sintered near-equiatomic NiTi samples (a) S0 and (b) S40 at low (left) and high (right) magnifications.	140
4.4. Cross-sectional images of sintered (with Nb) near-equiatomic NiTi samples (a) SN0, (b) SN40 and (c) SN60 at low (left) and high (right) magnifications.	141
4.5. DSC result of sample S0, SN0, SN40 and SN60.	146
4.6. A series of stress-strain curves of samples (a) SN0, (b) SN40 and (c) SN60 showing load-unload-recovery cycles of maximum strain of 2%, 4%, 6% and 8%. In comparison, those of foam HS2 in the previous study made by HIP method is provided. Curves are shifted along the x-axis for clarity. Arrows along the x-axis for each curve represent the thermally-recovered shape-memory strain. The stress at which the foam is unloaded is marked with a dot.	149
4.7. Stress-strain curves of foams SN40 and SN60 compressed to fracture. Digital images below the plot show foam SN40 before (left) and after (right) compression.	151
4.8. Loading and unloading stiffness as a function of maximum compressive strain of foams SN0, SN40 and SN60.	152
4.9. Unloading, heat recovery and plastic strain as a function of maximum compressive strain of foams SN0, SN40 and SN60.	154
5.1 Comparison of DSC curves for as-received, as-sintered pre-alloyed NiTi powders, and as-sintered pre-alloyed NiTi with 40 vol.% NaCl space holders (particle size of 62-250 $\mu\text{m}$ ).	157

		15
5.2	Micrographs of NiTi foams made with various ranges of NiTi particle size; (a) 44-177 $\mu\text{m}$ (b) 44-106 $\mu\text{m}$ , and (c) <106 $\mu\text{m}$ , all having 40 vol% NaCl (106-250 $\mu\text{m}$ ) and sintered at 1250°C for 10 hours.	159
5.3	Micrographs of sintered NiTi foams using a mixture of NiTi powder (44-62 $\mu\text{m}$ , with Ni and Nb addition) and 60 vol% NaCl (106-250 $\mu\text{m}$ ) at 11850°C for 10 hours.	160
5.4	Micrographs of Ni-rich NiTi foams (50.8-51 at%Ni) sintered at 1250°C for (a) 10 hours, (b) 20 hours and, (c) 36 hours. Left micrographs were taken at low magnification and right at high magnification.	161
5.5	Micorgraphs of monolithic Ni-rich (51 at% Ni) NiTi sintered at 1250°C for 36 hours. Left micrographs were taken at low magnification and right at high magnification.	162
5.6	Micrographs of sintered Ni-rich NiTi (51 at%Ni) foam (a) before and (b) after CIP and subsequent sintering.	164
5.7	DSC curves for sintered (1250°C for 12 h) monolithic and porous (40 % porosity) Ni-rich (50.8 at% Ni) NiTi after heat treatment (homogenizing at 1000°C for 30 min followed by aging at 500°C for 2 h).	168
5.8	Relation between $M_s$ and Ni content in arc melting NiTi [126]. Black and white circles represent water quenching condition from 500°C; black and white squares from 400°C.	169
5.9	DSC result of 50.8 at% Ni-Ti foam sintered at 1250°C for 36 hours and heat treated at 1000°C for 30 minutes, followed with aging at 500°C for 1 hour, and water quenching.	170

	16
5.10 DSC curve of Ni-rich (51 at% Ni) NiTi foam produced by sintered at 1250°C for 36 hours, followed by heat treatment. The vertical lines show the testing temperatures (room temperature and body temperature), indicating the NiTi phases present in each case.	171
5.11 Stress-strain curves of a Ni-rich (50.8 at%Ni) NiTi foam at (a) room temperature (foam R), and (b) body temperature (foam B).	173
5.12 DSC curve of Ni-rich (51 at% Ni) NiTi foam produced by sintered at 1250°C for 36 hours, followed by heat treatment. The vertical lines show the testing temperatures (room temperature), indicating the NiTi phases present in each case.	176
5.13 Stress-strain curves of a Ni-rich (51 at%Ni) NiTi foam (a) R' and (b) S', at room temperature.	177
5.14. Measurement procedures for the diffraction measurement: (a) schematic depiction of the beam path (beam size of 0.1 mm) used in <i>in situ</i> x-ray diffraction measurements, in order to ensure sampling of a sufficient volume; (b) load-unload-recovery loops for maximum strains of 3% and 6%. Dots indicate points where diffraction patterns were taken (filled dots during loading, unfilled dots during unloading, and half-filled dots after heat recovery).	182
5.15. Diffraction patterns of foam R' (a) at zero stress and (b) at 420 MPa. The magnified diffraction pattern in (b) in angles of 0-90° is shown in (c).	183
5.16. Indexed diffraction patterns for austenite (A) and martensite (M) in the foam at 0 MPa and 420 MPa.	184

	17
5.17. Evolution of Normalized diffraction intensity near peaks A(100) and M(100) (a) during loading from near-zero stress to maximum stress and (b) upon unloading from maximum stress to zero stress and after heat recovery.	185
5.18. Normalized areas of austenite and martensite reflections as a function of applied anelastic strain for a maximum applied strain of (a) 3% and (b) 6%. Superimposition of normalized areas of A(100) and M(100) as a function of strain up to 3% and 6% is shown in (c). Filled, unfilled and half-filled symbols represent the values upon loading, unloading and after heat recovery.	188
6.1 Microstructure of current NiTi foam (arrows indicate fenestration).	192
6.2 Mass loss versus time with and without ultrasonic agitation (Sample 1).	200
6.3 Microstructure of NiTi-F foams, Sample 13, (a and c) and NiTi-Cl foams, Sample 11.1, (b and d) before and after Keller's acid treatment for 60 min, respectively.	201
6.4 Effect of starting microstructure on mass loss percent and increase in porosity after 1 hours treatment. Squares represent NiTi-F foams (Sample 13 and 14) and triangles represent NiTi-Cl foams (Sample 11.1 and 11.2). Solid indicates Keller's reagent and unfilled symbol indicates 1 part HF treatment.	202
6.5 Microstructure of (a) NiTi-F foam (Sample 14) and (b) NiTi-Cl foam (Sample 11.2) after 1 part HF/HNO <sub>3</sub> acid treatment.	203
6.6 Effect of acid type and concentration on foam porosity.	205
6.7 Microstructure of foam treated by (a) 2 part HF for 30 min (Sample 4), (b) 1 part HF for 90 min (Sample 5), and (3) 0.5 part HF for 180 min (Sample 6).	206

	18	
6.8	Effect of changing acid and time. Data set is labeled in term of (acid type, treatment time, changing acid). CA stands for changing acid.	208
6.9	Microstructure of foams treated by Keller's reagent (Sample 8) (a), 1 part acid (Sample 9) (b), and 0.5 part acid (Sample 10.2) (c) with changing acid method for 3 hours. Left side presents an image at center and right is an image at edge of the treated foam.	211
6.10.	Microstructure of foams treated by 1 part acid for 3 hours without changing acid. (Sample 7).	211
6.11	Comparison of an optical micrograph (left) and Image J black and white image (right) of a control sample.	212
6.12.	Stress-strain curves of control sample (32% porosity) and an acid treated sample (40% porosity).	214
6.13.	Stages in the modeling of foam HS2 based on microtomographic image analysis; (a) 2D cross-sectional image from microtomography, showing solid (black) and pore (white) space; (b) 3D surface reconstruction from AMIRA; and (c) 3D solid model showing a full finite element mesh.	219
6.14.	Comparison of stress-strain curves of foam HS2 from experimental testing and FE simulation for maximum strain of 2%. (Courtesy of Panico and Prof. Brinson).	221
6.15.	Volume fraction of martensite as a function of strain and temperature.	222

## List of Tables

1.1	Mechanical properties of bone.	23
1.2	Mechanical properties of bone implant materials.	25
3.1.	Transformation temperatures and enthalpy on heating and cooling for NiTi powder, foam H and HS.	98
3.2.	Transformation temperatures and enthalpies for as-received NiTi powders and foams H and HS.	122
4.1.	Processing parameters and conditions of porous NiTi.	138
4.2.	Foam characteristics of near-equiatomic NiTi foams with Nb addition.	143
4.3	Phase transformation parameters of near-equiatomic NiTi samples	147
6.1	Summary of acid treatment conditions. Note: Keller's stands for Keller's reagent; 1 part HF stands for 1 part ratio of 1HF:4HNO <sub>3</sub> acid solution in diluting deionized water.	198

## CHAPTER 1

# Introduction

This chapter evaluates the current demand for bone replacement materials, and discusses recent progress in the field of porous metallic implants designed to meet this need. This is followed by a comprehensive survey of research into porous NiTi implants, focusing on processing-, properties- and biologically-related aspects. Critical factors affecting the next generations of porous NiTi for bone implant applications, and their relationship to the specific objectives of the current study, are identified as they arise from this earlier research.

## 1.1 Bone implants

### 1.1.1 Demand for bone implants

Medical implant demand in the U.S. is expected to rise 9.3 percent annually through 2011. Although most of these implants are expected to be cardiac implants such as stents, orthopedic implants such as bone cements, tissue, and spinal implants are also in high and increasing demand. In the early part of the last decade (2001-2002), the world orthopedic implant market had net sales in the range of \$14-15 billion, with expected annual gains of 7-13% [1, 2].

Of the \$14 billion spent on orthopedic implants in 2002, \$12 billion was spent on joint replacements such as knee and hip replacements. In 2002–2003, a total of 617,000 bone and joint

procedures were recorded by the NHS in England alone, over 77,000 of which were primary hip operations. Moreover, an estimated additional 19,000 (ca. 20%) hip operations are performed annually within the private sector; thus the true number of worldwide hip replacement procedures performed annually is likely to be well in excess of 100,000 [2].

The tremendous increase in demand for implants reflects the need to restore bone function and comfort in an expanding patient population, which is caused by many factors:

1) Aging population. As life expectancy increases, the median age of the population increases as well. The 65+ demographic has an elevated need for bone implants, and is projected to increase globally by 2–3% per year between 2000 and 2010;

2) Expanding pathology. In an aging population, implants are now necessary for treating a wider variety of pathologies, including cancers and degenerative diseases like osteoporosis;

3) Increased revisions. Most bone implants have a limited lifetime of 10-20 years; as life expectancy increases, more of these implants must be replaced through revision surgery.

4) Changes in lifestyle and expectations. The need for implants is also increasing in younger demographics, due to changes in lifestyle and increased overall expectations regarding quality of life. Sports-related injuries and corrective/cosmetic surgery, for example, create increased demand for implant materials in the younger population;

5) Technological advances. Improvements in the availability, flexibility, and quality of implants, and in the surgical techniques associated with them, have made bone implants viable for a wider range of patients and pathologies.

Conventional autografting and allografting (replacement of missing bone with the patient's own tissue, or that of a donor, respectively) alone could not adequately supply this high demand, since the amount of bone that can be safely harvested is limited, and the additional

surgical procedures required may be complicated by donor-site pain and morbidity, inconsistent healing, and disease transmission. Consequently, synthetic bone implant products are an important alternative that not only overcomes the problem of an inadequate supply of material, but can also avoid complications.

The ideal synthetic bone implant should be conceived of, however, not only as a filler for bone cavities but as a means to encourage osseointegration, i.e. as a scaffold for guiding bone regrowth and helping the body to repair its own lost tissue. Bone in-growth on a scaffold strengthens the damaged tissue by forming a bridge between the existing bone and the implant material. For successful bone regeneration, the interaction of three basic elements - bone cells, growth factors, and an appropriate matrix scaffold - is required. While one branch of research in bone implants (e.g., bone tissue and bioactive surface engineering, and bone-repair therapies) concerns itself with understanding the mechanisms of osteoinduction, and the complex interactions between local chemical and physical factors at the implant site, another, represented in this work, focuses on developing the base matrix material of the implant itself, making it suitable for the implant environment and accommodating towards bone ingrowth.

### **1.1.2 Requirements for bone implants**

In promoting healthy bone regeneration, the key function of any orthopedic graft material is to achieve an initial stabilization of the local tissue, while still permitting subsequent bone healing and/or ingrowth. To create such an ideal implant, the following basic properties have been identified as essential: 1) biocompatibility with bone, to obtain a positive response with the host's immune system, encourage osseointegration (i.e., a strong and intimate implant-to-bone interface), and enhance bone ingrowth; 2) mechanical compatibility with bone, to mimic natural

bone's response to loading as closely as possible, and reduce the effects of stress shielding; and 3) similarity in architecture with natural bone, to offer an optimal environment for bone ingrowth.

#### 1.1.2.1 Biomaterials for bone implant applications

Typically, biomaterials are defined as non-viable materials used in a medical device, which are highly biocompatible with the surrounding biological system and well integrated in the host tissue, and which do not elicit an immune, inflammatory, or toxic response beyond some tolerable level [3]. Since the regenerative and remodeling processes in bone are directly triggered by stresses and strains (i.e., bone subjected to mechanical loading regenerates, while bone not subjected to loading atrophies), mechanical behavior that allows proper load transfer to the surrounding bone is a necessary component of bone replacement biomaterials. In other words, selection of biomaterials for biomedical applications must be based not only on biological performance, but also physical functionality (i.e., mechanical properties matching those of bone, Table 1.1). In this section, therefore, bio- and mechanical-compatibility of materials for bone implants will be discussed together.

Table 1.1 Mechanical properties of bone [2, 3]

Bone components	Compressive strength(MPa)	Tensile strength(MPa)	Elastic modulus(GPa)
<b>Hard tissues</b>			
Tibia	159	140	18.1
Femur	167	121	17.2
Radius	114	149	18.6
Humerus	132	130	17.2

Cervical	10	3.1	0.23
Lumbar	5	3.7	0.16
<hr/>			
Bone components	Compressive strength(MPa)	Tensile strength(MPa)	Elastic modulus(GPa)
<hr/>			
<b>Cortical bone</b>			
longitudinal	193	133-150	17-25
transverse	133	50	12
<b>Cancellous bone</b>			
longitudinal	3.6-9.3	-	0.26-0.90
transverse	0.6-4.9	-	0.01-0.40
HA	-	9-120	80-117
collagen	-	100	1.5
<hr/>			

Bone implants have been made using biomaterials from a variety of categories, such as polymers, ceramics, metals, and their composites. Some examples of these materials and their mechanical properties are listed in Table 1.2. Generally speaking, polymers provide good biocompatibility and biodegradability, but inadequate mechanical properties for meeting the requirements of load bearing in the implant. Ceramics can also have good biocompatibility, but often poor mechanical properties as well, such as low strength, poor fracture toughness, limited fatigue resistance, and inherent brittleness. Metals typically have good mechanical properties, with excessively high strength and stiffness, but show poor biocompatibility, sometimes with the release of dangerous metal ions, which cause eventual unsuccessful bone-implant integration and require removal of the implant. As a whole, the materials above can be said to have adequate or good biocompatibility, but their mechanical properties either greatly exceed, or greatly underperform, those of bone. Composite materials with engineered interfaces (specifically,

interfaces mimicking the structure of the hydroxyapatite (HAP) crystal–collagen fiber interfaces in real bone), offering a combination of biocompatibility, mechanical strength, and toughness, have recently become another option. However, the interfacial behavior in these systems is not well understood, and insufficiently characterized in literature.

Table 1.2 Mechanical properties of bone implant materials [3-5]

Materials	Compressive strength(MPa)	Tensile strength(MPa)	Elastic modulus(GPa)
<b>Ceramics</b>			
Zirconia	2000	820	220
Alumina	4000	300	380
HAP	600	50	117
Bioglass	1000	-	75
AW glass-ceramic	1080	-	118
<b>Polymers</b>			
HDPE	25	40	1.8
UHMWPE	28	21	1
PMMA	144	21	4.5
PTFE	11.7	28	0.4
PEEK	-	139	8.3
<b>Metals</b>			
Pure Ti		785	105
Ti alloys	590-1117	900-1312	55-177
Co-Cr alloys	450-1896	600-1896	200-253
Stainless steel	170-310	465-950	189-205
Tantalum	50-70	63	2.5-3.9
NiTi (matensite)	300-800	800-2000	65-78

Among the conventional biomaterials above, metallic implants have been recognized as the most desirable materials for bone implants, because of their crucial toughness and fatigue

resistance in load-bearing applications. An implanted material must be strong enough, and durable enough, to withstand severe physiological loads over the years. The average load on a hip joint is estimated to be up to three times body weight, and the peak load during other strenuous activities such as jumping can be as high as 10 times body weight. In addition, hip bones are subjected to cyclic loading as high as  $10^6$  cycles per year [6].

Although metallic implants can meet these challenges, the susceptibility of metals to corrosion (and the resulting local and systemic effects), and the difficulty of achieving a suitable match between implant strength and stiffness and the behavior of bone, are still central aspects for consideration. Regarding the first issue, Ti and its alloys, 316L stainless steel, and Co–Cr have received the most attention, due to excellent corrosion resistance resulting from formation of passivating stable surface oxide layers (especially in Ti alloys). Many studies have reported success in reconstructive surgery using these materials [3]. However, the second issue, and particularly the high stiffness of metallic implants, is still a concern. It is estimated that 20% of hip replacement surgeries simply replace a pre-existing, unsuccessful implant procedures. Indeed, most hip implants must be replaced after 10-15 years [3], which can lead to costly and dangerous revision surgery. Of all revisions due to failed implants, 82% are necessitated by loosening of the implant-tissue interface, instability, or osteolysis (degeneration of bone formed around the implant) [7], which are believed to be caused by a phenomenon known as stress shielding.

It has been shown that the degree of stress shielding in bone-implant coupling is directly related to the difference in stiffness between the bone and implant material. As the stiffness of the bone implant is generally higher than that of the bone, loading on the bone is reduced by load transfer from bone to implant, which leads to less bone regeneration and more resorption.

Moreover, the modulus mismatch leads to excessive relative movement between the implant and the bone. Relative movements greater than a critical level will inhibit bone formation and ingrowth, and will result in fibrous tissue ingrowth or, in extreme cases, fibrous tissue encapsulation, thereby preventing proper implant osseointegration altogether [8].

One alternative to overcome stress-shielding effects is the use of porous materials. In addition to minimizing stiffness mismatch, porous materials allow bone in-growth during the healing process, with an expectation of osteoconduction and tight interlocking between the real bone and its artificial replacement. There are two main categories of porous implant materials: (1) solid implants with porous coatings; and (2) implants with pores distributed throughout. The first category, examples of which are porous hydroxyapatite (HAP) films on titanium or silicon substrates, generally shows poor bonding with bone, due to the limited depth of the porous region at the interface, and has unsatisfactory machinability due to its brittleness [9]. For these reasons, materials in the second category have attracted more interest in the last decade.

Generally speaking, materials with pores distributed throughout their volume can reduce stiffness mismatch (as explained in section 1.2, on the properties of porous materials), provide good anchorage and a high degree of biological fixation, due to bone ingrowth into the pores (such anchorage minimizes the need for mechanical fixation by screws and bone cements), and allow stresses to be transferred efficiently and consistently from the implant to the bone, leading to good long-term stability [10].

### 1.1.2.2. Architectures of bone implants

Porous implants have been preferred to solid implants, due to the permeability of open-pore structures, which promotes migration and proliferation of osteoblasts and other cells, as well as vascularization. Besides allowing for more natural healing, ingrowth of new bone tissue into implants also improves mechanical interlocking between the implant and the remaining natural bone, providing greater mechanical stability and long term durability at this critical interface [11]. To most accurately match an implant to bone structure (shown in Figure 1.1), it is first necessary to understand that bone structure, particularly with regard to porosity, pore size, connectivity and surface geometry.

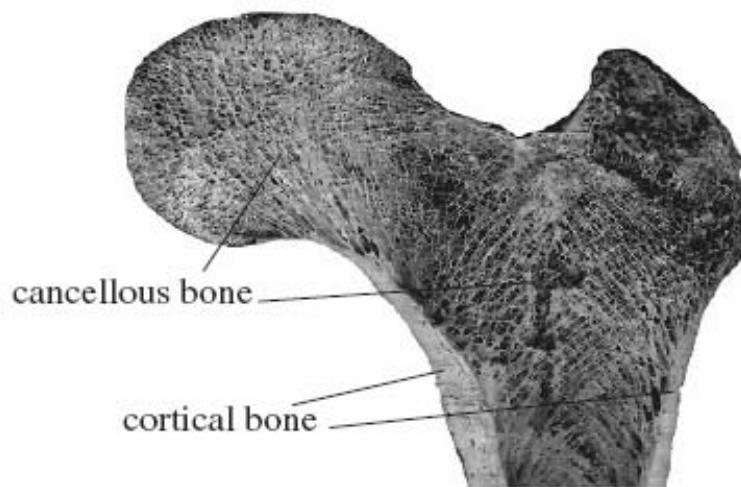


Figure 1.1. Bone structure in sectioned human femoral head [2].

*Porosity* is defined as the fraction of void space in a solid, and it is a morphological property independent of the material. There are two kinds of porosity: open porosity (where pores are connected to the outer surface of the body, and to each other) and closed porosity (where pores are isolated from the surface or from each other). Implants with high open porosity

are expected to perform better than those with low open porosity. Open and interconnected porosity is extremely important because the bone will grow in the interconnected pore channels near the surface, thereby maintaining its vascularity and long-term viability, and enabling it to fixate to the implant more firmly [12].

From the standpoint of ingrowth, therefore, fully-interconnected pore geometry in a highly porous structure with large surface area to volume ratio seems to be the ideal implant structure. However, biological studies have shown that either no significant difference exists between highly-porous and less-porous scaffolds, or the advantage of highly-porous scaffolds diminishes over time. Since high porosity sacrifices the mechanical strength of the scaffold, which can be critical for regeneration in load-bearing bones, a balance between microstructure and mechanical properties should be made.

*Pore size* also affects bone ingrowth [13]. In general, larger pores favor direct osteogenesis, since they allow vascularization and high oxygenation, while smaller pores result in osteochondral ossification, although the type of bone ingrowth depends on the biomaterial and the geometry of the pores. There is, however, like in porosity, an upper limit in pore size set by constraints associated with mechanical properties. The extent to which pore size can be increased while maintaining mechanical requirements depends on many factors, including the nature of the biomaterial and the processing conditions.

The minimum pore size required to regenerate mineralized bone is generally considered to be 100  $\mu\text{m}$ . Somewhat larger pores (100–150 and 150–200  $\mu\text{m}$ ), which may be expected to improve osteoconduction, indeed showed substantial bone ingrowth. Between 150  $\mu\text{m}$  and 400  $\mu\text{m}$ , however, there is no agreed-upon effect of pore size [14-16]. One study, for instance,

showed that there was a decrease in bone ingrowth when pore sizes increased in the range of 175  $\mu\text{m}$  to 325  $\mu\text{m}$  [17].

Pore sizes less than 100  $\mu\text{m}$  give increased bone ingrowth with increased pore size [10, 18]. However, pores 75–100  $\mu\text{m}$  in size resulted in ingrowth of unmineralized osteoid tissue and prevented vascularization, and the resulting lack of blood prevented bone growth [11]. Even smaller pores (10–44 and 44–75  $\mu\text{m}$ ) were penetrated only by fibrous tissue.

During testing under non-load-bearing conditions in a rabbit model, bone ingrowth was similar in all implants with small pore sizes (50, 75, 100 and 125  $\mu\text{m}$ ), suggesting that 100  $\mu\text{m}$  may not be the critical pore size for non-load-bearing conditions [19]. Thus, although the consensus from many studies seems to be that the optimal pore size for bone ingrowth is 100–400  $\mu\text{m}$ , this is still controversial. One reason for the continuing controversy may be that most data reflect only an average pore size, and that interconnectivity of pores is rarely if ever considered.

The pore-pore interconnections (sometimes called mesoporosity or throats, but which are hereafter called '*fenestrations*') are the pathways between pores that favor cellular and vascular penetration and promote bone ingrowth inside the pores. *In vitro*, the minimal necessary fenestration width (or 'size') is 20  $\mu\text{m}$ , but the most favorable width for cell penetration is >40  $\mu\text{m}$  [20]. *In vivo*, a fenestration size of over 20  $\mu\text{m}$  allows cell penetration and chondroid tissue formation within macropores; however, a fenestration size over 50  $\mu\text{m}$  can ensure mineralized bone formation. On the other hand, if the fenestrations are too small, growing cells become more likely block the windows, causing the death of any cells located in the central portion of the implant by choking off the supply of nutrients. Otsuki et al. also observed in bioactive titanium

implants that pores containing well-differentiated cells had wider fenestrations than pores containing poorly-differentiated cells, and narrow fenestrations inhibited tissue differentiation in pores [21]. Fenestrations act only as pathways to pores, thus the appropriate fenestration sizes for materials of varying average pore size may themselves vary. For example, Flautre et al. found that a 130  $\mu\text{m}$  fenestration size and a 175-260  $\mu\text{m}$  mean pore size provided the best osteoconduction results at the center of a HA ceramic at 12 weeks after implantation in a rabbit model [22].

*Surface roughness* is another feature found to accelerate tissue differentiation and bone ingrowth. It has been shown that rough surfaces anchor fibrin matrices better than smooth surfaces, and in this way facilitate the migration of osteogenic cells on the material's surface. For some smooth implant surfaces (e.g. that of titanium), coating with bioactive materials [23] or applying chemical and thermal treatments can induce rougher and more bioactive surfaces [24].

## **1.2 Properties of porous materials**

In this section, definitions for the key characteristics of porous materials are provided, because these definitions will be used throughout the remainder of the dissertation. To make clear at this early stage how and why porous materials offer superior performance as implant materials, the relationships between pore characteristics and physical and mechanical properties are also discussed.

### 1.2.1 Definitions of porous characteristics

*Porous materials* (or *foams*) consist generally of two main features: 1) solid material that forms a 3D network structure (sometimes called a *matrix*) responsible for the overall stability of the porous structure; and 2) voids (also called *pores* or *cells*), which are empty space interspersed in the material matrix. Two subfeatures of the solid matrix can also be defined: 1) *struts and walls* are structural elements with high aspect ratio that surround pores; and 2) *nodes* are structural joints, usually with low aspect ratio, at which three or more struts or walls meet. In homogeneous porous structures, the sizes (diameters and lengths) and shapes of the struts and nodes are related to the average diameters and shapes of pores.

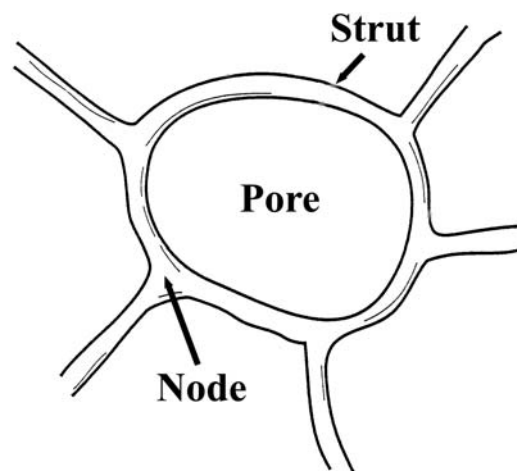


Figure 1.2. Schematic depiction of a closed-cell foam, with the key structural features of foams indicated.

The ratio of solid matrix mass to the total volume of a foam determines the *foam density* ( $\rho$ ), and the ratio of void volume to total volume determines its *porosity* ( $P$ , usually presented as a fraction or percentage). The relationship between foam density and porosity is  $P = 1 - \rho/\rho_s$ , where  $\rho_s$  is the density ( $\rho = \text{mass}/\text{volume}$ ) of the solid matrix material.

When porosity is small ( $<5\%$ ), pores tend to be isolated and the foam is called a *closed-cell foam* containing *closed porosity*). As porosity increases, a percolation threshold can be reached where pores will start to impinge and interconnect, yielding an *open-cell foam* containing *open porosity*. In cases where both open porosity and closed porosity coexist in a foam, their sum is referred to simply as *total porosity*.

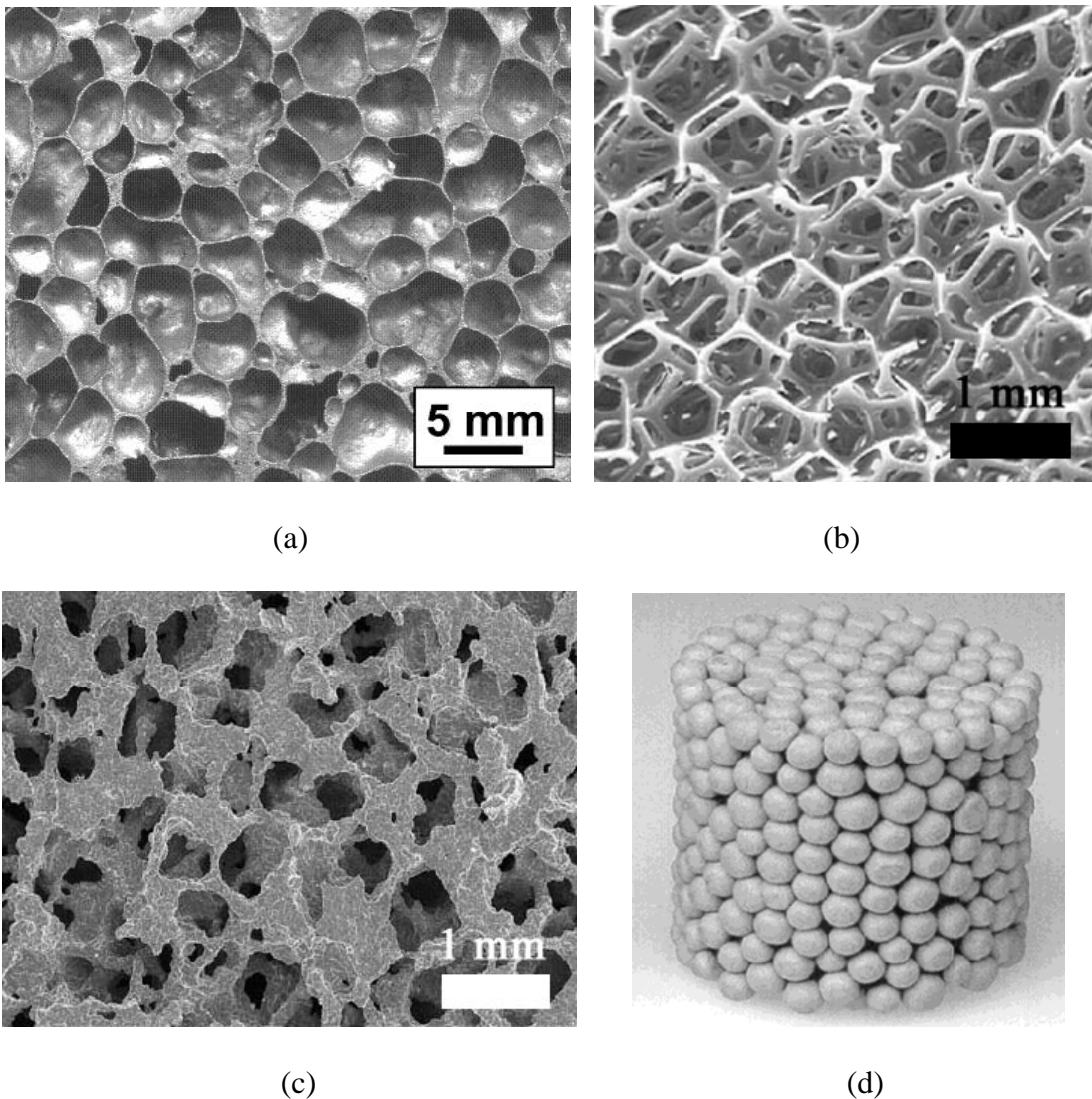


Figure 1.3 Example of a) closed-cell foam, made by decomposition of  $\text{TiH}_2$  in molten aluminum, b) low-density open-cell polyurethane foam [25], c) high-

density open-cell NiTi foam [26], and d) mixed open and closed cells, made by sintering of a bed of hollow stainless steel spheres [27].

For open structures, the size and shape of the connections between pores become important structural parameters. Interconnections between adjacent pores (or *fenestrations*) are the doorways for mass transport between pores, and accessibility to the pores from outside the foam. The *fenestration size* is a measure of the window size between adjacent, connecting pores.

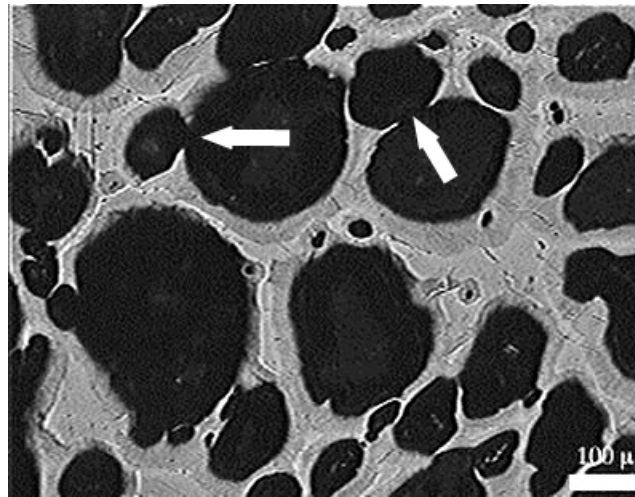


Figure 1.4. Example of a Ti foam with small fenestration size, processed by expansion of entrapped argon gas. Fenestrations between pores are indicated by arrows [28].

### 1.2.2 Pore-dependent properties of porous materials

Beside the obvious effects of porous structures in materials, such as light weight and high specific surface area, other properties, such as structural, mechanical, electrical and thermal properties, can be altered. In the context of bone implants, the first two properties are most important and will therefore be discussed here; details of the effects of porosity on electrical, thermal, and various other properties can be found elsewhere [29].

### 1.2.2.1 Structural properties

The advantage of high specific surface area is more pronounced in porous materials with open structures, due to the ability of such materials to transmit fluids or gases (a property referred to as *permeability*). For bone implants, permeability is an important feature, as it controls the migration of cells as well as the diffusion of nutrients and waste through the implant, which determine the success of bone ingrowth and thus also the quality of fixation between the implant and the surrounding bone (section 1.1.2).

To define the permeability of a porous medium rigorously, Darcy's law is used to relate the permeability ( $k$ , in units of squared length) to relevant macroscopically-defined length scales:

$$k = \frac{Q.l.\mu}{\Delta P.A} \quad \text{Equation 1.1}$$

where  $Q$  is the volumetric flow rate,  $A$  is the cross-sectional area over which this flow takes place,  $\Delta P$  is the pressure drop across the porous medium in the direction of flow,  $l$  is the length over which that pressure drop takes place, and  $\mu$  is the fluid viscosity.

Permeability is influenced by pore characteristics such as porosity, pore size and interconnectivity in the following ways. When the pore structure is uniform and isotropic, high porosity is required to allow highly-accessible pores. Large pore size is also desirable for enhancing permeability; as described by flow laws in foams, permeability is proportional to pore size squared [30]. For bone implants, an upper limit for pore size is, however, found in the form of a minimum necessary specific surface area (specific surface area scales roughly as the inverse of the square of the pore size). Fenestration size also influences tissue ingrowth and fluid, oxygen, and nutrient transport by permeation throughout the implant. It has been found that

porous structures made of large pores (with high porosity) joined by large fenestrations may play a key role in cell immigration and bone formation [31].

#### 1.2.2.2 Mechanical properties

It is well-known that having porosity in a material is generally quite detrimental to its mechanical properties. However, this fact works in the favor of bone implants made from strong materials such as metals, as porosity can be used to match implant mechanical properties (i.e. stiffness and strength) with those of bone, while still providing high porosity for ingrowth (polymers, it is noted, cannot provide the desired mechanical properties and the desired stiffness simultaneously, due to their lower intrinsic strength and stiffness). This property matching reduces *stress-shielding* effects, which shorten the life time of the implant through bone resorption and loosening.

Porosity reduces the effective load-bearing cross-sectional area, and pores act as stress concentration sites for strain localization and damage, decreasing both strength and ductility. Stress concentrations are worse in pores with angular, as opposed to rounded, edges. Inhomogeneous interconnected porosity causes an increase in the localization of strain, especially when pores cluster, while isolated porosity results in more homogeneous deformation. Pores also significantly affect fatigue behavior, being sites for crack nucleation, especially at or near the foam surfaces. Plastic deformation accumulates gradually at the pore corners and at highly clustered pores from cycle to cycle [32]. Plastic deformation will be more extensive and cracks will be more easily nucleated, especially in tension.

It should be noted that, since only compression testing on metallic foams with primarily open porosity was conducted in this dissertation, the discussion which follows will focus on mechanical behavior of open-cell metallic foams under uniaxial compression.

In term of compressive stress-strain behavior, typical open-cell metallic foams show linear elasticity (due to strut bending and buckling; it is noted, however, that some microplasticity can occur in this region, making it neither perfectly linear nor perfectly elastic) at low stress, followed by a long well-defined *plateau* region (associated with the collapse of pores by plastic deformation), and then a rapid increase in stress (compressive *densification*). For closed-cell foams, similar behavior is observed, except for a small increase in stress with increasing strain in the plateau region (instead of nearly-flat plateau) due to the fact that the *cell walls* (or *cell membranes*) separating the pores are also carrying stresses.

The compressive strength of a foam is defined as the stress where a significant and abrupt change in slope upon loading takes place, implying a macroscopic yield point of the structure. The stiffness of a foam cannot be extracted directly from the loading slope, as is normally done with solid materials; rather, the unloading slope is often used to avoid effects from reorientation and micro-deformation of struts, as mentioned above. To avoid confusion, such values are often referred to simply as *stiffnesses*, rather than Young's moduli (which implies ideally linear elastic behavior).

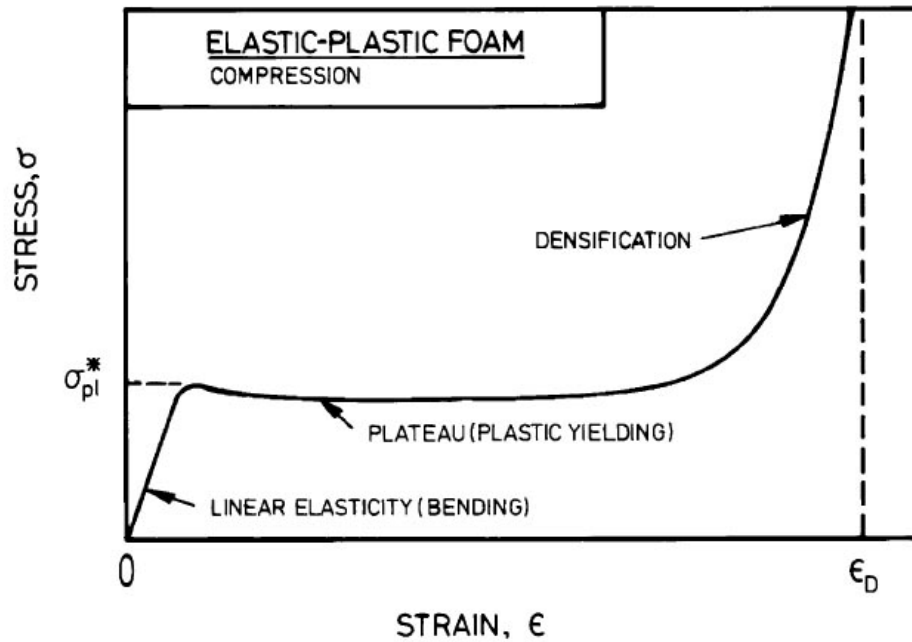


Figure 1.5. Example of a typical stress-strain curve in a open-cell foam [29].

The correlations of stiffness and strength with porosity were proposed by Gibson and Ashby in 1988 (they are generally called the Gibson-Ashby equations) [29], and are shown in equations 1.2 and 1.3:

$$\frac{E^*}{E_s} = C1 \left(1 - \frac{\rho}{\rho_s}\right)^{n1} \quad \text{Equation 1.2}$$

$$\frac{\sigma^*}{\sigma_s} = C2 \left(1 - \frac{\rho}{\rho_s}\right)^{n2} \quad \text{Equation 1.3}$$

where  $E$  is stiffness (or Young's modulus),  $\sigma$  is yield strength, and  $\rho$  is density. The superscripts \* and subscript  $s$  identify the properties of the foam and bulk material, respectively.  $C1$  and  $C2$  are constants representing the dependence of stiffness and strength on cell geometry, respectively;  $n1$  and  $n2$  are scaling exponents and vary with the type of material. For metallic

foams,  $C_1$  and  $n_1$  range from 0.1-4.0 and 1.8-2.2, while  $C_2$  and  $n_2$  range from 1.4-2.0 and 1.5-2.0, respectively.

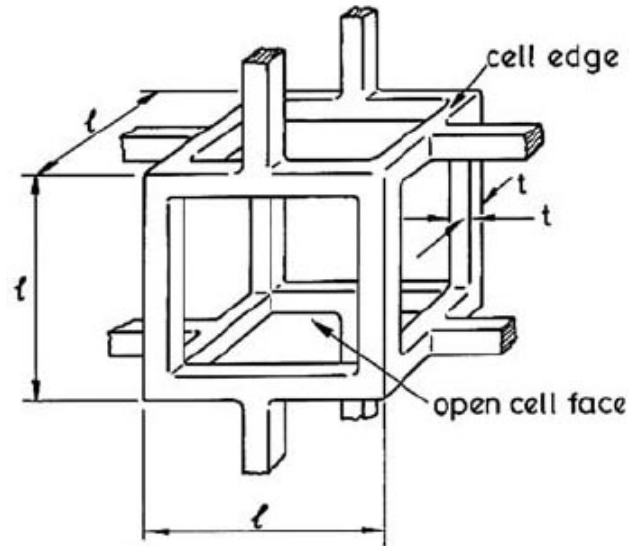


Figure 1.6. A unit cell of a foam corresponding to Gibson and Ashby equations.

To derive Equations 1.2 and 1.3, Ashby and Gibson considered a foam unit cell constituted by identical struts arranged in a cubic ( $l^3$ ) lattice (Figure 1.6), where the thickness of the struts ( $t$ ) is (for a given pore size  $l$ ) directly related to the density of the material. Despite the high interconnectivity and porosity characteristic of real foams (as shown in Figure 1.3), the geometry shown in Figure 1.6 is an oversimplification. In real foam architectures, a fraction of the material is accumulated in nodes, and there are flaws (such as microporosity) and non-uniform strut thicknesses, all of which have to be taken into account. These idealizations are usually empirically accounted for through the constants  $C_1$  and  $C_2$ .

More complicated porous systems such as trabecular bone can be discussed as an example. At different densities, trabecular bone forms different open-cell architectures (Figure

1.7), so the assumption that  $C$  takes a single value (i.e. that cell geometry is independent of density) is no longer applicable. Even though the  $C$  values are very scattered, the  $n_1$  and  $n_2$  values of trabecular bone are constant at 2 (Figure 1.8). This value of  $n_1$  indicates that the Young's modulus of trabecular bone varies as the density squared, and hence that linear elastic deformation is caused by strut bending. The fact that the compressive strength of trabecular bone follows the same scaling relation ( $n_2 = 2$ ), indicates strut buckling as a collapse mechanism (rather than brittle behavior, which might be expected from materials with  $n_2 = 3/2$ ).

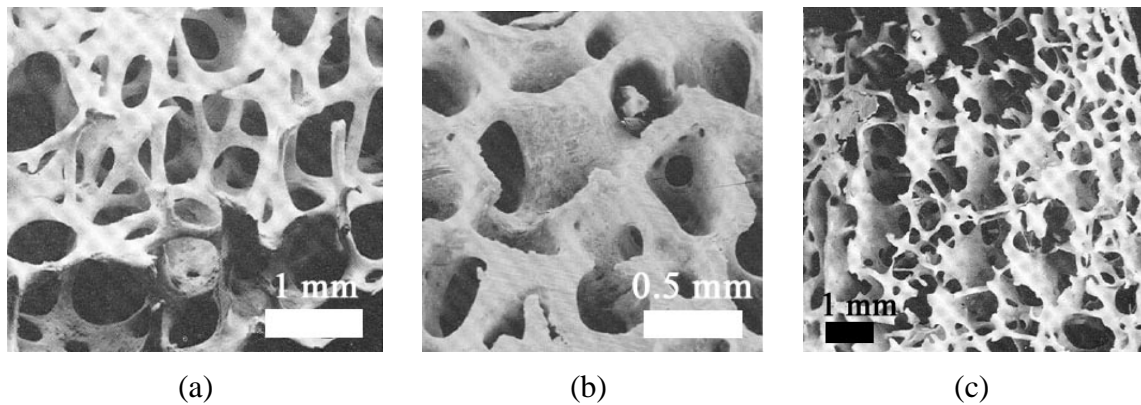


Figure 1.7. Different pore structures in trabecular bone from different sites: (a) low density, open-cell, rod-like structure in the femoral head, (b) higher density, perforated plate-like structure in the femoral head, and (c) intermediate density, showing an oriented structure with rods normal to parallel plates, in the femoral condyle [25].

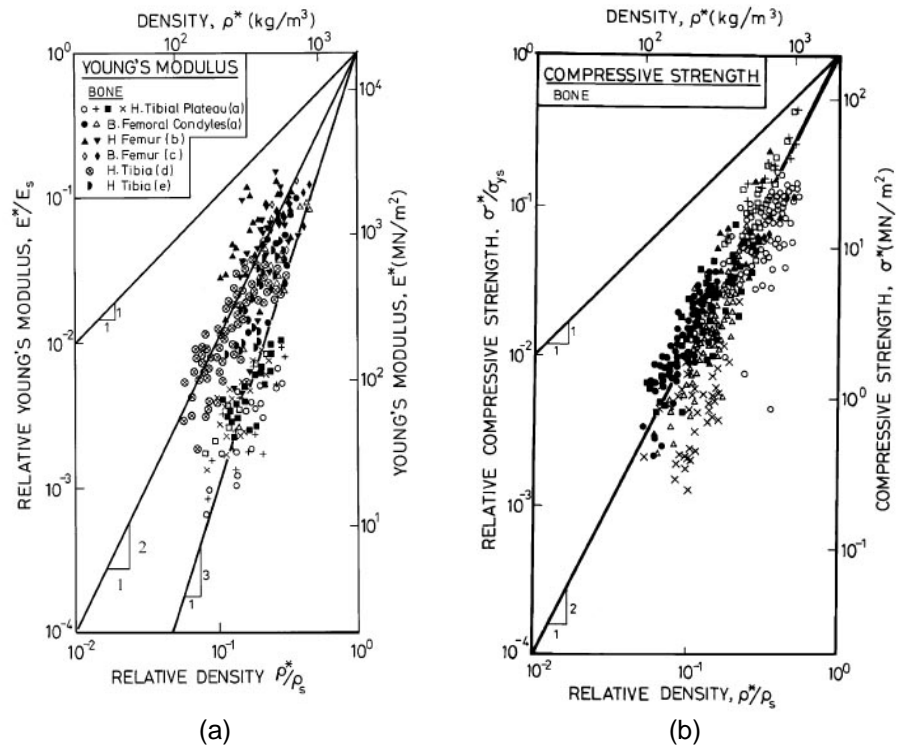


Figure 1.8. Plots of relative density and (a) relative Young's modulus and (2) relative compressive strength of trabecular bone [25].

### 1.3 Properties of Nickel Titanium alloy

NiTi or Nitinol (after NiTi and NOL, the Naval Ordnance Laboratory where the alloy was first discovered in 1962) is a well known multifunctional material, due to its superelasticity and shape memory effects. It has been used in medical applications since the 1970s, for instance in innovative hingeless graspers, stents, baskets, and MRI compatible needles for use in surgical robots. In this section, general information on NiTi that relates to this work, including micro- and macroscopic structure, shape recovery mechanisms, and mechanical properties, will be presented.

### 1.3.1 Macroscopic and microscopic structure in NiTi

According to the Ni-Ti phase diagram (Figure 1.9), NiTi is an ordered intermetallic compound centered on the equiatomic composition 50 at% or 55 wt% Ni, though the concentration range of technical interest is somewhat broader, between 49 and 52 at% Ni. These compounds usually exist as metastable phases down to room temperature. However, at low temperatures (such as room temperature) the composition window of the NiTi compound is very narrow, and so Ni-Ti based alloys often contain precipitates of secondary intermetallic phases distributed in a homogeneous matrix, either Ni<sub>3</sub>Ti on the Ni-rich side or NiTi<sub>2</sub> on the Ti-rich side. These phases modify the ratio of Ni and Ti remaining in the matrix, and thereby change its mechanical properties. They are difficult to remove after formation, since they are more stable than NiTi except at high temperatures. NiTi<sub>2</sub> can be especially harmful, as it often occurs near or on grain boundaries, and therefore causes embrittlement as well as accelerated corrosion.

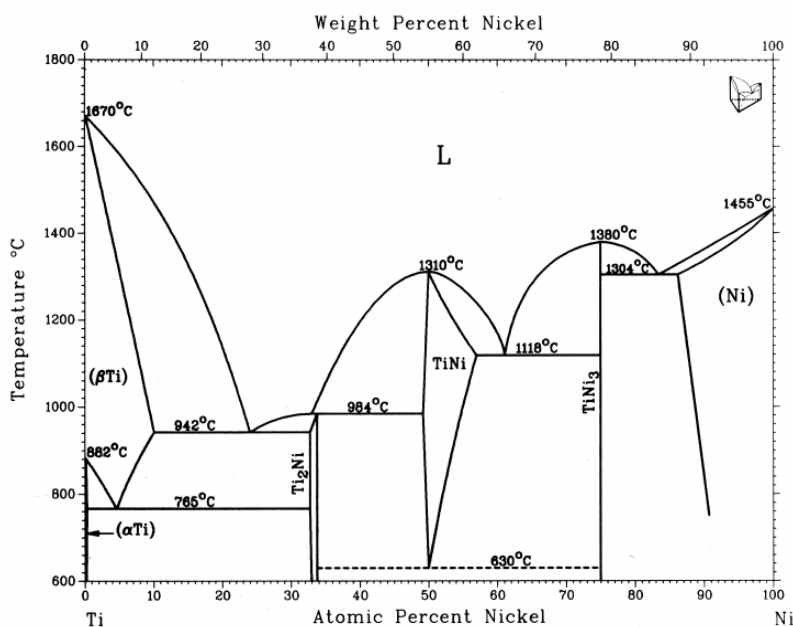


Figure 1.9. The Ni-Ti binary phase diagram [33].

Under solution-annealed conditions, near-equiatomic NiTi alloys are known to exhibit two different phases: the high symmetry, cubic B2 austenite (A) and the low symmetry, monoclinic B19' martensite (M). The austenite phase exists at relatively higher temperature (it is often called the high-temperature phase), and the martensite at lower temperature (low-temperature phase). In some cases and under certain conditions, including thermal cycling, cold working, partial annealing, and ageing, an intermediate trigonal R-phase (R) may appear between the austenite and the martensite.

### 1.3.2 Phase transformation behavior

The martensitic transformation (the transformation from austenite to martensite) can occur when the free energy of martensite becomes less than the free energy of austenite, i.e. below a critical temperature  $T_0$  at which the free energies of the two phases are equal. However, the transformation does not begin exactly at  $T_0$  but, in the absence of stress, within a finite temperature interval due to undercooling.

Upon cooling, austenite changes to martensite between the martensite start ( $M_s$ ) and martensite finish ( $M_f$ ) temperatures (this is called a martensitic transformation or forward martensitic transformation), while the reverse transformation of martensite to austenite occurs between the austenite start ( $A_s$ ) and austenite finish ( $A_f$ ) temperatures (this is called a reverse martensitic phase transformation). These upper and lower bounds of transformation are called *phase transformation temperatures*, are dependent on composition and processing, and can be determined by differential scanning calorimetry (DSC). Sometimes the peak of transformation (defined as  $M_p$  and  $A_p$  for martensitic and reverse martensitic phase transformation, respectively) is identified instead of transformation temperatures. The operating temperature of NiTi, in

relation to these transformation temperatures, determines the phases present (i.e. complete austenite above  $A_f$ , complete martensite below  $M_f$ , and a mix of phases between these temperatures).

The martensitic transformation is a *thermoelastic* solid-state phase transformation process, which refers to *diffusionless* crystal structure changes that proceed by the ‘shear-like’ motion of crystallographic planes at the transformation interface. Therefore, NiTi is capable of rearranging its atomic lattice structure to accommodate relatively large amounts of inelastic deformation, and subsequently recover that deformation after load removal, or upon the application of heat.

The martensitic transformation can be triggered either by introducing a temperature change, or by imposing a stress state in the material. The relationship between temperature and stress (as regards transformation) has been expressed in a Clausius–Clapeyron type equation as:

$$\frac{d\sigma}{dT} = -\frac{\rho\Delta S}{\varepsilon_t} = -\frac{\rho\Delta H}{T_o\varepsilon_t} \quad \text{Equation 1.4}$$

where  $\rho$  is the density of the transforming body,  $\Delta H$  is the enthalpy change of the transformation,  $T_o$  is the equilibrium temperature of the transformation, which is determined by the associated enthalpy and entropy changes, and  $\varepsilon_t$  is the linear strain of the transformation in the direction of the uniaxial stress. This equation is commonly interpreted as describing a linear relationship between the stress and temperature, meaning that a decrease in temperature is equivalent to an increase in stress.

Therefore, as the test temperature decreases, an increase in stress results, thereby a lower value of critical stress is required to induce transformation. Moreover, accompanying the

decrease of the forward transformation temperature, the critical stress to induce the transformation at a given temperature increases.

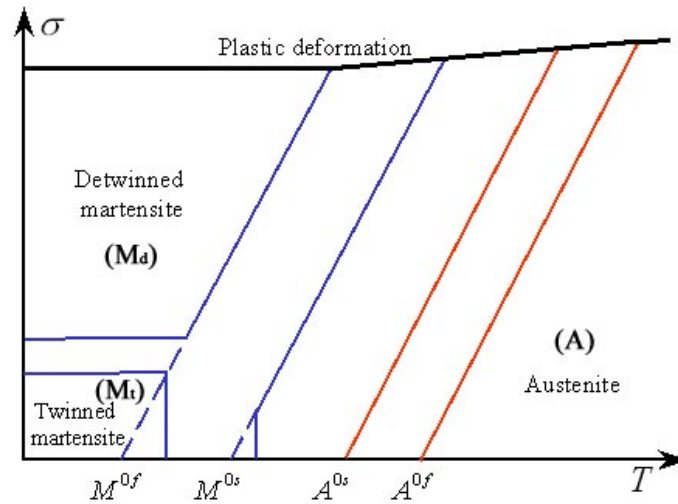


Figure 1.10. Stress-temperature phase diagram of NiTi.

### 1.3.3 Shape memory effect and superelasticity

The two fundamental properties of NiTi associated with this phase transformation are the shape memory effect (SME) and superelasticity (SE). Which mechanism dominates depends on the phases present: the shape memory effect is observed when NiTi contains martensitic phases, while superelasticity occurs in the austenitic state. Therefore, a NiTi specimen tested at low temperature (below  $M_s$ ) will exhibit the shape memory effect, while the same specimen tested at a higher temperature (above  $A_f$ ) may exhibit the superelastic effect.

#### 1.3.3.1 Shape memory effect

At low temperatures and in the absence of applied stresses, multiple martensite grains (known as variants) having the same crystalline structure but different orientations are formed by

nucleation and growth from the higher-symmetry austenite phase. This *twinned martensite* structure ( $M^t$ ) forms through ‘self-accommodation’, in which the differently-oriented variants grow in such a way that no observable macroscopic shape change results. This structure is illustrated schematically at the origin of the 3D plot shown in Fig. 1.11(a).

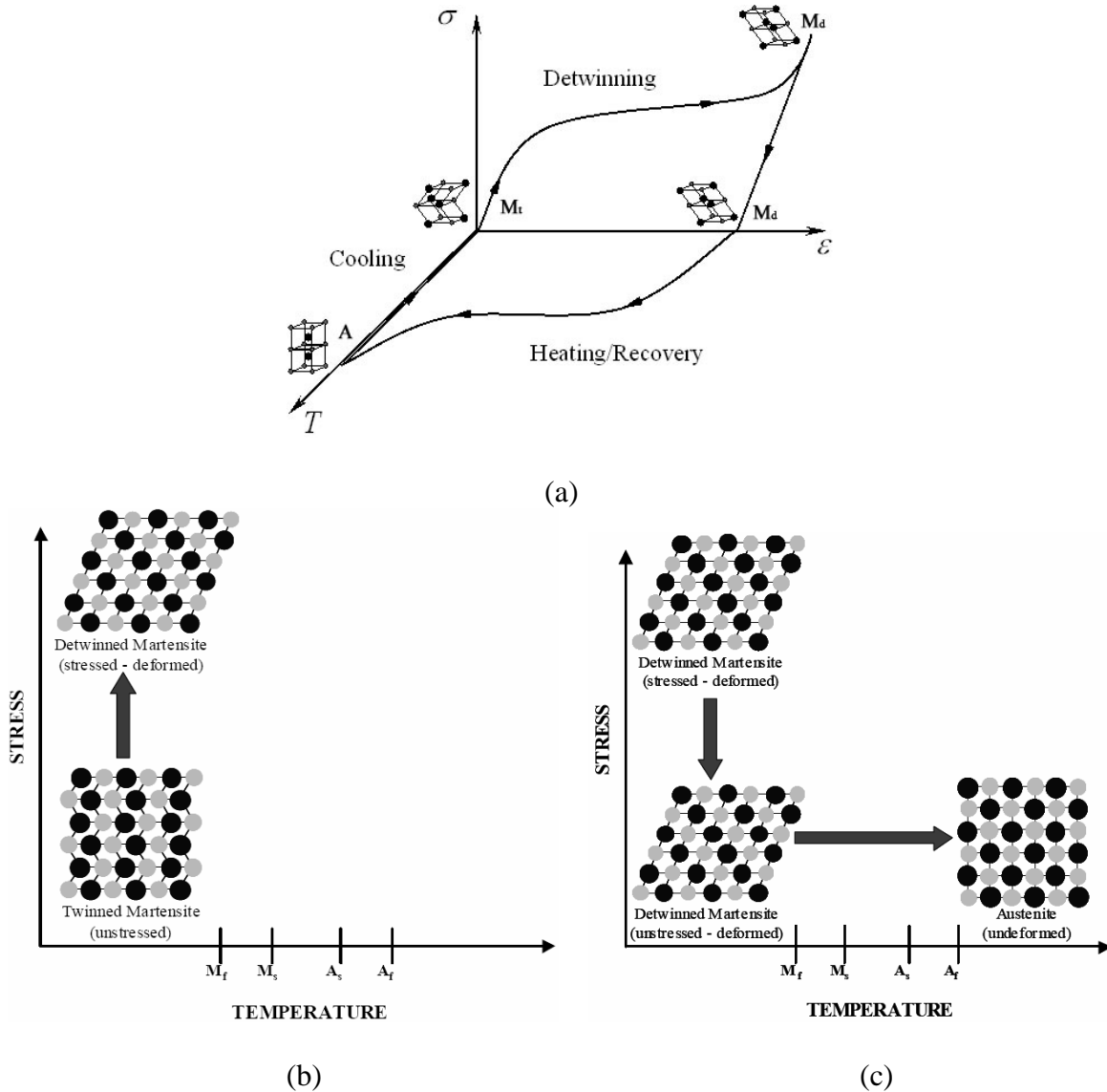


Figure 1.11 Shape memory effect presenting in (a) 3D stress-strain-temperature plot (showing load-unload-heat recovery path) and (b) 2D stress-temperature plot (left upon loading, right upon unloading and heat recovery) [34].

Under applied stress, deformation proceeds by *detwinning* of the  $M^t$  into *detwinned martensite* ( $M^d$ ), as illustrated in the "Detwinning" path shown in Fig. 1.11(b, left). This deformation results from the progressive rearrangement of the differently-oriented variants of the original twinned structure towards a common orientation (ideally, into a single variant). Variants with orientations favored by the applied stress grow at the expense of the others by the motion of twin boundaries, allowing a macroscopic, inelastic shape change without dislocation-slip-based plasticity, but with large changes in texture (crystallographic orientation). Other than a slight elastic relaxation, deformation caused by detwinning is not recovered upon unloading.

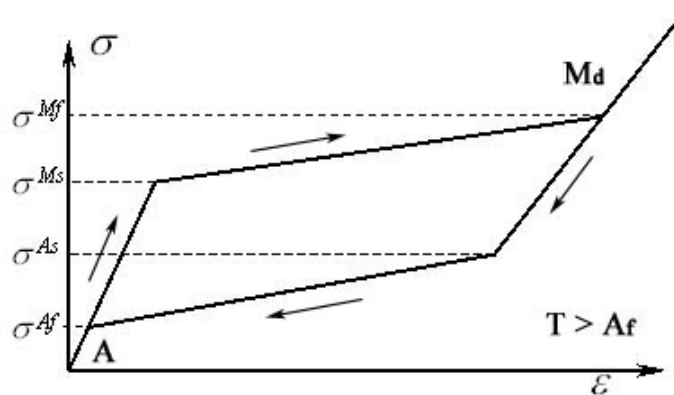
When the temperature is raised through the reverse transformation ( $A_s \rightarrow A_f$ ) interval, these detwinned martensite ( $M^d$ ) variants revert to the parent phase (A), as shown in the "Heating/Recovery" path in Fig. 1.11(b, right). If the system is unconstrained and low temperature deformations have not induced permanent plastic deformation, the macroscopic shape change due to detwinning is recovered and the alloy returns to its original shape, resulting in the so-called shape-memory effect. Cooling back below results in reversion to a new twinned microstructure ( $M^t$ ), as shown in the "Cooling" path of Fig 1.11(a).

Typically, the stress-strain curve observed in shape memory NiTi can be divided into 3 well-defined regions: 1) an initial low-stress plateau resulting from the stress-induced growth of one martensite orientation by detwinning, which can vary in shape from a continuous curve with an inflection point, to a well-defined horizontal plateau with a sharp yield point and upturn, depending on the alloy and its prior thermo-mechanical history; 2) at higher stresses, a near-linear (but not purely elastic) deformation due to elastic deformation of the detwinned martensite which intersects those already present, and which provide additional heat recovery strain (maximum heat recovery is accumulated up to this stage); and 3) a transition due to the onset of

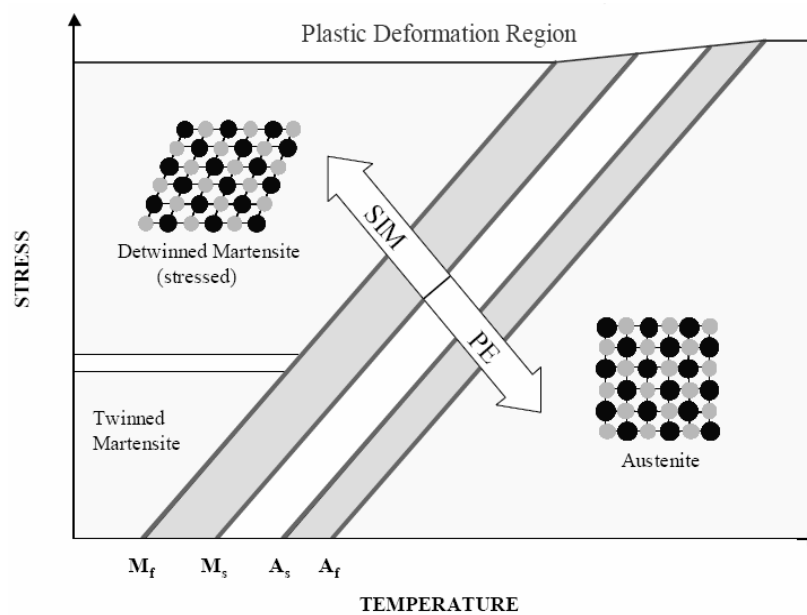
irreversible plastic deformation by dislocations, similar to the yielding behavior of conventional metals. If deformations are applied above this transition, those deformations become permanent, and the recoverable memory strain decreases. It is often stated that up to 8% strain is heat recoverable; however, the actual amount depends on the alloy, its thermomechanical history, testing direction, and deformation mode.

### 1.3.3.2 Superelasticity

*Superelasticity* in the austenitic phase (above  $A_f$ ) is produced by transformations driven by stress alone, unlike shape memory behavior. When the martensitic phase transformation is induced by applying stress to the austenitic phase (A), detwinned martensite ( $M^d$ ) is directly produced from austenite. Since the martensite phase is unstable at zero stress above  $A_f$ , large inelastic strains are recovered upon unloading, due to the reverse phase transformation back to austenite. Little or no permanent deformation is normally experienced by the specimen, giving an impression that the material has only undergone elastic deformation (hence the term superelastic).



(a)



(b)

Figure 1.12 Scheme of superelasticity effect presenting in (a) stress-strain curve and (b) stress-temperature diagram [34].

Three distinct stages are observed in the loading stress-strain curve of superelastic NiTi (Figure 1.12), which are distinguished by two transformation stresses,  $\sigma^{Ms}$  and  $\sigma^{Mf}$ : 1) a purely elastic region corresponding to elastic deformation of austenite at stresses below  $\sigma^{Ms}$ ; 2) a plateau of large transformation strains between  $\sigma^{Ms}$  and  $\sigma^{Mf}$ , associated with formation of stress-induced martensite during the forward transformation. Upon completion of this forward transformation at  $\sigma^{Mf}$ , NiTi is in the martensitic phase; and 3) elastic deformation of martensite above  $\sigma^{Mf}$ .

Upon unloading of the NiTi, elastic recovery of the martensite is seen until a stress of  $\sigma^{As}$  is reached. The reverse transformation then initiates at  $\sigma^{As}$  and completes at a stress  $\sigma^{Af}$ , below which the austenite unloads elastically. Due to the difference between  $\sigma^{Mf}$  and  $\sigma^{As}$ , and between

$\sigma^{Ms}$  and  $\sigma^{Af}$ , a hysteretic loop is obtained. This hysteresis is a very importance characteristic of NiTi, especially as regards damping capacity and energy absorption. Increasing the test temperature results in an increase of the values of critical transformation stresses, while the general shape of the hysteresis loop remains the same.

### **1.3.4 Variations of standard behavior seen in Ni-rich NiTi**

#### **1.3.4.1 R-phase participation in transformation**

Depending on the chemical composition, method of fabrication, and heat treatment of the alloy, the direct transformation from austenite (A) to martensite (M) can be complicated by the presence of an intermediate R-phase. R phase forms by nucleation and growth, initiated by dislocation and/or precipitates. Several transformation sequences are possible, stemming from various combinations of the A  $\rightarrow$  R, A  $\rightarrow$  M and R  $\rightarrow$  M transformations. In general, A  $\rightarrow$  R  $\rightarrow$  M is observed upon cooling, and M  $\rightarrow$  R  $\rightarrow$  A upon heating. However, due to large differences between the hysteresis of the martensite and the R-phase transformations, the transformation sequence on heating can be M  $\rightarrow$  A directly [35]. The transformation A  $\rightarrow$  R shows the same general properties (i.e., superelasticity and shape memory effects) as the transformation A  $\rightarrow$  M, because of the quasi-martensitic nature of this transformation. However, it consists only of small changes in the lattice parameters, and therefore causes only a distortion of the original austenite phase.

#### 1.3.4.2 Ni content

Ni-rich NiTi has been of great technological interest, due to the ability to adjust phase transformation temperatures through adjusting Ni content. It is well known that  $M_s$ , for instance, is directly related to the Ni concentration (i.e. addition of 0.1 at% Ni decreases  $M_s$  about 10°C in solution-annealed and water-quenched NiTi) [36]. Since the solubility of Ni decreases markedly with temperature (Fig. 1.9), precipitation of metastable  $Ni_4Ti_3$  phases (lenticular, disc-like shapes that precipitate coherently) generally occurs during processing. The presence of  $Ni_4Ti_3$  precipitates varies the effective Ni/Ti ratio in the NiTi matrix, and promotes formation of the R-phase.

#### 1.3.4.3 Heat treatment

Heat treatment (in particular, homogenization and aging) causes significant changes in NiTi behavior (especially transformation temperatures) by modifying microstructural features like dislocation density, grain size, and the fractions, sizes, and morphologies of  $Ni_4Ti_3$  and other precipitates. Homogenization treatments (e.g. 1000°C for 3 days) help homogenize the distribution of Ni within the alloy. As a result, the apparent  $M_s$  temperature is lowered, and the width of the martensitic transformation interval is smaller.

During aging, the volume fraction, size, interparticle spacing, size distribution, and arrangement of  $Ni_4Ti_3$  precipitates are altered over time. For example, the precipitate sizes increase as aging time increases, and eventually growing  $Ni_4Ti_3$  precipitates lose coherency. A wide range of aging temperatures (>350°C) can be used to increase  $M_s$  temperatures, while leaving austenitic transformation temperature and R-phases almost unaffected. In addition to

aging temperature and time, cooling rate is also a significant factor. Fast cooling generally results in high internal stresses, high amounts of R phase, and a decrease in transformation temperature.

#### 1.3.4.4 Oxygen and carbon content

Carbon and oxygen react readily with Ni and Ti to form carbides (i.e. TiC) and oxides (i.e.  $Ti_4Ni_2O$ ), respectively. Therefore, these impurities should be avoided as much as possible during production of NiTi from elemental powders. The level of such impurities directly depends on metal powder sizes, as small size provides high surface area to volume ratio for reaction.

Because Ti is more reactive with carbon than Ni and because  $Ti_4Ni_2O$  is Ti-rich, oxide and carbide formation decrease the local Ni/Ti ratio. This retards the martensitic transformation, and as a result, the forward transformation occurs at lower temperatures and the transformation interval becomes wider [37, 38]. Identifying oxygen or carbon contamination as the source of such changes can be experimentally difficult, especially since the oxide  $Ti_4Ni_2O$  has the same structure as the intermetallic  $Ti_2Ni$ .

When using pre-alloyed NiTi powder, the potential for increased oxygen and carbon content is smaller. However, particularly in Ti-rich alloys, precipitates of  $Ti_2Ni$  often present in solidified powders can play an important role in oxygen dissolution during later processing. Therefore, choosing starting powders with a low volume fraction of  $Ti_2Ni$ , and then processing them only under a controlled high vacuum, minimizing contact with carbon-rich materials (e.g. graphite crucibles), or even encapsulating the system, are the most effective way to minimize impurities and preserve the desired transformation and mechanical behavior.

#### 1.3.4.5 Additional elements

Standard NiTi-based alloys deliver quite useful properties in the transformation temperature range between -30 and 80 °C. The addition of ternary or quaternary alloying elements (such as Pd, Pt, Hf, Zr, Au, Al, Cu, Nb) can, however, be used to provide more flexibility toward specific applications. Examples of situations favoring NiTi alloying include: manipulation of transformation temperatures, increase in the stability of  $M_s$  with respect to thermal history, control of hysteresis loop width, increase in austenitic strength, decrease or increase in martensitic strength.

### **1.4 Porous NiTi**

A few years after the unusual shape-memory properties of NiTi were discovered, a porous form of NiTi was introduced [39]. In accordance with the discussions of Sections 1.2 and 1.3, porous NiTi can be expected to combine attributes of NiTi (e.g., shape-memory behavior or superelasticity, high yield strength and ductility unlike other intermetallics, high recoverable strains, good mechanical damping and large energy absorption, good corrosion resistance, and biocompatibility) and foams (e.g., low density and stiffness, high energy absorption, high surface area, and permeability). NiTi foams may thus find application as multi-functional materials such as bone implants [40-43], impedance-matching connectors between structural parts [33], energy-absorbing structures [44, 45], lightweight actuators [46] and hydrogen isotope separation materials [47].

Biomedical applications were the first and remain the main target for NiTi with open porosity. Porous NiTi represents a superior alternative to traditional porous metallic biomaterials (e.g., stainless steel, chromium-cobalt, titanium and tantalum) for the following reasons: (i) good biocompatibility, comparable to conventional porous stainless steel and titanium implant materials [48-50]; (ii) a combination of high strength (important to prevent deformation or fracture), relatively low stiffness (useful to minimize stress shielding effects) and high toughness (essential to avoid brittle failure); and (iii) shape-recovery behavior, facilitating implant insertion (e.g. through self-expanding and self-locking implants, similarly to deployable stents and staples [51]) and ensuring good mechanical stability within the host tissue (normal physiological stresses in the patient may stimulate continuous osteoconduction, useful for long-term fixation).

To optimize NiTi foams for bone implant applications, three key areas are under active study: (i) synthesis of foams with optimal architectures and microstructure, (ii) optimizing mechanical properties; and (iii) tailoring of biological interactions through modifications of pore surfaces. This section provides a comprehensive review on these three key aspects: processing-, properties- and biology-related aspects.

#### **1.4.1 Processing-related aspects**

Foaming NiTi through the liquid route is very challenging, due to its high melting point (1310 °C), relatively high density ( $6.45 \text{ g/cm}^3$ ), its extreme chemical reactivity with crucibles and atmospheric gases, and the need to tightly control composition (due to the narrow stoichiometric range of NiTi at low temperatures) in order to achieve the target shape-memory or superelastic properties. To date, therefore, only powder-metallurgy (PM) techniques have been used, for both

dense and porous NiTi products. Unfavorable porosity in dense products made with the PM process, paradoxically, is the basis for many foaming methods; the imperfect processes are utilized for making porous NiTi.

Powder metallurgy allows for use of either prealloyed NiTi powders or elemental Ni and Ti powders, each having the composition of interest. For producing porous superelastic NiTi, for instance, Ni-rich compositions (up to 51 at% Ni) are used in order to control transformation temperatures (which vary with Ni content) during heat treatment. The susceptibility of NiTi to composition change makes control of impurities (such as carbonitride,  $\text{TiC}_{1-x}\text{N}_x$ , and oxide,  $\text{Ti}_4\text{Ni}_2\text{O}_x$ ) and undesired intermetallic phases (such as  $\text{Ni}_2\text{Ti}$ ,  $\text{NiTi}_3$ , and  $\text{Ni}_4\text{Ti}_3$ ) more crucial, and increases difficulties and limitations in processing. In addition to this general need for well-controlled and homogeneous stoichiometry, porous NiTi must also secure a homogeneous distribution of pores and control over pore characteristics (i.e. pore size, pore shape, and porosity).

Consolidation methods for pre-alloyed powders are based only on diffusion bonding between NiTi particles, since the alloy is already synthesized. The resulting NiTi foams, therefore, typically have uniform chemical composition, and final porosity relates directly to the initial porosity in the powder compacts before the process. However, the processing time tends to be long, due to the slow diffusion of NiTi.

In the case of elemental powders, processing methods rely on an *in situ* reaction between Ni and Ti during the process to form the NiTi product. Since the formation of NiTi from Ni and Ti is highly exothermic and a liquid phase normally occurs, consolidation of powders in this process is generally fast. However, dimensional distortion and inhomogeneous composition

(with undesired intermetallic phases, residual elemental powders, and impurities such as oxides) are often found after such short processes. Pore structures typically rely on Kirkendall effects (due to the more rapid diffusion of Ni as compared to Ti), liquid capillarity (local melts separate particles), and reduction in specific volume (shrinkage), in addition to the original porosity of the green compact.

Even though producing NiTi foams by elemental powders seems to raise issues about control over the resulting product properties, it has been reported more widely than methods based on pre-alloyed powders, due to its flexibility (one can make any desired composition without requiring special powder production) and economy (elemental powders are less expensive than pre-alloyed powders, and require shorter processing times).

In the following section, PM techniques used in the production of porous NiTi are reviewed and categorized into two groups based on the starting form of the NiTi powder: elemental powder metallurgy and pre-alloyed powder metallurgy. The single exception is zone melting in a hydrogen atmosphere, the only melting process recently used to produce porous NiTi from NiTi ingots, which is appended to the end of this section because it does not belong in either of these categories. For each of the reviewed techniques, two areas will be covered: 1) a description of the process (including advantages and disadvantages); and 2) strategies (and technique modifications) to ensure homogeneity in microscopic composition and macroscopic pore structure, as well as to address processing issues.

#### 1.4.1.1 Elemental powder metallurgy

The principle behind PM techniques for making porous NiTi from elemental powder blends is to utilize the reaction between the elemental powders to form NiTi, in such a way that porosity originally present in the preform (or created during the synthesis step) is not eliminated. In this respect, there are two distinct types of approaches, reactive sintering and combustion synthesis, mainly differentiated by the thermal energy produced during each process.

##### I. Reactive sintering

Reactive sintering describes solid state interdiffusion, which can generate intermetallic phases at the interface between particles that inhibit the subsequent violent reaction (which normally occurs upon the formation of liquid). PM methods that can perform sintering at intermediate or high temperature ( $\sim 1000^{\circ}\text{C}$ ) can be used, such as conventional sintering, hot isostatic pressing (HIP), and capsule-free hot isostatic pressing (CF-HIP).

##### *Process description*

In conventional sintering, the mixed powders are compacted into a pellet and pressure-less sintered in a high-temperature furnace with or without high-purity inert gas (e.g., argon) atmosphere [52, 53]. HIP is a pressure-enhanced sintering technique wherein powders are encapsulated, i.e. evacuated in a canister which is gas-tight-welded so that an isostatic gas pressure ( $\sim 100\text{-}200\text{ MPa}$ ) can be applied to the powder during high temperature processing [28, 33]. Unlike conventional sintering, HIP is able to produce a complex product shapes. The capsule-free (CF-HIP) process has a similar set up to HIP, but without the use of a closed steel

HIP canister. Rather, the mixture is pressed and put in a steel crucible, where the hot pressure with argon gas protection is applied [54].

### *Process strategies*

#### Conventional sintering

Porosities of 35-40% (and high open-pore ratios) with relatively small pore sizes are typical in conventional sintering, and relate directly to green density voids left between the compacted particles. High *compacting pressure* reduces initial porosity before the process starts, increases radial expansion, and decreases axial shrinkage after sintering. By increasing *sintering temperature*, the fraction of liquid phases (when sintering above the eutectic temperature; but localized liquid formation is also possible when sintering below eutectic point) increases, and thus the axial shrinkage increases (at 1100°C, for example, severe distortion is observed) [55]. Pore size can be increased by increasing sintering temperature (as it increases liquid content). Long *sintering time* or *post annealing* is normally required in conventional sintering in order to complete the reaction (and reduce unwanted phases); however, relatively small pores [56] usually result (as the shrinkage of the original pores dominates over the formation of new pores [57]).

TiH<sub>2</sub> has been added as a *pore-forming agent* to help accelerate the process and widen pore size through its decomposition into Ti and H<sub>2</sub>. An increase of open porosity and a more homogeneous pore distribution were observed; however, the total porosity was still below 50% [53, 58]. The foams produced by Bertheville [59] using sintering under *calcium reducing vapor*

also showed similar porosity, but with a significant decrease in unwanted stable intermetallic phases and oxide impurities.

Recently, the *space holder method* was introduced to production of NiTi foams. The method is based on including space holding phases in the metal powders, in order to achieve greater pore volume (i.e., in order not to rely solely on green porosity). Space holder materials can be removed before, during, or after the metallic powder densification process. As the space holder particles are removed, pores are left in the metal powder compact, with geometries and amounts relatively close to those of the space holder itself. The space holder method, therefore, overcomes the issue of controlling pore size and pore volume fraction in porous NiTi. For instance, ammonium bicarbonate ( $\text{NH}_4\text{HCO}_3$ ) was blended into NiTi in volume fractions of 10-30% and, after sintering, the NiTi contained porosity of 30-60% with high densification in the NiTi struts. The porosity and pore size increased linearly with the amount of  $\text{NH}_4\text{HCO}_3$  used. NiTi foams with designed gradients in porosity could be made by this method as well [60].

## HIP

Porous NiTi made by hot isostatic pressing (HIP) can achieve a more fully-densified structure due to the higher pressure (200 MPa) applied during sintering. To introduce pores into NiTi products, Lagoudas et al [33] *entrapped and compressed argon gas* between partial melted powders during HIP. The gas then expanded as the pressure was decreased in the last step, yielding a porous structure with a predictable pore size. The final product was annealed at high temperature, below the melting temperature of NiTi, to produce a homogeneous structure. This argon sintering technique allows one to produce porous NiTi with channel-like pores and large open pores of 500  $\mu\text{m}$  size (interlaced with small closed pores), with a porosity of 42%. Small

*particle size* could also be used during HIP to enhance reactions between particles (and thus densification of the NiTi) without concern over a decrease in porosity, since the pores are filled with argon.

### CF HIP

A similar idea was tried using CF-HIP, with argon gas trapped within pores during densification, which subsequently expand into larger sizes. Pore size and porosity were in the range of 50-200  $\mu\text{m}$  and 30-43%. Pore characteristics such as pore shape, size, and distribution, could be controlled by adjusting the processing parameters. High *compacting pressure* favored the formation of homogeneous pore distributions, and high *hot argon pressure* favored the formation of round-shaped pores. Low *heating rate* (below 20°C/min) resulted in uniform pore size throughout the radial direction. When the heating rate was higher, the reaction between powders turned into an acute thermal explosion (as in the VCS process) and resulted in large pores in the center of the part. High average porosity of 56%, and larger range of pore size of 50-800  $\mu\text{m}$  (with spherical shape), was achieved by CF-HIP with the help of  $\text{NH}_4\text{HCO}_3$  pore forming agents (introduced and removed before CF-HIP) [61]. The use of high-pressure argon gas expansion applied after  $\text{NH}_4\text{HCO}_3$  was removed also helped achieve interconnecting open pores without significant a change in pore shape and porosity (~50%) [62].

## II. Combustion synthesis

Combustion synthesis (the term suggests a traditional combustion reaction involving oxygen, but oxygen is not explicitly involved in this method) proceeds when an initial compact of mixed elemental powders is heated to a temperature where those powders ignite and react

rapidly (and exothermically) to form the compound product (NiTi). Typically, such a reaction occurs at the lowest eutectic temperature in the system, and at the interfaces between the connecting particles. In general, combustion synthesis processes are characterized by high-temperatures (1500-4000°C, due to the large enthalpy of reaction of intermetallics), fast heating rates, and short reaction times (a few seconds to a few minutes). These features make combustion synthesis a facile and economically viable technique. However, to apply the method to NiTi, delicate processing control is needed to prevent alteration of the composition due to contamination and undesired phases formed upon reaction in such short processing time.

The concept of PM techniques using the combustion method is therefore based on initiating the exothermic reaction and then allowing the resulting reaction energy (i.e., heat and temperature rise) to contribute to the remainder of the consolidation. Combustion synthesis can occur in two modes: (1) linear or self-propagating, high temperature synthesis (SHS); and (2) bulk or volume, combustion synthesis (VCS) or thermal explosion synthesis.

#### *Process description*

In all cases, the mixture of Ni and Ti powders is pressed into a pellet, typically of cylindrical shape. The pellet is then ignited by an external source (e.g. a plasma arc [63], tungsten coil [64, 65] or laser [66], either locally at one end (SHS) [66-71] or uniformly (VCS) [72], to initiate the exothermic reaction. To complete the reaction throughout the compact, a self-propagating and self-sustained combustion wave is needed, which requires high exothermicity and also that the heat generation rate is greater than the heat dissipation rate. In SHS, a very strong exothermic reaction is needed to propagate from one end to the other end, while VCS is

more suitable for weak exothermic reactions, as reactions may occur simultaneously throughout the volume and therefore need not propagate very far.

### *Process strategies*

In contrast to reactive sintering, where sufficient time is provided to complete the low-energy reaction between Ni and Ti, combustion synthesis methods need a uniform reaction within a short very time, in order to avoid imperfect interdiffusion of the powders and/or formation of unwanted phases. The vigorous reaction between elemental powders makes controlling the process difficult, and accordingly the compositional homogeneity and pore structure of the final product depend on many factors, ranging from powder selection and preparation to reaction parameters in the ignition and propagation of the combustion wave.

In powder preparation, *powder size*, *powder mixing* and *powder compacting pressure* determine contact area between powders and green porosity. High compacting pressure results in high green density. More contacts between powders raise the thermal conductivity of the pellet and thus give a denser product [63]. Mean pore size and porosity (normally in the range of 40-60%) increase with increasing titanium powder size and green pellet size, and decreasing compacting pressure (i.e. decreasing initial porosity, which is normally 30-70%). However, insufficient mixing and excessively large powder size encourage composition gradients (due to big difference between the diffusivity of Ni and Ti), which results in high levels of residual Ni and Ti. Low initial porosity (high contact area) facilitates the formation of  $\text{NiTi}_2$ , resulting in high level of free Ni and low Ti. These stable phases reduce the heat released, causing reaction

imbalance and thus slowing down the synthesis. Therefore, the maximum initial porosity is drawn at 30% to limit powder contact area [73].

High *ignition temperatures* (ranging from 400-600°C) favor the formation of the NiTi phase over other intermetallics [73]. Small titanium powder size results in an increase in the combustion temperature and a decrease in the minimum ignition temperature [69]. To make homogeneous porosity, a uniform temperature profile within the pellet, and thus a short ignition time, are required. An integrated laser diode system was used as *ignition source* to achieve fine control of the heating and ignition process over short ignition times, in order to minimize the thermal gradients inside the pellets [66]. Chu et al. [74] modified the ignition technique by using a special ignition reagent composed of Ti and C powders. The ignition reagent was first ignited by a tungsten coil, which produced combustion reaction that then ignited the elemental Ni and Ti powders. In this way, high combustion temperatures (up to 3210°C) and high heat flux density in SHS processes can be reached. Green compacts with large diameter reduce heat losses and therefore increase combustion temperature, due to a small surface area to volume ratio [65, 74].

Since the synthesis reaction between Ni and Ti is weakly exothermic ( $\Delta H_f = 67$  kJ/mol), a preheating process is added before the ignition step to ensure that the minimal ignition temperature can be reached and thus that the process is self-propagating. *Preheating temperature* was shown to influence the amount of transient liquid phase present at the combustion front. Preheating results in higher combustion temperatures and thus higher wave velocities. As the reaction between powders becomes more complete, the amount of  $Ti_2Ni$  is reduced [63] and a higher open pore-ratio is achieved [53, 69].

Typically, porous structures obtained by SHS contain high porosity (40-70%) but less open porosity [56, 75], along with an inhomogeneous pore distribution, and large pore size

(sometimes with striations, or linearly-aligned elongated channels) in the longitudinal [76] or transverse direction [63]. These pore characteristics are attributed to the convective flows of liquid and argon gas during the combustion. By adjusting the *preheating schedule* (i.e. the steps from preheating to ignition), three-dimensionally well-connected porous structures (with porosity of ca. 64%) can be obtained, with pore size that increase with increasing preheating temperature [65]. However, excessive pre-heating has dramatic side effects, such as anisotropy in pore structure, formation of undesired macro-porosity, and extended product melting.

Biswas et al. [77] successfully fabricated single phase porous NiTi using improved ignition techniques in a VCS process, in combination with a controlled *post-reaction process*. Controlling the heating rate in this post-heat treatment was found to balance the conversion to a single phase of NiTi and the loss of porosity (and collapse of porous structure) due to strong interaction of liquid phase, both of which are favored by fast heating rates.

#### 1.4.1.2 Pre-alloyed powder metallurgy

In the fabrication of porous NiTi from pre-alloyed powders, high sintering temperatures of around  $0.95 T_m$  (where  $T_m$  is the melting point), with sufficient sintering times, are necessary due to the low sintering kinetics of NiTi powder and the lack of any additional energy source from reactions among powders. PM techniques such as conventional sintering, hot isostatic pressing (HIP), warm pressing, metal injection molding (MIM) and spark plasma sintering (SPS) have been applied to prealloyed NiTi powders.

### *Process description*

#### Sintering

For descriptions of conventional sintering and HIP, the reader is referred to the last section. Warm pressing is similar to die pressing, but utilizes axial pressing in a heated die. The MIM process combines the technique of polymer injection molding (used for automated production of parts with good flexibility in shape) with the advantages of PM (e.g. near net shape production). The process starts by mixing metal powders with a polymer binder to produce a feedstock, followed by molding the homogenized feedstock into shaped parts, removal of the polymer, and finally sintering. The process can be used only with prealloyed NiTi powders, due to anisotropic swelling of elemental powders during sintering.

#### Spark Plasma Sintering (SPS)

Spark plasma sintering (SPS), or field-activated pressure-assisted synthesis, is based on passing a high current density in the form of a short pulse (i.e., inducing a spark) through compacted and uniaxially-compressed powders in a graphite die (and using graphite plungers). The extremely high and localized temperatures (up to tens of thousands of degrees) produced by the spark activate diffusion processes (with the assistance of a subsequently-formed plasma) and encourage neck formation. This leads to sample densification at low temperature and with short fabrication times (on the order of a few minutes), and thus avoids any undesired reaction products that might be produced by conventional sintering.

### *Process strategies*

Since high sintering temperatures and times are generally required, modifications of PM methods are often developed to manipulate pore structures independently of the densification of NiTi struts.

#### Conventional sintering

Grummon et al. in 2003 [78] produced a high porosity open-cell NiTi structure via sintering a NiTi-slurry-coated polyurethane foam, but due to the use of polymer precursor the foam had significant contamination and was brittle. Recently, Sakurai [79] successfully made NiTi foam with more than 80% porosity by sintering reduced pressure-compacted NiTi slurry. However, foam made by this method was still difficult to process with accurately-controlled pore geometry.

#### HIP

Just as in the HIP of elemental powders, argon gas can be trapped in prealloyed NiTi during powder densification [28]. This argon gas can then be allowed to expand via creep of the matrix in a high temperature and low pressure environment, to form pores in the NiTi matrix. Porosity and pore size can be controlled by the initial amount of argon added and the expansion temperature and time. In this method, pores were found to be more rounded, due to the uniform internal pressure induced by the gas, and most pores were closed (when pores begin to rupture to the environment during expansion, pressurization is lost and expansion ceases). However, the

high creep strength and low creep ductility of NiTi prevented achievement of high porosities using the gas expansion method.

#### MIM and warm pressing

Space holder materials such as saccharose, PMMA, and sodium chloride (NaCl) have been used in MIM to produce porous NiTi with 50-70% porosity and 355-500  $\mu\text{m}$  pore size (KohlEUPM). However, the low melting point of saccharose causes difficulty with the feedstock, and PMMA results in oxides and carbides in the structure after removal. Using NaCl as a space holder seems to provide the desired pore structures without residual contamination; however, microporosity in the NiTi struts is observed due to insufficient densification during sintering. Similar results are also observed in warm pressing with NaCl space holders [80].

#### SPS

Non-uniform porous NiTi structures (i.e. structures with high density outside and low density inside) with porosities of 13-25% were produced by the SPS process [81]. Since final porosity relies on green density in this process, it can be manipulated by changing the particle size distribution in the NiTi compact. Decreases in pressure and temperature during SPS also lead to higher porosity.

#### Special section: Continuous zone melting method

The continuous zone melting method is the only liquid-state method used to produce porous NiTi to date. The technique involves unidirectional solidification of NiTi during a gas-

evolving crystallization reaction. A NiTi rod is continuously fed through a heated zone in a mixed atmosphere of hydrogen and helium. The hydrogen gas dissolves into the molten NiTi and is rejected as the melt solidifies on its way out of the heated zone. The directionality of the rejected gas (i.e. the pores) is determined by the direction of the solid-liquid interface, which propagates along the feeding direction. As a result, unidirectionally-elongated cylindrical pores (giving the so-called *lotus-type* structure) are obtained.

Sugiyama et al. [82] reported lotus-type NiTi (49.7 at% Ni) with 35% porosity and an average pore length of 350  $\mu\text{m}$ . Lower porosity and smaller pore size could be achieved to some degree by using lower hydrogen partial pressure. However, excessive hydrogen pressure (i.e. >2 MPa) resulted in inhomogeneous, large, elongated pores in the transverse direction. The residual hydrogen in the process could be minimized by heat treating and air cooling. Tensile testing suggested high strength in the direction of the long axis of the pores, as well as shape memory effects and superelasticity.

#### **1.4.2 Properties-related aspects**

The mechanical and transformation behavior of porous NiTi is extremely sensitive to both microstructure (i.e. austenite/martensite, precipitate, and impurity content) and pore structure, and hence to its processing procedures (thermal-stress history, foaming procedure, and heat treatment). Therefore, direct comparisons using the mechanical behavior of porous NiTi produced by different processing methods (or even the same method applied by various groups) is not attempted here. Rather, a broad overview of the mechanical properties of porous NiTi is provided, to evaluate the status of current porous NiTi materials (those with porosity and pore

size ranging from 20-80% and 50-800  $\mu\text{m}$ , respectively) in the context of the properties required of bone implants. Porous NiTi produced by similar processes, or with similar mechanical behavior, to those in this work will be discussed within the relevant chapters.

#### 1.4.2.1 Stiffness and yield strength

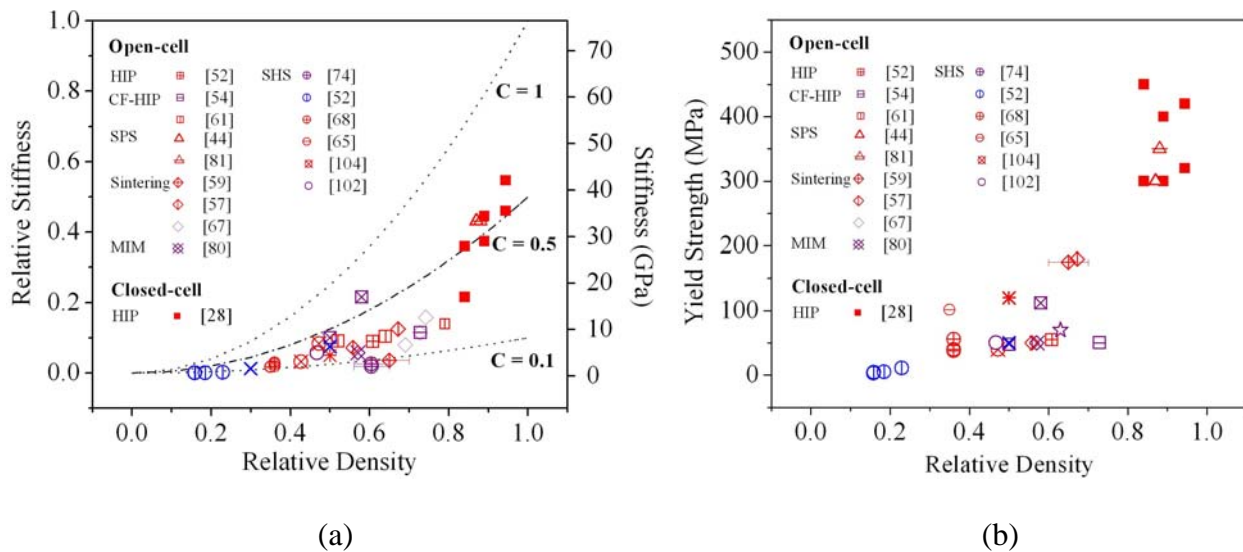


Figure 1.13. Relative density versus (a) relative stiffness, and (b) yield strength of currently produced porous NiTi. Different symbols (in the inset) indicate the processing methods. Open symbols represent open-cell foams; closed symbols represent closed-cell foams.

Figures 1.13(a) and 1.13(b) plot the relative loading stiffness  $E/E_s$  (as well as the absolute value of loading stiffness) and apparent yield strength of porous NiTi materials as functions of relative density  $\rho/\rho_s$ . The values of stiffness, yield strength, and solid density used in these plots were given by the authors of each work, or extracted from stress-strain curves provided in the article. In the latter case, stiffness was defined as the initial linear slope, and strength by the

elbow at which this slope quickly decreased, in the stress-strain curve. Even though slope upon loading does not represent reliable stiffness for these materials due to detwinning, it is used by necessity because unloading curves are usually not provided. The density and stiffness of monolithic NiTi used are  $6.45 \text{ g/cm}^3$  and  $69.5 \text{ GPa}$ , based on the properties of NiTi materials used in this dissertation, unless otherwise indicated by each article. Since most articles do not provide yield strengths of the monolithic NiTi, yield strengths of the foams are shown without normalization. Only compressive data are used, as compressive properties are the main focus of this dissertation. Most compression tests were done in load-unload-cycle fashion to observe superelasticity, with few using heat recovery investigation to see the shape memory effect.

Different symbols represent different processing methods: squares for HIP, diamond for conventional sintering, circles for SHS, triangles for SPS, stars for zone melting, x symbols for warm pressing, and asterisks for MIM). Filled and unfilled symbols indicate close- and open-cell structure, respectively. Color indicates the phases present at testing: red for austenite, blue for martensite, and purple for coexisting austenite and martensite.

In general, NiTi foams produced for open porosity in the range of 20-80% have stiffnesses in the range of 0.1-20 GPa (and usually below 10 GPa) and yield strengths below 200 MPa. The compressive strength of dense human bone when a force parallel to the bone axis is applied is 170-193 MPa, and 133 MPa when a normal force is applied (see section 1.1). This means that current NiTi foams suffice for heavy load bearing purposes.

Interpretation of the stiffness data is more complicated. Bone naturally grows with a stress-induced texture or orientation, which produces significant anisotropy in properties; in specific, the longitudinal to transverse stiffness ratio in cancellous bone may reach as high as 10 [83]. Therefore, the target stiffness for each study will vary by what location in the body it

targets, though most generally aim for around 1 GPa for cancellous bone and 10-20 GPa for trabecular bone. Generally speaking, then, open-celled NiTi foams are in the correct stiffness range. By contrast, NiTi foams with small and closed porosity (represented by the filled symbols in Fig. 1.13) exhibit comparatively high stiffness and yield strength, which are less attractive for bone implant applications.

The experimental data are very scattered, due to the differences in foam morphology and degrees of densification of the NiTi structure. Although fitting these data to the open-cell foam mechanics theory of Gibson and Ashby (equation 1.2 and 1.3) is not attempted here, it is worth noting that the relation of relative stiffness and density falls into a range of values for  $C$  of 0.1-0.5 when a scaling exponent of 2 (that of bone) is used, which implies ductile behavior.

#### 1.4.2.2 Recovery strain and fracture strain

While NiTi has a high recovery strain of up to 8% in tension (values can be different in compression), the recovery strain capability of porous NiTi is only about 3-4 %. Recovery effects vary from foam to foam. For example, Lagoudas found that the transformation in NiTi foam (made by HIP with argon expansion) was repeatable and that shape recovery (beyond elastic recovery) was approximately 2%, even when the sample endures maximum strains as high as 17% [33]; Zhu et al. showed that 100% heat recovery was possible when a maximum strain less than 2% was applied, but recovery effects decreased and deformations could not recover completely when the strain was more than 4% [44]. Nevertheless, this amount of recoverable strain is similar to that of bone, which is 2%, so that porous NiTi implants should survive the large elastic deformations which can occur inside the bone when the patient is

engaged in physical activities, and do so more easily than stainless steel, with only 0.8% elastic strain recovery.

Arciniegas et al. [72] observed 23% compressive strain to fracture in NiTi foam (produced by the VCS process) having ~65% porosity. Near the end of this test, densification took place and the stress rose steeply. The fractured specimen showed collapse of the structure in a direction perpendicular to that of the load application. These behaviors generally confirmed the ductile behavior of porous NiTi structures during deformation.

### **1.4.3 Biological-related aspects**

Since no biological work is reported in this thesis, detailed information on the biological study of porous NiTi is not intended here. Readers interested in more detailed information are referred to our recent full-length review article [84], which mostly surveys biological studies on porous NiTi spanning the six years from 2002 to 2007. Only a brief summary and processing-related highlights of this biological work will be given here.

The biocompatibility of NiTi and its unusual mechanical properties make it a superior alloy in monolithic, non-porous form for many bone implant applications. These include maxillofacial and dental implants, cervical and lumbar vertebral replacements, joint replacements, bone plates, bone tissue engineering, spine fracture fixation, anchorage and repair [85-90], and many review articles have been published on the biological performance of monolithic, non-porous NiTi [91-93].

Although the study of porous NiTi has developed rapidly over the past few years, biological studies are still at an early research stage compared to other porous Ti and Ti-6Al-4V alloys, and to dense NiTi. In the early stages of research on porous NiTi, the main objectives

were to develop fabrication processes for creating foams with desirable architectures and microstructures, and to understand the resulting mechanical and transformation behavior [86, 94, 95]. It was not until the last decade that many studies were performed on the biological performance of porous NiTi [40-42, 96-98]. In these studies, the consensus was that porous NiTi exhibited biocompatible behavior in vitro and in vivo. In 2001–2002, Shabalovskaya et al. [99, 100] published an exhaustive review on the biological performance of NiTi, focusing primarily on monolithic NiTi but also addressing porous NiTi implants. They pointed out the need for continued research on surface design, characterization of corrosion behavior (especially under load or mechanical deformation), the effects of surface condition and sterilization procedures on biological response, and long term in vivo and in vitro studies. Following this review, more work has been dedicated to the combined study of the biological evaluation of porous NiTi in parallel with studies on the development of new processing methods [62, 101, 102], more in-depth mechanical properties (including fatigue and damping) [103], and modeling [104-106].

As new processing methods arise and current processing methods are optimized, biological studies are being done on representative porous NiTi. Porous NiTi materials that appear in recent biological studies are typically made by SHS and CF-HIP processes (Figure 1.14) using elemental Ni and Ti powder, and are characterized by pore sizes of 100–500  $\mu\text{m}$  and porosity of 30–60%.

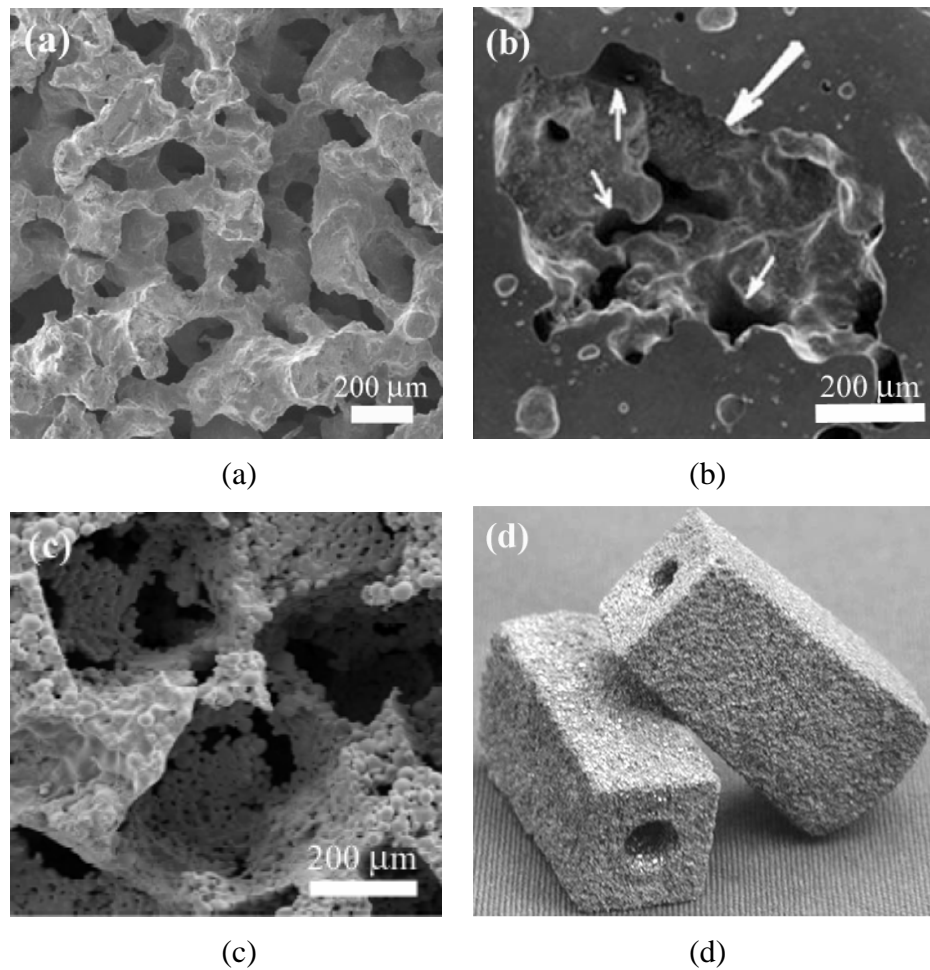


Figure 1.14. SEM micrographs of porous NiTi produced by three different methods; (a) SHS process ( $65 \pm 10$  % porosity, 100-360  $\mu\text{m}$ ) [98], (b) CF-HIP with argon expansion (42% porosity, 50-400  $\mu\text{m}$ ) [62], and (c) MIM and sintering with NaCl spacer (prealloyed powders, 70 % porosity, 355-500  $\mu\text{m}$ ) [80]. (d) photograph of commercially-available porous NiTi implant produced by SHS process (Actipore™, Biorthex, Canada), used in a study for intervertebral fusion application [190].

Broadly speaking, the goals of these biological investigations into porous NiTi fall into three categories: surface modification, biocompatibility analysis, and evaluation of specific

applications. The goal of surface modification is to prepare porous NiTi surfaces with minimal or negligible Ni release and corrosion rates. Current surface treatments used on porous NiTi include thermal annealing, oxygen plasma immersion ion implantation, pre-soaking in SBF solution, TiN and TiO<sub>2</sub>-PVD coatings, HA coatings, chemical treatment, and combinations thereof. In general, these surface modification methods help reduce Ni release rate by a factor of 3–24, to levels below the normal daily Ni intake (150-900 µg/day) [107]. The biocompatibility of porous NiTi has been confirmed by evidence of good adherence and rapid cell growth observed in both in vitro and in vivo studies. Acceptable cytocompatibility, genotoxicity, irritation, toxicity reaction, and sensitization are reported, as well as high bone ingrowth with good fixation. Positive results have been shown in a few studies using porous NiTi in simulated operating situations using intervertebral fusion devices and tissue engineering.

More comprehensive studies are needed on biological performance in order to develop the biomedical applications of porous NiTi. For this purpose, optimization and long term in vivo studies on surface-modified systems are still needed. The purpose of this research should be to establish which surfaces are the best to rapidly induce ideal metal–tissue interfaces, including bone regeneration and bonding on the alloy surface. It is also important to understand what bulk and surface structures are best for the alloy's stability within the body environment without reduction or loss of shape-recovery effects. The design of bioactive metal surfaces using biomolecular structures that instruct cells is one of the most promising approaches to ensure optimal biological performance of NiTi implants.

Manufacturing developments motivated by biological needs which may be expected in the near future include: (i) greater emphasis on final pore surface quality (i.e., NiTi surfaces with no potential Ni release sites) to minimize later surface treatments; (ii) synthesis of optimally

bioactive surfaces leading to higher bone ingrowth and biocompatibility; (iii) introduction of ternary or higher alloys; (iv) creation of tailor-made microstructural features such as pore fraction, size, shape, fenestrations and orientation, which will permit control over test parameters in biological experiments, reveal precisely the relationships between microstructure and bone ingrowth, and perhaps allow manipulation of biological response through the large superelastic strains achievable in porous NiTi. With the simultaneous consideration of processing methods, mechanical properties, NiTi composition, microstructural features and biological performance, more rapid optimization of porous NiTi for biomedical applications is likely to occur in the near future.

## 1.5 Objectives of Thesis

The main objective of this work was to develop processing procedures for porous NiTi that offer the following advances over existing technology: 1) controllable pore characteristics (porosity, pore size/shape, connectivity) to stimulate and accommodate a high level of bone ingrowth; 2) mechanical properties (yield strength, stiffness, recovery strain) matching those of bone, to minimize stress-shielding effects; 3) highly dense metal struts and walls, to prevent crack initiation and increase ductility; 4) simplicity and low cost of production; and 5) extended application in both shape-memory effect and superelasticity.

A strategy to fabricate porous NiTi so that pore characteristics can be well-controlled, while preserving high strength, low stiffness, and high recovery strain, is presented. This strategy is based on hot isostatic pressing (HIP) a mixture of pre-alloyed NiTi powders and salt space holders, followed by removal of the salt. Using this strategy, the porosity of the NiTi is controllable by varying the volume fraction of the salt, and the pore size and shape can be tailored in accordance with the geometry of the salt used. The effects of using different space holders, namely sodium fluoride (NaF) and sodium chloride (NaCl), on the final porous product are examined in sections 3.1 and 3.2, respectively. The influence of HIP temperature and further post-HIP sintering on foam properties is also presented.

The costliness of HIP processing drove subsequent work towards new strategies to simplify porous NiTi synthesis while maintaining high-quality microstructures and mechanical properties. The strategy followed here involves combining the NaCl space holder technique with transient liquid phase sintering of pre-alloyed NiTi and niobium powders, thereby integrating the

densification of NiTi struts and the removal of space holders into a single step. The effect of Nb addition to structural and physical properties of porous NiTi is discussed.

Some extension of the work towards understanding the mechanical behavior and microstructure development of porous NiTi is included in Chapter 5-6. Final conclusions drawn from the work are discussed in Chapter 7, and also included there are perspectives on possible future research directions, in terms of fundamental studies and potential applications.

## CHAPTER 2

### **General Experimental Procedures**

Experimental procedures that have been repeatedly used in sample synthesis and characterization in subsequent chapters have been collected and placed in this chapter, to ease the reader's search for detailed experimental information and to avoid tedious repetition. Less common experimental procedures can be found in the relevant sections and subsections.

#### **2.1 Foam synthesis**

##### **2.1.1 Hot isostatic pressing (HIP)**

Mixtures of pre-alloyed NiTi and space holder powders with predetermined sizes and volume fractions were mechanically blended in a twin-shell dry blender for 40 minutes. The mixtures were poured into mild steel cans with 35 mm outer diameter and 1.6 mm wall thickness and gently tapped. The steel cans were then evacuated, sealed by welding, and subjected to HIP densification by UltraClad Corp. (MA) at the desired temperature for 4 hours, under an argon pressure of 100 MPa.

##### **2.1.2 Sintering**

Sintering, used either as a follow-up process after HIP to improve foam microstructure (Chapter 3), or a stand-alone powder densification process (Chapter 4 and 5), was carried out

using the following steps. The sample to be sintered was placed inside a 15.88 mm inner diameter (ID) alumina crucible (with titanium foil getters above the sample, to reduce oxidation), and this crucible was slid into a 35 mm ID alumina crucible serving as a furnace chamber. Sintering was performed in a high temperature furnace under high vacuum (typical pressure 0.001 MPa) using a heating and cooling rate of 7 K min<sup>-1</sup>. A metal pathway surrounded with a liquid-nitrogen-filled housing was installed between the furnace and vacuum system as a trap to prevent any substances evaporated from the sample from passing into the vacuum pump.

### **2.1.3 Salt removal from HIP samples**

In sintered samples, space-holders were removed naturally by evaporation during the sintering process itself. However, in the case of HIP samples (from which the space holders could not evaporate, due to the closed can), additional salt-removal steps were necessary.

Consolidated NiTi-salt composite billets were cut with a diamond saw at a slow (150 RPM) cutting rate, to make samples with dimensions of 5 x 10 x 10 mm<sup>3</sup>. These samples were then suspended in circulating water under ultrasonic agitating system to dissolve the salt phase. The sample mass was measured regularly to track weight loss during dissolution. The dissolution process was terminated when the sample mass was stable and/or decreased to a predetermined value corresponding to the volume fraction and bulk density of NiTi. In the case of NaF space holders (water solubility of 4.2 g/L at 25°C), all the salt was considered removed after 2 weeks; despite the high water solubility (35.9 g/100 ml at 25 °C) [108] of NaCl, the leaching process lasted about two days. The leached NiTi foams were then cleaned twice in an ultrasonic water bath for 15 minutes, rinsed with acetone and furnace-dried at 100°C.

## 2.2 Foam characterization

### 2.2.1 Microstructure observation

Cross-sections of 3 mm thick slices of NiTi foams were mounted with Buehler Sampl-Kwick metallographic epoxy (1 to 2 ratio of epoxy liquid to powder). Mounted samples were then polished to reveal their pore structures using a Buehler autopolisher with the following sequence and conditions: 320 grit SiC paper (4 lbs/sample, 240-320 RPM contra rotation, until plane), 9  $\mu\text{m}$  diamond suspension on Buehler Ultrapol cloth (4 lbs/sample, 120-150 RPM complementary rotation, 6 min), and finally 0.05  $\mu\text{m}$  alumina suspension (same as previous condition). The samples were ultrasonically cleaned for 15-20 minutes between each step and, as a final step, rinsed with methanol for 7-10 seconds before drying with hot air.

In some cases, when a visibly well-defined pore edge was needed, infiltration with epoxy resin was performed prior to polishing. A thin layer of Buehler Epo Heat's mixture, consisting of resin (no. 20-8120) and hardener (no. 20-8122) in a volume fraction of 4 to 1, was put on the surface of the mounted sample. The coated foam sample was then placed under vacuum until air bubbles emerged from the pores and epoxy could no longer be observed through the epoxy (about 20 minutes). At this point, air was let in to press the epoxy into the open pores. Infiltration of epoxy into pores was done at least 3 times to assure full filling of pores. The sample was then heated at 60°C for 3 hours to cure the polymer.

Hitachi scanning electron microscopes (SEM; models 3400 and 3500) at 15.0 kV accelerating voltages were used to image sample cross-sections at various magnifications, and

qualitatively characterize pore features. A Nikon inverted microscope with a Diagnostic Instruments digital camera was occasionally used to obtain images for general observation.

### 2.2.2 Pore size measurement

Average pore size was determined by the line-intercept method from SEM images [109]. The SEM images were selected in such a way as to cover all regions of the foam cross-section, and each image reflected a foam structure containing at least 30-50 pores. A template of 10-15 random straight lines was drawn on transparency film (of the same size as the images), and this template was positioned over each image. The length of intersected pores ( $L_o$ ) was then measured and summed along a line, and the number of pores that fall on that line ( $N_{pore}$ ) was counted. Only macroscopic pores that were approximately 50  $\mu\text{m}$  or larger were taken into account in order to determine pore size produced via space-holder materials. Average pore size was then calculated as  $1.12L_o/N_{pore}$ .

### 2.2.3 Porosity measurement

In general, closed porosity was measured by helium pycnometry and total porosity by the Archimedes' method in water. Open porosity was calculated by subtraction of the closed porosity from total porosity.

Helium pycnometry is based on the displacement of a volume of gas by the solid phases in the sample and by all the other gas-impenetrable space which those solids enclose; in the context of this work, this means the volume of NiTi in the struts, plus the volume of all fully-closed pores inside those struts. Density and closed porosity are then calculated by knowing the mass of the sample.

A clean, dry sample was placed in an appropriate chamber (i.e., a chamber whose volume is less than about 150 % of the sample volume, or about 1 cm<sup>3</sup> in this case) in Micromeritics Accupyc 1330 Gas pycnometer. Helium was filled into this sample chamber, and then expanded at room temperature from the sample chamber into another chamber with known reference volume. The pressure of the gas was recorded both before and after this expansion.

Since the volumes of both chambers had been determined by a suitable calibration step, the sample volume could be calculated by the relationship between the pressure and volume of a fixed amount of helium at a fixed temperature, i.e. by Boyle's Law,  $P_1V_1 = P_2V_2$ , where  $P_1$  and  $V_1$  are the pressure and volume of the sample chamber, and  $P_2$  and  $V_2$  are that of both chambers combined. The measurement was automatically repeated 5 times to ensure complete removal of atmospheric gases and proper thermal equilibration of the sample with the helium gas.

Archimedes' method is based on the buoyancy principle, stating that any object immersed in fluid is subjected to a buoyancy force equal to the weight of the fluid displaced by the object. The displaced volume of fluid is the total volume of the object. The volume of that object is therefore the density of the fluid ( $\rho_{\text{water}}$ ) times the difference between the dry mass of the object ( $M_{\text{dry}}$ ), and the mass of the object when submerged in the fluid ( $M_{\text{wet}}$ ):  $V_{\text{sample}} = (M_{\text{dry}} - M_{\text{wet}})/\rho_{\text{water}}$ .

Experimentally, the setup for Archimedes' method measurements was a precision balance (read out to 0.1 mg) supporting a light wire basket, which hung beneath the scale and was submerged in a beaker of de-ionized water. Samples were cleaned to remove surface contamination and then covered with thin layer of vacuum grease, to confine the total volume (i.e. to prevent intrusion of water into the pores). Samples were weighed dry in air, and then while submerged in de-ionized water using the wire basket. Ten such measurements (with

acceptable 0.5 mg error between each measurement) were carried out for each sample, and the values were averaged. The density of water used in each calculation was dependent of the water temperature during the test [110]. The volume and porosity of the sample were then calculated. The density of monolithic NiTi used in porosity calculations was taken as  $6.45 \text{ g/cm}^3$  [111].

#### **2.2.4 Differential scanning calorimetry (DSC)**

Differential scanning calorimetry (DSC) was carried out on NiTi powders and foams using a Perkin-Elmer DSC-7 apparatus at a rate of 10 K/min under nitrogen cover gas. A specimen of 2-8 mg was placed in an aluminum pan with a hole in the pan cover to allow the passage of cover gas. Two temperature cycles were carried out between  $-60^\circ\text{C}$  (or in some cases  $0^\circ\text{C}$ ) and  $170^\circ\text{C}$ , and the second cycle was used to determine transformation temperatures (from the intersection between the baseline and the steepest slopes of the peak) and transformation enthalpy (from integration of the baseline-subtracted peak). Calibration was carried out using indium (6 mg) before each DSC run.

#### **2.2.5 Mechanical testing and characterization**

Compressive test samples were cut by electro-discharge machining (EDM) to a 2:1:1 parallelepiped shape. The foams were then lightly polished on 600 grit paper to remove the oxidized surfaces formed during the EDM process, which might affect the mechanical results. To eliminate possible differences in residual stresses, the foams were heat-treated (heat treatment varied by sample condition) prior to the compressive test.

The mechanical behavior of foams was investigated by uniaxial compression experiments at ambient temperature in a screw-driven load frame using a cylindrical cage ensuring

parallelism. Prior to and after the experiment, compliance measurement of the system (use exactly the same set up without a sample) was carried on. The calibration of the system using aluminum (Al) standard (6 mm in diameter and 12 mm in height) was done by evaluating the stiffness after the correction with previously-measured compliance (Young's modulus of Al is ~70 GPa).

Engineering strain was determined from crosshead motion, corrected by the compliance of the system. Two kinds of compression test were used in this work: compression to a desired strain or until failure, and compression in a series of load-unload-heat recovery cycles. For compression to a desired stress/strain or until failure, samples were simply compressed with a displacement rate of 0.05 mm/min (except where otherwise noted) until the expected value was reached, or when the load dropped suddenly.

For the load-unload-heat recovery cycles, each sample was loaded and unloaded at a constant crosshead displacement rate of 0.05 mm/min between a minimum strain of 0% and a maximum strain  $\epsilon_{max}$ . At the end of each mechanical loop, the sample was then heat-treated above the austenite-finish ( $A_f$ ) temperature, by the same method used prior to the test, to trigger the shape memory recovery. The sample length was measured by a micrometer with 1  $\mu\text{m}$  precision at 3 points during each cycle: before loading, after unloading, and after heat treatment.

Fig. 2.1 depicts representative stress-strain curves for a maximum strain of 5%. The methods for evaluating strains and average stiffnesses are illustrated on each plot. Average loading and unloading stiffness values,  $E_{load}$  and  $E_{unload}$ , were determined from the slopes of best linear fits of the loading and unloading curves, respectively, while ignoring the stress-strain data between 0 and 10 MPa (all compressive stresses and strains are reported as positive value in this thesis, since tensile testing was not performed), which were considered inaccurate due to sample

settling effects. For unloading stiffness calculations, the data between the maximum stress  $\sigma_{\max}$  and  $\sigma_{\max} - 10$  MPa were also discarded, to avoid the steep stress drop at the beginning of unloading (assigned to machine mechanical hysteresis). It is apparent that stiffness values can vary noticeably from point to point, as compared to the average value, indicating that the foams are not deforming in a purely elastic manner (we thus use the term average "stiffness" rather than "Young's modulus").

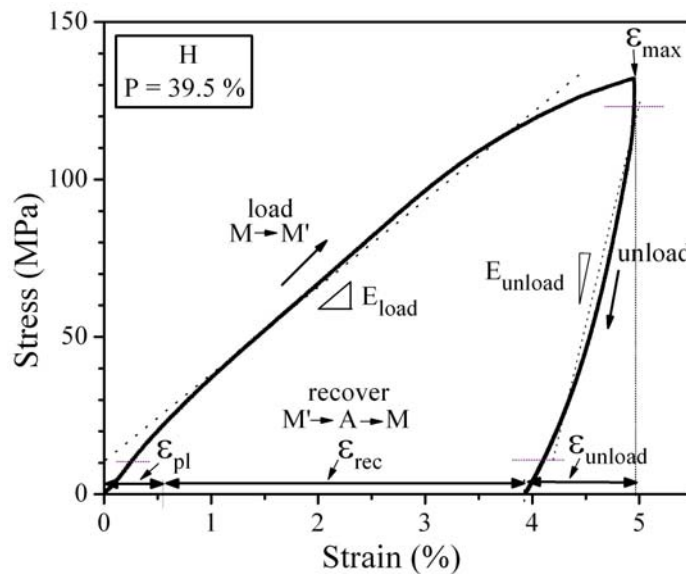


Figure 2.1. Representative compressive stress-strain curve for a maximum strain of 5% (from foam H in Chapter 3). Evaluation method for loading and unloading stiffnesses, and for the unloading, shape-memory and plastic strains are illustrated, together with the phases expected (A - austenite, M – martensite, M' – detwinned martensite).

The unloading strain was calculated from the change of sample length upon unloading from maximum to zero stress, as measured by a micrometer with 1  $\mu\text{m}$  precision. Similarly, the thermal strain recovery was calculated from the difference in sample length before and after the

heat-recovery treatment. Finally, the plastic strain was calculated from the difference in sample length before and after the full thermo-mechanical loop.

## CHAPTER 3

### **Porous NiTi Produced by Hot Isostatic Pressing (HIP) and Space-Holder Method**

The objective of this phase of the thesis work is to develop a processing method for porous NiTi that allows controllability over porosity and pore characteristics (pore size, shape, and connectivity), which are determinant for the desired mechanical and biological properties in bone implants.

As reviewed in section 1.4.1, many powder metallurgy techniques have been used with elemental powders or pre-alloyed NiTi powders to fabricate porous NiTi, but none of them allows for independent control over structural features. These conventional methods proceed in such a way that porosity originally present in the preform, or created during the synthesis step, is not eliminated. Although many versions of these methods have been developed, the ability to control porous structure seems to rely mostly on processing parameters and initial powder packing. Tailor-made porous structures are achieved only with difficulty, and processing windows are narrow.

This issue can be solved by the use of a temporary space-holder phase in order to allow direct manipulation of porosity and pore size/shape through the content and morphology of the space holders, respectively. The temporary space-holder is used during the initial cold compaction of metallic powders into a preform, and is then removed prior to or during the densification of metallic powders. As a result, a metallic foam with open porosity of the fraction

and morphology of the space holder is produced. This method has been used previously for Ti-, Al-, Ni-, Cu-, and Fe-based foams [112-119] with various space-holder materials, including sodium chloride [112] or carbamide [113, 114] for aluminum foams, polymers [115] or potassium carbonate [116] for copper foams, sodium carbonate for nickel foams [117], and ammonium bicarbonate [118] or magnesium [119] for titanium foams.

To apply this solid-state replication method to the fabrication of NiTi foams, two issues must be addressed. The first issue pertains to the low diffusivity of NiTi resulting from its ordered crystal structure, which makes full densification of NiTi powders by pressureless sintering difficult to achieve. We address this concern by using HIP to enhance densification of an encapsulated NiTi powder preform in the presence of space-holder powders. As compared to conventional sintering, this method decreases the time for densification and improves the quality of the bond between metal particles.

In parallel to the present work (from 2005 to 2008), some studies proposed the use of selected space-holders compacted with elemental or pre-alloyed NiTi powders in the following powder metallurgy techniques: ammonium bicarbonate ( $\text{NH}_4\text{HCO}_3$ ) in capsule-free hot isostatic pressing (CF-HIP) [61], saccharose and polymethyl methacrylate (PMMA) in HIP, and sodium chloride (NaCl) with a polymeric binder in metal injection molding (MIM) and sintering [80]. Pore collapse and risk of contamination due to binder and space-holder decomposition might still be of concern for the above NiTi foams, and for other high-melting metal foams densified with temporary space-holders [114, 117, 118]. In the current study, pore collapse will be avoided because the selected space holders will act as permanent (rather than temporary) space-holders during the HIP densification. A second step will then be needed, wherein the space-holder is removed after densification.

Second, the space-holder must be chemically unreactive with NiTi at the densification temperature. We choose here salts, specifically sodium fluoride (NaF) and sodium chloride (NaCl), due to their thermodynamic stability in contact with nickel and titanium, high melting points (993°C and 801°C, respectively) which allow high densification temperatures associated with NiTi, and relatively high solubility in water (0.42 and 35.9 g/100 mL at 25°C [108]), helpful for the removal process. Furthermore, they are commonly-available, low-cost salts which can be easily recycled by precipitation after dissolution from the foam.

The typical morphologies of NaF (99.995% purity) and NaCl (99.0% purity) powders used in this work are illustrated in Fig. 3.1(a) and 3.1(b): NaF powders have a blocky, equiaxed shape, while NaCl powders are cuboidal and have a more regular shape than the NaF. Both powders were procured from Alfa Aesar, MA and sieved in the range of 62-250  $\mu\text{m}$ . Pre-alloyed near-equiatomic (48.6 at.%Ni) NiTi powders with 99.9% purity supplied by Special Metals Corp., NY were used as a matrix material. The NiTi powders are 44-177  $\mu\text{m}$  in size, are nearly spherical, and have smooth surfaces (Fig. 3.1(c)). Small satellites are present, indicating that the powders were produced by liquid spraying. This same batch of NiTi powders was used in the previous monolithic NiTi study in Dunand's research group [120-122] and throughout this thesis with and without sieving to the desired sizes (indicated in each experiment).

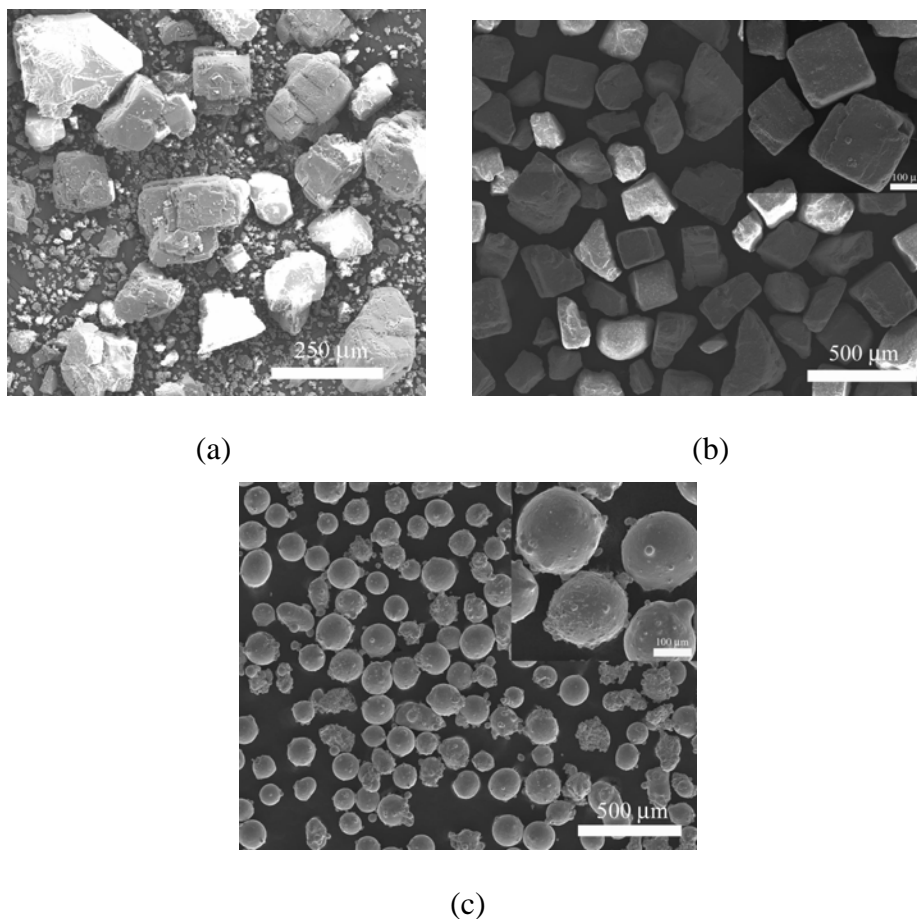


Figure 3.1 (a-c) SEM micrographs of initial powders: (a) NaF, (b) NaCl and (c) NiTi.

The experiments were designed to investigate not only the effect of salt geometry on the resulting foam structure, but also foaming temperatures with regard to the melting point of the salt (in other words, the physical state of salt). In particular, the HIP temperature of NiTi/NaF mixtures was kept below the melting point of NaF ( $993^{\circ}\text{C}$ ) such that NaF remained solid during HIP, while that of NiTi/NaCl mixtures was above the  $801^{\circ}\text{C}$  melting point of NaCl, such that NaCl was in the liquid state during HIP. The effect of HIP temperatures and of subsequent sintering steps, in terms of structure and properties, is discussed in the following sections.

### **3.1 Shape-memory NiTi foams produced by replication of NaF space-holders**

In this section, we present the microstructure and physical and mechanical properties (including shape-memory properties) of an open-cell NiTi foam produced by the above solid-state replication method, using pre-alloyed NiTi powders and NaF.

#### **3.1.1 Experimental processing**

A mixture of 59.9 vol.% NiTi and 40.1 vol.% NaF powders was HIPed at 950°C for 4 hours under a pressure of 100 MPa (section 2.1). The HIP temperature was selected to be high enough to allow densification of the NiTi powders (950°C corresponds to a homologous temperature of 0.77, given the NiTi melting point of 1310°C) while remaining below the NaF space-holder melting point of 993°C.

After salt removal (section 2.1), samples were divided into two groups: a first group (labeled H for HIP) was characterized in the as-HIPed condition while a second group (labeled HS for HIP/sinter) was subjected to a subsequent sintering step under high vacuum at 1250°C for 24 h before being characterized with the same procedures, listed below.

The microstructure and phase transformation behavior of these foams were investigated by SEM and DSC, as explained in section 2.2. Mechanical test samples were annealed in an oil bath at  $160 \pm 2^\circ\text{C}$  for 5 min and oil-quenched to room temperature, to reduce any effect of the prior stress and thermal history. The compression experiments were conducted on each sample in the load-unload-recovery fashion described in detail in section 2.2, i.e. by loading and unloading

at a constant crosshead displacement rate of 0.05 mm/min between a minimum strain of 0% and a maximum strain  $\epsilon_{\max}$ , with  $\epsilon_{\max}$  increasing in 1% increments from 1 to 6% for foam H, and from 1 to 8% for foam HS over six, respectively eight, consecutive loops. After its eighth cycle, foam HS was subjected to a final compressive loop to a maximum stress of 482 MPa and strain of 15.6%.

### 3.1.2 Foam properties

#### 3.1.2.1 Microstructure

Representative SEM micrographs of foams H and HS are shown in Figs. 3.2 and 3.3, respectively. Fig. 3.2 (a) provides a view of the microstructure of foam H at low magnification, which illustrates that a porous structure was achieved after hot isostatic pressing and salt removal. The overall porosity of foam H is  $39.5 \pm 0.1\%$  and its closed porosity is  $2.8 \pm 0.6\%$ ; by subtraction, the open porosity is 36.7%. A vast majority of open porosity in the overall porosity was expected, since the salt leaching process implies an open and connected pore network. The small discrepancy between the open porosity (36.7%) and the NaF initial volume fraction (40.1%) is assigned to inhomogeneities during packing of the powder blend in the HIP can, explainable by the large mismatch in densities between NiTi (6.45 g/cm<sup>3</sup>) [111] and NaF (2.78 g/cm<sup>3</sup>) [108]. In fact, this large density mismatch is the reason why coarser NaF powders were not used, despite the improvement in powder packing (and thus eventual densification) provided by blends with powders of different sizes: it was not possible to uniformly mix coarser NaF (250-350  $\mu\text{m}$ ) with the present NiTi powders.

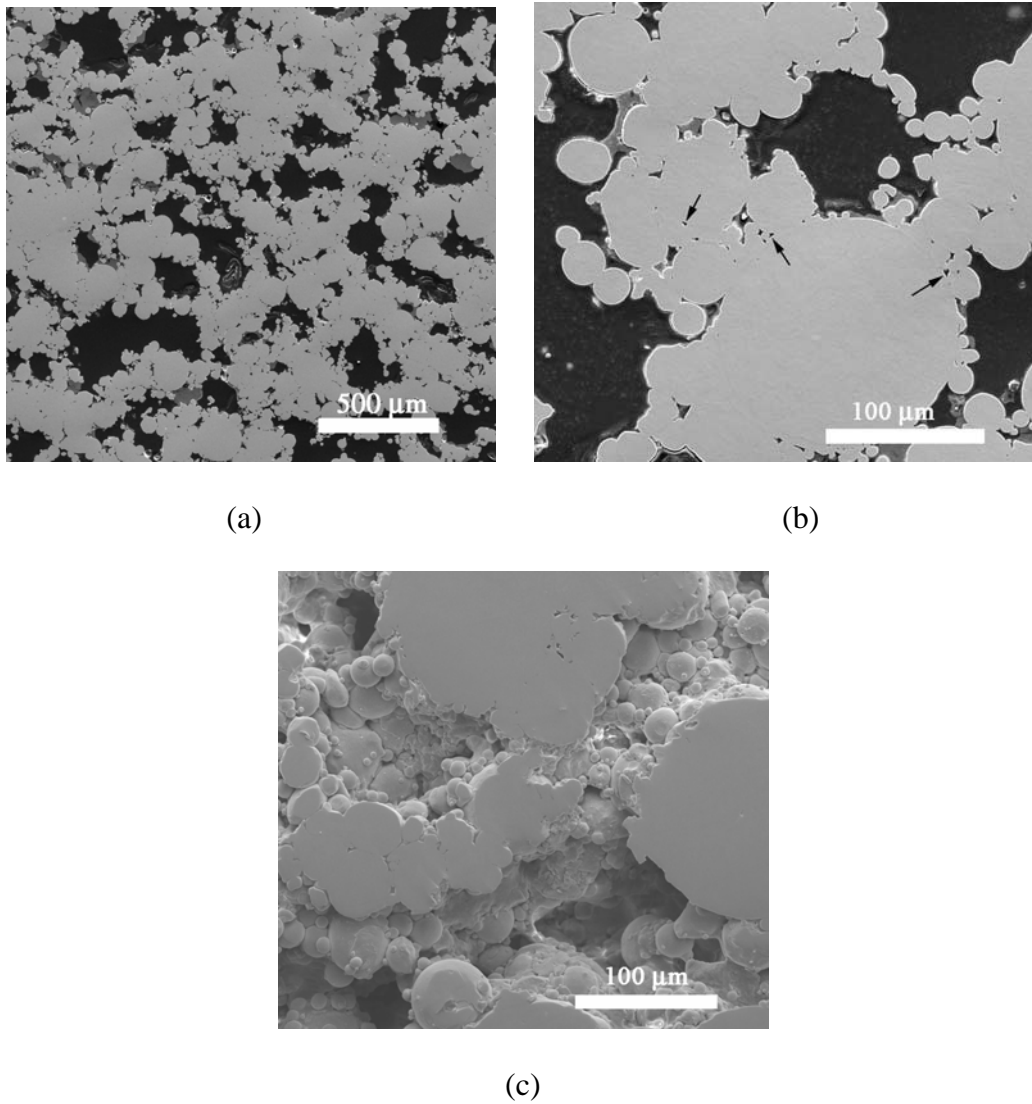


Figure 3.2. SEM micrographs of 39.5% porosity foam H (densified by HIP and with salt removed): (a, b) resin-filled pores at low and high magnification, (c) unfilled pores.

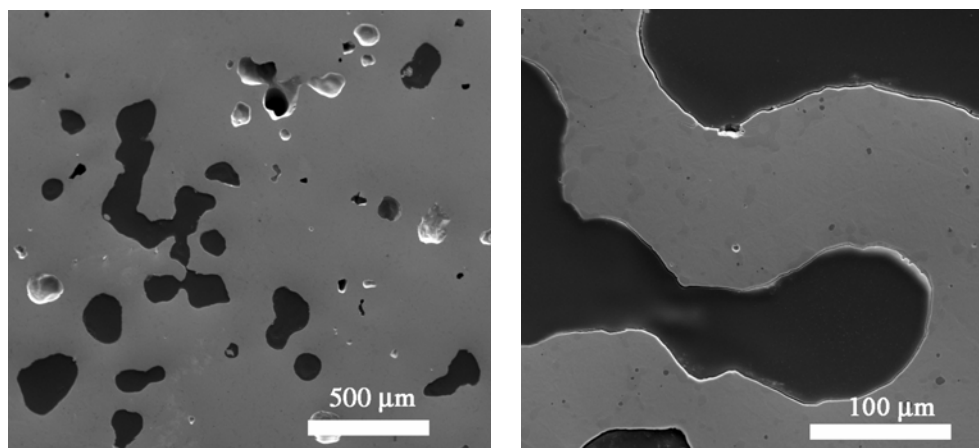
A higher magnification image of foam H (Fig. 3.2 (b)) shows that individual NiTi powders are still identifiable but that they are connected with each other through sizeable necks. Closed porosity is probably associated with the small pores present between partially densified

powders (some of which are marked with arrows in Fig. 3.2 (b)). These fine pores, with sizes typically under 10  $\mu\text{m}$ , were probably never filled with NaF. Incomplete sintering is also confirmed by the presence of individual NiTi particles lining the surfaces of the large pores, as shown in Fig. 3.2 (c) for a sample not infiltrated with epoxy. The closed porosity is expected to be empty, because no salt was observed during metallographic examination, and because the salt fraction is well above the percolation threshold. Moreover, neither reaction between NiTi and NaF (which may have occurred during HIP) nor corrosion of the NiTi (which may have occurred during salt dissolution) was observed.

The large pores (with size as large as 400  $\mu\text{m}$ ) correspond to the salt particles and have an irregular shape with average sizes of  $242 \pm 32 \mu\text{m}$ , similar to those of the NaF powder (Fig. 3.1 (a)). Some of the largest pores may have been due to agglomeration of a few NaF particles. The irregular shape of the large pores also indicates that, during the HIP process, the NaF powders do not deform significantly. This suggests that pore shape and size can be controlled by the NaF space-holder, but not to the same extent as in replicated foams using liquid metal infiltration, [123] since densification of the NiTi powders also determines the quality of the pore surface. As shown in Fig. 3.2(a-c), individual rounded NiTi powders are still visible, thus giving a rough topography to the inner surface of the larger pores.

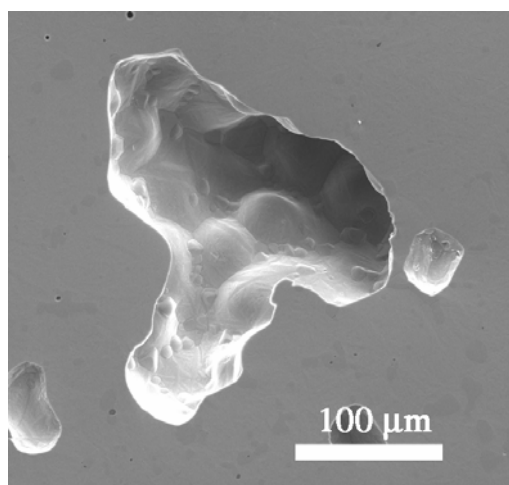
Optimization of the HIP parameters or further sintering after the HIP process may increase the densification of the NiTi powders and eliminate these fine pores. For the former option, higher HIP pressure and/or higher HIP temperature (using higher-melting salts such as  $\text{BaF}_2$  or  $\text{SrF}_2$  which have been used successfully for replication of Zr-based foams [124, 125] could be used.

In the present work, a high-temperature sintering step was chosen to further densify the NiTi powders, resulting in foam HS. SEM micrographs of foam HS (Fig. 3.3(a-c)) show the effect on the microstructure of the subsequent high-temperature sintering step. Individual NiTi powders are not visible anymore, unlike for foam H, and the fine cusped pores between NiTi powders have disappeared. This step altered significantly the pore shape and size: the large pores previously occupied by NaF exhibit smaller average sizes ( $177 \pm 41 \mu\text{m}$ ), more rounded shapes and much smoother inner surfaces than those in foam H.



(a)

(b)



(c)

Figure 3.3. SEM micrographs of 19.6% porosity foam HS (processed like foam H and additionally vacuum-sintered): (a, b) resin-filled pores at low and high magnification, (c) unfilled pores.

Also, a significant increase in the overall degree of densification was observed, which was confirmed by density measurements showing a total porosity of  $19.6 \pm 0.1\%$  which is half of the pre-sintering porosity and close to the percolation limit. Accordingly, about one third of the porosity ( $6.6\% \pm 0.2\%$ , more than twice the pre-sintering value) is now closed, while two thirds ( $13.0\%$ , much reduced from the pre-sintering value) remain open. Foam HS thus represents an upper limit in foam densification, beyond which alternate processes might be better suited, e.g., pore expansion by entrapped gas, as done by Greiner et al. [28] who reported porosities of 19-20% after 100 to 200 hours of expansion at  $1200^\circ\text{C}$ . In that study, however, the NiTi porosity was fully closed. Sintering of foam H at lower temperature and/or shorter time is expected to produce foams with structures and porosities intermediate between those of foams H and HS.

#### 3.1.2.2 Phase transformation behavior

DSC thermograms of the NiTi powders and foams H and HS are shown in Fig. 3.4. To first order, the martensite start and finish ( $M_s$  and  $M_f$ ) and the austenite start and finish ( $A_s$  and  $A_f$ ) temperatures are given in Table 3.1, together with the transformation enthalpies calculated from the area of the transformation peaks. These transformation temperatures are typical of stoichiometric, or slightly nickel-poor, NiTi compositions [35].

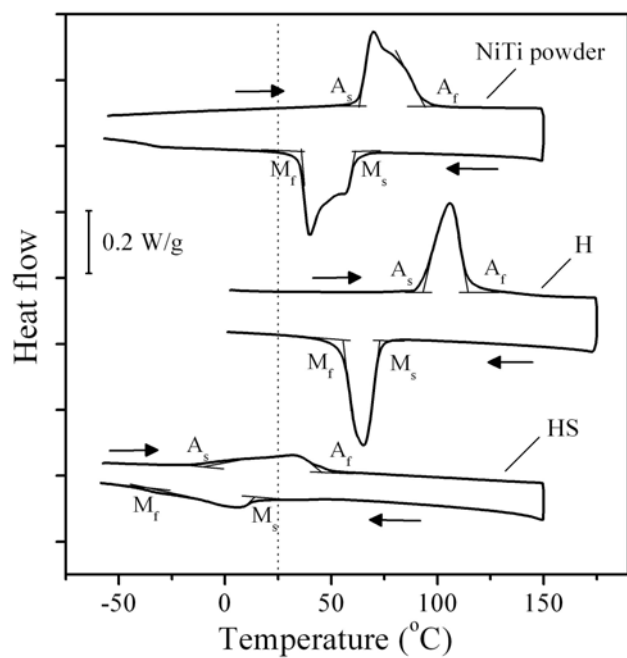


Figure 3.4. DSC curves of NiTi powder and foams H and HS.

Table 3.1. Transformation temperatures and enthalpy on heating and cooling for NiTi powder, foam H and HS.

	Powder	Foam H	Foam HS
<b>Heating</b>			
$A_s$ (°C)	63	92	-18
$A_f$ (°C)	93	114	47
<b>Enthalpy (J/g)</b>	23.8	23.9	10.9
<b>Cooling</b>			
$M_s$ (°C)	61	73	24
$M_f$ (°C)	35	55	-45
<b>Enthalpy (J/g)</b>	23.8	24.0	11.3

Foam H exhibits phase transformations typical of bulk NiTi, with peaks resulting from the transformation between the low-temperature martensitic B19' phase and the high-temperature austenitic B2 parent phase (and lacking a second peak for the R-phase). The transformation enthalpies for foam H on both heating and cooling are very close to published values for bulk NiTi (24.3 J/g) [111]. This implies that neither the HIP process nor the salt dissolution step significantly affected the composition of foam H.

Given its  $M_f$  value of 55°C, foam H is fully martensitic during mechanical testing at ambient temperature after oil quenching from the annealing temperature of 160°C. In addition, the reverse transformation upon heating is complete well below the temperature of 160°C used to induce the shape-memory effect.

Comparison between the NiTi powders and foam H (Fig. 3.4 and Table 3.1) shows that after HIP processing, the transformation enthalpies of NiTi remain nearly the same, indicative of full transformation, but that the transformation temperatures are increased by about 10-30°C. The significantly lower transformation temperatures and the presence of double peaks on both heating and cooling, may be the result of internal stress in the powders due to fabrication by rapid solidification (inferred from their spherical shape).

As compared to foam H, foam HS shows a decrease in the transformation enthalpies (by about a factor 2), a decrease in transformation temperatures (by about 50°C for  $M_f$  and  $A_f$  and 110°C for  $M_s$  and  $A_s$ ), and an increase in the spread between start and finish temperatures (Fig. 3.4 and Table 3.1). The shift in transformation temperature as well as the reduction in transformation enthalpy observed for foam HS is indicative of composition changes occurring during the 24 h vacuum-sintering treatment. It is likely that residual gases in the furnace were sufficient to oxidize (or nitride) preferentially titanium, resulting in a slightly Ni-rich

composition: for Ni-content in excess of approximately 49.6 at.%, the  $M_s$  temperature drops precipitously by about 90 °C for each at.% Ni [126]. The broadening in the transformation peaks for foam HS may also reflect that some regions of the foam (probably near the surfaces, where reaction with gas was more extensive) are more Ti-depleted than others (away from the surface), and the reduction in transformation enthalpy may indicate that parts of the sample (near the surface) do not transform at the lowest used temperature of -60 °C.

Given its  $M_s$  value of 24 °C, foam HS consists of metastable austenite at the onset of mechanical testing at ambient temperature, thus affecting its mechanical properties, as described in the next section.

### 3.1.2.3 Mechanical and shape-memory properties

Fig. 3.5 (a and b) shows stress-strain curves from the series of compressive load-unload-recovery tests on foams H (39% porosity) and HS (19% porosity). Strain recovery by reverse transformation upon heating after each compressive load-unload loop is indicated by a horizontal arrow for each cycle.

It is apparent from Fig. 3.5 (a) that foam H exhibits near linear stress-strain curves, with plastic strain accumulated after each cycle increasing from 0.5 to 5%. Five load-unload-recovery cycles were carried out before the final cycle (maximum strain of 6% and maximum stress of 135 MPa) led to large-scale damage, visible as a stress drop before unloading. In the first five cycles, the shape-memory recovery (expressed as a fraction of the plastic strain) is near constant at 85-89%, but decreases to 71% for the last cycle where damage had accumulated.

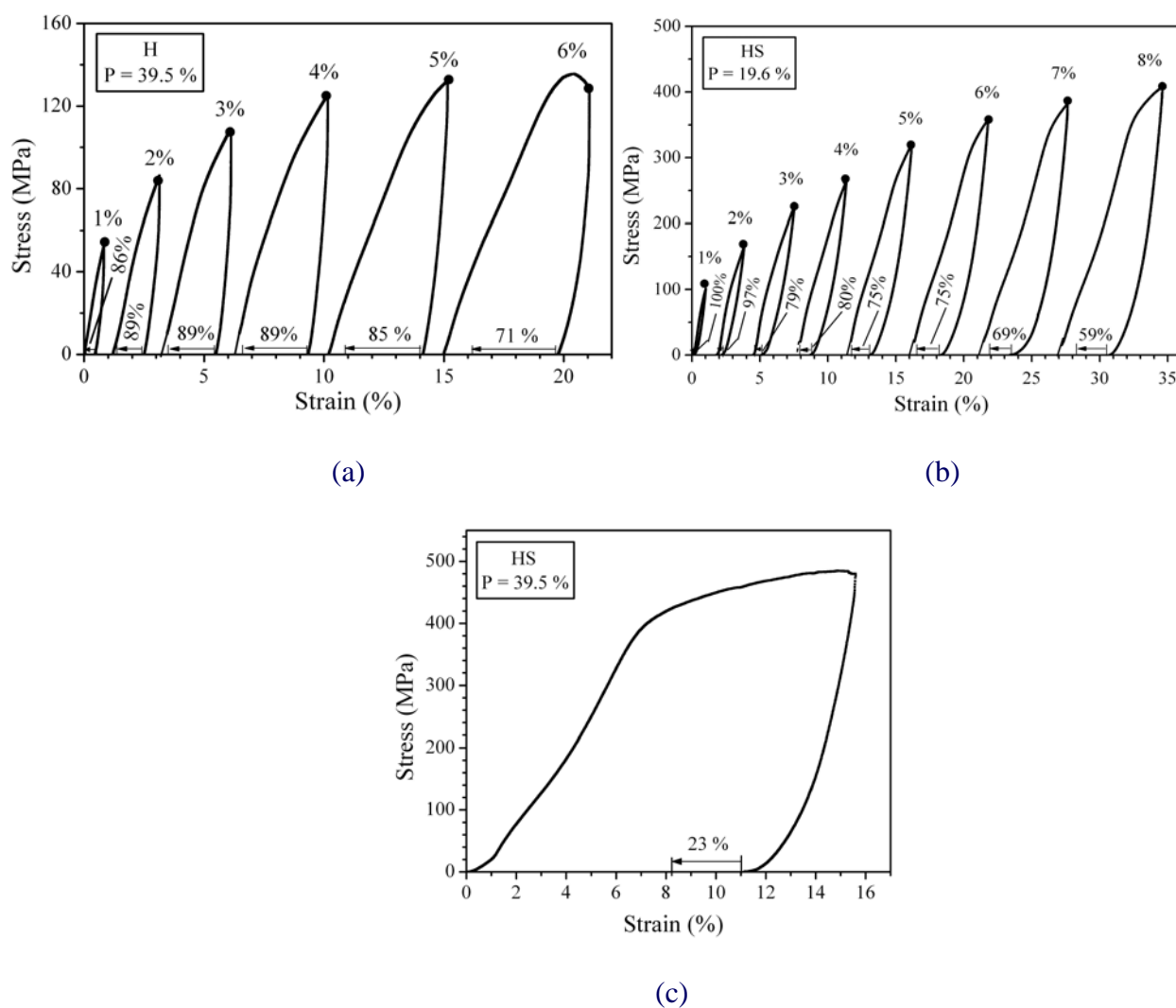


Figure 3.5. Series of compressive stress-strain curves (load-unload) for increasing maximum strains for: (a) foam H; (b) foam HS. Curves are shifted along the y-axis for clarity. Arrows along the y axis for each curve represent the thermally-recovered shape-memory strain. The stress at which the sample is unloaded is marked with a dot. (c) final compressive stress-strain curve for foam HS up to maximum strain of 15.6%.

Foam HS (Fig. 3.5 (b)) shows a load-unload-recovery behavior that is generally similar to foam H, but with some important differences, as expected from its lower porosity and lower transformation temperatures. For a given maximum strain, the stress is much higher, corresponding to a higher average stiffness on loading. On unloading, however, the reversible strain is higher than for foam H, corresponding to a lower unloading stiffness. Also, as compared to foam H, the magnitude of the shape-memory recovery of foam HS is much reduced, and somewhat reduced when normalized by the plastic strain accumulated after each load-unload cycle.

Finally, the last cycle shown in Fig. 3.5 (c) is characterized by a near-linear range up to a stress of ~400 MPa and a strain of ~7%, followed by a plateau with a much lowered slope up to the highest stress of 482 MPa and a strain of 15.6%, terminated by the beginning of stress drop. A much reduced, but still sizeable, shape memory strain (2.7% or about a quarter of the residual strain after unloading) was measured. It is also noticeable from the unloading curve (in particular from the sharp strain recovery below 25 MPa) that foam HS shows superelastic strain recovery, which is followed by a sizeable shape-memory strain recovery during the thermal excursion.

Detailed discussion and comparison of mechanical behavior in foams H and HS to literature values is provided below.

### *Strength*

The ultimate compressive stress of 135 MPa obtained from foam H with 39.5% porosity (Fig. 3.5 (a)) is low as compared with porous NiTi with the same level of porosity produced by different methods: 245 MPa for austenitic NiTi with 42% open porosity produced by gas

expansion [33], 180 MPa for austenitic NiTi with 30-40% open porosity produced by sintering of elemental powders [58], 275 MPa for austenitic NiTi with 27% partially open porosity produced by capsule-free HIP [127]. Direct comparison is again complicated by the different phases present (and thus the inherent strength of the NiTi material present in the foam), and the fact that foam H had been subjected to five prior stress-strain-recovery cycles, which may have produced damage. It is, however, likely that the highly irregular pore shape (acting as internal notches, or stress concentrators) contributes to the relatively low strength observed in foam H.

Foam HS showed a marked improvement in ultimate strength (which is in excess of 482 MPa, Fig. 3.5 (c)), as expected from the reduced level of porosity, the more equiaxed pore shape, and the smoother pore surfaces. For comparison, an austenitic foam with 16% closed porosity displayed no fracture up to a stress of close to 1000 MPa [28].

### *Stiffness*

Foam H is fully martensitic, so detwinning is expected to occur during loading. While no stress plateau is visible, the anomalously low value of the loading stiffness, which is plotted in Fig. 3.6 for all loops, is a strong indication that detwinning occurs continuously during the loading part of the stress-strain curve. This is confirmed by two further observations. First and most directly, a significant shape-memory effect is measured after thermal excursion, as indicated in Fig. 3.5. Second, the unloading stiffness, which is expected to be mostly elastic (assuming no reverse detwinning), is 3-4 times higher than the loading stiffness (Fig. 3.6), which must thus contain significant contribution from detwinning. We note, however, that the unloading stiffnesses (12-16 GPa) are significantly lower than predicted from Ashby's theory for

open cell, cellular foams, which is expected to be  $(1 - P)^2 E_{\text{NiTi}} = 22\text{-}25$  GPa based on porosity  $P = 0.395$  and Young's modulus  $E_{\text{NiTi}} = 61\text{-}69$  GPa [128] . This discrepancy on unloading may be due to some reverse detwinning or, more likely, to an inherently lower elastic stiffness due to deviation from the cellular architecture assumed for the above model, and the presence of non-load-bearing metal extrusions in the pores. If foam H were mechanically cycled without intermediate shape-memory recovery, the loading stiffness would be expected to become similar to the measured unloading stiffness, i.e., 12-16 GPa, since detwinning on loading would be exhausted in the first cycle. This stiffness range is exceptionally low as compared to other metallic foams, a property that may be useful for bone-replacement implants whose stiffness should ideally match that of bone (12-17 GPa for compact bone [29])). It is difficult to compare the stiffness of foam H, which is martensitic, with that of other published NiTi foams, which are all austenitic and can thus show extraordinary low stiffness due to the superelastic effect. For example, an open-cell austenitic NiTi foam with the same range of porosity (42%) and pore size (500  $\mu\text{m}$ ) as foam H, but produced by SHS followed by gas expansion [33], has a similar stiffness (15 GPa) at 60°C (above  $A_f$ ) as that measured here for foam H.

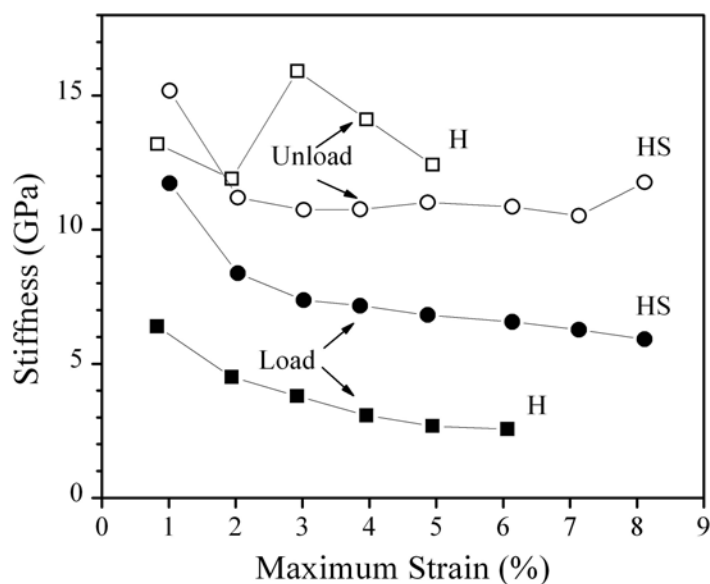


Figure 3.6. Loading and unloading stiffness as a function of maximum compressive strain for foam H and HS.

Given that foam HS has much lower porosity than foam H and consists of metastable austenite, it is not surprising that its loading and unloading stiffnesses are quite different from those of foam H. The lower porosity increases its Young's modulus, but its austenitic structure allows for the activation of superelastic deformation on both loading and unloading thus reducing its average stiffness. As shown in Fig. 3.6, the interplay between these different mechanisms (elastic and detwinning deformation for foam H and elastic and superelastic deformation for foam HS) leads to the unusual situation where stiffness for foam HS is higher on loading but lower on unloading than for foam H. Thus, on loading, martensite detwinning in foam H produces larger strain (and thus lower stiffness) than the stress-induced formation of martensite in foam HS. However, on unloading, foam H does not show significant reverse

detwinning, while foam HS recovers strain superelastically by a reverse martensite-austenite transformation.

As a result, load and unload stiffnesses are in a relatively narrow range of 6-12 GPa for foam HS. For comparison, an austenitic sample with 16 vol.% of closed porosity produced by gas expansion showed an average loading stiffness (from 0 to 400 MPa, similar to the last loop of foam HS) of about 15 GPa [28].

#### *Shape-memory strain recovery*

Fig. 3.7(a) presents for foam H unloading strain, shape memory recovery strain, and residual plastic strain (these strains are illustrated in section 2.2 and are determined from the six load-unload-recovery curves in Fig. 3.5(a)). It is apparent that the shape-memory strain increases near linearly with the maximum applied strain, up to a maximum value of 3.2%. In bulk NiTi too, the shape-memory strain increases near linearly with the applied strain, a behavior associated with the stress plateau during which detwinning takes place [121]. Such a constant-stress plateau is, however, not visible in foam H, or rather the whole loading branch of the stress-strain curve can be considered as a steadily increasing plateau where twinning occurs continuously.

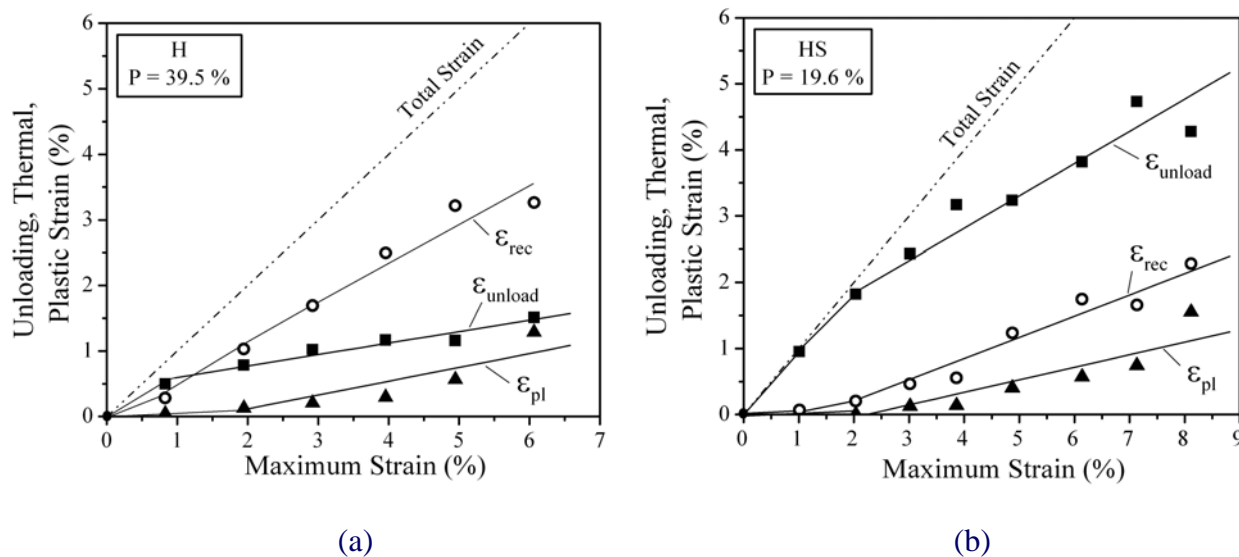


Figure 3.7. Unloading, shape-memory and plastic strain as a function of maximum compressive strain for: (a) foam H; (b) foam HS.

The compressive shape-memory recovery capability of foam H is similar to that for pore-free NiTi produced from the same pre-alloyed powders [121]. For a residual strain after unloading of  $\sim 2\%$  (accumulated at the end of the 3% load-unload cycle in Fig. 3.5(a)), foam H recovers 89% of this strain, while pore-free NiTi recovers 87% [129]. For a residual strain of  $\sim 4\%$  (4.4% for bulk NiTi and 3.9% for foam H after the 5% cycle in Fig. 3.5(a)), the shape-memory recovery is again very similar (83% for bulk NiTi and 85% for foam H). The maximum stresses to achieve those strains are, however, much higher for bulk NiTi ( $\sim 370$  MPa for 2% residual strain, and  $\sim 910$  MPa for 4.4% [129]) than for foam H (108 and 131 MPa, respectively). Thus, at least for the relatively low shape-memory strains studied here ( $< 3.2\%$ ), the foam strain recovery is similar to bulk NiTi, but necessitates much lower stresses for a given deformation level.

The maximum shape-memory recovery strains (3.2% for the 5% and 6% cycles, Figs. 3.5(a) and 3.5(a)) are, however, lower than the maximum value of 4.5% recoverable in compression for bulk NiTi (albeit after deformation to a much higher stress of ~1300 MPa) [129]. A likely reason is the early onset of dislocation plasticity and damage in foam H at regions of stress concentrations, which inhibit the shape-memory recovery.

Improvements in the foam architecture would likely increase the maximum recoverable shape-memory strain in foamed NiTi. Also noteworthy for foam H is the large unloading strain of 1.5% for the maximum strain of 6%. For comparison, pore free NiTi has about the same unloading strain of 1.6% for the same maximum strain of 6% [129], but at a much higher maximum stress of 900 MPa. As discussed earlier, this large unloading strain in foam H is the result of the anomalously low value of its unloading stiffness, which may be associated with some reverse twinning and/or large elastic deflections due to uneven pore geometries. Thus, foam H, when compressed to a relatively modest (as compared to bulk NiTi) stress of 135 MPa, is capable of recovering a total strain of 4.8% by combination of unloading and shape-memory strains, with a relatively low plastic, unrecoverable strain of 1.3%.

#### *Superelastic strain recovery*

Fig. 3.7(b) shows that recovery in foam HS is dominated by the unloading strain through a combination of elastic and superelastic effects. A sizeable shape-memory strain is furthermore achieved during the thermal excursion. The coexistence of both superelastic and shape-memory effects can be explained as follows. Before loading, the sample is fully austenitic, but very close to forming martensite (given its  $M_s$  temperature of 24 °C). On loading, stress-induced martensite

is formed, and a fraction of this martensite disappears on unloading, producing the superelastic strain. But another fraction of the martensite remains in the sample after full unloading, given that the  $A_f$  temperature of 47 °C is well above room temperature.

Only upon subsequent heating to 160 °C does this martensite disappear, producing the shape-memory strain. For an applied strain of 7% at a stress of 380 MPa, a maximum unloading (elastic and superelastic) strain of 4.7% is achieved, which is compounded by a subsequent shape-memory recovery strain of 1.7%, for a total recoverable strain of 6.4%. A similar total recovered strain of 6.6% is achieved for the 8% cycle (with a maximum stress of 406 MPa), with slightly less unloading strain and slightly more recovery strain (Fig. 3.7(b)). For comparison, an austenitic NiTi foam with 16% closed porosity exhibited an unloading strain less than 2.5% for a similar maximum stress of 400 MPa [28]. However, foam HS was not heat-treated to develop optimal superelastic properties, so comparisons with other literature results on superelastic NiTi foams are not attempted.

### 3.1.3 Conclusions

Open-pore NiTi foams with shape-memory properties were fabricated by a solid-state replication method, wherein a mixture of pre-alloyed NiTi and NaF powders was densified by hot isostatic pressing at 950°C into a billet, from which the NaF space-holder was subsequently removed by water dissolution. The resulting martensitic NiTi foam, with a mostly-open porosity of 39.5% and a pore size of 240 µm, exhibited pores with a ragged internal surface, due to incomplete sintering of NiTi powder particles. The following mechanical properties in compression were measured: (i) a near linear loading stress-strain curve, with a very low average

stiffness of 3-6 GPa, as a result of detwinning on loading; (ii) a near linear unloading stress-strain curve, with an average stiffness of 12-16 GPa, indicative of elastic deformation; (iii) an ultimate compressive strength of 127 MPa at 6% strain; and (iv) a large shape-memory recovery, with 85-89% of the strain accumulated on unloading recovered after a thermal excursion, and a maximal value of 3.2%.

After sintering at 1250°C, the foam showed a reduced porosity of 19.6% (a third of which was closed), smaller and smoother pores, and a shift in transformation temperature, most probably due to oxidation. This metastable austenitic foam exhibited the following mechanical properties: (i) near linear loading and unloading stress-strain curves, with an average stiffness of 6-12 GPa, as a result of the superelastic effect; (ii) much higher ultimate strength (>482 MPa) and strain (>15.6%); (iii) a sizeable shape-memory-recovery (60-97%), which, when added to the elastic and superelastic recovery strain on unloading, provided a total recovery strain of up to 6.5%.

In this approach (using sodium fluoride, NaF, as a space-holder together with prealloyed NiTi powders), the HIP densification temperature (950°C) was kept below the melting point of NaF (993°C) to avoid melting the space-holder. However, this relatively low temperature (as compared to the 1310°C melting point of NiTi) led to incomplete densification of the NiTi powders. This problem was solved by a sintering treatment of the NiTi foam after NaF removal, which, however lead to a large reduction in foam porosity. For optimal, single-step densification of NiTi powders in the HIP process, it is thus desirable to exceed the melting point of the space-holder to reach temperatures high enough for rapid diffusion in the metal.

### **3.2 Shape-memory NiTi foams produced by replication of NaCl space-holders**

The motivation for using molten NaCl as space-holder is to access high temperatures during HIP densification, so as to improve the metal powder densification kinetics, without the use of a high-melting space-holder such as NaF ( $T_m=993^\circ\text{C}$ ) for NiTi foams or BaF<sub>2</sub> and SrF<sub>2</sub> ( $T_m=1368$  and  $1473^\circ\text{C}$ ) for Zr-based foams [124]. As compared to these fluorides, sodium chloride is inexpensive, has much higher solubility in water (thus facilitating dissolution), does not form fluoride ions during dissolution (which can pit the foam and have high toxicity, becoming problematic if the foam is to be used as biomedical implant), and can be easily synthesized in various powder shapes [123], allowing modification of pore shape, connectivity and surface roughness.

In the past, NaCl has been used as a space-holder for aluminum foams made by liquid metal infiltration [130], or by sintering [131] and spark plasma sintering [132], but always below its melting point. NaCl space-holders were also used in a MIM process for making porous NiTi [80] but were removed before the sintering process, which took place at a temperature higher than its melting point. Thus, to our knowledge, this is the first time that metallic powders have been densified in the presence of a molten (rather than solid) space-holder to produce a metallic foam.

Two HIP temperatures were used here. The first HIP temperature of  $950^\circ\text{C}$  was chosen to compare the H1 foams with those obtained at the same HIP temperature using solid NaF space-holders, as described in the previous section. The second HIP temperature of  $1065^\circ\text{C}$  was

selected because it is as high as possible without exceeding the Fe-Ti eutectic temperature of 1085°C, which may have led to liquid formation by a reaction of NiTi with the HIP steel can.

### 3.2.1 Experimental processing

NiTi and NaCl powders (Figure 3.1 (b-c)) were mixed with a volume percentage of 60.0 and 40.0%, respectively. Two HIP cans were prepared and subjected to HIP densification for 4 h under a pressure of 100 MPa at two different temperatures, 950 and 1065°C (both well above the 810°C melting point of NaCl).

After salt removal (section 2.2), one group of foams was characterized in the as-HIPed condition; these foams are labeled H1 and H2 for HIP at 950 and 1065°C, respectively. Another group underwent an additional sintering step at 1250°C prior to characterization, and these foams are labeled HS1 and HS2 for HIP at 950 and 1065°C, respectively. The foams were sintered for 4 h, except for an additional HS2 specimen sintered for 24 h (hereafter referred to as HS2').

The pore characteristics, phase transformation behavior, and compressive behavior of the foams were determined according to the procedures provided in section 2.2. Compression test samples were heat-treated in an oil bath at  $160 \pm 2^\circ\text{C}$  for 5 min, and then oil-quenched to room temperature, prior to the compressive test. A first set of foams (H1 and HS1) was tested at a displacement rate of 0.05 mm/min, and the tests were ended when load dropped suddenly. A second set of foams (H1, HS1, H2 and HS2) was then subjected to a series of load-unload-heat recovery cycles with 1% increments in maximum loading strain, until signs of a load drop due to foam failure/damage appeared upon loading, or until a maximum strain of 8% was reached.

### 3.2.2. Foam properties

#### 3.2.2.1 Microstructure

Porous NiTi with an interconnected porous structure, as shown in Figs. 3.8-3.10, was successfully produced by the present method. There is no evidence of unwanted interactions between the molten NaCl and solid NiTi, which could pose serious challenges to use of molten space-holders during metal powder densification, on several fronts. First, the molten space-holder may react chemically with the metal. However, the free energies of formation of solid and liquid NaCl are much lower than those of  $\text{NiCl}_2$  and  $\text{TiCl}_4$  [133], and there appears to be no mixed halides containing both Na and Ni or Ti. Second, the molten space-holder may dissolve the metal. For the NiTi-NaCl combination, this is unlikely to occur since synthesis of equiatomic NiTi powders was reported to be possible in molten NaCl+KCl salts at 680-800 °C, starting from elemental Ni and Ti powder, and the resulting NiTi particles exhibited a reversible martensitic transformation indicating high purity [134]. Third, the molten space-holder may wet the metal powders, thus preventing their densification by creating a thin layer of liquid between them. This did not occur in the present case, indicating that molten NaCl poorly wets NiTi and/or that the NiTi powders were sufficiently densified during the HIP temperature ramp prior to NaCl melting.

The rectangular cross-sectional shape of the pores of HIP-densified foams H1 and H2 (Figs. 3.8(a-b) and 3.9(a-b)) indicates that the solid NaCl particle shape (Fig. 3.1(c)) is well replicated and that NiTi powders densified into a rigid matrix before the NaCl melted, during the temperature ramp of the HIP process, which occurred under pressure. The lack of trapped NaCl in closed porosity also indicates that NiTi densification was sufficient prior to NaCl melting to

prevent liquid NaCl from infiltrating the surrounding NiTi powder. It is unknown whether molten NaCl wets NiTi, but the HIP pressure was most probably high enough to induce pressure infiltration if much open porosity had been available in the NiTi preform. Thus, it appears that NiTi pre-densification was sufficient for the liquid NaCl to remain within the blocky pores and prevent their collapse from the HIP pressure, but without much liquid infiltrating the small spaces remaining between the surrounding NiTi powders. Also, most of the pores in the H1 and H2 foams are more regular in shape than those in previous foams made with solid NaF spaceholder by HIP at the same temperature (950 °C; section 2.1); this is due to the more uniform shape of the NaCl particles (Fig. 3.1(b)).

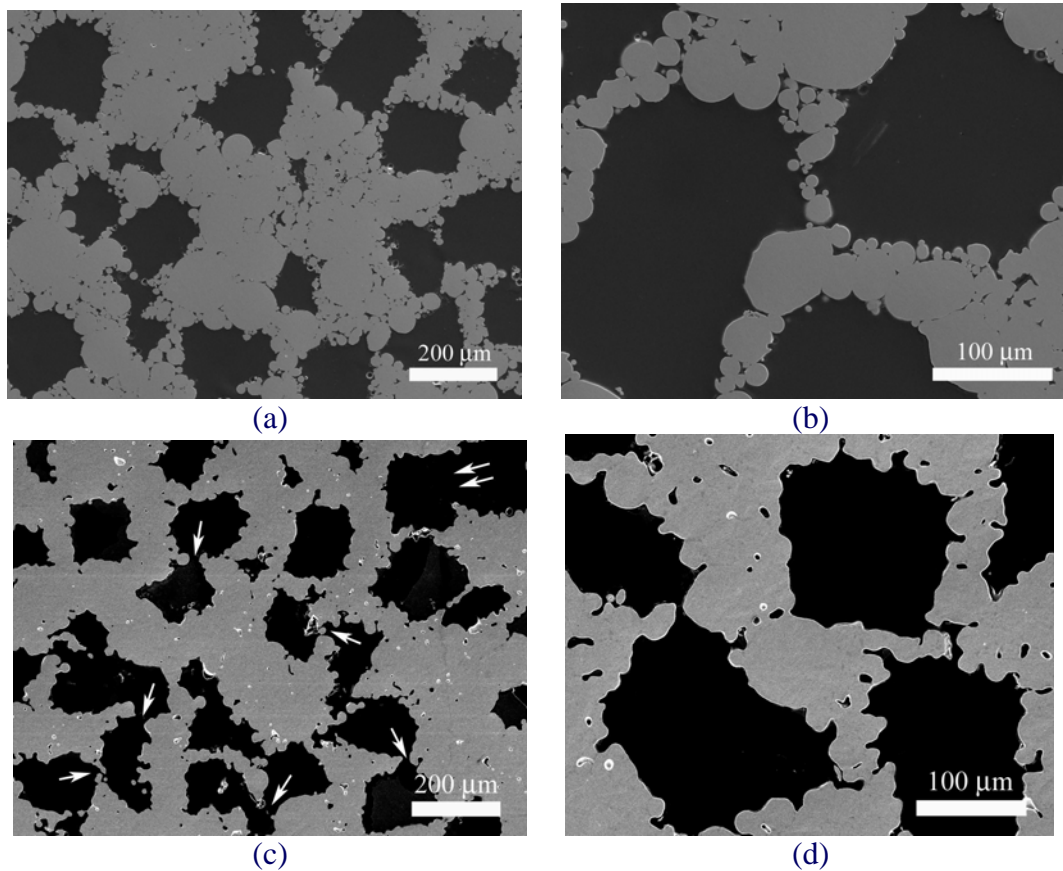


Figure 3.8. SEM micrographs of foam cross-sections with resin-filled pores: (a, b) foam H1 (HIP densified at 950°C, P=36%) and (c, d) foam HS1 (with additional 1250°C sintering, P=35%).

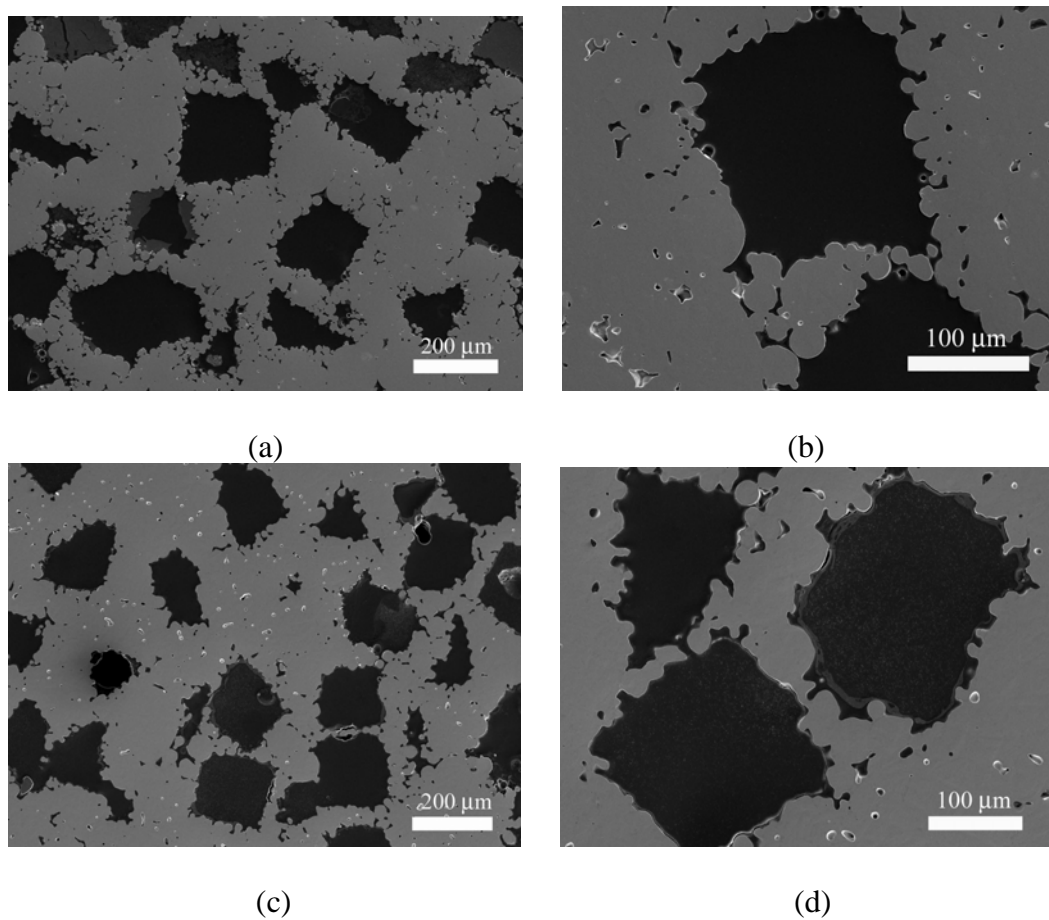


Figure 3.9. SEM micrographs of foam cross-sections with resin-filled pores: (a, b) foam H2 (HIP densified at 1065°C, P=32%) and (c, d) foam HS2 (with additional 1250°C sintering, P=32%).

### Effect of HIP Temperature

Partially-densified, spherical NiTi particles are clearly visible in the walls of foam H1 (Fig. 3.8(a-b)), so that the large pores have a very rough surface and the walls contain numerous small pores which seem to be often closed. By contrast, the degree of densification between spherical NiTi powders is much improved in foam H2. Accordingly, the surface roughness of the large pores and the porosity within the metallic walls are reduced, translating into stronger walls and improved foam strength.

### Effect of Sintering Following Low-Temperature HIP

Foams H1 and HS1 have total porosity  $36 \pm 0.1\%$  ( $31 \pm 0.1\%$  open porosity) and  $35 \pm 0.1\%$  ( $34 \pm 0.2\%$  open porosity), with pore sizes  $167 \pm 13 \mu\text{m}$  and  $151 \pm 23 \mu\text{m}$ , respectively. Although pore size and fraction before and after sintering are almost the same, the pore walls of foam HS1, sintered after the low-temperature HIP step, show significantly higher levels of densification than those of foam H1. In fact, pore wall densification was similar to that in foam H2, densified at higher temperature, as visible by comparing Figs. 3.8(b) and (d); in both these cases, smoother surfaces in the large pores, and a reduction of the small pores within the walls, were visible.

### Effect of Sintering Following High-Temperature HIP

The total porosity in the foams HIP-densified at the higher temperature ( $32 \pm 0.1\%$  for H2 and  $32 \pm 0.5\%$  for HS2) is lower by ~3-4% than for the foams H1 and HS1 (densified at the lower temperature), but their open porosity remains high ( $30 \pm 0.1\%$  for H2 and  $28 \pm 0.7\%$  for

HS2). Pore sizes for foams H2 ( $156 \pm 22 \mu\text{m}$ ) and HS2 ( $130 \pm 16 \mu\text{m}$ ) are unchanged as compared to foams H1 and HS1, within the large experimental error. Except for the small decrease in open porosity, there is no clear difference between foams H2 and HS2, as evident by comparing Figs 3.9(b) and (d), indicating that the sintering step had very little effect on the foam microstructure, including the surface roughness of the large pores.

#### Effect of Sintering Time

Densification of the pore walls (*i.e.*, removal of the small pores within the walls and smoothing of the wall surface) is improved, however, by extending the sintering time at  $1250^\circ\text{C}$  from 4 to 24 h, as demonstrated in Fig. 3.10 for foam HS2'. The large pores show much smoother surfaces when compared to foam HS2 (Fig. 3.9(d)), and most of the small pores within the metallic walls have disappeared. The total porosity is slightly reduced (from  $32 \pm 0.5\%$  for HS2 to  $31 \pm 0.1\%$  for HS2') but the open porosity is constant at 28%. This indicates that the closed porosity (associated mostly with small pores within the walls) has been reduced from 4% for foam HS2 to 3% for foam HS2'.

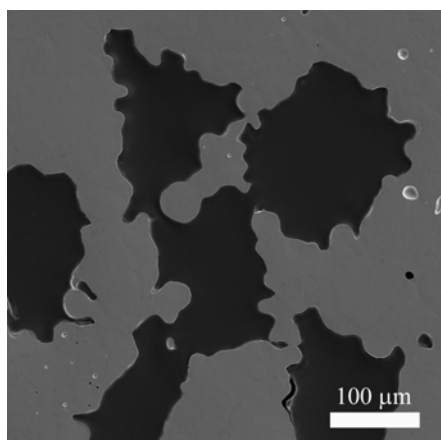


Figure 3.10. SEM micrograph of cross-section of foam HS2' (same process as HS2, except for longer sintering duration at  $1250^\circ\text{C}$ ,  $P=32\%$ ).

Furthermore, fewer small pores were observed in the present foams after HIP, when compared with foams produced using NaF. This was due to better sieving of NaCl, and may explain why the present foams showed much less densification after 24 h sintering as compared to equivalent foams made with NaF space-holders with a larger fraction of small particles.

The porosity of the foams after the HIP process (32-35%) is lower than the expected value of 40% based on the NaCl volume fraction initially present in the mixed powders. The cause might be a heterogeneous distribution of NaCl particles in the initial powder mixture during filling into the HIP can, or a small relocation of molten NaCl to walls of the HIP cans through connecting pore channels, as it is squeezed by the high HIP pressure. Closed porosity of about 2-3% is present as small pores ( $\sim 10 \mu\text{m}$  in size), due to incomplete densification between NiTi powders and possibly trapped NaCl vapor which prevents full densification. This amount is small compared to the microporosity observed (from micrographs) in other studies that rely only on pressureless sintering with NaCl space-holders [80] or on the use of gas-decomposable space-holders [61].

The average pore size is in the range of 130-170  $\mu\text{m}$  for all foams, which is above the minimum value at which bone ingrowth is possible ( $\sim 50 \mu\text{m}$ ) [19]. The pore size was determined by the size of NaCl particles (62-250  $\mu\text{m}$ ), with some large pores resulting from their agglomeration. This indicates that pore characteristics (pore fraction, shape and size) can be tailored in the NiTi foams by the fraction, shape and size of the NaCl used as space-holder.

After sintering at 1250 °C for 4 h (foams HS1 and HS2 in Figs. 3.8(c-d) and 3.9(c-d)), the pores remain rectangular in shape, indicating that diffusivity (both surface and bulk) is insufficient to alter significantly these large pores. The pore surfaces smooth out only

incompletely, again indicating that the diffusivity is low. However, foam HS2' sintered for 24 h shows clear smoothing of the pore surfaces (Fig. 3.10). The sintering temperature of 1250 °C cannot be raised further, given that it is close to the melting temperature of NiTi (1310 °C), and that the solidus of NiTi decreases rapidly even with small deviations from stoichiometry [111]. Since increasing sintering times significantly beyond 24 h is costly and may lead to contamination from residual gases in the vacuum furnace, increasing the HIP time, temperature and pressure are more practical approaches to further improve the densification of the NiTi powders. Indeed, raising the HIP temperature from 950 to 1065 °C seems to be as effective as adding a sintering step at 1250 °C, when comparing the microstructure and mechanical properties of foams HS1 and H2. Use of elemental Ni and Ti powders during HIP densification with molten NaCl space-holders may also be an alternate option as exothermic reaction would help densification.

The benefits of HIP densification on powder consolidation are likely to be more visible at higher porosity, where thinner NiTi walls need to be densified while still maintaining the pore structure without pore collapse. A simple sintering approach with transient space-holders may be problematic for such foams, as some difficulties were noted [80] when producing NiTi with 70% porosity using pre-alloyed NiTi powder and NaCl space-holder.

No NaCl residues were observed in cross-sections. This concurs with chemical analysis results (performed Luvak Inc., MA), which detected 0.041 and 0.065 wt.% sodium and chlorine, respectively, in a 2 g sample of foam HS2. These levels correspond to only about 2 mg of residual NaCl, which is so small that it is unlikely to originate from residual NaCl within the 2-3 vol.% of closed pores. Residual NaCl in open pores is not expected, especially after vacuum sintering, when the foams were subjected to a dynamic vacuum of ~0.001 Pa, much lower than

the vapor pressure of liquid NaCl (estimated as 18 kPa at 1250°C by extrapolating available data [135]). This opens the possibility to simplify the NaCl removal process by replacing the lengthy water dissolution step with a vacuum evaporation step, which may further be carried out at a temperature where sintering of the foam walls can also take place.

One concern in the microstructure of the present foams is that the fenestrations connecting adjacent pores might be much smaller than the pore size, restricting the ingrowth of bone tissue in foams used as implants, unlike the larger fenestrations in porous NiTi (42% porosity) produced by capsule-free hot isostatic pressing [61]. Narrow fenestrations are indicated by arrows in Fig. 3.8(c), but these two-dimensional sections may not represent the true width of the fenestrations (indeed, one large fenestration is marked with a double arrow in Fig. 3.8(c)). Since the pore connectivity directly reflects the contact area of the space-holder powders, changes in NaCl powder volume fraction, shape and size (as compared to NiTi powder size) may lead to more open fenestrations. Alternatively, widening of the fenestrations by chemical dissolution may also be possible.

### 3.2.2.2 Phase transformation behavior

Figure 3.11 shows DSC curves for all four foams upon heating and cooling which, for clarity, are shifted along the y-axis. The presence of a single peak upon cooling indicates the absence of any intermediate phase between the high-temperature austenitic phase and the low-temperature martensitic phase. The transformation enthalpies and temperatures determined from these curves are listed in Table 3.2: they are nearly identical for all foams and are typical of bulk NiTi (enthalpy of 24.3 J/g [111]). The near constant transformation enthalpy confirms that no

signification reaction with molten NaCl or oxidation took place during the HIP densification, water dissolution, or optional sintering steps. The transformation temperatures of the NiTi foams are affected little by the foaming process (transformation temperatures for the as-received powders are lower most probably because of their rapid cooling). However, foam H1 has somewhat lower transformation temperatures (by 5-6 °C) than foam H2, which was densified at a higher temperature, and the DSC curves of the two foams subjected to the additional sintering step (HS1 and HS2) are broadened by 10-15 °C as compared to foams H1 and H2. This broadening of the DSC curve after sintering may be the result of different cooling rates or possibly slight oxidation, leading to a slight enrichment in Ni in the regions near the surface.

Finally, the transformation temperatures for all NiTi foams are above body temperature, so these foams are martensitic at both body and room temperature (where mechanical tests were performed), and consequently are expected to deform by detwinning of the martensitic grains and recover by thermal transformation through the shape-memory effect, as discussed in the next section.

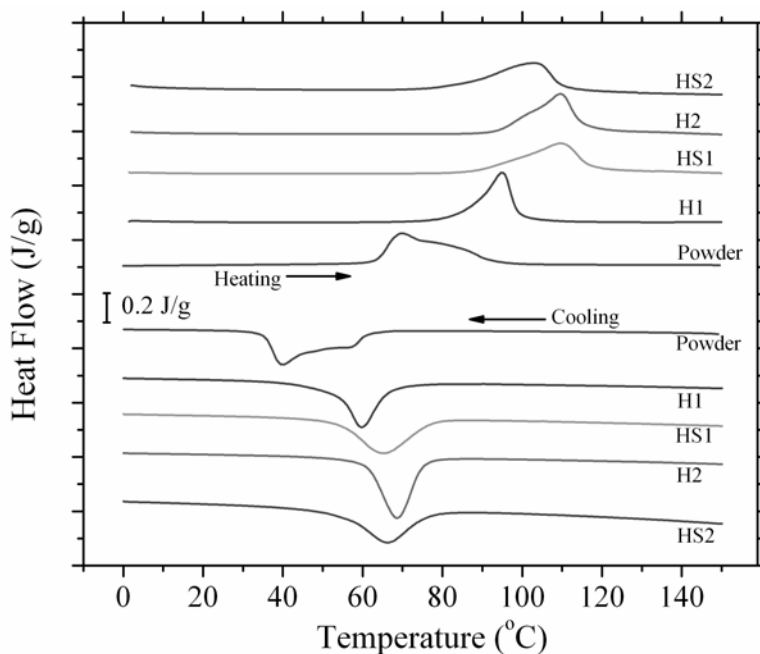


Figure 3.11. DSC curves of NiTi powder and foams H1, H2, HS1 and HS2.

Table 3.2. Transformation temperatures and enthalpies for as-received NiTi powders and foams H and HS.

	<b>Powder</b>	<b>Foam H1</b>	<b>Foam HS1</b>	<b>Foam H2</b>	<b>Foam HS2</b>
<b>Process</b>	as-received	HIP (950°C)	HIP + Sinter (950+1250°C)	HIP (1065°C)	HIP + Sinter (1065+1250°C)
<b>Heating</b>					
<b>A<sub>s</sub> (°C)</b>	63	85	81	91	77
<b>A<sub>f</sub> (°C)</b>	93	98	106	104	103
<b>Enthalpy (J/g)</b>	24	22	24	25	22
<b>Cooling</b>					
<b>M<sub>s</sub> (°C)</b>	61	65	72	71	68
<b>M<sub>f</sub> (°C)</b>	35	54	51	59	47
<b>Enthalpy (J/g)</b>	24	22	23	24	22

### 3.2.2.3 Mechanical and shape-memory properties

Figure 3.12 shows compressive stress-strain curves for foams H1 and HS1 for experiments performed under monotonic loading conditions. Foam H1 reaches a stress of ~200 MPa and a strain ~6% before the stress drops. By contrast, foam HS1 can withstand compressive stresses of 1060 MPa after being deformed to ~42% strain. This illustrates the strong improvement in wall strength achieved by sintering, despite nearly unchanged size, shape and fraction of the large pores.

The load-unload-heat recovery cycles of foam H1 and HS1 are shown in Figs.3.13 (a) and (b), with curves shifted along the strain axis for clarity. Foam H1 underwent five cycles (up to 5% maximum strain), before damage in the sixth cycle at 6% strain led to a stress drop. After sintering, foam HS1 underwent eight compressive cycles (up to 8% maximum strain at 400 MPa) without failure. The cycling behavior of both foams (Figs. 3.13 (a-b)) is in agreement with the monotonic curves of Fig. 3.12.

Finally, the cyclic compressive behavior of foam H2, which was HIP-densified at the higher temperature, is shown in Fig. 3.13 (c), and is nearly identical to that of foam HS1 (Fig. 3.13 (b)). The eight curves for foam HS2 (deformed in 1% increments to a maximum strain of 8%) in Fig. 3.13(d) are similar to those of foams HS1 and H2, as expected from the similar foam microstructures. Shape-memory recovery was observed in all cycles of all foams and represents a large fraction (59-100%) of the plastic strain after unloading.

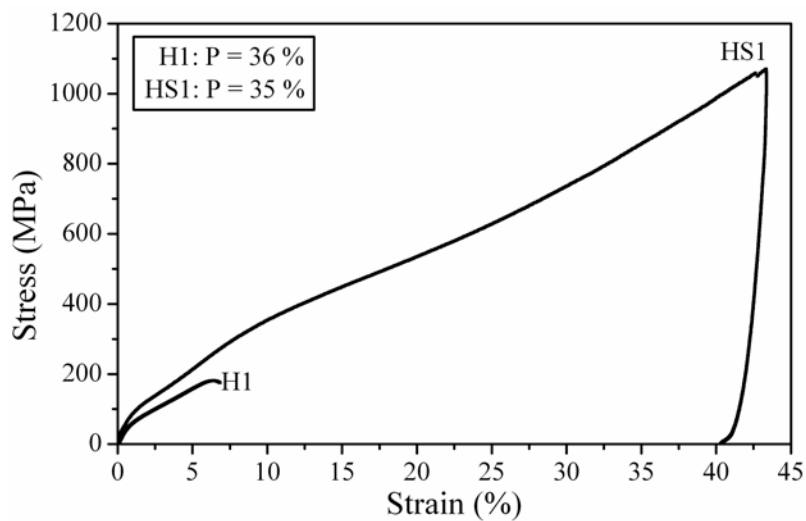
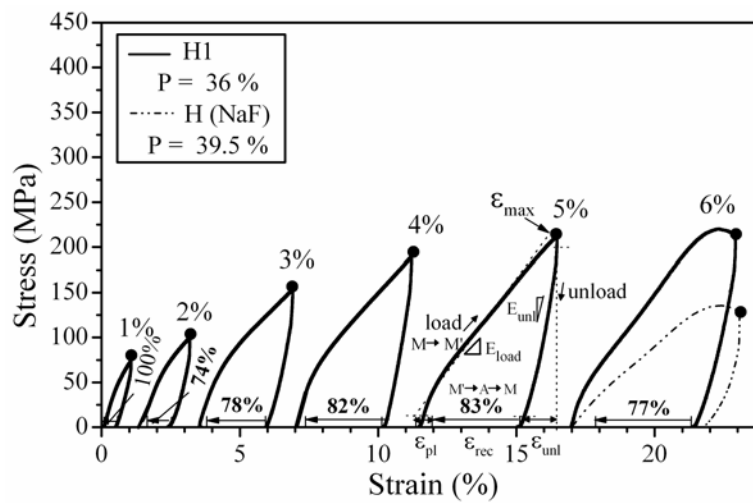


Figure 3.12. Compressive stress-strain curves for foams H1 and HS1 upon monotonic loading until onset of stress drop.



(a)

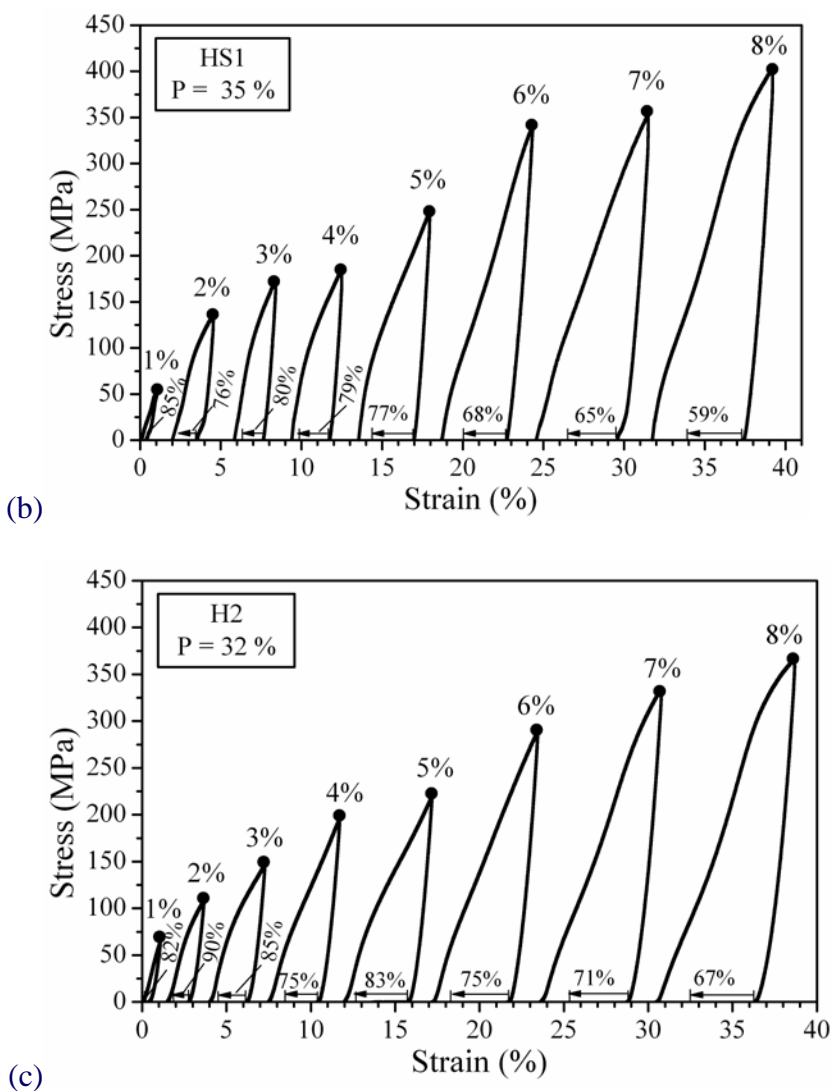


Figure 3.13. Series of compressive stress-strain curves (load-unload-recovery cycles for increasing maximum strains) for: (a) foam H1, including the last stress-strain curve of foam H produced with NaF space-holders (Chapter 3); (b) foam HS1; (c) foam H2. Curves are shifted along the x-axis for clarity. Arrows along the x-axis for each curve represent the thermally-recovered shape-memory strain. The stress at which the foam is unloaded is marked with a dot. Parameters used in evaluation method for loading and unloading stiffnesses, and for the unloading, shape-memory and plastic strains are illustrated, together with the phases

expected (A - austenite, M – martensite, M' – detwinned martensite), in the stress-strain curve to 5% maximum strain in Fig. 3.13(a).

### *Strength*

The maximum strength of foam H1 with 36% porosity (200 MPa at strain of 5.3 %, Fig. 3.12) is close to those of austenitic NiTi foam (245 MPa) with 42% porosity produced by gas expansion [33] and austenitic NiTi foams (180 MPa) with 30-40% porosity, produced by sintering of elemental powders [58]. This is twice the strength, at the same strain, of martensitic NiTi foam with 50% porosity produced from NaCl space-holders using warm pressing and sintering [80]. However, foam H1 starts to fail at ~6% strain, which suggests a weaker porous structure.

Martensitic NiTi foams produced with NaF as space-holder show the same tendency to early failure (section 3.1), but with a lower failure strength (135 MPa), explainable by higher porosities (39.5%) both between the walls (due to the space-holder) and within the walls (due to incomplete densification). This is illustrated in Fig. 3.13(a), where the last stress-strain curve (at 6% maximum strain) of a NiTi foam HIP-densified with NaF space-holder is superimposed on that of foam H1 produced here with NaCl.

After the additional sintering step, foam HS1 has a much higher maximum strength (>1000 MPa at > 42% strain) than foam H1, as expected from the higher level of densification of the walls (Figs. 3.8(a-b) vs. Figs. 3.8(c-d)). Foam H2 (HIP-densified at the higher temperature) has a maximum strength comparable to that of foam HS1 (HIP and sintered), as expected from their similar levels of wall densification (Figs. 3.8(c-d) vs. Figs. 3.9(a-b)). Additional sintering of foam H2 does not improve its strength, in agreement with the lack of improvement in wall

densification. Only after extensive sintering (24 h) are the walls more densified (foam HS2', Fig. 3.10), but this is a lengthy procedure that increases risks of contamination or oxidation. A simpler approach to further improve foam strength and wall densification is to conduct the HIP-densification for longer time (beyond the time of 4 h used here) and/or higher temperature (beyond the temperature of 1065 °C used here), which may necessitate the use of a diffusion barrier between the steel can and the powders.

### *Stiffness*

The stress-strain curves of foam H1 (Fig. 3.8(a)) show an inflection at stresses of 50-80 MPa, indicative of yield, which is expected to occur by detwinning given the martensitic structure of the NiTi. Beyond yield, however, the strain-hardening is high, so that the overall shape of the curve on loading is almost linear. This near linearity is even more marked for foams HS1 and H2 (Figs. 3.8(b-c)), which may be due to onset of detwinning at very low stresses. The average stiffness on loading, which is determined here as a linear best fit of data between 10 MPa and maximum stress, then represents a combination of elastic and detwinning deformation. On unloading, however, deformation is completely elastic (assuming no reverse detwinning) and the stiffness is then closer to a true Young's modulus. As expected, the unloading stiffness is much higher (by a factor 2-5) than the average loading stiffness, as shown in Fig. 3.14 for all foams studied here.

The loading stiffness seems to be nearly independent of the maximum strain achieved, except possibly at the lowest strain of 1%, but this might be due to measurement errors at low stress. By contrast, the unloading stiffness increases significantly with increasing maximum

strain, which probably reflects densification of porosity between and within the pore walls. The unloading stiffness of foams H1, H2 and HS2 (10-18 GPa) is within the stiffness range of cortical bone (12-17 GPa), making these foams attractive for bone implant application. For comparison, NiTi foam produced from NaF space-holders with 39.5% porosity (foam H1) exhibited similarly-low unloading stiffnesses (12-16 GPa), but with a much lower failure stress of 135 MPa. The unloading stiffnesses  $E$  of foams H1, H2 and HS2 are lower than values predicted by the Gibson-Ashby relationship,  $E=(1-P)^2 E_{\text{NiTi}} = 26-29$  GPa, using a porosity  $P=35\%$  and the Young's modulus of monolithic NiTi  $E_{\text{NiTi}} = 61-69$  GPa (2). This may be the result of slight reverse detwinning during unloading. Only foam HS1, with unloading stiffnesses of 18-25 GPa beyond 3% maximum strain, comes close to these theoretical values (Fig. 3.14). The reason for this increased stiffness is unknown.

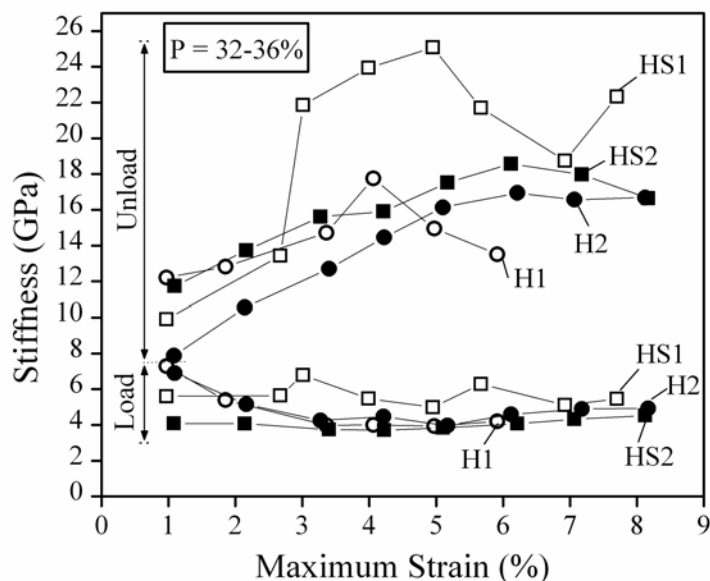


Figure 3.14 Loading and unloading stiffness as a function of maximum compressive strain for all foams.

### Strain recovery

Figure 3.15 (a-d) shows these three strains as a function of the maximum strain for each of the eight loops to which all foams were subjected (Fig. 3.8). It is apparent from Fig. 8 that all three strains increase near linearly with the maximum strain, and that the shape-memory recovery strain has the largest magnitude, followed by the elastic unloading strain and the plastic strain.

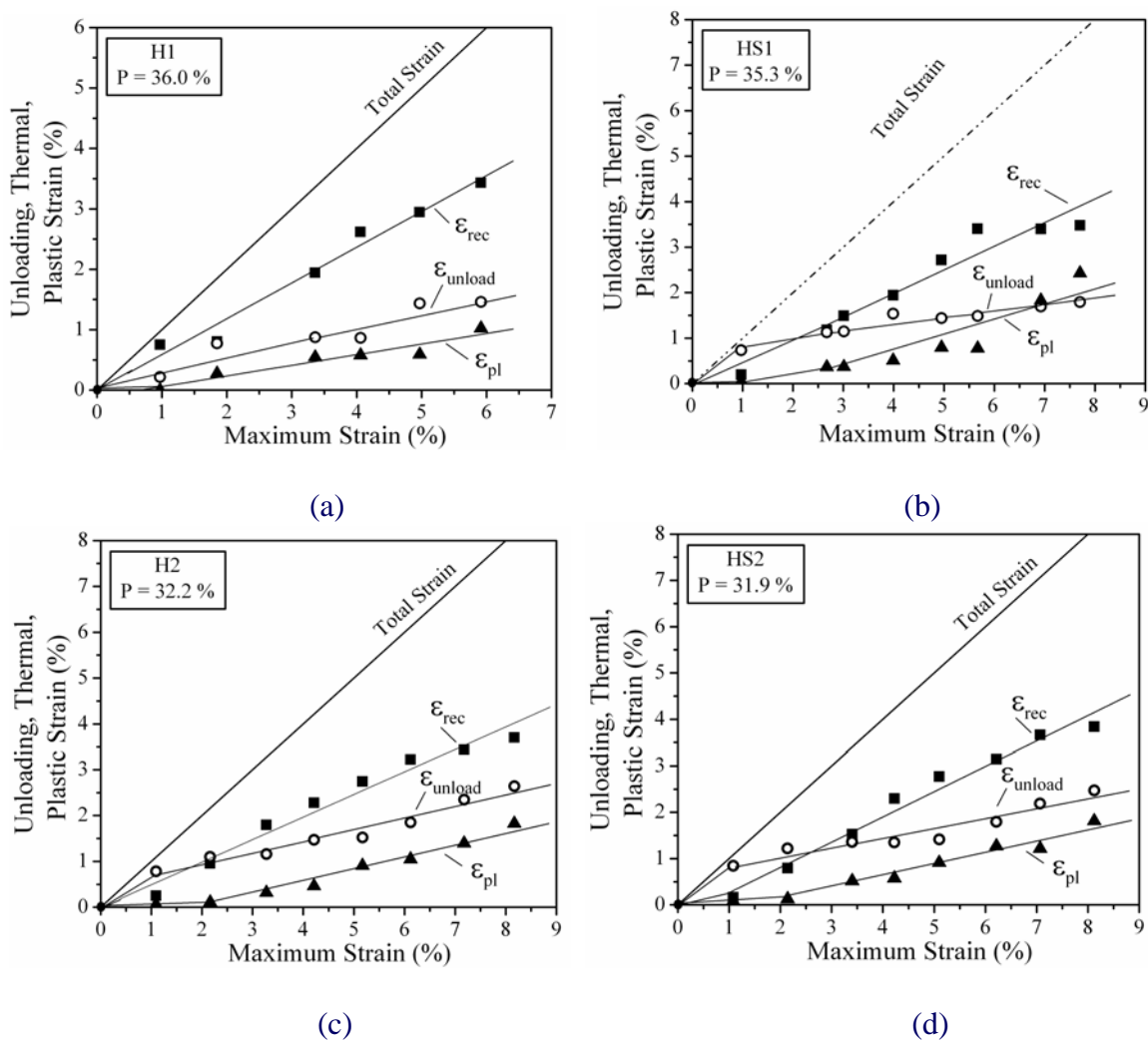


Figure 3.15. Unloading, shape-memory, and plastic strain as a function of maximum compressive strain for all foams.

For example, at the maximum strain of 8%, these strains are about 4, 2.5 and 1.5%, respectively. These three strains are nearly the same, at a given maximum strain up to 6%, as those measured on a NiTi foam produced by HIP densification of NaF space-holders with somewhat higher porosity (39.5 vs. 32.2%). This suggests that the shape recovery behavior of these replicated NiTi foam is not affected by the pore shape or size (which were somewhat different between these foams). Also, the same amount of unloading strain at the same maximum strain was also reported in a martensitic NiTi foam (with a higher porosity of 50%) produced with NaCl space-holders by hot pressing and sintering [61].

### 3.2.3 Conclusions

This chapter has demonstrated a new foam replication process, wherein metallic powders (NiTi) are densified in the presence of a permanent space-holder (NaCl) by hot isostatic pressing at temperatures (950 or 1065 °C) above the melting point of the space-holder (801 °C), so as to improve densification of the metal powders. Despite the melting of the space-holder during the process, there was no sign of reaction with the NiTi powders. After NaCl dissolution, the NiTi foams consisted of 32-36% interconnected porosity with pores size of 70-400 μm. The pores maintained the angular shape of the original NaCl particles, indicating that substantial NiTi densification occurred prior to NaCl melting. Thus, NaCl can be used as a space-holder for NiTi (and other metallic) foams, despite its low melting point, with the following advantages as compared to higher-melting permanent space-holders such as fluorides or oxides used to date: (i) no temperature limit for densification; (ii) lower cost; (iii) greater flexibility in powder (and thus pore) shape; (iv) faster dissolution in water; (v) reduced corrosive attack of metal during dissolution; and (vi) lower toxicity. The latter point is particularly important if space-holder

residues remain in foams used as bone implants, since it is difficult to ascertain with high reliability that all space-holders are completely removed from the foam.

The compressive stress-strain curves of the foams are characterized by: (i) a near linear loading branch, with an average stiffness of 4-6 GPa due to a combination of elastic and detwinning deformations; (ii) a high failure stress in excess of 1,000 MPa (except for the foam HIP-densified at 950 °C, having insufficiently-densified NiTi walls); (iii) a near-linear unloading branch, with a higher stiffness of 10-25 GPa due to elastic recovery strains; (iv) a shape-memory recovery strain increasing linearly with the maximum applied strain, and reaching a value of ~4% for an applied strain of 8%.

These foams are excellent candidates for bone implant applications, since they exhibit a unique combination of attributes: (i) simple processing route, (ii) desirable mechanical properties (low effective stiffness to alleviate stress shielding; high strength and ductility to prevent failure; shape-memory capability useful to operative deployment of the foam), (iii) biocompatibility (for NiTi) and very low toxicity (for NaCl, if traces remain in the foam); and (iv) large pores fully open to the surface (for bone ingrowth).

To produce superelastic porous NiTi, this method can be applied directly, but with Ni-rich pre-alloyed NiTi powder or near equiatomic pre-alloyed NiTi with Ni addition, and a post heat treatment to ensure optimal superelasticity. Such an extension, however, is considered beyond the scope of this work, and the focus is now turned into searching for a new process that is lower in production cost and simpler than the HIP process, in order to allow more experimental study and ultimately optimization of porous structure and properties.

## CHAPTER 4

### **Porous NiTi Produced by Transient Liquid Sintering and Space-Holder Method**

This chapter provides an alternative of producing porous NiTi (either shape memory or superelastic) with modified conventional sintering to (i) obtain high densification (reduce microporosity) in NiTi struts while maintain desired macroporosity in porous structure, and (ii) lower cost of production as well as allow flexibility in processing routes.

Though PM techniques are known for providing good densification, however, porosity in densified microstructures is still observed, and provides weak points for fatigue fracture and crack initiation. In addition to the porosity common to all consolidated powder parts, and caused by initial green porosity, porosity can arise from one's choice of starting materials and process mechanisms. Elemental powders, for instance, will gain some porosity from alloying effects. While the Kirkendall effect raises porosity in solid-state interdiffusion (i.e., densification below the eutectic temperature) of elemental powders, capillary effects play a main role in liquid-mediated sintering (at or above the eutectic temperature) [136].

Several studies have been dedicated to reducing porosity while increasing homogeneity in NiTi products. For instance, Bertheville [137] used a calcium reductant source during sintering of elemental powders in an argon atmosphere to prevent secondary phases. Almost-dense, single-phase NiTi parts were produced with optimized low heating rates and a long time sintering at 920°C. More rapid synthesis of dense (99% relative density) and homogeneous NiTi products using spark plasma synthesis (SPS) [138] and field-activated, pressure-assisted

processes with a combined choice of high current intensity and selected powder size [139] have been reported. Pressureless double-stage sintering [136, 140] was used to produce NiTi with > 80% density. Elemental Ni and Ti powders were consolidated at 900°C by solid-state diffusion (slow, but resulting in low porosity and preserving geometry integrity), followed with transient-liquid sintering or combustion at higher temperature for further densification and rapid homogenization. A similar approach was demonstrated using hot isostatic pressing to produce 99% dense parts [200]. To reduce the tendency for formation of other Ni-Ti phases (e.g. Ni<sub>3</sub>Ti, NiTi<sub>2</sub>), pre-alloyed NiTi powders have been used in some works. Mari and Dunand [121] used HIP and Krone et al. [201] applied hot isostatic pressing (HIP) and metal injection molding (MIM) of low-impurity pre-alloyed NiTi powders to produce NiTi parts with 98% and 90% density, respectively. These NiTi parts were proven to exhibit excellent shape memory or superelastic behavior.

In production of porous NiTi, in which a low density of the product body but a high local density inside the NiTi walls is needed, the aforementioned methods are not applicable. Instead, conventional PM techniques for NiTi parts with lower density as discussed in section 1.4 have been considered. Space-holder materials were introduced to PM methods in order to allow direct manipulation of porosity and pore size/shape through the content and morphology of the space holders, respectively, as shown in the previous chapter. However, residual microporosity in NiTi walls, due to insufficient densification, is often observed (Figure 4.1). This can affect the mechanical properties and other performance indices of the foams; in bone implant applications, for example, pores smaller than 50 μm are not efficient for bone ingrowth.

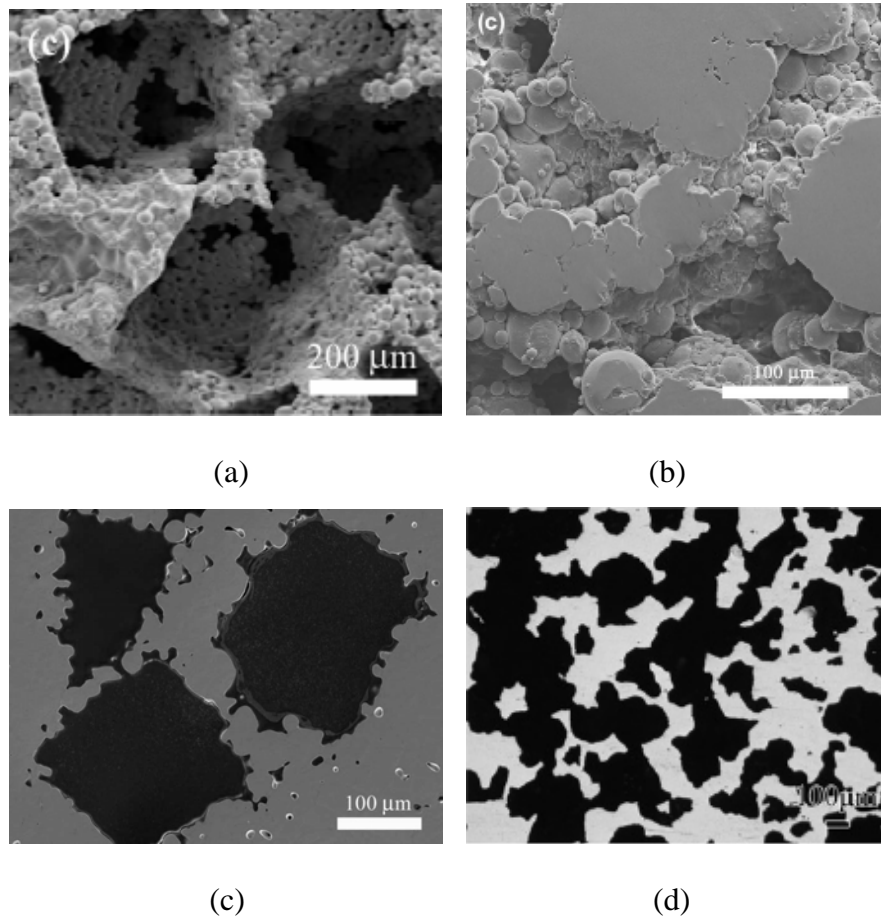


Figure 4.1. Micrographs of porous NiTi produced by PM combined with space-holder methods: a) MIM with NaCl [80]; b) HIP with NaF (section 3.1); c) HIP with NaCl (section 3.2); d) capsule-free HIP with  $\text{NH}_4\text{HCO}_3$  [61].

Although pressure-assisted processes such as HIP or extended sintering have been examined, poor densification of the NiTi powders could not be overcome. The space holders being mixed with NiTi powder, generally speaking, prevent efficient powder packing so that solid-state sintering is insufficient to bond the metal part after their removal. Using elemental Ni and Ti powders as starting materials might be one way to enhance densification (as seen in

Figure 4.1(d)), due to the exothermicity of the reaction, but might also lead to spurious secondary phases.

Recently, transient liquid phase sintering has been used in foam making processes for high temperature metals, for example Ni-based foams using transient liquid bonding of Inconel 625 nickel-based superalloy powders on carbon [141] or polymer foam templates [142], or IN625 superalloy foams using supersolidus liquid phase sintering in conjunction with a polyoxymethylene space holder [143]. Near-dense structures were achieved in the cell walls/struts while, in the latter case, pore structure nearly replicates the geometry of the space holders. Brazing materials were also used to enhance reactive eutectic brazing when joining NiTi to itself, for example, pure Cu and Ti-15Cu-15Ni foil used for NiTi parts in infrared vacuum brazing [144], Ag-Ti and Ag-Cu-Ti alloys for NiTi in microwave brazing [145], and pure Nb for building honeycomb structure from Ni-rich NiTi strips under vacuum heating [146].

In this work, we demonstrate a new PM technique for porous NiTi, which combines: 1) eutectic liquid brazing of NiTi powders to ensure high densification of NiTi struts; and 2) a space holder method to manipulate desired qualities of the porous structure. Pre-alloyed NiTi powders were used as a starting material to prevent the exothermic reaction of Ni and Ti that leads to unwanted Ni-Ti phases [147], to achieve exact compositions (difficult when oxidized Ti powders are used), as well as Kirkendall porosity and anisotropic shrinkage. NaCl was selected for the space holder material, as it has been successfully used in the previous chapter, and thus provides a direct comparison with previous studies.

Niobium was chosen as a brazing material. Grummon et al. [146] recently suggested that the NiTi-Nb system offers reactive eutectic sintering with NiTi at 1170°C (140 degrees below the melting point of NiTi, Figure 4.2) and has terminal phases with low mutual solubility. Therefore,

Nb is a good candidate to perform transient liquid sintering, creating a permanent connection between NiTi powders, while causing only slight changes in NiTi fraction. No reaction between Nb and NaCl is expected. Niobium exhibits excellent biocompatibility and is non-toxic in tissue interaction (Nb-coated implant paper). In addition, NiTi-Nb alloy (in specific,  $\text{Ti}_{44}\text{Ni}_{47}\text{Nb}_9$ ) was found to sustain passive oxide layers with extremely low solubility and high protective ability, imparting high corrosion resistance [148]. Although previous use of Nb in NiTi has focused on the shape memory properties of arc-melted NiTiNb for coupling/pipe joint applications, or more recently, on large hydrogen dissolution and diffusion in arc melted/hot worked membranes for hydrogen purification [149-151], implant applications might be a new promising use for NiTiNb alloys.

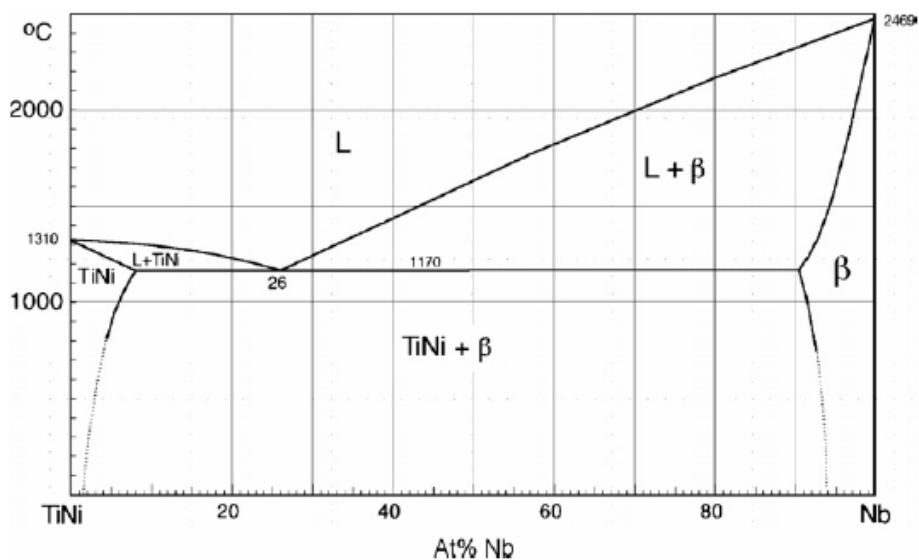


Figure 4.2. Quasi-binary NiTi-Nb phase diagram.

Here, we demonstrate the use of Nb additions to produce shape memory (near-equiatomic) and superelastic (Ni-rich) porous NiTi. The microstructures, phase transformations, and mechanical behavior of the NiTi foams were studied.

## 4.1 Experimental procedures

### 4.1.1 Processing methods

The pre-alloyed NiTi (48.6 at.%Ni) powders were sieved to 44-63  $\mu\text{m}$  particle size. Nb powders (99.8% purity, Alfa Aesar, MA) of particle size 1-5  $\mu\text{m}$  were mechanically blended with the NiTi powders, with a composition of 3.1 at.% Nb to 94 at.% NiTi (or 5.3 wt.%Nb to 94.7 at.%NiTi), in a twin-shell dry blender for 2 hours. Near-cubical NaCl powder space holders (99.0% purity from Alfa Aesar, MA) were sieved to 100-250  $\mu\text{m}$  size and added to the NiTi/Nb mixture with the following volume fractions: 40 and 60 vol.% (NaCl/metal ratios of 2/3 and 3/2 by volume). A control mixture (with Nb but 0 vol.% NaCl) was also produced. The resulting mixtures were further mixed for 2 hours and cold pressed in a 1.25 cm diameter die with a pressure of 350 MPa. A 1 cm-long green pellet of each mixture was produced. These pellets were sintered (as described in section 2.1) at 1185°C (15°C above NiTi-Nb eutectic temperature) for 10 hours. The conditions and an assigned notation of each sample are summarized in Table 4.1.

Two Nb-free NiTi pellets, without and with 40 vol.% NaCl space holders, were also made to directly evaluate the effect of Nb addition. They were created by the same procedures, but subjected to a higher sintering temperature of 1250°C for 36 hours. In all cases, the NaCl space holders melted (the melting point of NaCl is 801°C) and evaporated during the heat-up to the sintering temperature.

Table 4.1. Processing parameters and conditions of porous NiTi.

Sample notation	Fabricating method	Nb addition	Vol.% of NaCl
S0	Sintering	0 wt.%	0 %
S40	Sintering	0 wt.%	40 %
SN0	sintering	5.3 wt.%	0 %
SN40	sintering	5.3 wt.%	40 %
SN60	sintering	5.3 wt.%	60 %

#### 4.1.2 Material Characterization

Microstructure of all foams was observed in optical microscope. Pore sizes and porosities were measured for samples SN0, SN40 and SN60 as described in section 2.1. The thermal behavior and mechanical behavior were observed by DSC and compression testing (see section 2.2). To eliminate any effect from the heat-affected zone and obtain a fully martensitic structure, the specimens were annealed for 20 min in 120°C air, cooled for 20 min at room temperature, immersed for 2 min in liquid nitrogen, and maintained for at least 10 min at room temperature before mechanical testing.

Mechanical testing for each specimen then followed the following procedures. After initial preparation above, the specimen was compressed to the strain of 2%, before unloading to near zero stress. The specimen was then heat-treated and quenched in liquid nitrogen (same as above) to observe any shape memory effect upon heating. The dimensions of the specimen before loading, after unloading and after heating (i.e. at room temperature, before quenching in liquid nitrogen) were measured by a point probe micrometer with a precision of 1  $\mu\text{m}$ . The load-unload-recovery cycles were then repeated up to loading strains of 4%, 6% and 8%,

consecutively. Unloading, recovery and plastic strains as well as loading and unloading stiffnesses for each cycle were determined (section 2.2). After heat recovering from the last cycle (8% strain), specimens SN40 and SN60 were deformed in compression at the same strain rate (0.15 mm/min) until fracture.

## 4.2 Foam properties

### 4.2.1 Microstructure

Cross-sectional images of samples S0 and S40 at two different magnifications are shown in Figure 4.3. Despite quite a strong green compact and no residual space holder, the near-equiatomic NiTi powders in sample S0 were not well-densified, as large spaces between particles were visible (Figure 4.3(a)). Although some connected adjacent particles were observed, the sintered portion of the specimen is very low. For the same reasons, poor sintering is observed in the struts of porous NiTi created with the same sintering procedure (S40, Figure 4.3(b)) although high volume fraction and near-replicated pore geometry was achieved. This proves that preparation of porous NiTi having high overall porosity but high metal strut densification via conventional pressureless sintering is a major challenge. Undesirable microporosity (from insufficient powder densification) was therefore present in NiTi walls, in addition to desirable macroporosity (from empty space after removal of the salt).

The 36 hours of sintering allowed was still not enough to encourage adequate diffusion among loosely-compacted NiTi powders, although the sintering temperature (1250°C) is nearing its upper limit (the melting point of NiTi, 1310°C). Little densification is possibly due to low diffusion coefficients of the NiTi intermetallic powders which could be enhanced by reducing

powder sizes. However, risk of oxidation is increased with decreasing the powder size (due to high surface area) which retards the diffusion and sintering. The selected NiTi powder size (43-62  $\mu\text{m}$ ) was small enough to allow a good distribution of large NaCl particles (100-250  $\mu\text{m}$ ), yet large enough to minimize thin NiTi struts between NaCl (which reduce pore connectivity and are therefore not preferable for bone implants). Changing the NiTi powder size (e.g. to a wider size distribution) might be one approach to increase the packing factor of the green compact, and hence improve the chances of densifying NiTi particles; nevertheless, the densification of the NiTi matrix could not be dramatically increased.

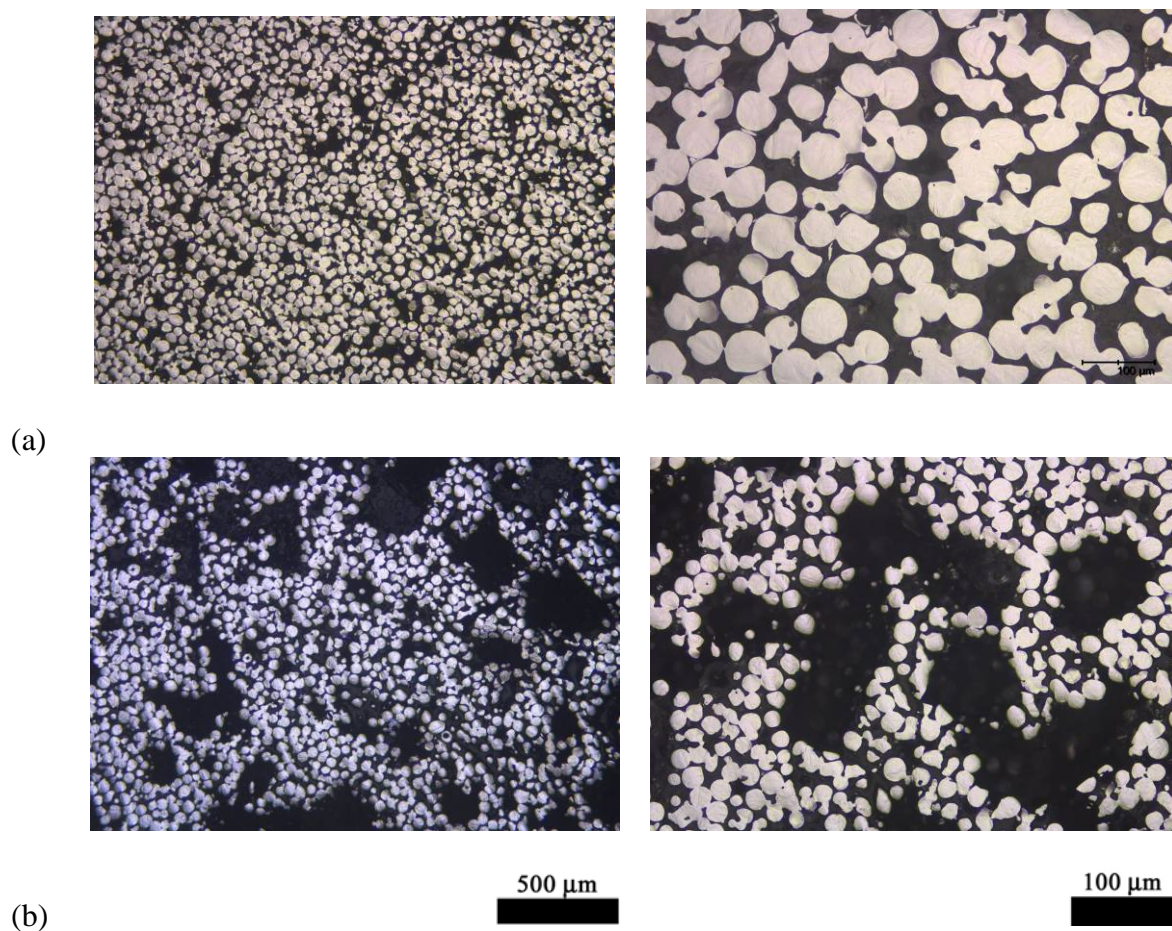


Figure 4.3. Cross-sectional images of sintered near-equiatomic NiTi samples (a) S0 and (b) S40 at low (left) and high (right) magnifications.

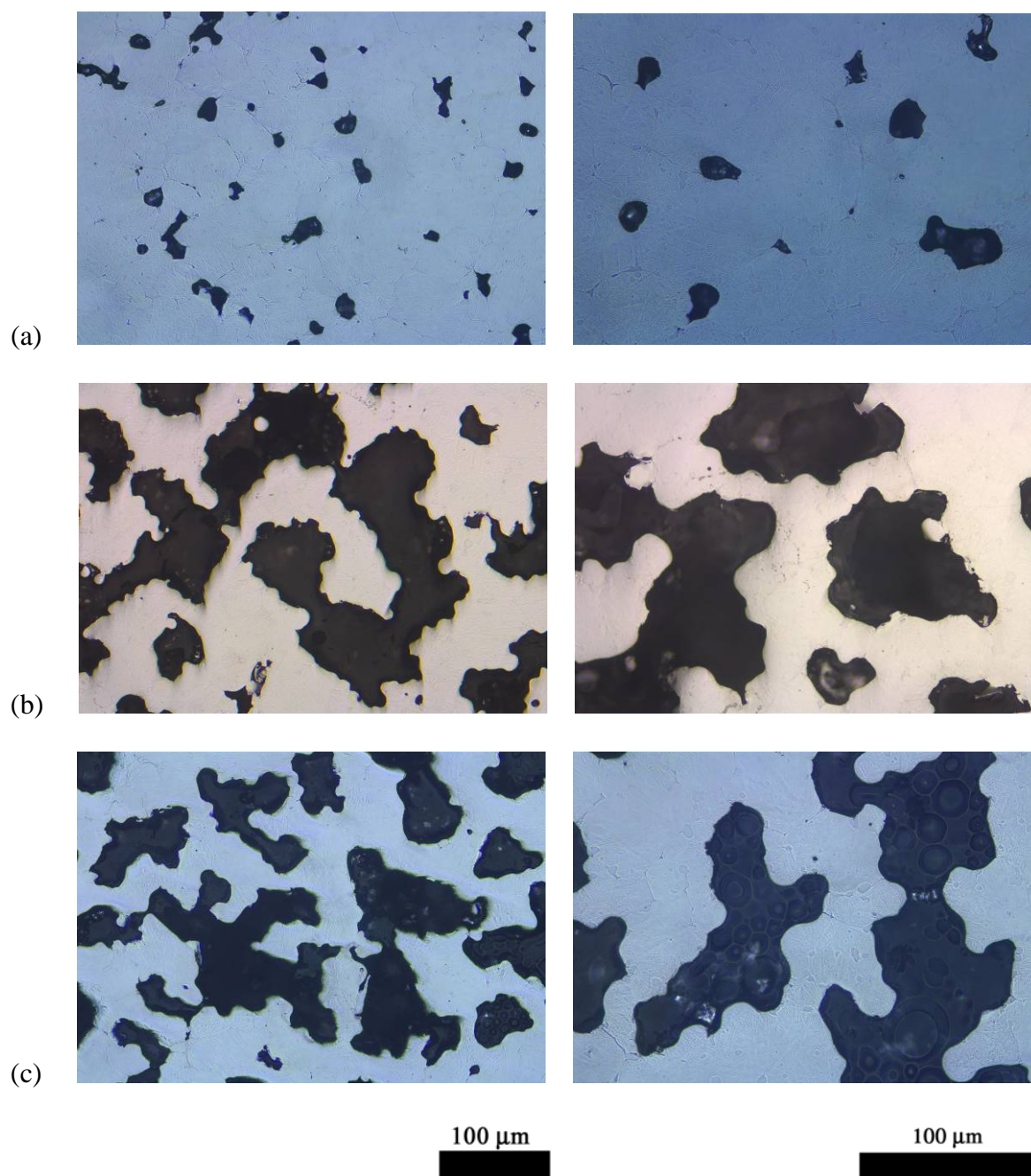


Figure 4.4. Cross-sectional images of sintered (with Nb) near-equiatomic NiTi samples (a) SN0, (b) SN40 and (c) SN60 at low (left) and high (right) magnifications.

In contrast, the samples with Nb addition showed high densification of NiTi in all cases, without or with space holders (Figure 4.4). This confirms that transient liquid phase sintering right above the eutectic temperature enhances densification over standard solid-state sintering. The Nb-rich regions located at particle interfaces and at the necks between NiTi particles are likely eutectic NiTi-Nb, acting as “glue” between particles. Their uniformity suggests that small Nb powders (1-5  $\mu\text{m}$ ) were well-dispersed in the NiTi-NaCl mixture, which could not be achieved by larger Nb powders (e.g. using 40  $\mu\text{m}$  mesh size).

Upon heating above the eutectic temperature (1170°C), local sites where eutectic (26 at.%Nb-74 at%NiTi), hypoeutectic, or hypereutectic compositions were reached contained eutectic liquid phase (see phase diagram, Figure 4.2). Capillary forces in the narrow channels between NiTi particles stimulate eutectic liquid infiltration. Low interdiffusion between the NiTi particles and eutectic liquid allows sufficient time for the eutectic liquid to wet and penetrate throughout nearly the entire sample. Its presence also permits particle sliding to rearrange the microstructure, leading to rapid densification in the cell walls. At high magnification, a dendritic NiTi-rich solid solution phase can be observed at the interface (indicative of a gradient of dissolved Nb content) between NiTi and eutectic (also observed in Grummon et al [146]).

For sample SN0, where no salt was added, the NiTi matrix has high densification compared to sample S0. The network of empty spaces between particles was eliminated. However, 5% remaining porosity (Table 4.2) was present in the form of numerous round pores 10-30  $\mu\text{m}$  size, and some larger (50-80  $\mu\text{m}$ ) elongated pores distributed evenly at some of the junctions between NiTi particles in the sample.

In NiTi foams with space holders, i.e. samples SN40 (40 vol.% NaCl, Figure 4.3(b)) and SN60 (60 vol.%NaCl, Figure 4.3(c)), pores with approximately the size (100-300  $\mu\text{m}$ ) of NaCl particles are present, with a homogeneous distribution. Nb-rich regions along NiTi particle surfaces were again observed. The pore structure has high connectivity and smooth pore surfaces, but also a slight change in pore shape from the shape of the space holders. The characteristics of each foam are displayed in Table 4.2. The total porosity of the samples is lower than the volume of space holder added in the powder mixture. Open porosity constitutes the majority of total porosity in all foams except SN0, where most porosity is closed.

Table 4.2. Foam characteristics of near-equiatomic NiTi foams with Nb addition.

Samples	Amount of NaCl (vol.%)	Total porosity (%)	Open porosity (%)
SN0	0 %	$5.1 \pm 0.5$	$1.5 \pm 0.5$
SN40	40 %	$33.2 \pm 0.3$	$32.6 \pm 0.6$
SN60	60 %	$43.0 \pm 0.3$	$42.9 \pm 1.3$

The 5% residual closed porosity in sample SN0 (without space holders), however, suggests a limitation for liquid-phase densification due to capillary effects. Residual porosity is perhaps due to local concentrations of initial porosity in the green compact and/or insufficient liquid formed during sintering. In the former case, packing of the NiTi particles should be studied with the goal of lowering the green compact porosity (and hence strengthening the capillary forces between particles. Because these forces are roughly proportional to  $1/r$ , smaller NiTi particle size could also be used to reduce porosity; however, excessively small powders

could fill between NaCl particles and cause narrow fenestration size after the salt removal. The latter case can be resolved by using a higher proportion of Nb powder (i.e.  $>3.1$  at% Nb) with the NiTi. The greater the Nb addition, the more eutectic liquid is formed. On the other hand, a higher volume fraction of liquid could also cause distortions of the cell structure.

In this study, the residual porosity after liquid phase sintering was not considered a critical issue, since our aim was to produce porous final products. This porosity (unlike that from solid-state sintering) is expected to rearrange through liquid phase movement and finally merge with the open macroporosity left behind by the space holder removal, rather than appearing as microporosity inside the NiTi walls, as observed in other methods (e.g. HIP with space holders). Accordingly, the closed porosity in foams SN40 and SN60 is near zero (Table 4.2). Liquid phase activity also resulted in smooth pore surfaces and high pore connectivity, while pore size and pore shape remained almost unchanged. The fact that the structures' open porosity was preserved shows that the capillary forces in the small spaces between NiTi particles keep the transient liquid out of the large pores created by NaCl removal, as expected from a wetting liquid.

The microstructure of a NiTi foam in Chapter 3, produced by hot isostatic pressing of NiTi powders with 40 vol.% NaCl at  $1065^{\circ}\text{C}$  for 4 hours, followed by sintering (as well as salt removal) at  $1250^{\circ}\text{C}$  for 4 hours, was used (Figure 4.1(c)) for comparison in all respects. The porous structure of the current foams has the same range of pore size and porosity as the earlier foams, but higher connectivity, larger ratio of fenestration to pore size (qualitative observation from images), and smoother pore surfaces, even though it was formed using a simpler and lower-temperature method. Since forming a complete transient liquid phase takes only a few minutes, sintering time could also be lower, as long as the Nb powders are well-distributed in the preform,

and the liquid formed at the local sites has time to wet the NiTi and connect throughout the powder compact.

Regarding the amount of Nb, high Nb content leads to more Nb-rich phases. Although the net Nb content used in this study (3.1 at% Nb at 1185°C) is in the NiTi-rich ( $\alpha$ ) region (see phase diagram), high local concentrations of Nb present in the vicinity of the original Nb particles will bring about other phases as well, such as eutectic and Nb-rich ( $\beta$ ) phase upon solidification. The eutectic (dark lines along some particle interfaces) and Nb-rich phase (light, globular/elliptical regions at the interfaces or interiors of grains) are present in all samples. Similar structures were observed in Seigert et al [152], where small Nb solid solution precipitated in cast-NiTi matrix with 9at%Nb addition. These Nb-rich phases are unstable and can gather and grow if high temperature treatment is used [153]. Also, high Nb content can cause more complex cast microstructure and Nb phase separation. The dark, coarse, blocky  $Ti_3(Ni,Nb)_2$  phase precipitating from liquids reported elsewhere [153, 154] was not observed here. Finally, it is noted that these additional phases cannot transform, thus impeding recovery behavior (as discussed in the next sections). Therefore, small amounts of Nb are optimal for enhancing sintering while still maintaining a majority of NiTi-rich phases, and the associated mechanical properties of NiTi alloy.

#### 4.2.2 Phase transformation behavior

The DSC results of near-equiatomic NiTi samples shown in Figure 4.8 indicate a martensitic phase transformation (i.e., martensite to austenite) upon heating and reverse transformation (i.e., austenite to martensite) upon cooling between -60°C and 150°C in all cases.

The heat of transformation and transformation temperatures ( $A_s$ ,  $A_f$ ,  $M_s$ ,  $M_f$ ) of each sample were measured and are presented in Table 4.3. Deviations in the thermal behavior of NiTi sintered in the presence of Nb from those without Nb addition are as follows: 1) lower heat of transformation, relative to the literature value of pure NiTi (24 J/g), by 8 and 10 J/g for the samples with and without NaCl, respectively; 2) broader martensitic transformation temperature interval ( $M_s$ - $M_f$ ) by 30-40°C, but nearly unchanged reverse transformation interval ( $A_f$ - $A_s$ ); 3) wider peak to peak hysteresis ( $A_p$ - $M_p$ ); and 4) decreased transformation temperatures (10-20°C even lower (SN0) in case of foams (SN40, SN60)). The transformation temperatures of foams, however, are quite constant regardless of the difference in volume fraction of NaCl used. At room temperature after pre-heat treatment, the NiTi samples containing Nb should consist of martensite with a small content of austenite.

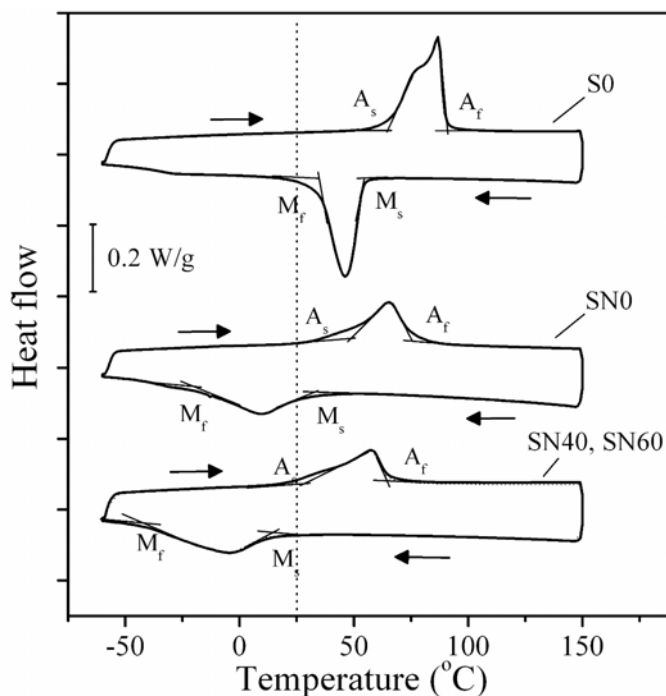


Figure 4.5. DSC result of sample S0, SN0, SN40 and SN60.

Table 4.3 Phase transformation parameters of near-equiatomic NiTi samples

Samples	Heat of transformation (J/g)		Transformation temperatures (°C)				Transformation hysteresis/intervals (°C)		
	heating	cooling	A <sub>s</sub>	A <sub>f</sub>	M <sub>s</sub>	M <sub>f</sub>	A <sub>p</sub> - M <sub>p</sub>	A <sub>f</sub> - A <sub>s</sub>	M <sub>s</sub> - M <sub>f</sub>
S0	22.6	21.6	75	90	54	35	42	25	19
SN0	16.7	16.1	47	76	31	-21	55	29	52
SN40	13.0	14.1	31	65	14	-39	70	34	53
SN60	13.7	14.3	33	65	16	-42	70	32	58

The direct effect of other phases (eutectic, NiTi solid solution, Nb-rich precipitates) is a decrease in heat of transformation, as well as broadening of the transformation peaks. These phases are non-transformable, and obstacles for the transformation in the NiTi itself. For example, after load is applied, plastic deformation of local NiTi phases and Nb rich particles may increase the resistance of the thermo-elastic martensite to freely transform to austenite upon heating.

Also, the addition of Nb increased the local Ni/Ti ratio in the NiTi-rich B2 phase responsible for the recovery effect, and increased the proportion of the Nb-rich phase, which resists transformation of B2 phase in the eutectic. Therefore, transformation becomes more difficult, and transformation temperatures are decreased. Piao et al. [202] presented a relation of Nb content to martensitic start temperature ( $M_s$ ) in NiTiNb arc-melted alloys. For the alloy where Nb equally dissolves onto Ni and Ti sites,  $M_s$  decreases with increasing Nb content (by as much as 60°C, up to ~5 at% Nb) and is constant at high Nb content (>5 at%Nb). Even though the decline of  $M_s$ , ~20°C, is not that significant in this case (6 at.% Nb), taking into account the

difference in processing method, starting materials and heat treatment, the correspondence is still valid.

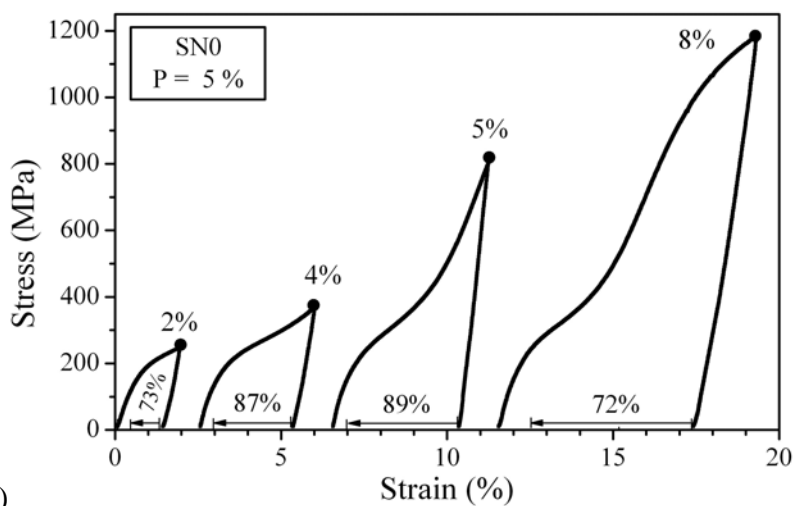
Without Nb addition, the sintered sample (S0) exhibits a peak to peak hysteresis ( $A_p$ - $M_p$ ) of about 40°C, while a wider hysteresis (by ~15°C) was observed in the 6 at% Nb-NiTi sample (SN0). Similar values in as-cast NiTi before and after adding 6 at% Nb were reported in literature [152]. It also agreed that, by adding Nb,  $M_p$  is significantly decreased while  $A_p$  is only slightly lowered, resulting in larger hysteresis. While preferred for pipe joint applications, wide hysteresis will cause lower recovery stresses, and require a larger supercooling (i.e., a lower minimum temperature) in order to complete the martensitic transformation (as  $M_f$  is much lower), which is not useful for bone implants.

The slight difference in thermal behavior (lower transformation temperature, hysteresis, heat of transformation) of samples SN40 and SN60 from SN0 might come from the variation in the final structure caused by the existence of NaCl particles. For example, they might obstruct the liquid pathway, thus varying the amount and position of Nb-related phases (relating to Ni/Ti ratio) in the final sintered structure.

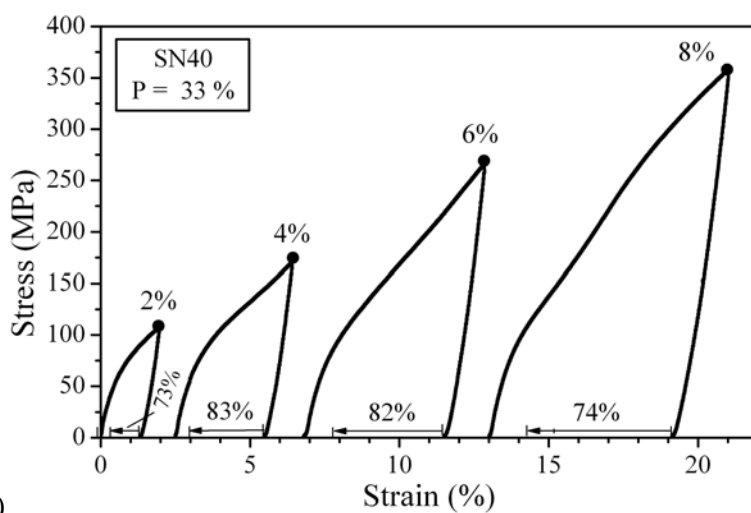
#### 4.2.3 Mechanical and shape recovery behavior

The mechanical behavior during load-unload-recovery cycles of samples SN0 (5% porosity), SN40 (33 %porosity), and SN60 (43% porosity) are compared in Figure 4.9. In general, all samples survive cycling to a maximum strain of 8% without failure, and behave like typical shape memory NiTi foam materials in compression (as observed in Chapter 3): no stress plateaus, near linear curves on loading, and large recovery upon heating after unloading. Loads

at maximum strain points were lower with increased porosity, as expected. The percentage of heat recovery in all samples after each maximum strain is about the same (70-85%), and is only slightly larger in near-dense samples.



(a)



(b)

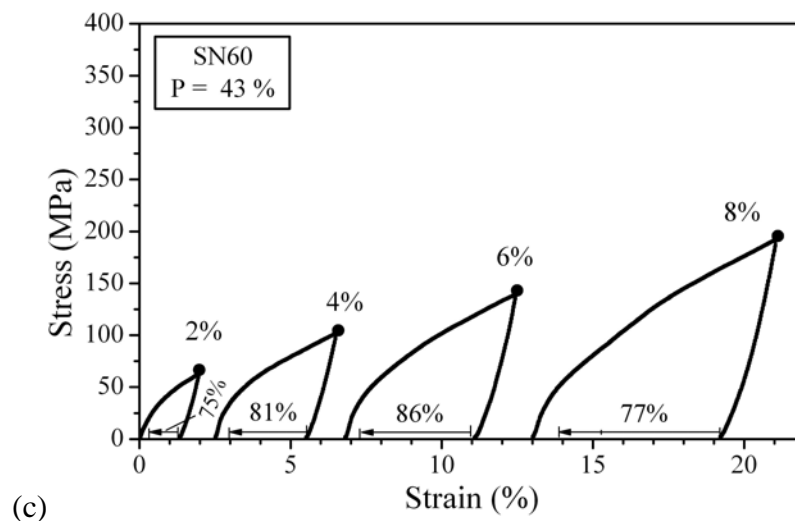


Figure 4.6. A series of stress-strain curves of samples (a) SN0, (b) SN40 and (c) SN60 showing load-unload-recovery cycles of maximum strain of 2%, 4%, 6% and 8%. In comparison, those of foam HS2 in the previous study made by HIP method is provided. Curves are shifted along the x-axis for clarity. Arrows along the x-axis for each curve represent the thermally-recovered shape-memory strain. The stress at which the foam is unloaded is marked with a dot.

Upon fracture (Figure 4.10(a)), sample SN40 reached a very high engineering fracture stress of 2010 MPa and strain of 57.4 %, while sample SN60 achieved 1611 MPa and 58 %, respectively. The stress-strain curves up to fracture showed smoothly-climbing behavior without any stress drops, past the yield strength of NiTi matrix, up to the first signs of fracture. A macroscopic image (Figure 4.10(b)) of sample SN40 after fracture illustrates the ductile behavior typical of the NiTi foams.

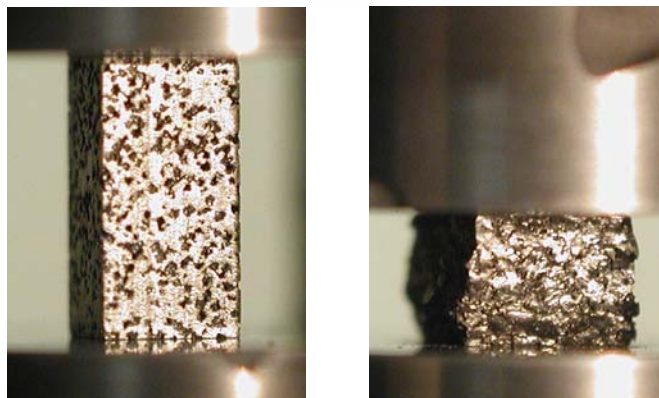
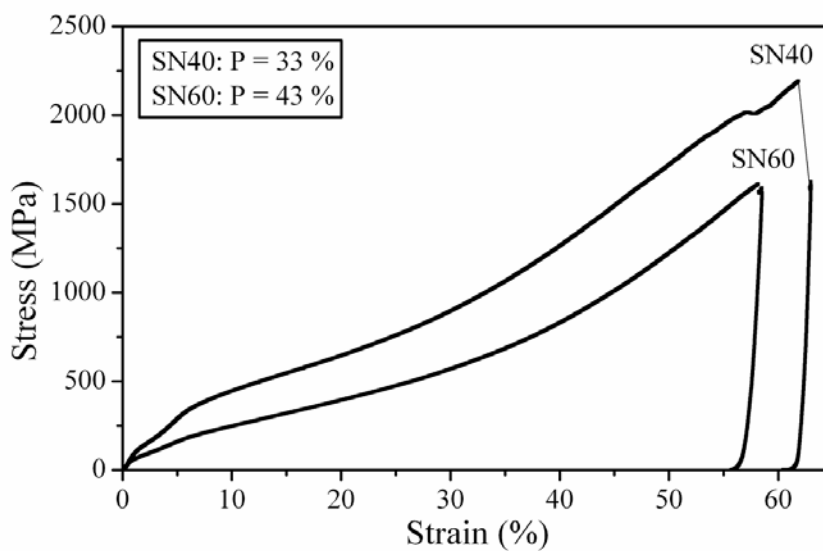


Figure 4.7. Stress-strain curves of foams SN40 and SN60 compressed to fracture. Digital images below the plot show foam SN40 before (left) and after (right) compression.

Stiffness and recovered strain as a function of maximum cycle strain (Figure 4.9) for each sample is displayed in Figures 4.11 and 4.12, respectively.

Similar stiffness values (Figure 4.11) are usually derived from stress-strain curves of the same sample at different maximum strains, except in the 6% cycle of foam SN0, where loading

stiffness is relatively high due to impending yield (occurring at 1000 MPa in the 8% cycle). The NiTi-Nb foam SN0 (5% porosity), exhibiting ductile behavior and high strength, also has high stiffness comparable to that reported in literature for solid NiTi (61-69 GPa) [28]. Loading stiffness is lower than unloading stiffness (due to twinning) in all cases, and stiffness is reduced with increased porosity, as expected. However, the Gibson and Ashby prediction  $E = (1-P)^2 E_{\text{NiTi}}$  is higher (by ~13 GPa) than experimental values, possibly due to variation from detwinning effects upon unloading.

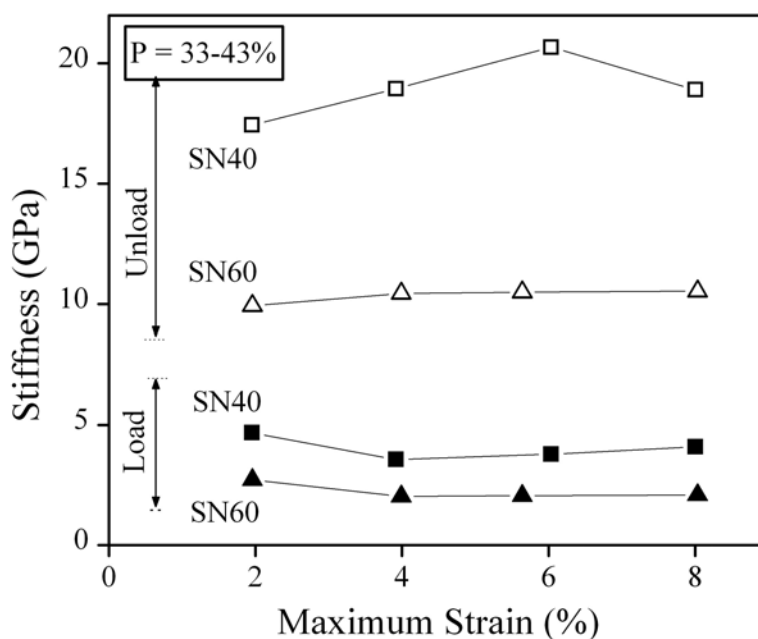


Figure 4.8. Loading and unloading stiffness as a function of maximum compressive strain of foams SN0, SN40 and SN60.

Comparing to the foam HS2 in Chapter 3, NiTi-Nb foam (SN40) at the same porosity (32%) gives a comparable strength and a slightly lower stiffness which is closer to the desired range of stiffness of bone. The existing eutectic or Nb-rich phase is present in a sufficiently small

proportion that it did not seem to significantly affect the mechanical properties of the alloy, though high densification was obtained with this method. For example, Uchida et al. [155] found that Nb rich particles may hinder the reorientation of martensite variants and lead to increases in constraint stress, but we do not observe such an effect here.

The only feature in which NiTi-Nb foams are clearly inferior to NiTi foam is heat recovery ratio (<85 %), which could not reach 100% at low strain (Figure 4.9). This may be rationalized as follows. Upon compression, plastic deformation in non-NiTi rich phases is higher with increasing total strain. Since these phases do not show transformation, and through their bond to the NiTi, will constrain its transformation, the overall recovery ratio of alloy is decreased. In this case, owing to a low amount of Nb, and thus few Nb-rich phases, plastic deformation mainly occurred in the NiTi matrix. The transformation of NiTi matrix is slightly more difficult due to the presence of other phases, therefore, strain recovery ratio is slightly lower. This recovery ratio, however, stays almost constant (70-85%) even at 8% maximum strain applied, while recovery strain in foam HS2 decays with larger maximum strain.

Heat recovery strain is larger than unloading strain and plastic strain (Figure 4.12). The values of strain increase linearly with maximum strain applied and the extent of strain recovery (unloading and heat recovery strain) is independent of porosity (i.e., the same for 5% and 42% porosity), in agreement with the findings in Chapter 3. At 8% maximum strain, a total strain of ~6.5% (4.2% from heat recovery and 2% from unloading) can be recovered in all samples.

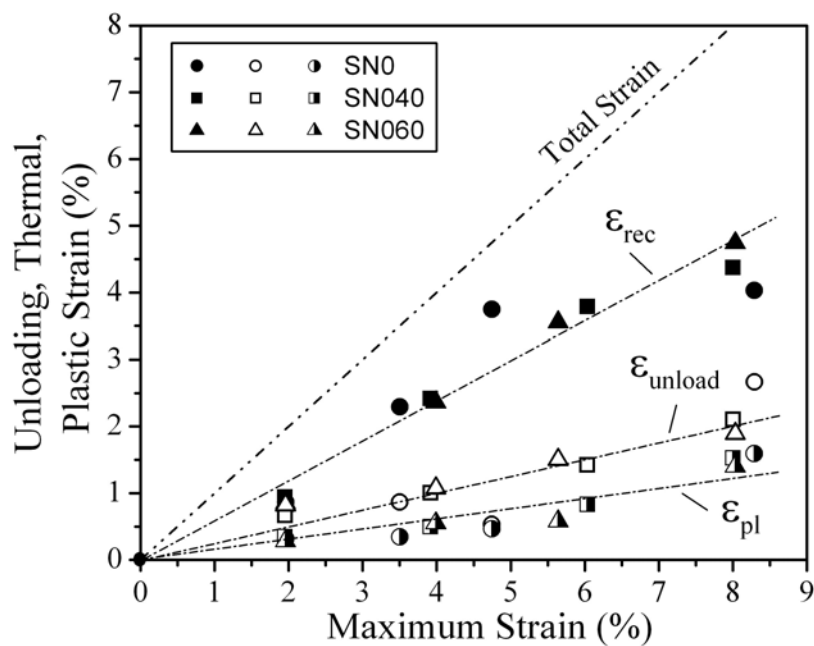


Figure 4.9. Unloading, heat recovery and plastic strain as a function of maximum compressive strain of foams SN0, SN40 and SN60.

### 4.3 Conclusions

Transient liquid phase sintering of NiTi-Nb mixtures was used in combination with the NaCl space-holder method to produce porous near-equiatomic NiTi and Ni-rich NiTi foams with controlled porosity, high densification in the NiTi struts, and a favorable pore architecture. This technique shows promise as a production route for high-porosity (~60-70%) porous NiTi, having lower cost and greater flexibility than the HIP process (Chapter 3), and with comparable mechanical properties.

To produce near-equiatomic NiTi foam, Nb powder (~6 at.%) was simply added to the NiTi + NaCl powder mixture before die pressing and conventional sintering. For making Ni-rich NiTi foam, a new technique, double-layer sintering, was used which is similar to the previous

method, but in which two separate layers consisting of a eutectic mixture (NiTi + Nb powders) on top of a foam making mixture (Ni-rich NiTi + NaCl) are die pressed into a single compact. Conventional sintering is used to first sinter the foam layer, and then melt the eutectic layer, which afterward wicks into the foam layer to enhance densification without closing the desired macropores. This novel method offers an alternative way of producing superelastic porous NiTi in a single-step process with separate control of NiTi densification factor and overall macroporous foam structure.

## CHAPTER 5

### **Processing Development in Sintering of Porous NiTi**

This chapter recounts early attempts in this thesis work to fabricate porous NiTi by conventional sintering and NaCl space-holder methods. The scientific aim of the work described here was to use single-step sintering (rather than the more costly HIP process) to produce Ni-rich (instead of near-equiatomic) NiTi foams having large recovery strain and low stiffness. This single-step sintering process followed the procedure provided in section 2.1. Since sintering was performed under vacuum, the NaCl was evaporated from the sample, and water dissolution was not required.

The first sections below (sections 5.1-5.4) investigate general sintering parameters that affect foam microstructure and behavior. The subsequent section (section 5.5) focuses on sintering of superelastic Ni-rich NiTi foams. The final sections (section 5.6) investigate the mechanical behavior of Ni-rich NiTi foams.

#### **5.1 Effect of sintering on transformation behavior**

To investigate the effect of sintering parameters on the transformation behavior of NiTi, DSC results from pre-alloyed NiTi powders were compared with results from the same powders after pressing and sintering at 1250°C for 12 hours, with and without NaCl. Similarity in transformation behavior between the as-received and pressed/sintered powders was observed: the heat of transformation was nearly unchanged, and the transformation temperatures increased by

about 20°C. This difference, including a superimposed two-step transformation in the as-received powders, is assigned to differences in cooling (i.e. to rapid densification in the sprayed as-received powders, versus furnace cooling in the pressed/sintered powders) [38]. Dissimilarities after sintering in the presence of NaCl (i.e., in a foam sample), in the form of lower heat of transformation (4-5 J/g) and a wider range of transformation temperatures, suggest potential difficulties in the transformation behavior of foams. In general, however, sintering NiTi did not significantly alter the transformation behavior.

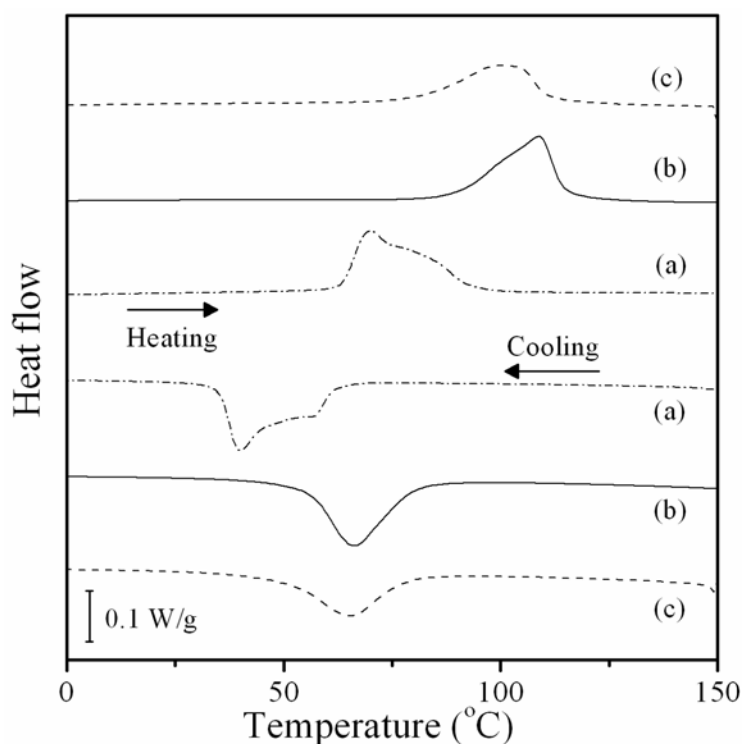


Figure 5.1 Comparison of DSC curves for as-received, as-sintered pre-alloyed NiTi powders, and as-sintered pre-alloyed NiTi with 40 vol.% NaCl space holders (particle size of 62-250  $\mu\text{m}$ ).

## 5.2 Effect of particle size and powder mixing

In the foams (whether produced by HIP or sintering), uniformity in final structure was determined mostly by the distribution of NaCl powders in the initial NiTi-NaCl preforms. Due to the difference in density between NaCl ( $2.165 \text{ g/cm}^3$ ) and NiTi ( $6.45 \text{ g/cm}^3$ ), powder mixing can lead to separation: high density powders sink to the bottom and low density powders rise to the top. Without the benefit of binders, mixing of high- and low-density powders is best achieved by wise selection of the particle size ratio. Since NaCl particle size is essentially fixed at 100-250  $\mu\text{m}$  by the requirements of implant materials, NiTi particle size must be varied to optimize mixing.

NiTi foams using three ranges of NiTi particle size were sintered at  $1250^\circ\text{C}$  for 12 hours (Figure 5.2). Metallographic observation of these foams, in combination with observations made during mixing, suggested that NiTi particles smaller than the NaCl particle size ( $<100 \mu\text{m}$ ) provided the best mixing. However, from the perspective of implants, very small NiTi particles ( $<40 \mu\text{m}$ ) could also lead to undesirably thin walls of NiTi separating adjacent pores (i.e., adjacent NaCl particles), and hence to lower connectivity. For these reasons, NiTi particle sizes within the range of 44-106  $\mu\text{m}$  are preferred.

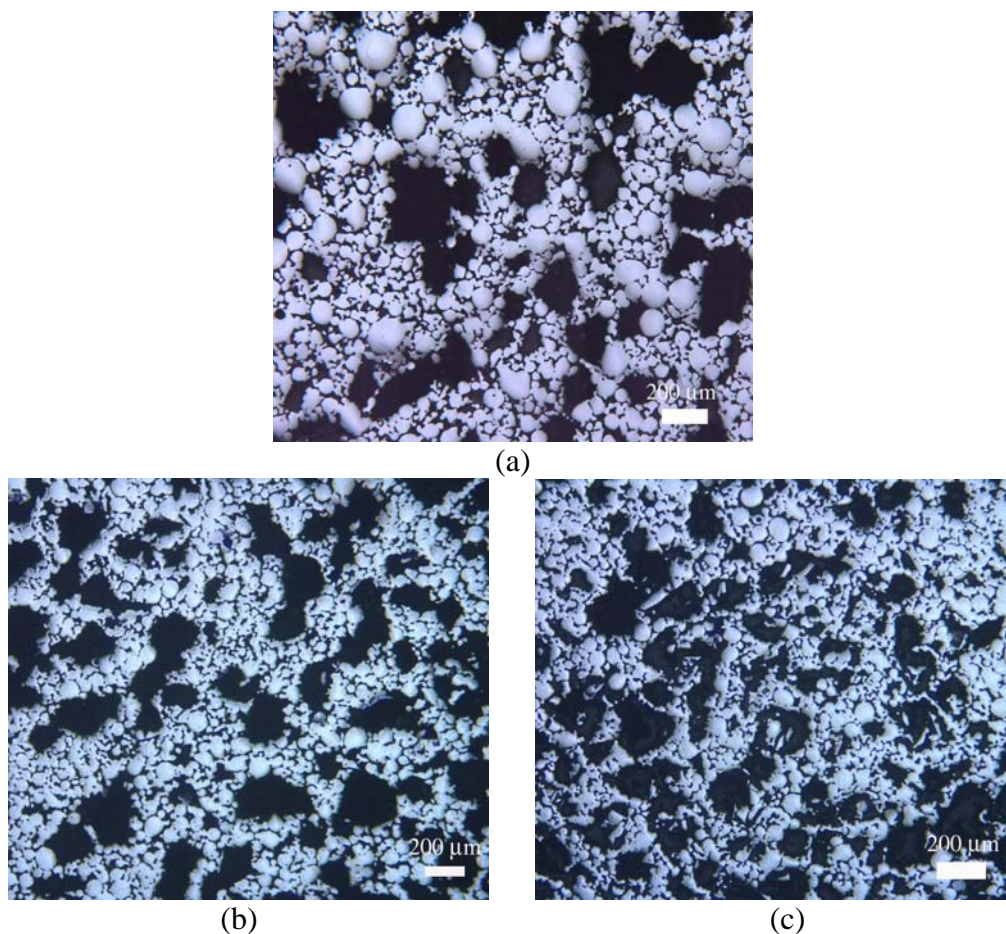


Figure 5.2 Micrographs of NiTi foams made with various ranges of NiTi particle size; (a) 44-177  $\mu\text{m}$  (b) 44-106  $\mu\text{m}$ , and (c)  $<106 \mu\text{m}$ , all having 40 vol% NaCl (106-250  $\mu\text{m}$ ) and sintered at 1250°C for 10 hours.

It was observed that addition of small metal powders (Ni, 8.902  $\text{g}/\text{cm}^3$ , and/or Nb, 8.57  $\text{g}/\text{cm}^3$ , both  $<10 \mu\text{m}$ ) to the NiTi powders before introducing the NaCl resulted in better dispersion of the mixture. The mechanism is unknown, and likely to be complex. The small powders may fit within the spaces left between the larger NiTi and/or NaCl powders.

In addition to powder characteristics, mixing parameters also affect the degree of mixing. For instance, separation of powders can be reduced by reducing free fall. Using a short container

(but one still having a volume 3 times that of the mixture) reduces the free fall distance during tumbling, as does mixing with the bottle forming an angle with respect to the vertical direction. By carefully optimizing such parameters, well-distributed powders, and thus uniform foam structures with high porosity, could be obtained (Figure 5.3).

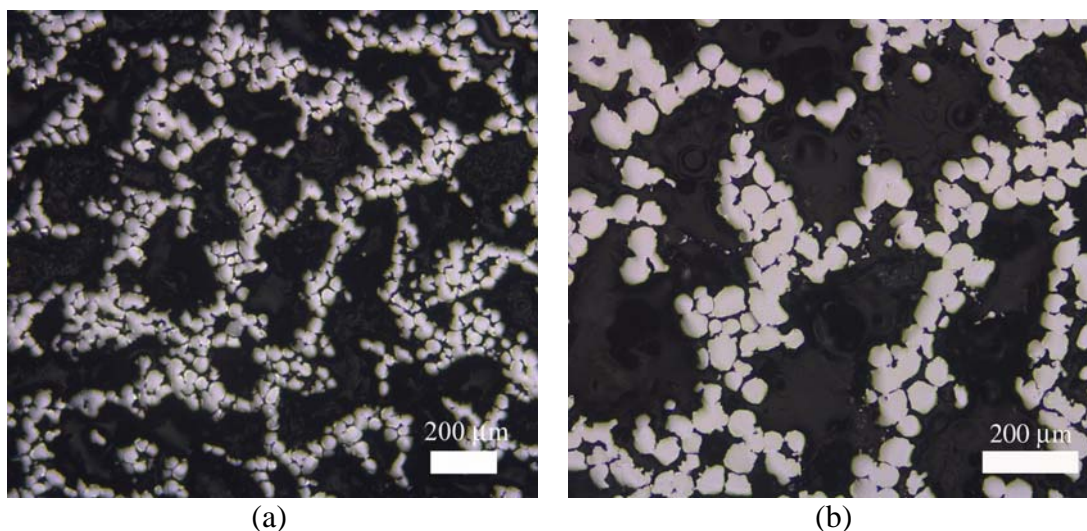


Figure 5.3 Micrographs of sintered NiTi foams using a mixture of NiTi powder (44-62  $\mu\text{m}$ , with Ni and Nb addition) and 60 vol% NaCl (106-250  $\mu\text{m}$ ) at 11850°C for 10 hours.

### 5.3 Effect of sintering time

The influence of sintering time on densification of foam structures was studied using Ni-rich NiTi foams produced by sintering for various time (Figure 5.4). At 1250°C, sintering for 20 hours greatly improved densification of the NiTi walls, relative to sintering for 10 hours. Overall porosity changes followed the same trend: 33% total (with 32% open porosity) for 36 hour sintering, vs. 43% total (with 39% open porosity) for 10 hour sintering. Sintering for 36 hours did not, however, further affect the foam microstructure or closed porosity in the NiTi walls. This closed porosity was directly related to poor densification during the sintering process, rather

than the presence of NaCl, because monolithic Ni-rich NiTi sintered under the same conditions as the foam in Figure 5.4(c) (1250°C for 36 hours) still showed 14% porosity (Figure 5.5). Therefore, better initial powder packing and/or dramatic improvement in sintering is needed to address this issue.

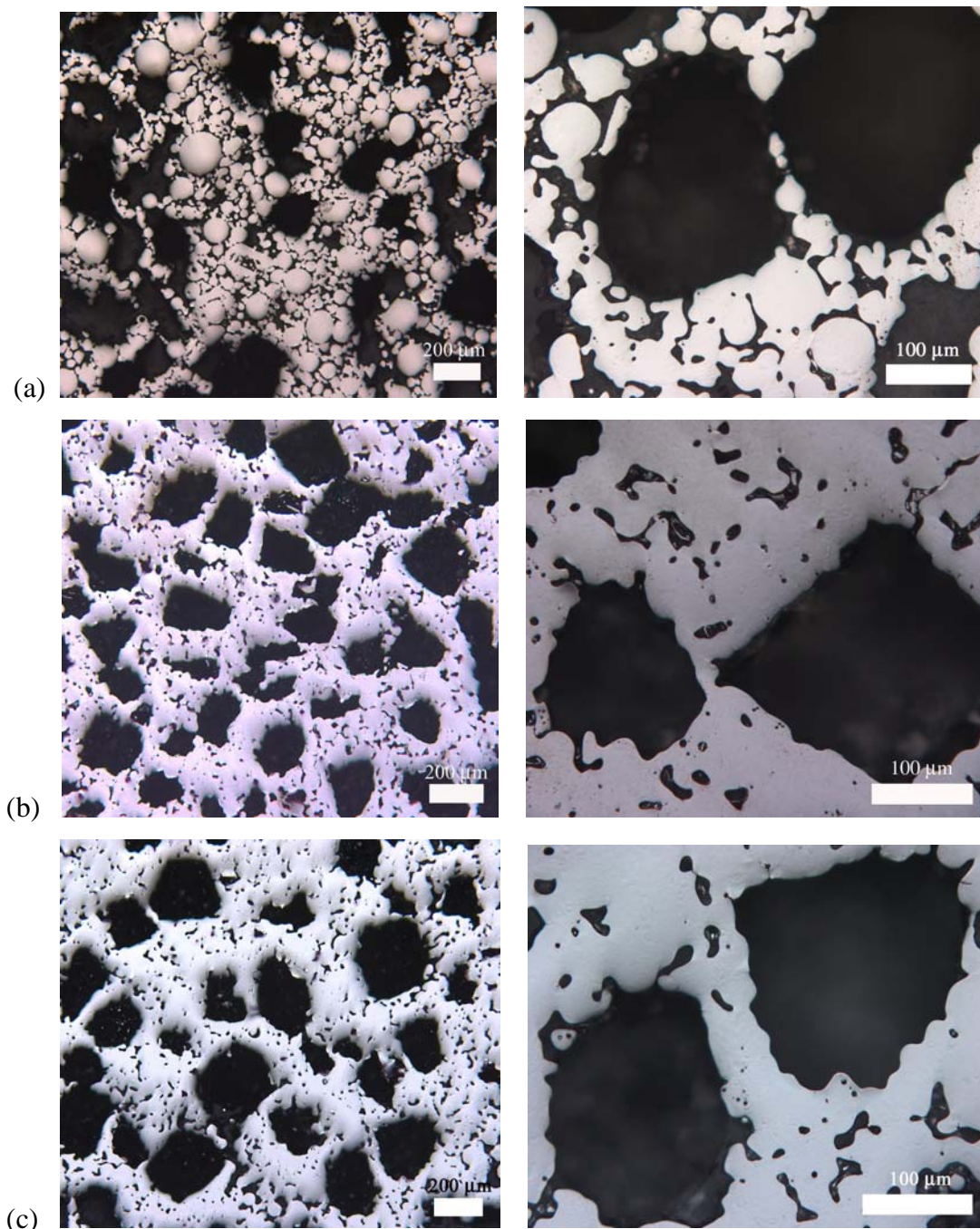


Figure 5.4 Micrographs of Ni-rich NiTi foams (50.8-51 at%Ni) sintered at 1250°C for (a) 10 hours, (b) 20 hours and, (c) 36 hours. Left micrographs were taken at low magnification and right at high magnification.

Porosity produced by poor sintering contributes to both the closed and open porosity measured in a foam sample, since some of the small pores which would otherwise be closed in a monolithic sample (Figure 5.5), will in a foam be connected with the large open NaCl-replicated pores (Figure 5.4, bottom row). As a consequence, a low calculated value of closed porosity does not, by itself, indicate a well-densified foam structure. At the least, a value of open porosity not greater than the NaCl fraction must be measured before such a conclusion is drawn; in the best case, it will be supported by metallographic examination.

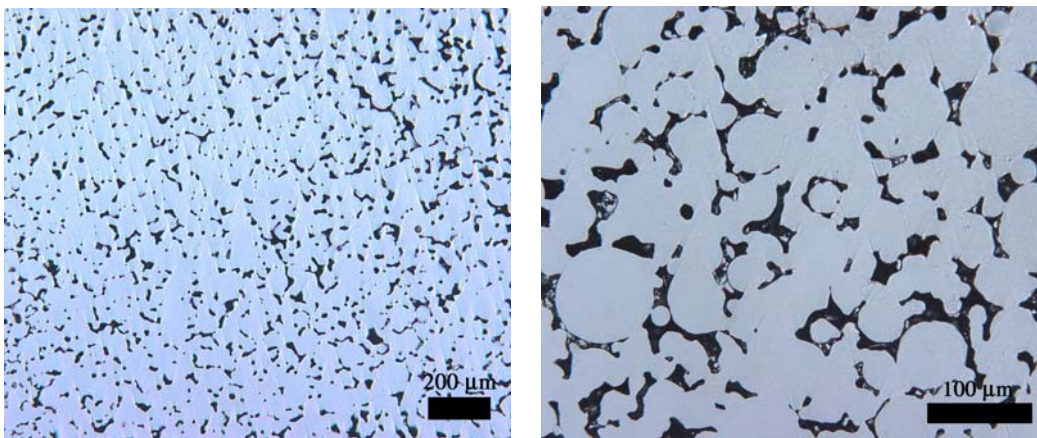


Figure 5.5 Micrographs of monolithic Ni-rich (51 at% Ni) NiTi sintered at 1250°C for 36 hours. Left micrographs were taken at low magnification and right at high magnification.

## 5.4 Effect of cold isostatic pressing (CIP) after sintering

Cold isostatic pressing (CIP) is a powder metallurgy technique based on compacting powders at room temperature using equal pressure in all directions. In CIP, powder or powder preform is generally contained within a flexible mold (e.g., a polyurethane or rubber bag) of appropriate geometry, which is then immersed in a pressure medium (e.g., oil or water) to which high pressure is applied. High density and microstructural uniformity, with flexibility in part size and geometry, can be achieved using CIP.

In an attempt to reduce the closed porosity inside the struts of sintered NiTi foam, CIP was used in conjunction with a subsequent sintering step. However, instead of applying pressure only outside the bag, the pressure medium was added to the inside of the bag as well, to infiltrate the foam and thereby directly apply pressure to the accessible inner surfaces. Using this modified method, the pressure medium can reach the surfaces of all the open, macroscopic pores and, via the applied pressure, densify the NiTi struts (Figure 5.6), collapsing the closed pores inside. Subsequent sintering was used to further densify the strut microstructures.

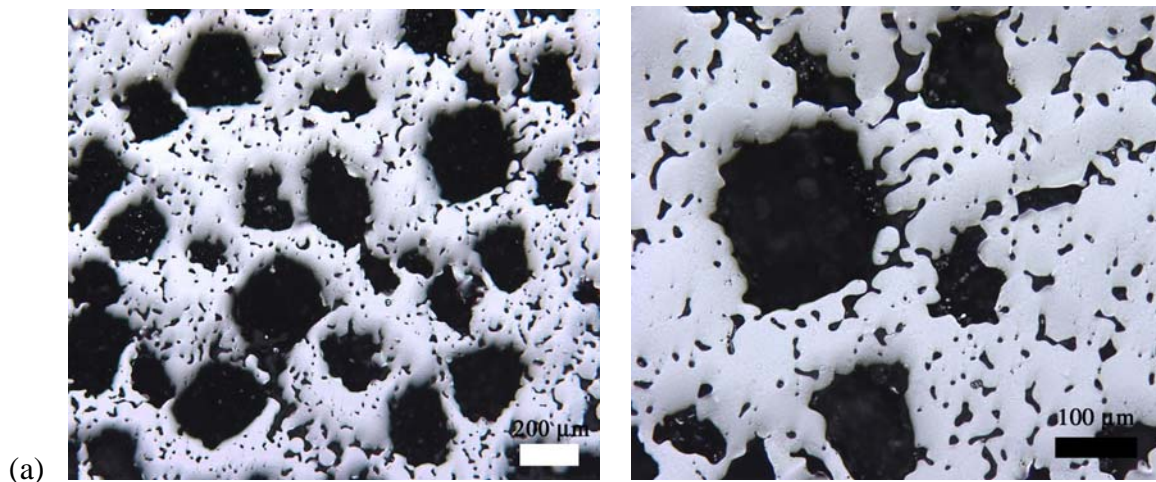
### 5.4.1 Experimental procedures

An as-sintered Ni-rich NiTi foam (51 at% Ni,  $5 \times 5 \times 10 \text{ mm}^3$ ) was placed in a rubber bag filled with de-ionized water ( $250 \text{ cm}^3$ ), and entrapped air was then removed using a vacuum pump. The bag was sealed tightly and examined to ensure that no space was left inside the bag not filled with water. The bag was immersed in oil (the pressure medium) inside a high pressure vessel. A hydrostatic pressure of 280 MPa was applied to the oil for 30 minutes. The foam was

then removed from the bag and cleaned ultrasonically with acetone. The foam was subsequently sintered at 1250°C for 6 hours.

#### 5.4.2 Results and discussion

According to optical micrographs, the porous macrostructure was maintained after CIP, which indicates that the pressure medium infiltrated the macroscopic pores, and hence that the structure was not only compressed from outside. Some closed pores inside struts indeed disappeared; however, the majority remained, especially inside the larger NiTi nodes. No further attempts were made using the method, since the improvements in structure were not significant, despite the lengthy and involved multi-step process. It is possible that the poor improvements were due to insufficient pressure given the high compressive dislocation yield stress of NiTi (typically in excess of 800 MPa), but the applied pressure of 280 MPa was already maximal for the available CIP equipment.



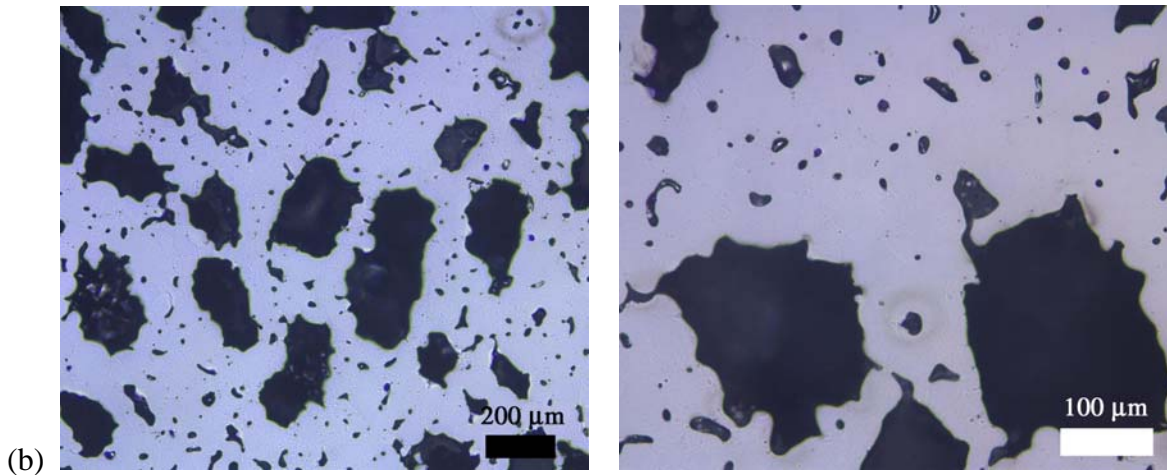


Figure 5.6 Micrographs of sintered Ni-rich NiTi (51 at%Ni) foam (a) before and (b) after CIP and subsequent sintering.

### 5.5 Effect of Ni addition and heat treatment on transformation behavior

To make NiTi foams that exhibit superelasticity during implantation, transformation temperatures (especially  $A_f$ ) below body temperature are required. The near-equiatomic NiTi foams described elsewhere in this work, however, provide  $A_f \sim 60^\circ\text{C}$ , and consequently exhibit shape memory effects rather than superelasticity at ambient and body temperature.

It is well known that the transformation behavior of Ni-rich NiTi (>50.5 at% Ni) can be manipulated through homogenization and aging. During homogenization, precipitates are dissolved, and the microstructure of NiTi is homogenized. The homogenized microstructure is very soft and is easily deformed plastically by dislocation slip, and hence superelasticity is not expected. During aging, precipitation takes place and causes hardening (preventing the movement of dislocations, and thus slip), leading to stress-induced transformation and superelasticity. Therefore, from the point of view of transformation behavior, an increase in Ni

content will lower martensitic transformation temperatures (especially  $M_s$ ) after homogenization, while aging will raise  $M_s$ .

### 5.5.1 Heat treatment procedure

Heat treatment was done under vacuum using an infrared lamp furnace. A 20 mm ID quartz tube was used as the furnace chamber; the upper end of this tube was connected to a mechanical pump, while the lower was sealed around a type K control thermocouple, which extended into the hot zone from below. An as-sintered NiTi sample was cut using a low speed diamond saw to  $\sim 5 \times 5 \times 5 \text{ mm}^3$ . The sample was placed on a molybdenum plate sitting in a shallow graphite cylindrical cup (15 mm ID, 2 mm tall from bottom). A cylindrical titanium tube (15 mm OD, 60 mm height) used as a getter was put around the sample and fitted into the graphite cup. The inner wall of the Ti tube was wrapped with a thin molybdenum foil to prevent direct contact with the NiTi sample. A round Ti foil (15 mm diameter) was put on top of the Ti tube as another getter. This entire setup is hereafter called the sample holder.

The sample holder was slid vertically into the quartz tube, until the sample was in the hot zone of the infrared lamps and the sample holder was resting on the control thermocouple, which fit into a drilled hole in the bottom of the graphite cup. In this configuration, the control thermocouple served as a support, and at the same time measured the temperature very close to the sample. Argon gas (10 psi) was used to flush the system three times before a final evacuation. The temperature controller was programmed to run a desired thermal cycle (continuous homogenization and aging) with a high heating and cooling rate. After aging, the bottom end of the quartz tube (into which the thermocouple supporting the sample holder was

fixed) was removed, and the sample holder (with the sample still inside) was dropped into a water bath (i.e., quenched to room temperature) within 5 seconds or less after removed from the heating zone.

### 5.5.2 Observations

The effect of Ni content on the transformation behavior of sintered monolithic and porous NiTi was evaluated using a composition of 50.8 at% Ni. Both samples were sintered at 1250°C for 12 hours, furnace cooled, and subsequently heat treated under the same conditions: homogenization at 1000°C for 30 minutes, aging at 500°C for 2 hours, and quenching in water to room temperature. The nearly-identical DSC results for the samples (Figure 5.7) indicate little or no influence of microstructure on transformation behavior, but a significant influence of heat treatment. A single-step transformation upon heating, and followed by a two-step transformation upon cooling, reflect a forward martensitic transformation of B19' martensite to B2 austenite and a reverse transformation from B19' to B2 with an intermediate R phase, respectively. The latter phase indicates precipitates or dislocations that suppress the direct transformation.

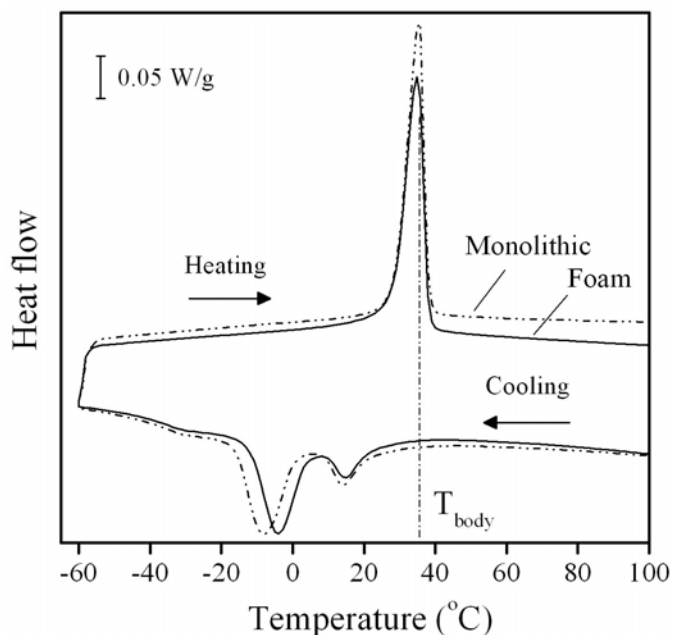


Figure 5.7 DSC curves for sintered (1250°C for 12 h) monolithic and porous (40 % porosity) Ni-rich (50.8 at% Ni) NiTi after heat treatment (homogenizing at 1000°C for 30 min followed by aging at 500°C for 2 h).

The heat of transformation in both samples was almost half the theoretical value of 24 J/g, and the transformation temperatures of both samples were below body temperature (with the exception of  $A_f$  which was very close to 37°C). This is in good agreement with the work of Funakubo et al.[156], where  $M_s$  was seen to decrease after 2 hours aging (depending on aging temperature) as Ni content increased above 49.6 at%. For NiTi with 50.8 at% Ni aged at 500°C for 2 hours, the reverse transformation start temperature bifurcated into two values (ca. 20°C and -5°C), with about 25°C separation.

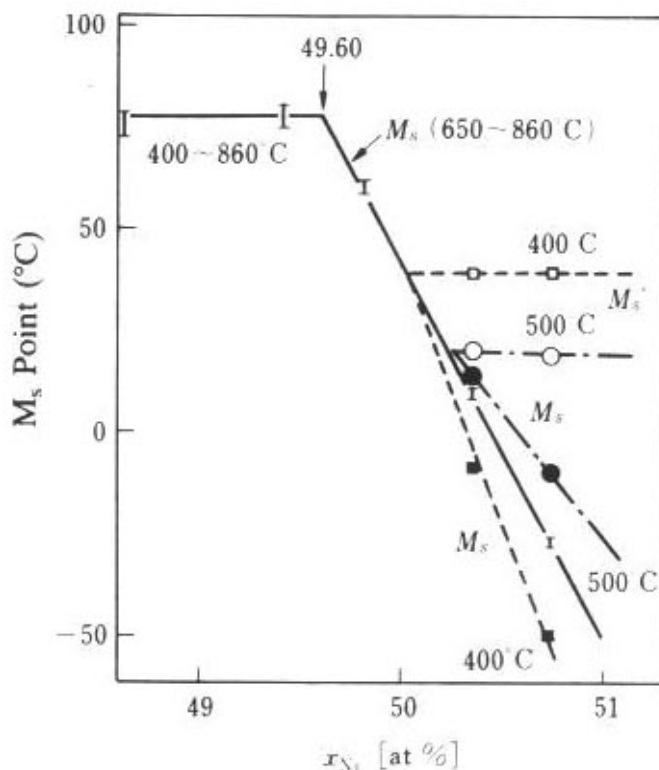


Figure 5.8 Relation between  $M_s$  and Ni content in arc melting NiTi [126]. Black and white circles represent water quenching condition from 500°C; black and white squares from 400°C.

According to this prediction,  $M_s$  should not change much with increase in Ni content using this aging condition. This was proven in similar experiments (not shown here) using 50.9 - 51 at% Ni NiTi foams, which resulted in almost identical DSC results. On the other hand, decrease in aging time from 2 hour to 1 hour at the same aging temperature caused a significant decrease in transformation temperatures (to below body temperature), as shown in Figure 5.9.

Although the transformation temperatures were close to the target values, mechanical testing of this foam should still be performed, in parallel with optimization of heat treatment process.

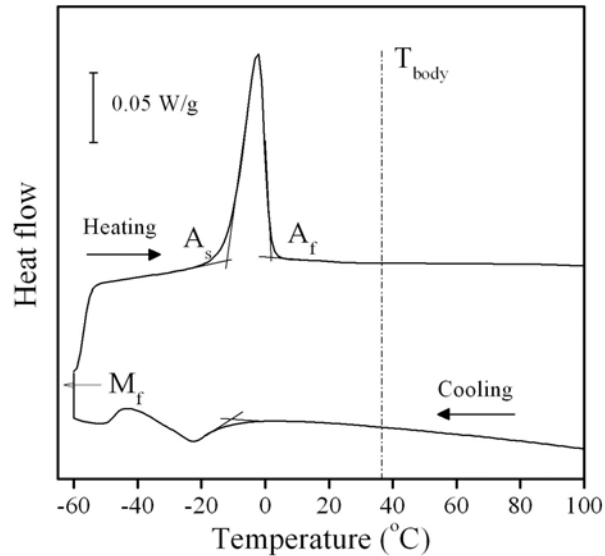


Figure 5.9 DSC result of 50.8 at% Ni-Ti foam sintered at 1250°C for 36 hours and heat treated at 1000°C for 30 minutes, followed with aging at 500°C for 1 hour, and water quenching.

## 5.6 Mechanical property evaluation of Ni-rich NiTi foam

### 5.6.1 Effect of service temperature

The service temperature of a NiTi foam determines the appearance of the phases (M: martensitic; A: austenitic) which dictate its thermomechanical behavior. In this section, two relevant service temperatures, room temperature and body temperature, were used during compressive testing of identical Ni-rich NiTi foams, with the effective result that two different phase states (A+(M) and A, where parentheses indicate a relatively small amount of that phase) were tested.

## Experimental procedure

Porous Ni-rich (50.8 at% Ni) NiTi (42-44% porosity) was produced by sintering at 1250°C for 10 hours. The sample was then homogenized at 1000°C for 30 minutes, followed by aging at 500°C for 2 hours, before water quenching to room temperature. The microstructure of this foam was shown in Figure 5.4a, and its transformation behavior in Figure 5.10.

Two identical compression samples (4x4x8 mm<sup>3</sup> each) were prepared (see section 2.2). One (labeled foam R) was tested at room temperature (25°C), and the other (labeled foam B) at body temperature (37°C). Temperature was monitored during testing in both foams using a wire thermocouple in contact with one side of the foam.

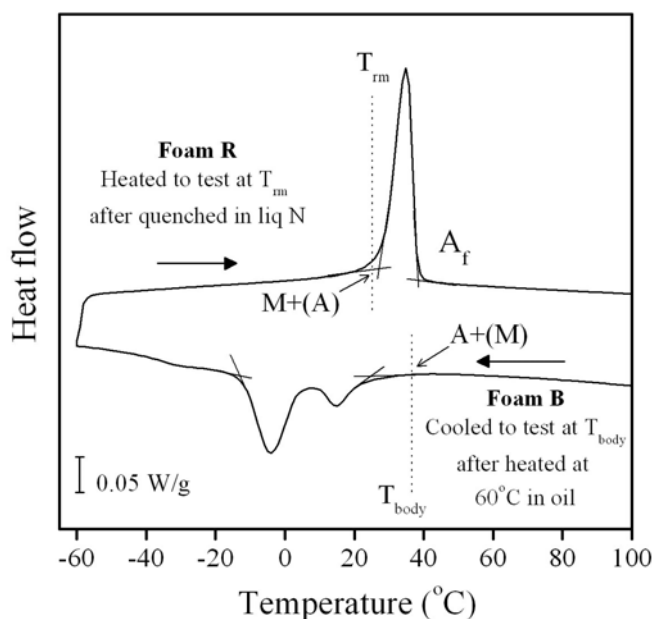


Figure 5.10 DSC curve of Ni-rich (51 at% Ni) NiTi foam produced by sintered at 1250°C for 36 hours, followed by heat treatment. The vertical lines show the testing temperatures (room temperature and body temperature), indicating the NiTi phases present in each case.

Prior to the room temperature testing, foam R was quenched in liquid nitrogen to ensure a complete martensitic transformation, and then stored at room temperature until testing. According to DSC (Figure 5.10) the foam was, at room temperature, near fully martensitic, with only a small austenitic phase also present. Compressive load-unload-recovery cycling (section 2.2) was carried out with an increment of 1% with maximum strains increasing from 1% to 7% at room temperature (25-28°C). The heat recovery in hot oil (60°C) was done after each load-unload cycle and the sample dimensions were measured before and after the heat recovery process. Before each loading step, the foam was quenched again in liquid nitrogen (as above) to ensure consistency. The sample dimensions were measured before loading, after unloading, and after heat recovery.

For testing at body temperature, the compression test was performed inside a box furnace. Foam B was placed inside the furnace and heated to 60°C in situ before the test began, to ensure a complete forward transformation to austenite, and then cooled down to 37-39°C (fluctuating within a test), where the test was performed. One continuous series of 12 load-unload cycle was performed, incrementing from a maximum strain of 1% to a maximum strain of 8% without interruption.

## Result and Discussion

Both foams survived testing without failure up to maximum strain of 7-8% and compressive stress >160 MPa (Figure 5.11). The loading stress corresponding to the maximum strain was slightly higher in foam B than foam R, while the loading and unloading stiffnesses of foam B (2.5-3 and 3-4 GPa) were less than one-third those of foam R (6-12 and 11-15 GPa). This

indicates that foam B exhibited more superelasticity, as larger recovered strains were observed upon unloading (e.g. 5%, after loading to 8% maximum strain), while foam R exhibited shape memory behavior. Foam R recovered 60-100% of the accumulated strain, and only 3.5% strain upon unloading. At a maximum strain of 7%, a strain of 2.7% could be thermally recovered.

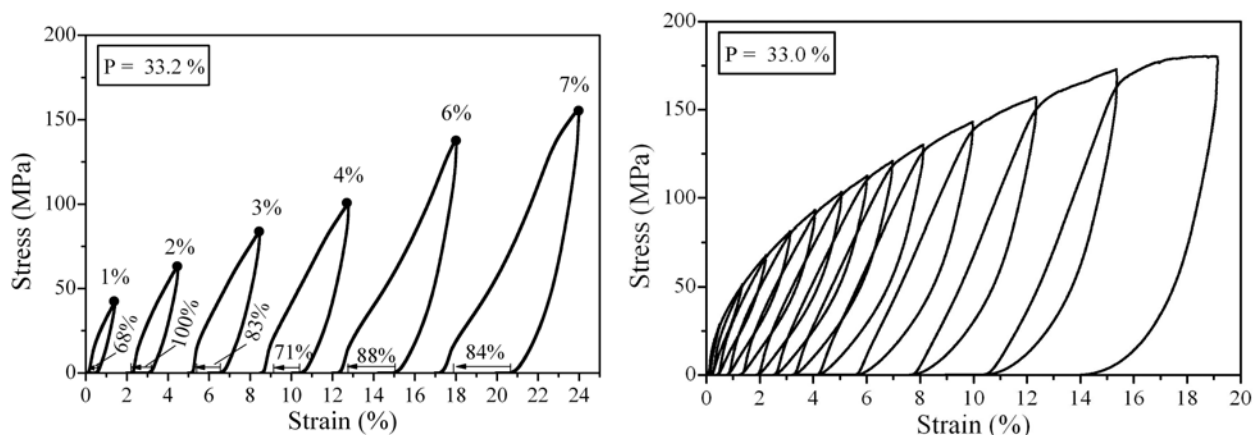


Figure 5.11 Stress-strain curves of a Ni-rich (50.8 at%Ni) NiTi foam at (a) room temperature (foam R), and (b) body temperature (foam B).

The percent shape recovery upon heating of foam R (43.0% porosity) was in the same range as that of foam produced by HIP, for example foam H1 (HIPed at 950°C for 4 hours, with 39.5% porosity). The unloading stiffness was also the same (11-15 GPa, vs. 12-18 GPa in foam H1), even though the degree of densification of the NiTi walls in foam R was markedly lower. The effect of matrix densification was more pronounced in the load-bearing capacity - foam H1 carried twice as much load at a given applied strain (even higher load-bearing was seen in other HIPed foams). However, foam R survived high strains, while foam H1 failed at 6% applied strain, and also provided higher unloading strain (twice as much as foam H1). This might be attributable to the presence of austenite in foam R.

At room temperature, foam R consisted of M+(A) phases. Upon loading, while M was detwinned ( $M \rightarrow M_M^d$ ), (A) was transformed under stress to detwinned martensite ( $M_A^d$ ), which resulted in additional loading strain capacity. The detwinned martensite phase originating from (A) was also reversible upon unloading, allowing additional unloading strain. Upon heating, only the detwinned martensite  $M_M^d$  underwent a martensitic transformation, so the percentage recovery was not affected by the A phase, but depended purely on the properties of the NiTi matrix itself.

For foam B, testing at body temperature ensured almost complete austenite. For each cycle, after an initial linear elastic region, a gradual decrease in apparent stiffness (i.e. in slope) upon loading was observed in the transformation plateau region (rather than the constant-slope behavior typical of superelastic NiTi). A high stress was required to induce the  $A \rightarrow M_M^d$  transformation. This might be attributed to strain hardening induced by precipitates. Upon unloading, a high fraction of the strain was recovered, especially in early cycles. The loading and unloading stiffness are similar, due to the reversible nature of elastic and inelastic behavior in the A phase. Since the test cycles were done without heat recovery,  $M_M^d$  phase formed from pre-existing M (if any existed) and was not recovered. Strains due to this un-recovered  $M_M^d$ , along with any plastic deformation in the foam structure (e.g. apparent in near-linear, low-slope regions at the end of last cycle) simply accumulated throughout the series of tests, and as a result, full recovery upon unloading was not observed, particularly when high strains were applied.

Almost exactly the same behavior was observed by [33], where austenitic NiTi foam (produced by HIP of elemental powders, followed by heat treatment at 540°C for 30 minutes) with 300  $\mu\text{m}$  pore size and 42% porosity was studied. Compared to foam B, they observed a slightly higher strength, roughly the same stiffness (3 GPa), and the same recovered strain upon

unloading from a given applied strain, despite lacking the microporosity present in foam B. However, dips in the stress-strain curve (due to microcracking) observed in their work during loading were not observed in foam B.

### 5.6.2 Effect of phase composition

In this part, the effect of phase composition at a single test temperature was studied. Two identical NiTi foams were tested in compression using identical procedures, but different prior heat-treatment conditions (and thus different phase compositions).

#### Experimental procedures

A Ni-rich (51 at% Ni) NiTi foam (R') was produced by sintering at 1250°C for 36 hours, heat treating at 1000°C for 30 minutes, aging at 500°C for 2 hours, and water quenching. In contrast to foam R, foam R' was heated in oil at 60°C for 5 minutes, before cooling in room-temperature oil and ultrasonic cleaning. As a result of this altered heat treatment, foam R' contained mostly austenite with a small amount of martensite (A+(M)) at room temperature (Figure 5.12).

A control sample (foam S', 14% porosity, Figure 5.5) was made and treated using the same process as foam R' but without salt, and tested with the same procedure. The DSC results for both foams were identical, as suggested in section 5.7. Compression testing was performed on both foams at room temperature.

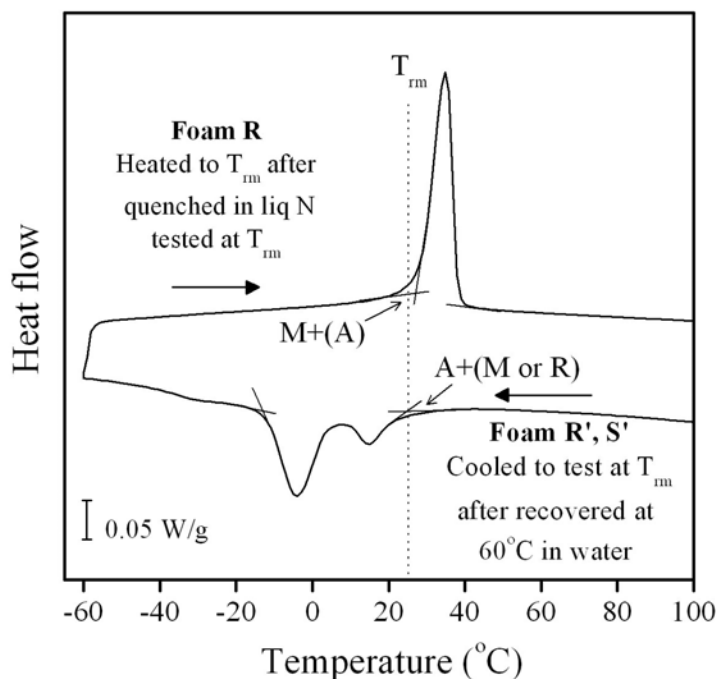


Figure 5.12 DSC curve of Ni-rich (51 at% Ni) NiTi foam produced by sintered at 1250°C for 36 hours, followed by heat treatment. The vertical lines show the testing temperatures (room temperature), indicating the NiTi phases present in each case.

## Result and Discussion

In comparison with foam R, foam R' (Figure 5.13a) had better strut densification (due to its longer sintering time of 36 hours) and different phase composition (A + (M or R-phase), instead of (A) + M). As a result, foam R' reached higher loading stress at a given strain, and showed slight differences in stress-strain behavior. The stress-strain behavior of foam R' is understandable by the same mechanisms described above for foam R, except with a larger contribution from the A phase. Specifically, a pronounced sharp initial loading stiffness (due to a mixture of the elastic behavior of A and the beginning of detwinning in M) and visible

transformation plateau (due to additional  $A \rightarrow M_M^d$  transformation) were observed. However, despite their differences on loading, the unloading stiffnesses of foams R and R' were quite similar. High strain recovery during unloading (about half of the applied strain) was also seen in both foams, since this phenomenon relies on the amount of  $M_M^d$  phase before unloading starts, not on the original phases present. Impressively, recovery upon heating (77-100%) and stresses for given applied strains were comparable to those of other foams produced by HIP and sintering.

Sample S' can be considered a control specimen, representing the matrix from which foam R' was made (which, like S', contained small isolated pores). Its qualitatively similar behavior (Figure 5.13b) therefore implies that the general shape of the stress-strain curve, and the strain recovery, were unaffected by the macro-porosity. As expected, its stiffness and strength (12-15 GPa during loading, and 23-24 GPa during unloading, about twice those of foam R') were affected by the absence of macro-porosity.

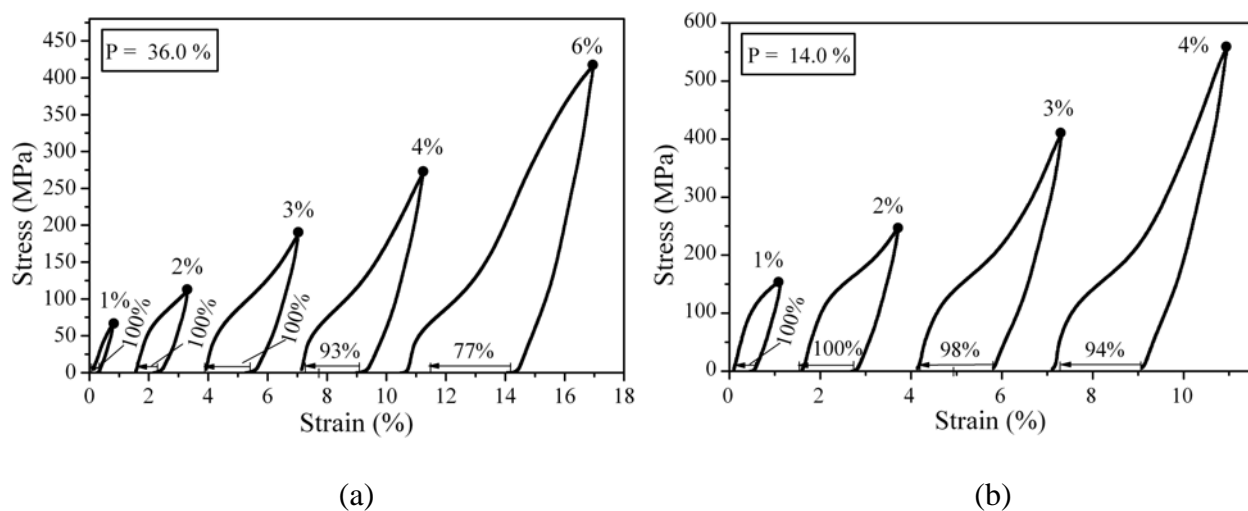


Figure 5.13 Stress-strain curves of a Ni-rich (51 at%Ni) NiTi foam (a) R' and (b) S', at room temperature.

In conclusion, NiTi foams (containing two levels of porosity - macroporosity from the salt space holders, and microporosity within the NiTi struts) were produced by sintering for long periods of time, and exhibited desirable mechanical properties comparable to those produced by a more complicated process (HIP followed by sintering). The remaining concern over these foams is more focused on how the microporosity (sometimes called "secondary porosity") would affect biological performance (small and/or closed porosity is not available for bone ingrowth, and may affect negatively fatigue resistance). A controlled structure with two distinct levels of porosity, such as might be produced by two distinct space-holder particle sizes, might be considered to ensure openness and useful size in secondary porosity.

### 5.7.1 Synchrotron x-ray study of phase transformation of porous Ni-rich NiTi

Characterization using synchrotron x-ray facilities is crucial to understanding the links between microstructure, pore structure, and foam properties, since it can be used to detect and distinguish individual deformation/transformation processes occurring in NiTi without interfering with them. Due to the high intensity of synchrotron sources, mechanical properties from large sampling volumes and intricate geometries can be obtained. *In situ* diffraction measurements during compression offer information on internal stress and strain distributions [157] during loading and unloading (i.e., during simulated use). These will clarify the effects of pore structure and alloy microstructure on local deformation and fracture patterns, which are known to be highly non-uniform in foams and which must therefore be mapped with intense radiation and small spot sizes. Moreover, performing in-situ synchrotron x-ray diffraction measurements grants unique, quantitative, phase-specific information on the evolution of lattice parameters [158-160] and strain, phase volume fraction [161, 162], and texture [163, 164] during loading and unloading. This technique has been widely used for monolithic NiTi [165] (including stents) but never in porous NiTi.

The work described below concerns synchrotron x-ray diffraction studies, using foam samples cut from the same billets as foams R', on phase fraction determination during load-unload-recovery cycling.

### 5.7.2 Experimental procedure

Ni-rich NiTi foam identical to foam R' in the previous section was used in synchrotron x-ray experiments at beamline 11DC of the Advanced Photon Source at Argonne National Laboratory (Argonne, IL). In situ diffraction experiments using a beam size of  $100\ \mu\text{m} \times 100\ \mu\text{m}$  at an energy of 80.7 keV (wavelength of  $0.1536\ \text{\AA}$ ) were carried out during uniaxial compression testing in a mechanical testing rig placed in the path of beam line. The diffraction patterns were collected at constant applied stress on a Mar345 image plate detector (with a diameter of 345 mm) placed 109.1 cm from the sample. A beam stop was used to block the direct transmitted beam, and a ceria standard was used at the same position (slid in and out) as the sample to calibrate diffraction angle.

The compression instrument was screw driven, allowing remotely-controlled crosshead movements in the vertical direction by the rotation of a motor. Attempts to use an Omega pre-wired strain gage glued onto the sample surface failed, because the strain gages detached during testing due to incompatibility in size with the sample. Displacement values were therefore collected by hand from the crosshead motion, and the compliance of the system (measured before and after each test) was subtracted in order to determine the nominal strain. The strain rate used was less than  $5 \times 10^{-4}\ \text{s}^{-1}$ , and the stress limit of this setup was 1,000 MPa. The test was done near room temperature (28-30°C) and temperature monitored by a thermocouple in contact with the sample surface. At this temperature, the sample at the onset of testing was mainly austenite, with only a small amount of martensite (see above section). Consecutive load-unload-recovery cycles were performed to roughly the desired strains of 1%, 2%, 3%, 4% and 6%, guided by the stress-strain curve obtained in the above section. The sample was heated in hot

water at 60°C after each load-unload cycle to induce its shape recovery effect. The dimensions before and after heat recovery were measured with careful handling (to prevent direct contact with heat from hands). The load-unload-recovery cycle at 3% and 6% strain was repeated 3 times to explore the development of phase transformations over repeated cycles.

Diffraction patterns were taken at near zero stress, intervals of 18 MPa upon loading to the maximum desired stress, at the maximum stress itself, at 36 MPa intervals during unloading and after heat recovery under no applied stress. To ensure that a sufficient number of grains was sampled by the beam (insufficient sampling leads to spotty diffraction rings and difficulty in analysis), the sample was translated perpendicular to the beam direction in a geometric pattern chosen to expose the sample volume of 12 mm<sup>3</sup> to the beam during the course of each measurement with the total exact exposure time in a sample (257±1 seconds for the cycle of 3% and 268±1 seconds for the cycle of 6%) (see Figure 5.14(a)).

Image plate data from the load-unload-recovery cycle at 6% strain (i.e., the first cycle) were analyzed using the software FIT2D to integrate all 2D diffraction rings across 360 degrees and extract 1D intensity distributions as a function of the d-spacing. Peak positions were noted, and individual reflections were then identified for analysis. The areas underneath selected reflections of the austenite and martensite phases were analyzed (using single-peak Gaussian fitting in MATLAB) were then plotted as a function of strain.

## 5.7.3 Result and discussion

Figure 5.14(b) shows the load-unload-recovery cycles for maximum nominal strain of 3% and 6%, as observed in foam R'. Selected diffraction patterns (dots on the stress-strain curve) were analyzed: at near-zero stress, during loading and at maximum stress (filled dots), during unloading and after complete unloading (unfilled dots), and after the heat recovery process (half-filled dots).

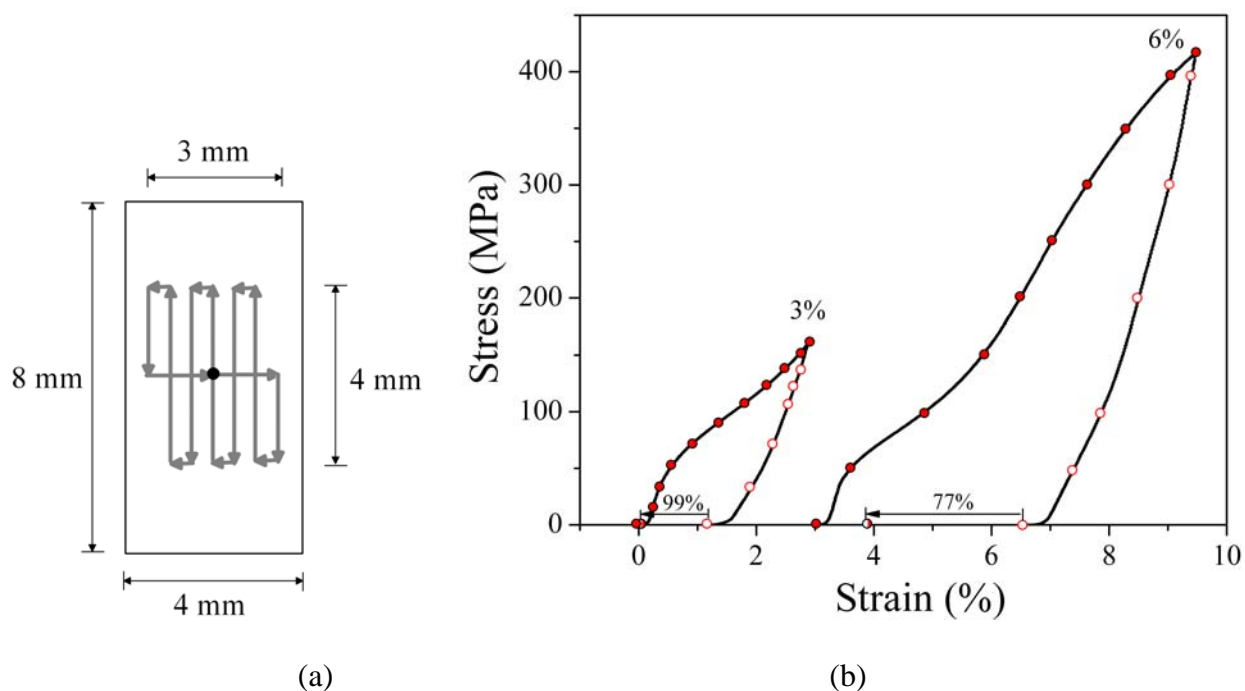


Figure 5.14. Measurement procedures for the diffraction measurement: (a) schematic depiction of the beam path (beam size of 0.1 mm) used in *in situ* x-ray diffraction measurements, in order to ensure sampling of a sufficient volume; (b) load-unload-recovery loops for maximum strains of 3% and 6%. Dots indicate points where diffraction patterns were taken (filled dots during loading, unfilled dots during unloading, and half-filled dots after heat recovery).

Diffraction patterns of the foam at zero stress and at the maximum stress for a maximum strain of 6% are shown in Figure 5.15. In the unstressed state (Figure 5.15(a)), the foam consists mainly of austenite, while at the maximum stress a mixture of austenite and martensite has formed (the additional martensitic reflections are clear in Figure 5.15(b). Weak texture can be observed in the diffraction rings 5.15(c), in the form of several rings stronger at  $0^\circ$  (horizontal axis) than  $90^\circ$  (vertical axis).

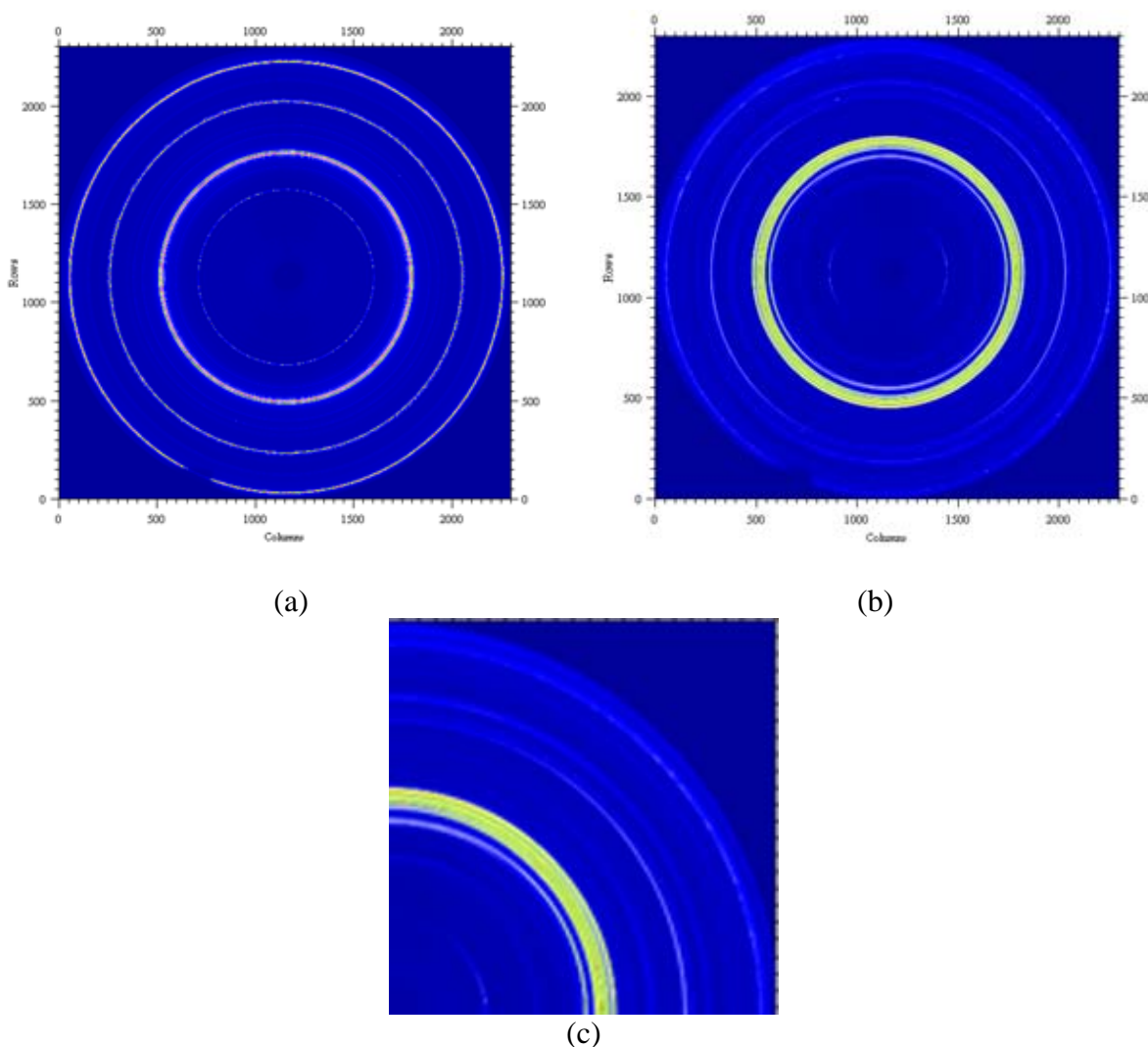


Figure 5.15. Diffraction patterns of foam R' (a) at zero stress and (b) at 420 MPa. The magnified diffraction pattern in (b) in angles of  $0-90^\circ$  is shown in (c).

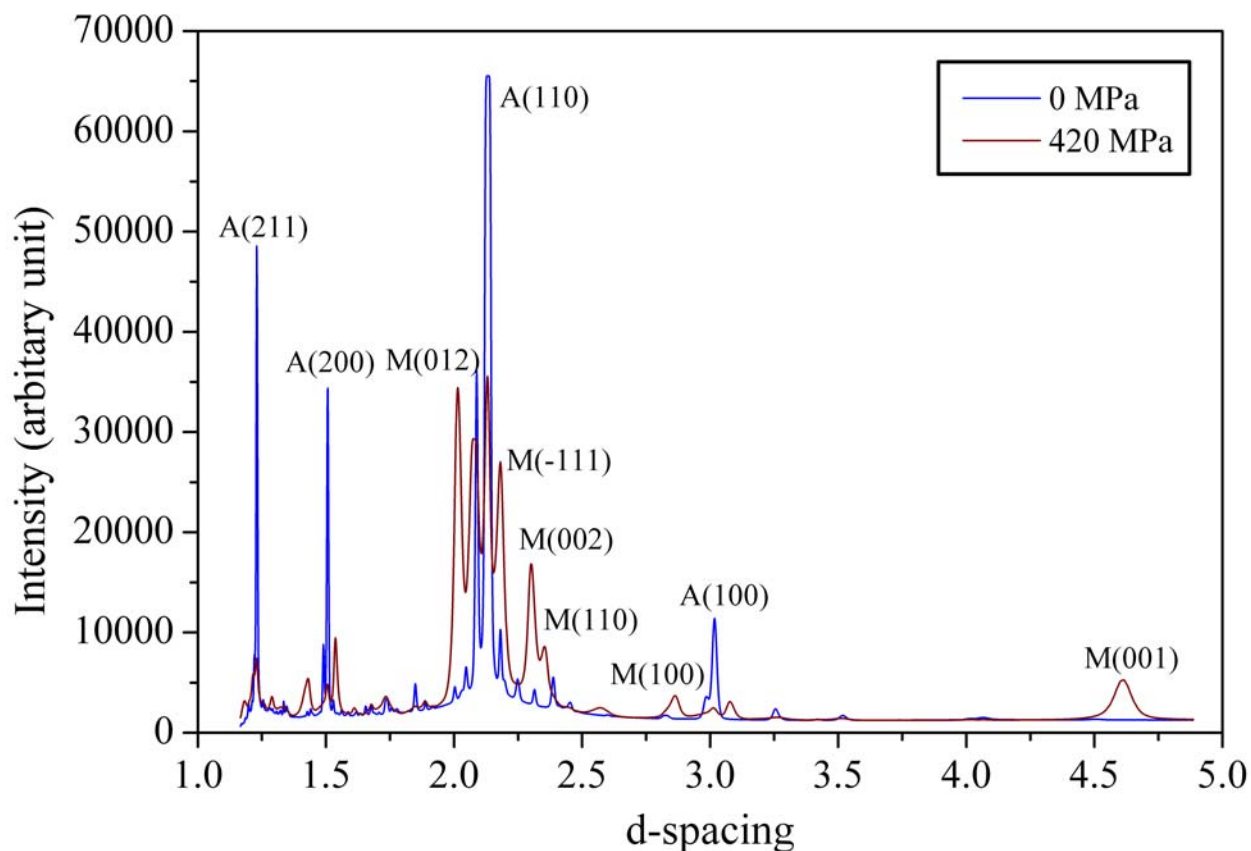
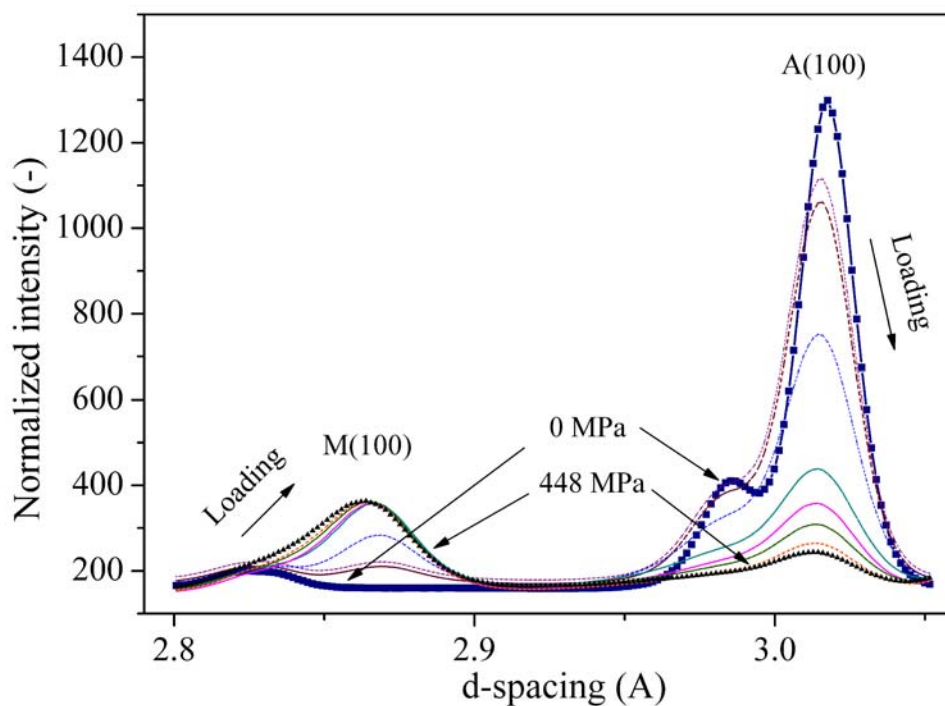


Figure 5.16. Indexed diffraction patterns for austenite (A) and martensite (M) in the foam at 0 MPa and 420 MPa.

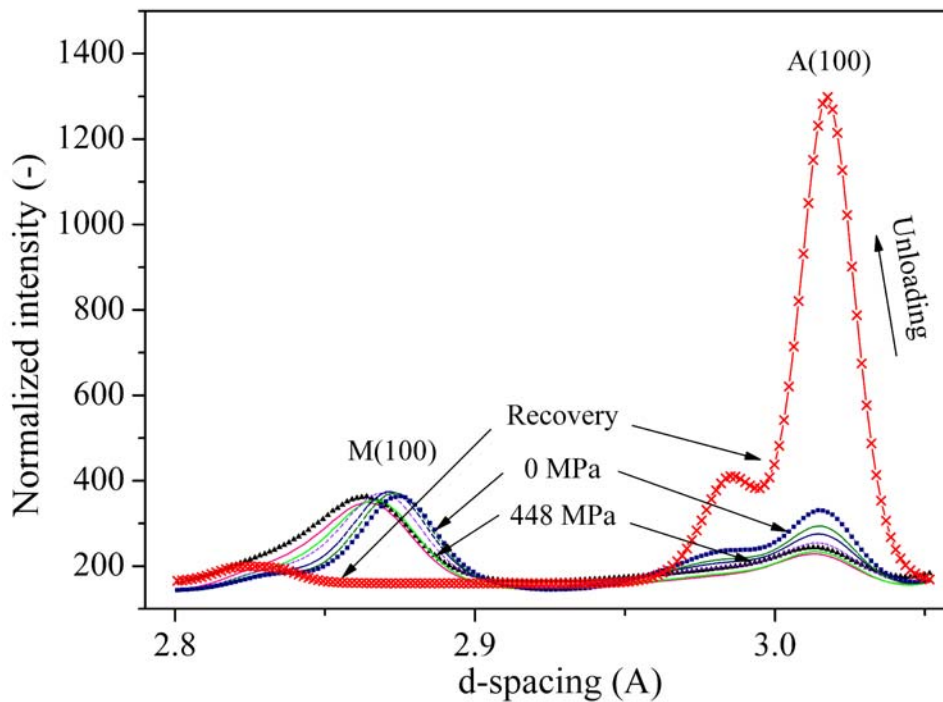
The intensities of these reflections as functions of d-spacing (in a range of 1.2-4.8 Å) were calculated using FIT2D from each diffraction pattern. Two fitted datasets are shown as examples in Figure 5.16. To determine the volume fractions of each phase at a given applied stress, the reflections from each phase must be quantitatively analyzed. Ideally, a full multi-peak fitting algorithm (i.e. a Rietveld analysis normally used in neutron diffraction analysis) should be used for this analysis, and such an analysis will be performed at a later date. A simpler analysis was used here, based on fitting Gaussian functions to individual peaks, specifically to the

reflections A(100), A(200) and A(211), and M(001), M(002), M(100), and M(110). Each peak was baseline-corrected and cropped to a d-spacing range of interest, then integrated to find the area under the peak.

At room temperature and after cooling down from the heat treatment at 60°C, foam R' contains mostly austenite and possibly some R-phase (it is impossible to distinguish R-phase reflections from austenite reflections, on account of near-identical crystallography). With increasing stress, the martensite peaks increase in intensity and gradually shift to smaller d-spacing (Figure 5.17), while the intensities of the austenite peaks decrease but with a less pronounced shifting in d-spacing. These shifts in d-spacing are due to elastic strain in each phase; determining the corresponding stresses carried by each phase at a particular applied macroscopic load (i.e., determining load-sharing behavior) will be an interesting area for future analysis.



(a)



(b)

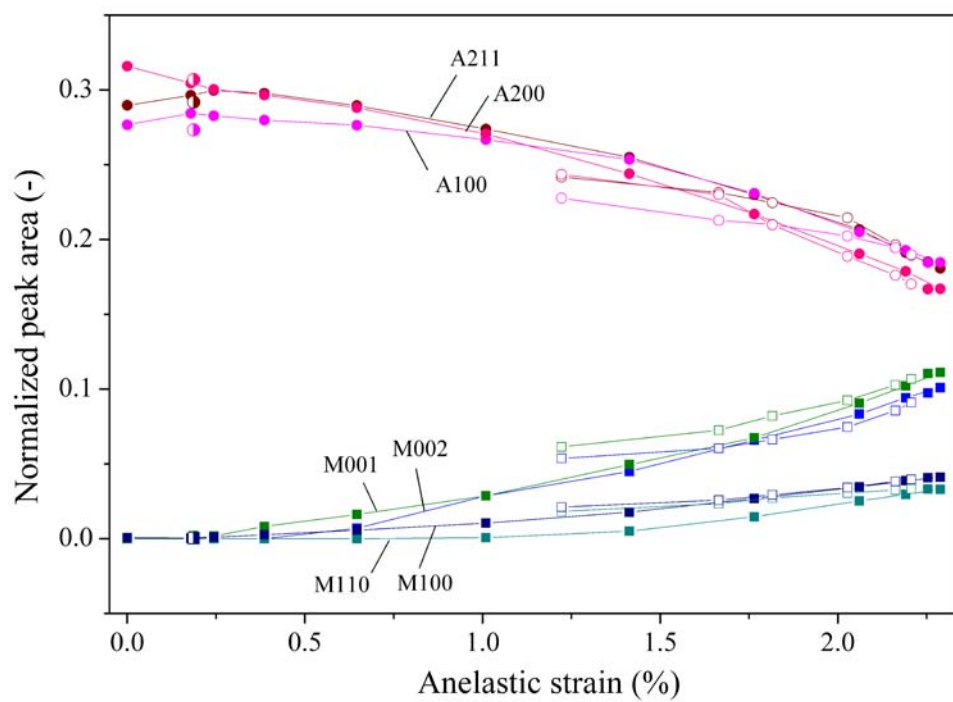
Figure 5.17. Evolution of Normalized diffraction intensity near peaks A(100) and M(100) (a) during loading from near-zero stress to maximum stress and (b) upon unloading from maximum stress to zero stress and after heat recovery.

Since the entire spectrum of each phase is not taken into account, direct comparisons between the calculated peak areas cannot strictly be used to determine volume fractions (because, for instance, texture evolution can cause growth or recession of certain individual peaks, even when volume fraction is constant). In addition, the sample is not 100% austenitic in the unstressed state, so there is no absolute standard of peak area against which to normalize subsequent areas. However, the relationship between the amount of austenite transformed to martensite and the increasing amount of martensite (and opposite) with applied strains is reflected in the progression of peak areas of each phase. Each peak area of a diffraction pattern

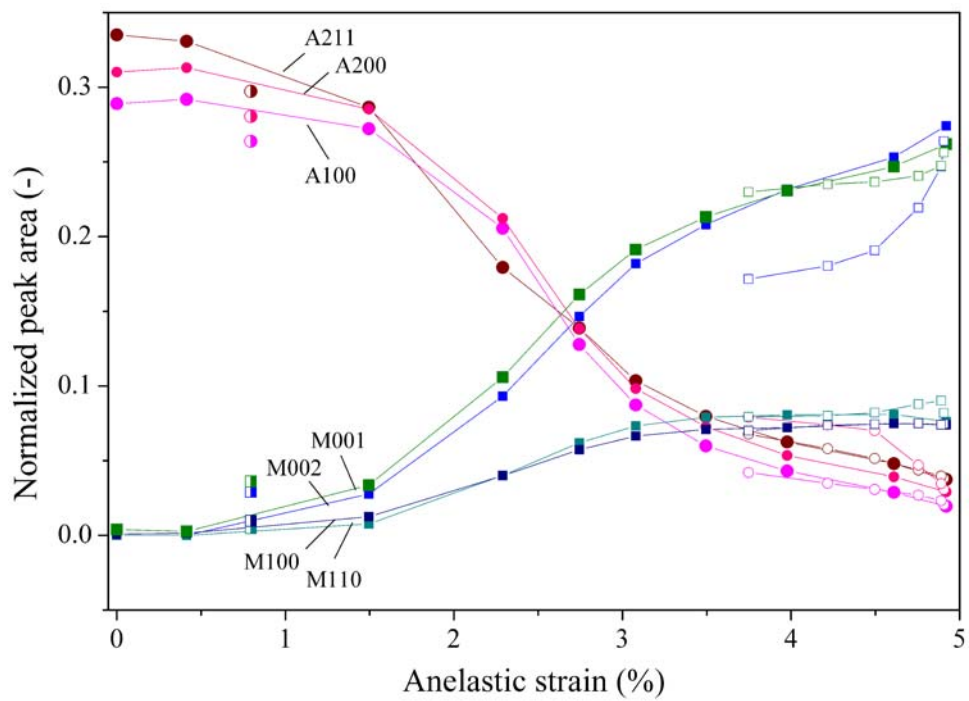
was normalized by the sum of the 7 selected peak areas in that diffraction pattern in order to minimize errors caused by variation in incident beam intensity between individual diffraction patterns. The alteration in the incident beam intensity was possibly due to a daily routine refill of beam intensity.

The normalized areas of selected reflections are plotted against the macroscopic anelastic strain in Figure 5.18. Anelastic strain was determined by subtracting the elastic strain of NiTi foam (calculated assuming a stiffness of 26 GPa at each applied stress) from the total macroscopic foam strain measured during the compressive test. This graph allows direct observation of the effect of phase transformation on anelastic (superelastic and/or plastic) strain.

The peak areas of selected austenite reflections A(100), A(200) and A(211) decrease at nearly the same rate on loading while two growth rates of martensite reflections were observed: faster in M(001) and M(002), and slower in M(100) and M(110). This suggests that the former orientations are more preferred as martensitic transformation products (also has higher texture observed on the diffraction rings). The peak area change is slow at first and becomes faster with strain (Fig.5.18(a)). This non-linearity reflects the non-linear deformation behavior of cellular nature of the foam, unlike in dense NiTi [203] in which peak area change (phase volume fraction) is linear.



(a)



(b)

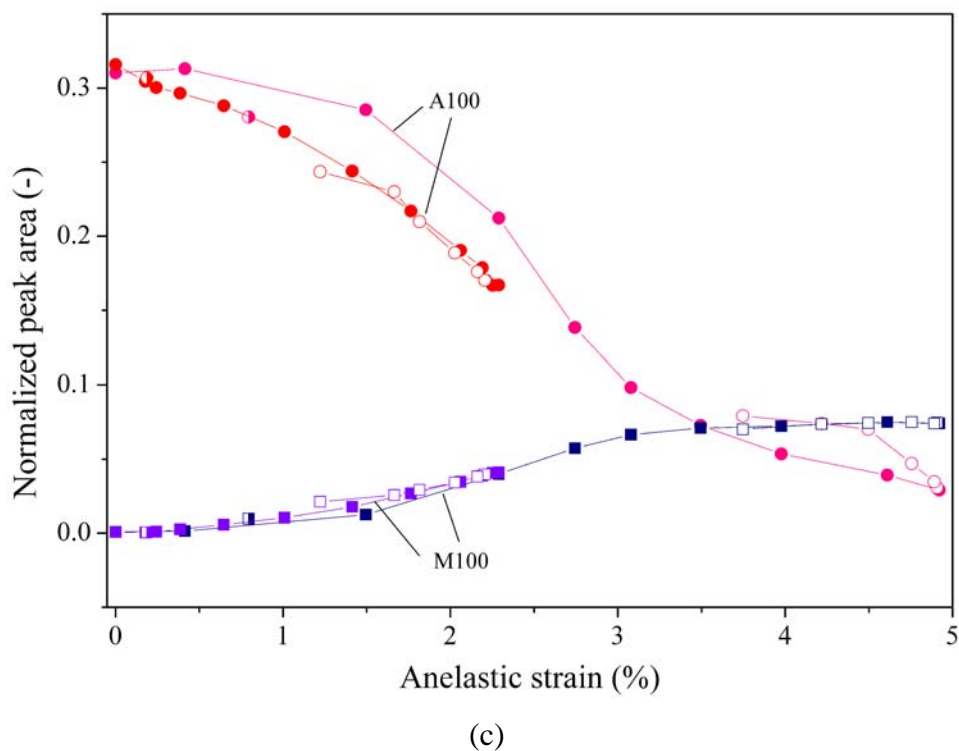


Figure 5.18. Normalized areas of austenite and martensite reflections as a function of applied anelastic strain for a maximum applied strain of (a) 3% and (b) 6%. Superimposition of normalized areas of A(100) and M(100) as a function of strain up to 3% and 6% is shown in (c). Filled, unfilled and half-filled symbols represent the values upon loading, unloading and after heat recovery.

Upon unloading, the areas of austenite peaks increase and those of martensite peaks decrease, implying reverse transformation (superelasticity). Residual amounts of transformed phase were observed after complete unloading. After thermal recovery, however, residual transformed material was present only in fractions near those seen during loading at an equivalent strain.

The area changes of the same sample compressed to maximum strain of 6% (Fig. 5.18(a)) show the same behavior as those seen during compression to 3% strain (Fig. 5.18(b)). The rate of peak area change with strain in the cycle of 3% was nearly reproduced during compression to

6% strain (Fig. 5.18(c)). However, as higher strain was applied, an inflection appeared during loading in all austenite and martensite areas at ~2.6% strain, where area progression/regression rates start to decrease. This suggests that transformation becomes more difficult, possibly due to plastic deformation with higher applied strain (accumulated plastic strain of 0.2% and 0.8% after the cycle of 3% and 6%, respectively).

During unloading, the rate of peak area change with respect to that during loading could be varied from reflection to reflection and is influenced by the following effects; (1) natural hysteresis in NiTi due to superelasticity, and (2) limited transformable strain due to plastic deformation.

First, the hysteresis in the NiTi foam (Fig. 5.14(b) indicates that the stress required to achieve a given strain on unloading is lower than that on loading. Therefore, the presence of hysteresis increases the change in peak areas (higher slope in Fig. 5.18) during unloading. The hysteresis in the sample compressed to 6% strain is higher than that compressed to 3% strain (unloaded from a lower stress), so this effect is more pronounced in the former. Moreover, the amount of hysteresis (degree of slope on unloading) can be different in each reflection where different strain was applied (Fig. 5.18(b)).

Second, during loading, some struts in the foam may deform plastically (i.e. by dislocation movement or by detwinning), while adjacent struts (due to differences in size, shape, or orientation) remain elastic or stress-induced transformed. Since peak areas are not sensitive with elastic deformation, elastic strains were excluded and do not show any effect in Fig. 5.18. During unloading, the plastically deformed struts deform less than their elastic/transformed counterparts; if all deform to the same average strain, therefore, the plastic struts will unload to a lower stress, while the elastic/transformed struts will remain at a higher stress. In other words,

plastic struts will resist unloading of their elastic/transformed neighbors. In the case of NiTi with no plasticity, unloading corresponds to reverse transformation and the peak area follows the reverse trend on loading (if no effect from hysteresis). If large fraction of struts is going plastic, reverse transformation becomes quicker on unloading (or an unloading strain is less at a given amount of phase is reversed).

In the foam at low overall strain (3%), the number of plastically deformed struts is low, so there is relatively little effect on the rate of reverse transformation. In a heavily-deformed foam (6%), many more struts have become plastic, and their effect on the average phase state of the foam is greater. This foam shows more rapid reverse transformation upon unloading. However, after heat recovery, plastically deformed areas were not completely recovered and left residual unrecovered austenite and martensite.

Another possible cause of deviation in areas between unloading and loading is texture development which should be studied in the future.

## CHAPTER 6

**Additional Work on Porous NiTi Produced  
by Hot Isostatic Pressing****6.1 Improvement of interconnectivity in porous NiTi**

Pore connectivity is a critical aspect of architecture in porous materials which determines pore accessibility. In implant applications, it is pore connectivity, rather than the size of the pores themselves, which is considered the main limiting factor for osteoconduction [166]. Not only is a minimum pore size of approximately 100-150  $\mu\text{m}$  required, but windows connecting adjacent pores (hereafter, *fenestrations*) of at least 40  $\mu\text{m}$  width are necessary for the long-term health of bony in-growth.

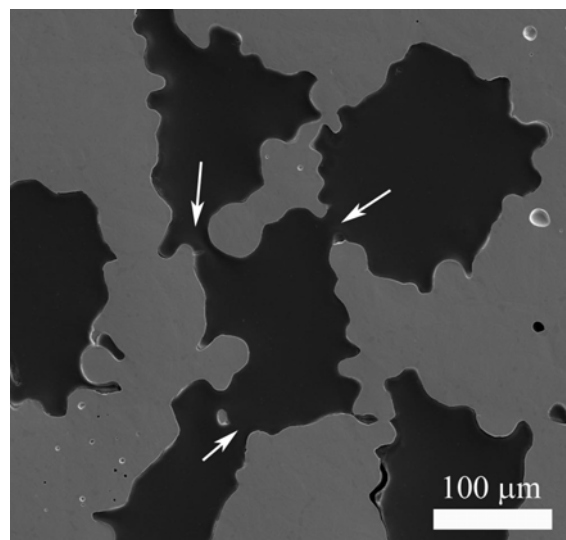


Figure 6.1 Microstructure of current NiTi foam (arrows indicate fenestration).

In this work, NiTi foams produced by HIP and the space-holder method (Chapter 3) have an average fenestration size (Figure 6.1) very near this minimum limit. Increasing fenestration size to maximize *in vivo* performance is therefore needed, while appropriate mechanical performance suitable for bone implants must also be maintained.

Fenestration size can be manipulated during foam synthesis, or afterwards (i.e., as a post-treatment). In the former approach, where space holder or porogen materials are used, control of fenestration can be achieved by ensuring a large contact area between adjacent particles, which results in high connectivity after the particles are removed. For example, the use of high aspect ratio, rod-like urea particles in producing porous hydroxyapatite results in highly-interconnected structures after urea burnout. The rod-like shape (200  $\mu\text{m}$  in diameter and 2 mm in length) provides a high probability of particle overlap, and as a consequence, average fenestration sizes of 120  $\mu\text{m}$  are achieved with acceptable compressive strength in the foam. Increasing the volume fraction of space holders in the mixture can also increase the number of contacts between particles; however, a significant effect on fenestration size is not guaranteed [80].

In the latter approach, used in the work described below, a post-processing dissolution step using acid or alkaline solution is applied to change the internal structure of the synthesized foams. Stirred aqueous NaOH solutions of pH 13 have been used, for instance, to decrease the density of low-density aluminum foams from 10% to 5% [167]. Ultrasonically-agitated 10% HCl solutions used in the removal of sodium aluminate space-holders from Ni-Mn-Ga foam showed a side effect on metal dissolution, leading to larger pores with thinner nodes and struts. An increase in foam porosity of 20% (from 55%) was observed after additional 24 hours in acid [168].

Although the purpose of these studies was mainly focused on increasing porosity, dissolution treatments seem to be quite a promising way to increase interconnectivity (fenestration size). Due to curvature dependence of corrosion rate, a window with high aspect ratio (fenestration) tends to dissolve faster than other areas (pore surface). Moreover, acid treatment could smoothen notch-like features (less stress concentration areas) and thicken surface oxide (more biocompatible). However, the acid, concentration, duration, and method of treatment must all be wisely selected in order to obtain more interconnecting porosity without jeopardizing mechanical properties. In specific, uniform (or as close to uniform as possible) metal dissolution rates should be ensured through out the porous structure. Uncontrolled, non-uniform removal rates can cause microscopically (i.e. pitting and grain boundary corrosion) and macroscopically (i.e., high porosity near sample surface and low porosity near sample core) non-uniform porous structures, leading to degraded foam properties and loss of dimensions. Well-controlled differentiated dissolution rates can, on the other hand, offer a gradient in porous structure of foams, which may be desirable for other reasons.

To design experimental conditions for the present work, factors which might affect the NiTi removal rate, specifically NiTi sample microstructure, acid bath (type/concentration/volume), and treatment details (procedure/duration), were considered.

#### NiTi foams

Two NiTi foams, with different pore structure but in the same range of porosity (32-39%), were used in the acid treatment studies to observe the effect of microstructure on dissolution behavior. NiTi foams made with NaF space holders (Chapter 3.1) have an irregular

pore structure with low to intermediate random connectivity, and foams made with NaCl (Chapter 3.2) have regular cuboidally-shaped pores connected by small fenestrations (~5 times smaller than NaCl particle size).

### Acid Type

Proper compatibility between the acid and NiTi can ensure a controlled, uniform NiTi removal without significant defect formation, e.g. through grain boundary attack or pitting. In this work, Keller's reagent (0.5 HF: 2.5 HNO<sub>3</sub>:1.5 HCl: 95.5 H<sub>2</sub>O, by volume) and several aqueous HF/HNO<sub>3</sub> solutions were used. Keller's reagent is a well-known etchant used in the preparation of Ti-alloy and NiTi samples to highlight grains and phases during metallographic observation [169]. Many variations of HF/HNO<sub>3</sub> solutions have also been used in the past, and for various purposes. HF:HNO<sub>3</sub> solution with 1:4 volume ratio, for instance, has been used to modify the physical and chemical surface properties (i.e., to achieve a homogeneous structure without corrosion, and to form a protective TiO<sub>2</sub> oxide layer) of NiTi foam implants before *in vivo* testing [170]. HF:HNO<sub>3</sub> solution with 1:20 volume ratio has been used in a pickling process to remove the oxide-rich surface films from NiTi stents [171, 172]. The surface layer removed in this pickling was in the range of 10-30 μm thick for durations of less than 30 minutes. Man et al [173] applied HF:HNO<sub>3</sub>:H<sub>2</sub>O solution of 1:4:5 volume ratio for selective etching of NiTi from NiTi/TiN composites, in order to make a three-dimensional TiN dendritic structure (i.e., an inverse NiTi network). About 30 μm of NiTi was removed in 30 minutes. Although the dissolution rate in these works are different, varying by the morphology of the NiTi surface being dissolved, it can generally be stated that up to 30 μm of NiTi can be removed in less than

30 minutes. If a similar rate is surmised here, the original fenestration size of NiTi foams in this work (~40  $\mu\text{m}$ , from qualitative image observation) could be widened to about 100  $\mu\text{m}$  within about one hour.

The metal dissolution rate in a real foam depends not only on the available surface area to volume ratio, but also the accessibility of the foam's internal surfaces to the acid. In general, high metal-acid contact area (i.e., high porosity, large pore surface area) and high acid concentration (specifically, the concentration of acid available for reaction in the foam interior) lead to an increase in metal dissolution rate. Conversely, if the acid cannot reach into some areas of the foam (e.g. the interior pores), or if it reaches into such areas only slowly (when compared to the dissolution rate itself), metal removal will vary by region, and the final foam structure will be non-uniform. High acid concentrations can give this result, significantly etching the exterior of the foam before the acid reaches the interior. Therefore, acid concentration should reflect a balance between aggressive but non-uniform dissolution, and lengthy but uniform dissolution. Here, the HF/HNO<sub>3</sub>/H<sub>2</sub>O acid solution was varied from concentrations of 0.5 to 10 parts HF with a constant ratio of 1HF:4 HNO<sub>3</sub> (i.e. 0.5 HF:2HNO<sub>3</sub>:97.5H<sub>2</sub>O to 10HF:40HNO<sub>3</sub>:50H<sub>2</sub>O) in order to strike such a balance.

#### Treatment conditions

To accelerate the acid-metal dissolution process, ultrasonic agitation was used and its effect was studied. As acid comes into contact with NiTi surfaces, NiTi is dissolved into the acid, and this can decrease the local acid concentration. Refreshing the NiTi-acid interfaces with new acid would minimize such concentration changes and gradients, and increase metal dissolution.

While ultrasonic agitation could keep acid locally fresh due to macroscopic acid circulation, it could cause micro-scale cavitation which prevents acid from penetrating into inner pores. Therefore, these contradicting effects of ultrasonic agitation are considered here. Different durations from 30 minutes to 3 hours were used in the acid treatment, to observe the dissolution behavior with time. The upper limit of the duration was set at 3 hours, to ensure the process remains practical and efficient.

### **6.1.1 Experimental procedures**

NiTi foams (ca. 0.5-1 g in mass and ca. 4x4x8 mm<sup>3</sup> in size) used in this study were made by identical HIP methods but with different space holders: NaF and NaCl, labeled NiTi-F and NiTi-Cl, respectively. To ensure that the foam interiors were properly penetrated by the solutions, foams were pre-wet via a series of soakings starting with 100% ethanol (which penetrates well, but which must be removed before the acid is introduced) and ending with 100% deionized water (which penetrates less efficiently, but is the necessary solvent for the acid). Each soaking step consisted of 10 minutes in an agitated ultrasonic bath, and the soaking bottles were shaken every 5 minutes to remove any bubbles displaced from the foam interior during penetration of the solvent. The foams were then stored in de-ionized water until acid treatment. It is further noted that the deionized water used in acid mixing and foam wetting steps was boiled before use, to remove any bubbles, and then kept in vacuumed container. Acid treatments, following the treatment conditions listed in Table 6.1, were performed in closed 45 mL polyethylene containers. The amount of acid used was approximately 30 mL per run.

Table 6.1 Summary of acid treatment conditions. Note: Keller's stands for Keller's reagent; 1 part HF stands for 1 part ratio of 1HF:4HNO<sub>3</sub> acid solution in diluting deionized water.

Sample	Foam	Initial mass (g)	Initial porosity (%)	Acid type	Time (min)	Change acid
1	NiTi-F	0.51	32.0	Keller's	122	N
13	NiTi-F	0.41	29.8	Keller's	60	N
14	NiTi-F	0.42	29.8	1 part HF	60	N
11.1	NiTi-Cl	0.50	29.5	Keller's	60	N
11.2	NiTi-Cl	0.47	29.5	1 part HF	60	N
4	NiTi-Cl	0.48	32.4	2 part HF	30	N
5	NiTi-Cl	0.43	31.5	1 part HF	90	N
6	NiTi-Cl	0.77	32.1	0.5 part HF	180	N
7	NiTi-Cl	0.67	31.9	1 part HF	180	N
8	NiTi-Cl	0.7	31.9	Keller's	180	Y
9	NiTi-Cl	0.9	32.5	0.5 part HF	180	Y
10.2	NiTi-Cl	0.41	29.8	1 part HF	130	Y
Control	Solid NiTi	0.34	-	1 part HF	20	N

After acid treatment, the samples were rinsed and then washed (3 times, 30 min each) with deionized water using an ultrasonic cleaning system. pH-sensitive indicator paper was used to verify the absence of any residual acid on the sample surfaces after washing. If a change of acid was required (such changes occurred every hour, when used), the used acid was poured out and fresh acid was poured into the same reaction container within 10 seconds.

The treated NiTi foams were characterized for mass loss, change in porosity, and microstructure, as described earlier in the standard procedures (Chapter 2.2). The best treatment was selected and used to prepare a representative set of NiTi foams to be subjected for further characterization. Image J software was carried out to evaluate porosity, average pore size and fenestration size in the foams before and after treatment. Compression testing (section 2.2) to failure was conducted using a 100kN load cell, to assess mechanical performance after treatment.

## Additional detailed procedures

Since Image J analysis was used to characterize NiTi foam only in this chapter, this additional part is dedicated to their detailed experimental procedure.

ImageJ is a free program from the National Institutes of Health (NIH), designed to analyze black and white images. ImageJ was used in this work to count the number of pores, determine the area of each pore (in pixels) and the average pore size, and distinguish between groups of pores having some average size. During ImageJ analysis, the images were modified from color to 8-bit black and white images via a user-defined intensity threshold. This threshold is selected from within the 0-256 grayscale range, and each pixel with intensity below the threshold value will be set to black, while each pixel above the threshold will be set to white. The desired threshold intensity is chosen to identify as many of the pores as possible. Different images may require a different amount or combination of manipulation, depending on the magnification, surface quality and flatness, and lighting conditions under which each was taken.

### **6.1.2 Results and discussion**

This section contains two main parts: 1) effects of the experimental variables on foam microstructure, for optimization of the acid treatment procedure; and 2) interconnectivity and mechanical properties evaluation of foams treated using the best acid treatment conditions.

### 6.1.2.1 Effect of experimental parameters on microstructure alteration

#### *Ultrasonic agitation*

The effect of ultrasonic agitation was evaluated for a NiTi foam made using NaF space holders (Sample 1). For the first hour, this sample was treated without ultrasonic agitation, and was washed and characterized for mass loss after 2, 7, 22 and 62 minutes in Keller's reagent. Then the sample was placed in an ultrasonically-agitated bath of the same solution, for one hour. The rate of mass loss was almost negligible without ultrasound, but increased significantly when the sample was placed under ultrasonic agitation. Consequently, agitation is necessary for the acid treatment, and was used for the rest of the experiments.

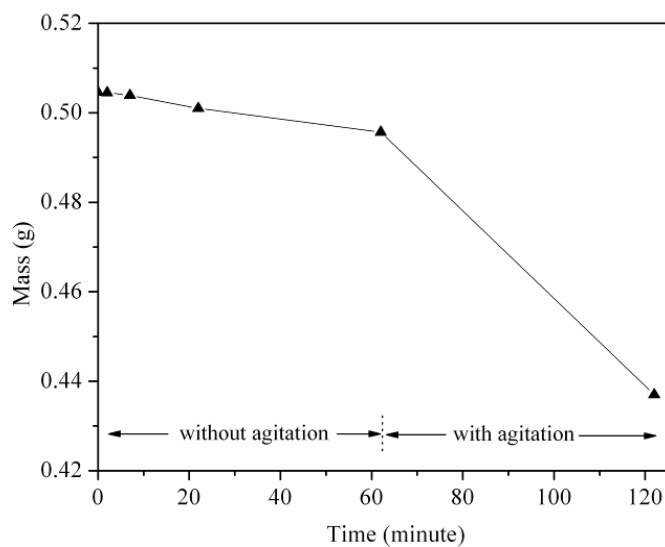


Figure 6.2. Mass loss versus time with and without ultrasonic agitation (Sample 1).

*Initial microstructures*

The microstructures of NiTi-F and NiTi-Cl samples, shown in Figures 6.3 (a and b) illustrate the difference in initial foam morphology. NiTi-Cl foam had a more uniform distribution of cuboidally-shaped pores and lower microporosity, in comparison to NiTi-F foam, while NiTi-F had greater initial connectivity (larger pore size, and thus fenestration size) and irregularly-shaped pores.

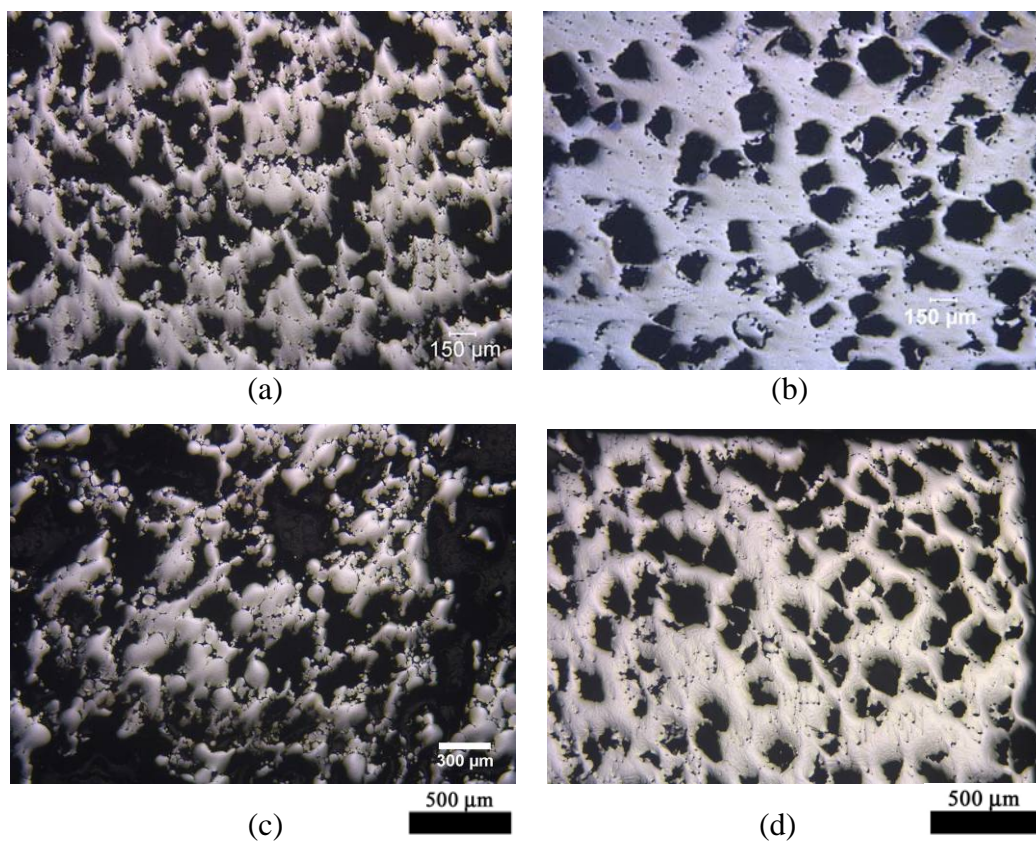


Figure 6.3 Microstructure of NiTi-F foams, Sample 13, (a and c) and NiTi-Cl foams, Sample 11.1, (b and d) before and after Keller's acid treatment for 60 min, respectively.

After treatment with Keller's reagent for 60 minutes, NiTi-F foam (Sample 13) achieved greater increases in porosity and percent mass loss (independent measurement, plotted in Figure

6.4) than NiTi-Cl foam (Sample 6.2). The higher accessibility and irregularity of the NiTi-F foam (which contains many sharp edges) seem to expose more surface with the acid, even in the innermost parts of the foam.

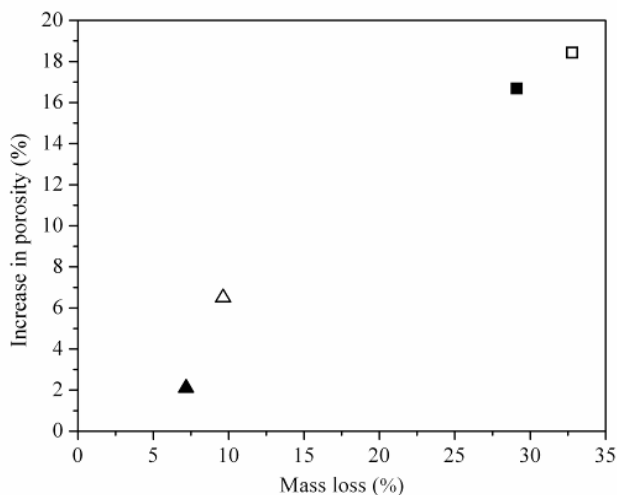


Figure 6.4 Effect of starting microstructure on mass loss percent and increase in porosity after 1 hours treatment. Squares represent NiTi-F foams (Sample 13 and 14) and triangles represent NiTi-Cl foams (Sample 11.1 and 11.2). Solid indicates Kellers's reagent and unfilled symbol indicates 1 part HF treatment.

However, loss of material (in the form of crumbling at the outer parts of the samples) caused by insufficient densification in the initial microstructures was observed for both foams, though it was more obvious in the NiTi-F foam. Poor sintering left undesirably high internal surface area for interaction with the acid. As a result, rapid metal dissolution occurred in the outer parts of the foams, before the acid could reach the inner parts, causing weakening in the outermost regions.

The non-uniform loss of material was found in the use of different acid (1 part HF) as well (Figure 6.5). This indicates that initial microstructure significantly affect acid pathways and thus metal dissolution.

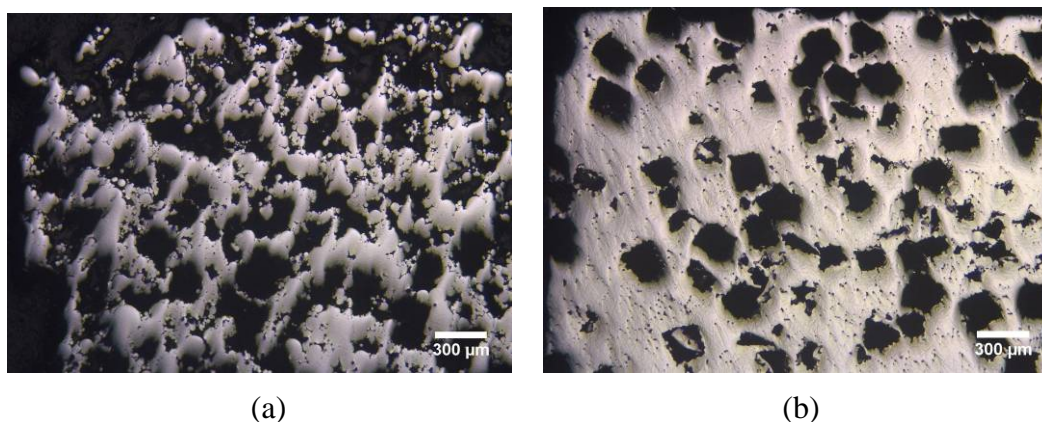


Figure 6.5 Microstructure of (a) NiTi-F foam (Sample 14) and (b) NiTi-Cl foam (Sample 11.2) after 1 part HF/HNO<sub>3</sub> acid treatment.

NiTi foams containing highly-interconnected pore structures and high densification within the NiTi struts are, therefore, recommended in the future to enhance the effect of acid treatment while minimizing damage. For example, NiTi foams should be sintered at high temperature (e.g. 1250°C) to further densify the NiTi struts before the acid treatment, or, if the foam is not already too damaged after treatment, sintering after acid treatment might be used to achieve a dense final NiTi structure. In the case of NiTi-Cl foams, initial connectivity should be improved to increase acid penetration, for example by changing to a less angular NaCl particle shape (and thus improving contact area between particles), or by using the transient liquid sintering approach described in Chapter 4.

*Acid type and concentration*

Two acid types - Keller's reagent and 1HF:4HNO<sub>3</sub> solution - were used in acid treatment trials with NiTi-Cl foams (foam mass ca. 0.4 g in each case). These foams were sintered at 1250°C for 10 hours before the acid treatment to: 1) improve densification in the NiTi structure, so that dissolution was more localized in fenestrations and less prone to causing NiTi particle pullout from the struts; 2) ensure a more complete removal of salt from the foam; and 3) remove oxide layers on the NiTi surfaces so that the acid could react directly with fresh metallic NiTi.

For 1HF:4HNO<sub>3</sub> solution, different ratios (0.5 -10 parts) of acid solution in diluting deionized water were applied. A practical limit was found at 3 parts HF, where the treated foam was severely damaged and bubbles were evolved rapidly from the corrosion reaction. For this reason, choices of 1HF:4HNO<sub>3</sub> solutions were subsequently limited to 0.5, 1 and 2 parts HF concentration. The percent mass loss versus percent increase in porosity after treatment with Keller's reagent (Sample 11.1), or with 0.5 (Sample 6), 1 (Sample 5, 11.2) and 2 (Sample 4) parts of 1HF:4HNO<sub>3</sub> solution at various times is shown in Figure 6.6.

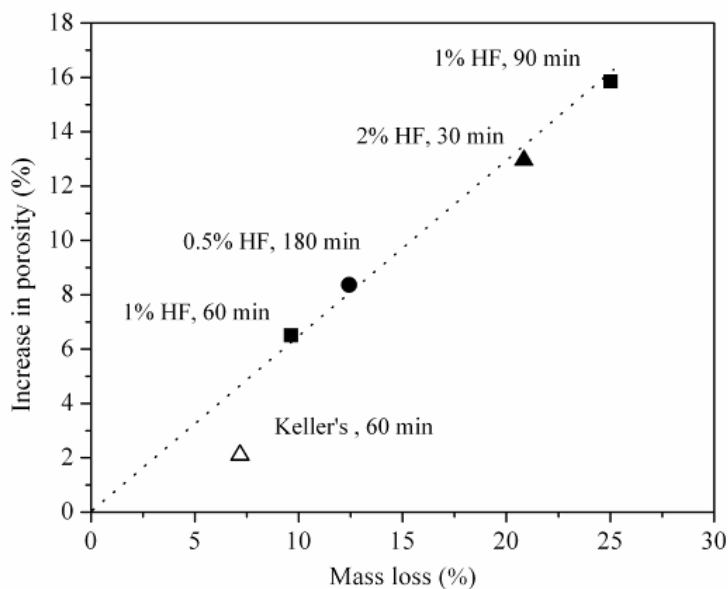


Figure 6.6 Effect of acid type and concentration on foam porosity.

The ratio of percent mass loss to percent increase in porosity was the same for all 1HF:4HNO<sub>3</sub> solutions, regardless of concentration. Compared to these, Keller's reagent gave a lower increase in porosity for a given percent mass loss, which suggests loss of outer dimensions (i.e., damage by crumbling). Among the 1HF:4HNO<sub>3</sub> solutions, 2 parts HF offered attractively high mass loss and porosity changes in a relatively short time (30 minutes). However, fragile surfaces were observed on this foam after treatment (Figure 6.7), which indicates a higher dissolution at the outside the foam than the inside. In contrast, treating with 1 part HF for 3 times longer (90 minutes) provided comparable percent mass loss and increase in porosity with a more uniform structure. A similar structure was also found in foam treated with 0.5 part HF, but with only a small change in porosity after a lengthy treatment time (180 min).

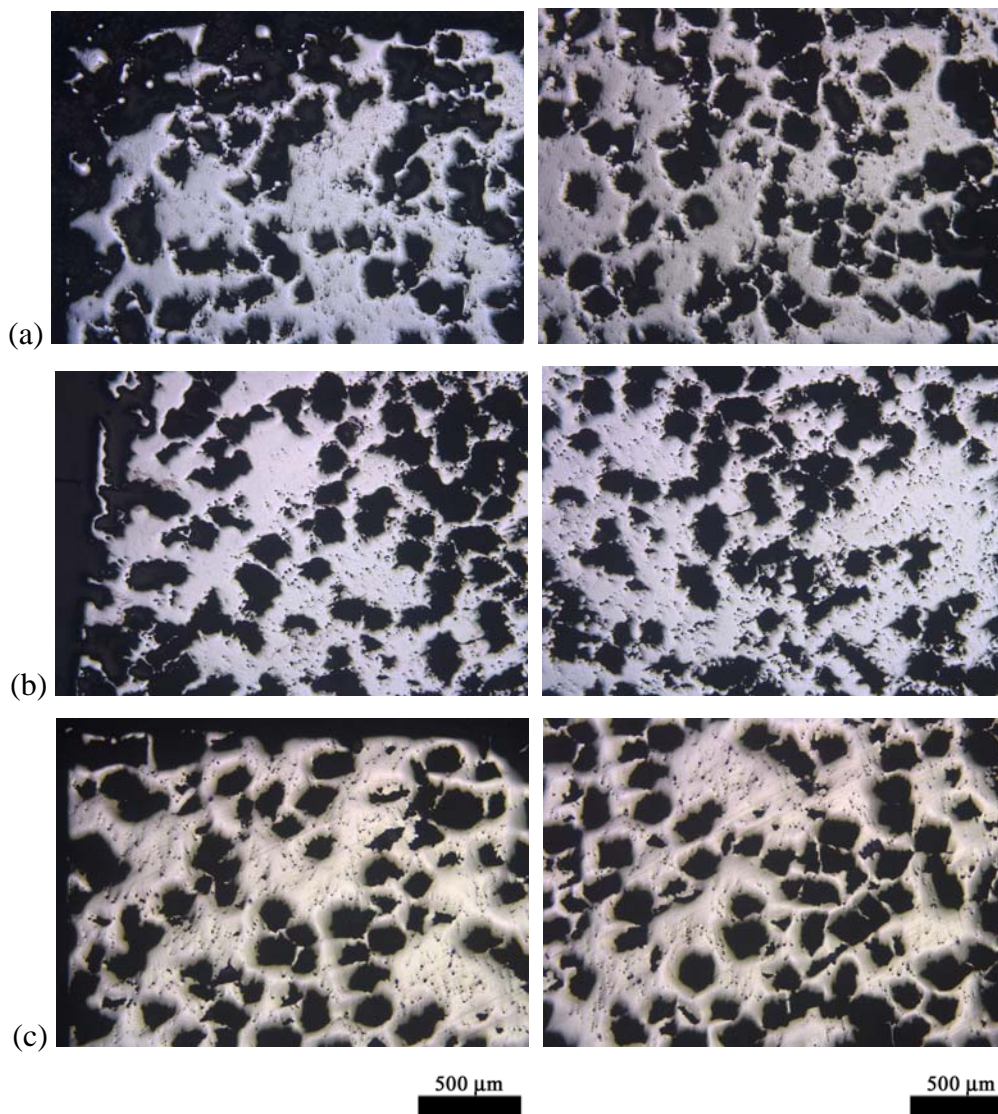


Figure 6.7 Microstructure of foam treated by (a) 2 part HF for 30 min (Sample 4), (b) 1 part HF for 90 min (Sample 5), and (3) 0.5 part HF for 180 min (Sample 6).

Gas bubbles are one of the indicators of process efficiency. Bubbles can be formed as a product of the metal-acid reaction. For example, HF decomposes to  $H^+$  and  $F^-$  in solution, after which  $F^-$  reacts with metal (+) ions, resulting in corroded metal and leaving  $H^+$  at the reaction sites, which can recombine into gaseous hydrogen. Whether this byproduct will retard the dissolution process or not depends on how fast it is produced and how fast it can be removed from the foam. If gas bubbles are produced quickly and cannot be removed quickly enough, they

can stay in or at the openings of pores and mechanically prevent further penetration of the acid towards interior pores (a situation called vapor lock). In addition, the buildup of  $H^+$  in this case lowers the concentration gradient locally, and chemically slows down dissolution. In the case of low  $H^+$  production, by contrast,  $H^+$  will diffuse away slowly from the surface without forming bubbles.

It was observed that Keller's reagent produced gas bubbles earlier and in greater amounts than the other solutions. This might be an effect of HCl, which is a strong acid and has high level of dissociation in water (significantly higher than HF), such that more  $H^+$  ions (more bubbles) are produced in solution. Therefore, foams treated with Keller's reagent showed weak outer foam structures. Using low acid concentration slows dissolution rates and reduces byproduct generation rate, allowing a more uniform foam structure after treatment. However, insufficiently low concentration might delay the dissolution process and might cause tint etching, wherein the metal can passivate and form a stable oxide. In this work, 1 part HF was more promising than the other solutions as a way to simultaneously increase porosity and achieve uniform porous structures in a short amount of time.

Some steps prior to or during the acid treatment could also affect the dissolution process. The pre-wetting steps before acid treatment (described above) were expected to reduce vapor lock by displacing air trapped in the pores before the treatment, and thereby assisting the acid in accessing pores during the treatment. As a suggestion for future work, infiltration of acid into foams using vacuum might be another way to allow metal dissolution throughout the porous structure and without the interference of gas bubbles.

### *Treatment time and changing acid*

Under identical conditions (1 part HF for 3 hours using ultrasonic agitation), NiTi-CI foam (Sample 10.2) treated with acid refreshed every hour showed a higher ratio of porosity change to mass loss than foam (Sample 7) treated without acid refreshing (Figure 6.8).

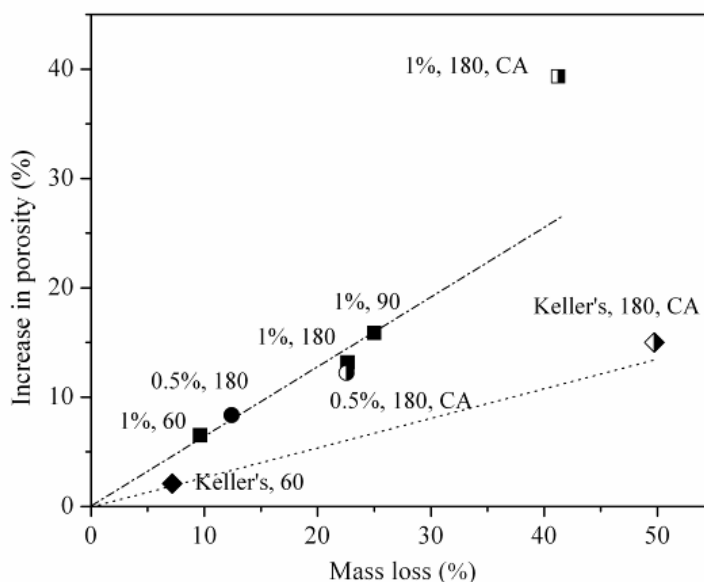


Figure 6.8 Effect of changing acid and time. Data set is labeled in term of (acid type, treatment time, changing acid). CA stands for changing acid.

Indeed, foam treated without refreshing showed almost the same percent changes as foam treated with the same acid (1part HF) but half the treatment time (Sample 5, shown in the previous section). This implies that treatments without acid refreshing reached a plateau behavior characterized by a slow dissolution process. Since the amount of acid in each bath is sufficient for a complete dissolution, this saturation phenomenon might come from diminished driving force behind the reaction. This could, in turn, result from a change in acid pH, or a diminished

concentration gradient at the metal surfaces. A similar result was also observed in treatment with 0.5 part HF, though the effect was smaller. Refreshing the acid helps remove depleted metal from the surface, and replaces it with a fresh metal-acid surface that maintains a high concentration gradient. For this reason, refreshing the acid should have a greater influence on the dissolution process than increasing acid volume, and furthermore, treatment duration should be important only within a short period after the treatment starts. However, it should be noted that acid refreshing could accelerate excessive change in dimension in the treatment with Keller's reagent (Sample 8).

The effect of time can be determined if new fresh acid is continuously run through the pores, where the driving force of dissolution by concentration gradient exists. With regard to this, a similar setup to permeability testing [174] is suggested as one future approach. To promote penetration of the acid through the porous structure using pressure, a foam will be inserted tightly into a polyethylene tube and then flushed with acid by gravity. In this way, fresh acid will be in contact with pore surfaces at all times, the permeability of acid through the pores can be measured continuously, and evolved gas bubbles could be continuously flushed out to the air.

Representative images of foams treated with various acids (Sample 8, Sample 9, and Sample 10.2) and acid refreshing methods (the best condition to improve porosity) are shown in Figure 6.9. Non-uniformity in microstructure, i.e. larger and more connected pores at the edges of a sample than in the center, was shown in all cases. Keller's-treated foam showed the greatest difference between exterior and interior (Sample 8, Figure 6.9(a)), with a mass loss of 45% and a porosity increase of 15%. The outer edges of this foam completely crumbled away, and the remaining pores close to the edge did not show significant improvement. 1 part HF-treated foam

showed pores near the corners which were larger and had a smoother appearance (Figure 6.9 (b)). The outside edges were still intact, and the corners were still square, in contrast to the jagged edges of Keller's-treated sample (Figure 6.9 (a)). The 0.5 part HF-treated sample experienced a 22% mass loss and a 12% increase in porosity. Although the pores on the edges showed connectivity and, like the 1 part HF treated foam, had smoother edges, 0.5 part HF required a longer time to achieve the same porosity increase than did 1 part HF. The microstructure of foam treated by 1 part HF solution (without refreshing the acid) is provided for comparison. Stability of sample dimensions was observed in the foam treated in changing acid method even though high porosity was obtained. Therefore, using 1 part HF with acid refreshing for treating NiTi-CI foams seems to be the best dissolution condition, and was chosen for making representative foams for interconnectivity and mechanical properties evaluation.

The dissolution rate of solid NiTi (HIPed without space-holders) in 1 part HF acid was determined to be 52  $\mu\text{m}/\text{hour}$  and  $1.71 \times 10^{-10} \text{ g}/\mu\text{m}^2/\text{hour}$ . The dissolution rate of the treated foam was calculated as 5.3  $\mu\text{m}/\text{hour}$ , or  $1.75 \times 10^{-11} \text{ g}/\mu\text{m}^2/\text{hour}$ . This shows that the dissolution rate in NiTi foam was about 10 times slower than dense NiTi, even accounting for higher surface area.

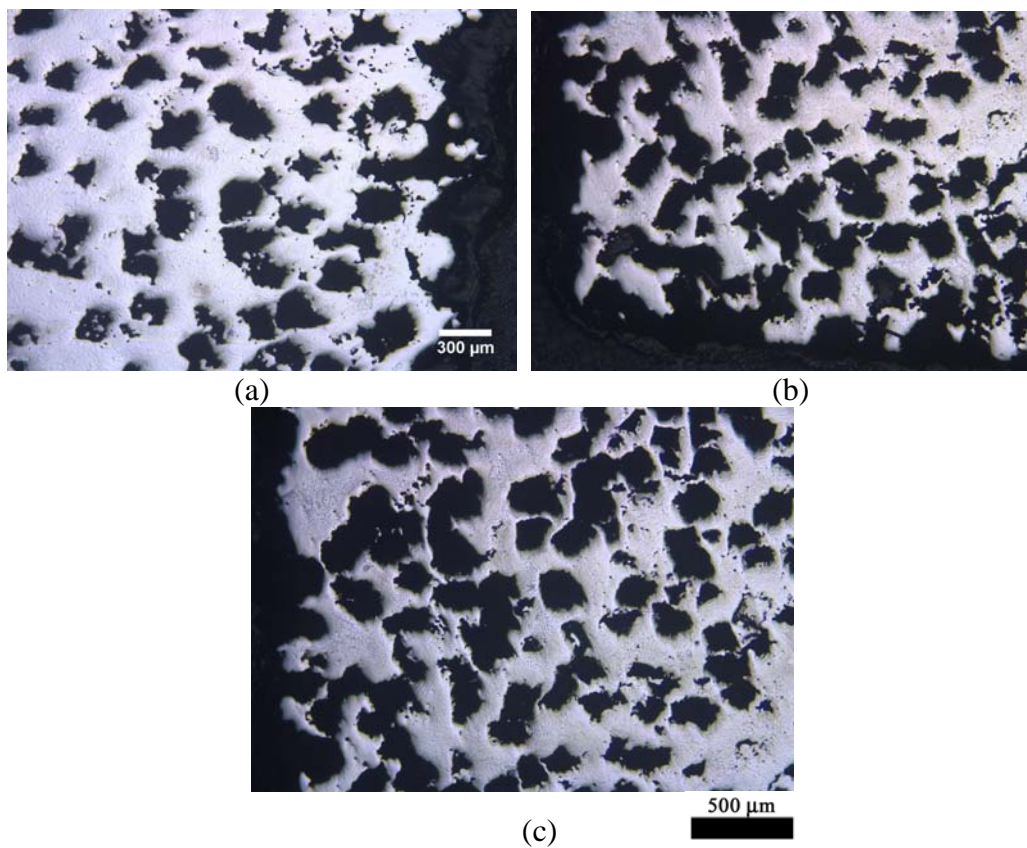


Figure 6.9. Microstructure of foams treated by Keller's reagent (Sample 8) (a), 1 part acid (Sample 9) (b), and 0.5 part acid (Sample 10.2) (c) with changing acid method for 3 hours. Left side presents an image at center and right is an image at edge of the treated foam.

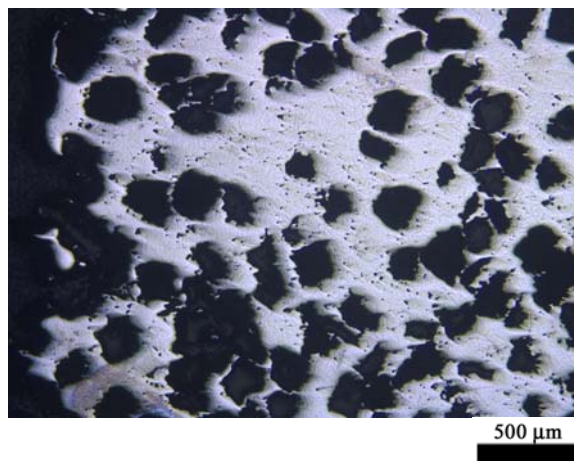


Figure 6.10. Microstructure of foams treated by 1 part acid for 3 hours without changing acid. (Sample 7).

### 6.1.3 Properties evaluation of treated foams

This section provides an evaluation of NiTi-CI foams treated with 1 part HF acid with periodic acid refreshing, in term of interconnectivity/fenestration and mechanical behavior. Since the samples needed for these tests ( $>4 \times 4 \times 8 \text{ mm}^3$ ) were larger than the standard samples ( $4 \times 4 \times 5 \text{ mm}^3$ ) used above, the acid treatment method was slightly adjusted to ensure the smallest gradients in dissolution depth/microstructure and the greatest stability in foam dimensions. Foams of  $6 \times 6 \times 12 \text{ mm}^3$  were treated with acid for 2 hours, refreshing once (i.e., every hour). As-HIPed NiTi-CI foams were used as control samples for all tests.

#### *Interconnectivity evaluation*

ImageJ analysis from 2D optical micrographs was used to evaluate pore size and interconnectivity. Figure 6.11 shows the accuracy of conversion of a control sample micrograph into a black and white version for ImageJ analysis. Ten images of the control sample and four images of the treated sample (Sample 7) were used in the analysis.

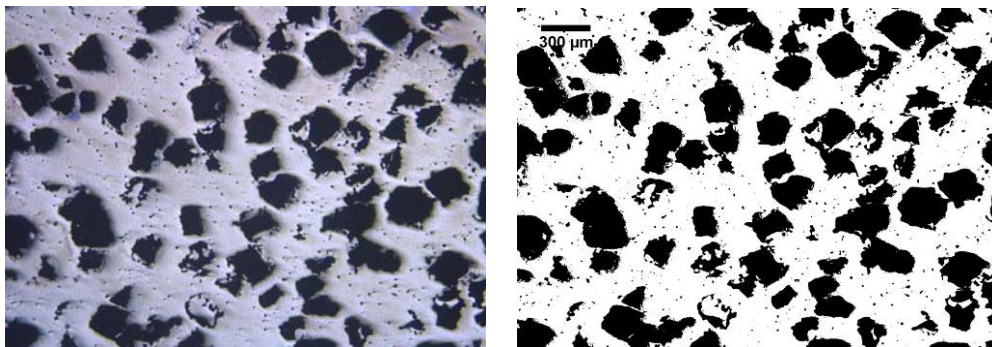


Figure 6.11 Comparison of an optical micrograph (left) and Image J black and white image (right) of a control sample.

The control sample had an average pore area fraction of 32.3 % and count of 94 pores, while the treated sample had an average pore area fraction of 45.5 % porosity and a count of only 56 on the same total image area ( $\sim 3.6 \times 3 \text{ mm}^3$ ). The decrease in pore count and increase in porosity can be contributed to merging of individual pores to create pore networks. In addition, the average pore diameter (calculated from average pore area) showed that the mean pore size is increased (from  $150 \pm 81 \text{ }\mu\text{m}$  in control sample to  $228 \pm 67 \text{ }\mu\text{m}$ ), which suggests that the increase in porosity was likely caused by acid-dissolved fenestration material.

### *Mechanical evaluation*

The maximum strain (before failure) for the control sample (32% porosity) was 58.0%, and the maximum strain for the treated sample (40% porosity) was 55.5%. In addition to surviving large strains, both foams carried large stresses of 1855 MPa and 1125 MPa, respectively (Figure 6.14), and have low apparent stiffness (quasi-linear behavior upon loading) of 3.1 GPa and 1.9 GPa, respectively. The compressive strength and stiffness of the treated sample are lower than those (with the same porosity,  $\sim 40\%$ ) produced by the transient liquid sintering approach (1600 MPa, 2.2 GPa) in Chapter 4, but still remain in a suitable range for bone implant applications. Since the foam was compressed until failure, the stiffness upon unloading (which reflects the stiffness of NiTi without the effect of detwinning) was invalid. Therefore, a comparison with theoretical value of stiffness calculated from the Gibson and Ashby equation is not attempted. However, the scaling law of stiffness with porosity is preserved for foams produced by transient liquid sintering and foams treated with acid. In specific, the ratio of loading stiffness in both kinds of foam at 32% porosity and  $\sim 40\%$  porosity is very similar (1.6

for the former, 1.8 for the latter). This suggests the effect of acid on foam microstructure did not deteriorate mechanical function in the NiTi struts, though more data are needed to substantiate this conclusion.

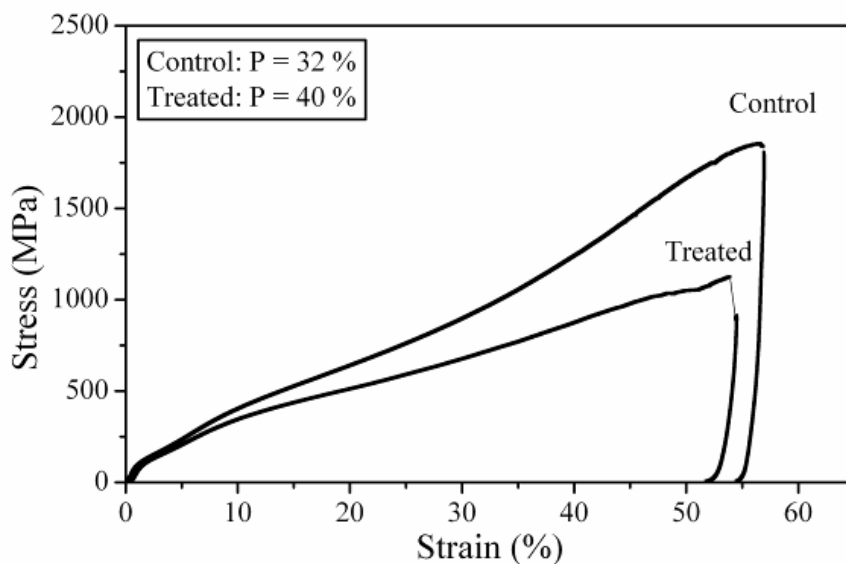


Figure 6.12. Stress-strain curves of control sample (32% porosity) and an acid treated sample (40% porosity).

#### 6.1.4 Conclusions and suggestions

Acid post-treatment proved capable of altering the microstructures of NiTi foams toward higher porosity and larger fenestration size, while maintaining mechanical performance in the range needed for bone implant materials. The higher interconnectivity of acid-treated foams will be useful for tissue and bone ingrowth, preventing loosening, and retaining dynamic strength in implants. The effects of the key acid treatment variables have been evaluated, and the best acid

concentration was found to be 1 part 1HF:4HNO<sub>3</sub> acid solution under ultrasonic agitation, and with periodic refreshing of the acid bath. An increase in porosity of 10%, and in fenestration size of ~20 μm, were achieved in 2 hours of treatment for a foam with initial porosity and fenestration of 32% and 40 μm, respectively.

Future work should focus on further increasing the fenestration size, and on improving the uniformity of the porous structure after treatment. Optimization of acid treatment seemed to be progressing toward low concentrations and a continuous flow of acid. Three-dimensional micro-tomography would be a promising approach to observe pore interconnectivity non-destructively in the future.

## 6.2 Tomographic analysis and modeling of porous NiTi

Materials design has become increasingly dependent on simulations and computational analyses to predict material behavior, with the result that materials or products having desirable properties are being developed in less time and for lower cost, with less need for expensive (and destructive) experimental testing. In order to apply computational design of materials specifically to improving mechanical properties, the interactions between microstructural features and applied loads must be understood. In the context of porous materials, the microstructural features of note include pore fraction size, morphology, and connectivity. If the impact of these features can be properly simulated and predicted, porous materials can be engineered for optimal microstructures and behavior to produce superior products.

Finite element (FE) analysis is one of the most popular analysis tools for exploring the relationships between intrinsic material properties, material structure or architecture, and overall mechanical behavior. FE simplifies the analysis of complex materials by subdividing (tessellating, or meshing) them into many smaller and simpler interdependent sections (elements), which deform in accordance with constitutive laws and laws of conservation. These laws give rise to differential equations which, under prescribed boundary conditions of force and/or displacement, can be solved to predict the deformations of the elements, and thus of the material or body as a whole.

Although the geometries and surfaces of the material bodies subjected to FE analysis are often idealized, FE can also be applied to 3D representations of real bodies. In order to produce

accurate simulations from such representations, however, high-accuracy visualization is required. Various 3D characterization techniques, such as microtomography and serial-sectioning, can provide such visualization, and high computing power now makes it possible to process large volumes of data from these methods for 3D representation. Three-dimensional representation of data provides valuable insights into material structure and composition which cannot be accurately captured with 2D images. One insight which can contribute to this work, for example, is quantitative analysis of pore connectivity.

Among the available 3D visualization methods, microtomography is usually favored because of its non-destructive nature. During microtomography, a series of radiographic images is taken of the sample (in the context of metals, these are usually x-ray radiographs) as it rotates about an axis normal to the incident radiation. These images are subjected to a 'reconstruction' algorithm which transforms them into a stack of cross-sectional images representing the sample at various points along the axis of rotation (i.e., similar to the stack of images achieved by destructive serial sectioning). From these cross-sectional slices, a high-resolution 3D representation of the material and its microstructure can be computationally 'rendered' and analyzed. That is, a voxel-based representation of the material is built up from a collection of pixel-based representations.

This digital image-based modeling technique was first proposed by Hollister et al. [175] for modeling the porous microstructure of human bone. It was applied to mechanics, failure prediction, and generally towards an understanding of progressive bone structure weakening. Similar techniques have since been used for evaluation and prediction of the mechanical and structural properties of other porous materials, for example, porous stainless steel,

hydroxyapatite, titanium scaffolds, and lotus-type porous carbon steel in tension and compression [176].

For porous NiTi, finite element models based on three-dimensional reconstruction from quantitative computed tomography (QCT) scans have been used to investigate morphological properties [177], calculate active surface area [178], and evaluate bone density in porous NiTi interbody fusion devices [179]. However, relatively little finite element research has been geared towards detailed investigation of the mechanical behavior of porous NiTi.

The general goal of this investigation was to develop and validate microtomography-based three-dimensional FE models of porous NiTi, and use these models to predict mechanical and strain recovery behavior. More specifically, the goal was to: 1) render microtomography images as 3D volumes that could be used as FE models; 2) determine the morphological and material property parameters that produce the closest agreement in mechanical behavior between experiments and these models; and 3) determine the ability of FE models to subsequently predict the experimental properties of porous NiTi.

The foam used in the investigation was foam HS2, whose mechanical properties were described in Chapter 3.2. This foam was scanned using a micro-CT system (Skyscan 1172; Microphotonic, USA) with 3  $\mu\text{m}$  isotropic resolution (i.e., a voxel size of  $3 \times 3 \times 3 \mu\text{m}^3$ ). The scan consisted of 1000 slices along the axis of rotation, corresponding to about 3 mm.

FE modeling was conducted by Michele Panico and Professor L. Catherine Brinson of the Department of Mechanical Engineering, Northwestern University. What follows is a summary of this modeling work, based on the 2008 doctoral dissertation of Michele Panico.

Using the series of reconstructed 2D cross-sectional images (Figure 6.13(a)) provided by the micro-CT, the commercial program AMIRA was used to identify the surfaces of the foam

(external as well as internal, or pore, surfaces), and to represent these using a 3D triangular mesh (Figure 6.13(b)). AMIRA's meshed surfaces were then converted into a 3D solid model (Figure 6.13(c)) using the ABAQUS CAE processor, and this model was tessellated using tetrahedral elements based on the triangular surface elements.

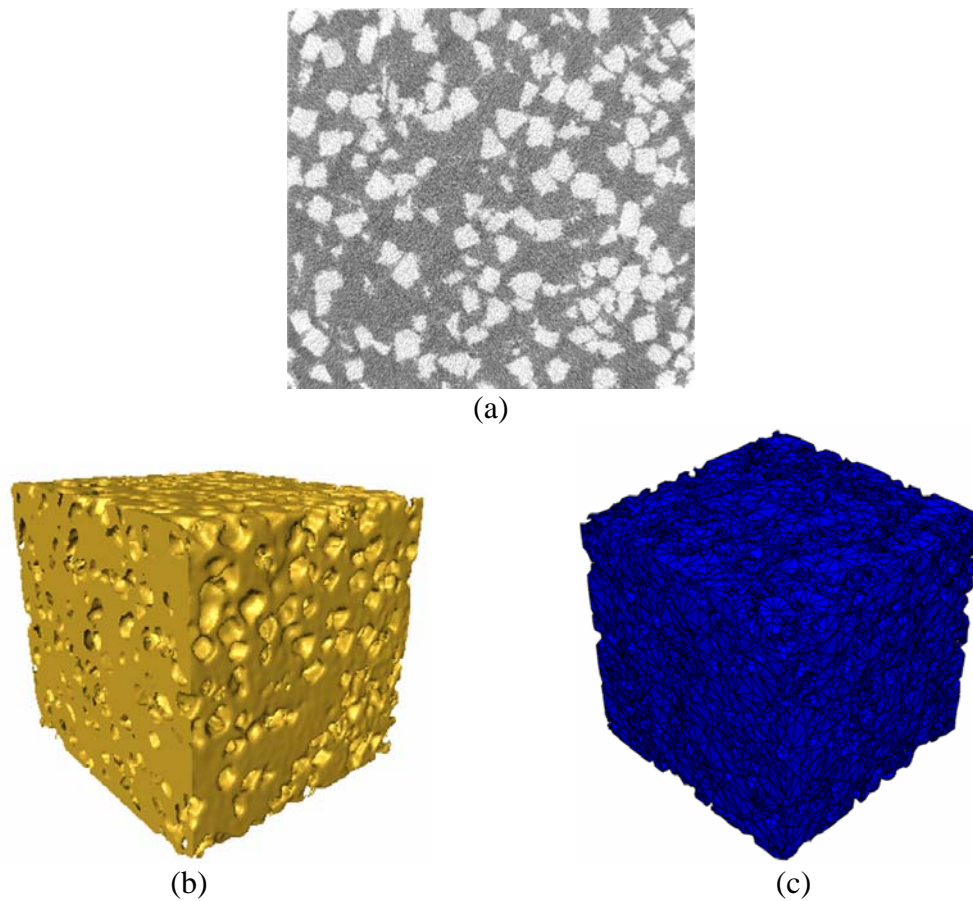


Figure 6.13. Stages in the modeling of foam HS2 based on microtomographic image analysis; (a) 2D cross-sectional image from microtomography, showing solid (black) and pore (white) space; (b) 3D surface reconstruction from AMIRA; and (c) 3D solid model showing a full finite element mesh.

The resulting model was found adequate for quantifying most of the important pore structural features, except for the surface roughness of large pores and the existence of small porosity. Both these are thought to reflect the finite resolution and contrast of the microtomography, exacerbated by AMIRA's finite triangulation of the surfaces. As a result of these infidelities, the model contained mostly large, open pores, and porosity was lower than the experimental value. Despite them, it was proven that the 3D solid model could more accurately simulate the initiation and evolution of phase transformations (i.e., martensite to detwinned martensite) than a plane strain 2D model, on account of having more information in the third dimension.

Mechanical behavior assessment for foam HS2 during load-unload-heat recovery cycles was done using the FE model for low maximum loading strains of 1% and 2%, and these were compared to the experimental results. As described in the dissertation: "The material parameters used in the simulation were calibrated to reproduce the characteristic transformation temperatures of the foam and the experimental stress-strain behavior for the cycle with 1% applied strain. The following simulation sequence is adopted: i) 1% macroscopic strain is applied on the top surface of the sample; ii) the strain is released and the material is unloaded; iii) the model is heated to 127°C in order to produce reverse phase transformation; iv) the room temperature 25°C is re-established; v) the same process is repeated with an applied macroscopic strain of 2%."

During the first loading cycle, detwinning was found to initially diffuse throughout the whole foam, and then become more localized around areas of stress concentration. The engineering stress and strain during the second cycle, taking into account strain hardening, were also predicted (Figure 6.14). The total residual strain from irreversible martensite formation and

plasticity in the foam was well predicted after this cycle. However, the non-linear unloading phenomenon could not be reproduced within the model framework.

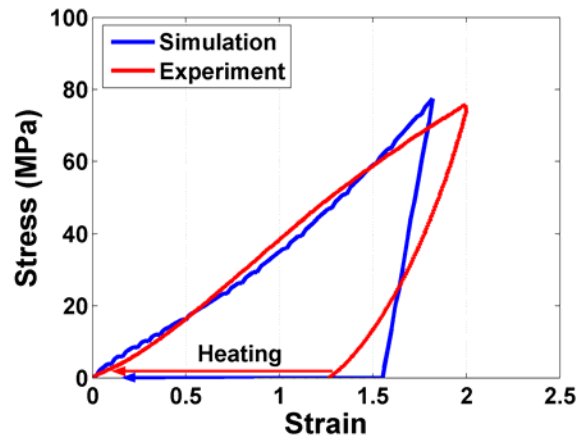


Figure 6.14. Comparison of stress-strain curves of foam HS2 from experimental testing and FE simulation for maximum strain of 2%. (Courtesy of Panico and Prof. Brinson).

Phase transformation behavior (represented by the volume fraction of detwinned martensite) as a function of strain and temperature was also predicted (Figure 6.15). Upon loading to maximum strain of 2%, the average volume fraction quickly increased as a consequence of the low initial material hardening, and then increased more slowly at higher strain (Figure 6.15). Moreover, the transformation finish temperature increased as a higher maximum strain was applied (Figure 6.16).

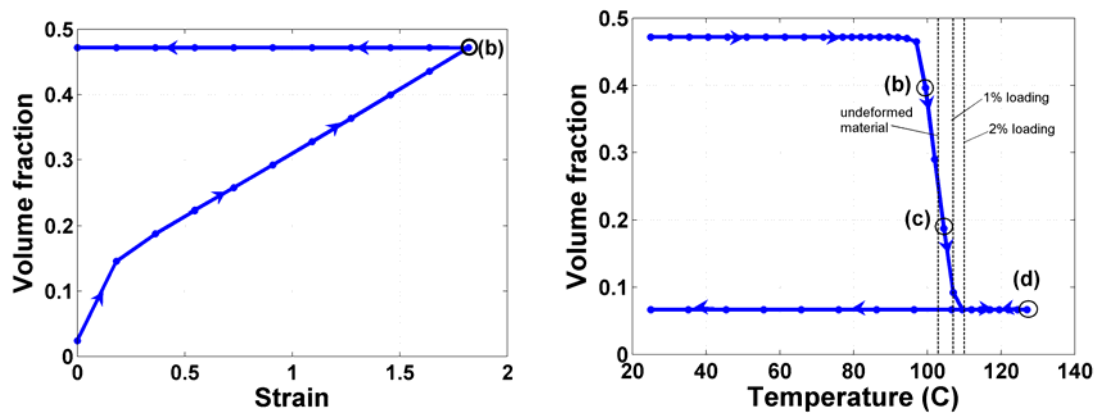


Figure 6.15. Volume fraction of martensite as a function of strain and temperature.

## CHAPTER 7

### **Conclusions, Anticipated Benefits and Future Work**

Brief summaries for each experimental method, and the conclusions drawn from work using those methods, have already been provided in the appropriate chapters. In the first section of this final chapter, those summaries are briefly recounted; in the second section, they are placed into the context of the literature so that the impact of this work within various related fields can be evaluated. In the final section, suggestions are made for future researchers who may want to fill in gaps left by this and other work.

#### **7.1 Summary**

Integration of the temporary space-holder method with powder metallurgical techniques based on pre-alloyed, near-equiatomic NiTi were demonstrated in the foregoing chapters, through fabrication of porous NiTi having high-density NiTi cell walls or struts and controllable open-cell porosity.

Hot isostatic pressing (HIP) was utilized to densify NiTi struts in the presence of salt space-holders (NaF or NaCl), followed by a salt removal process. Martensitic porous NiTi containing interconnecting pores (near-replicated space-holder geometries), pore sizes of 100-400  $\mu\text{m}$ , and porosities of 32-40% (90% open-pore ratio), were successfully made. The compressive load-bearing capacities of these foams could be as high as 1185 MPa at strains of

55%. High recovery strains of more than 4% upon heat recovery and 2% upon unloading were observed. The stiffness of the foams was in the range of 10-20 GPa, which is close to that of cortical bone.

Subsequent sintering (at temperatures above the limits of the HIP process) was shown to further optimize densification in the NiTi structure. Higher Ni contents and higher volume fractions of space-holder could be applied directly to the technique (although the method was originally demonstrated using porous shape-memory NiTi) to create low-density, low-modulus, superelastic NiTi foam.

With the help of melting point depression from Ni, Ni-rich (50.8-51 at% Ni) NiTi foams could also be produced by single-step conventional sintering with NaCl space-holders (and without an additional salt removal step). Appropriate heat treatments could bring out superelastic behavior in the foams at body temperature, and shape-memory behavior at room temperature. NiTi foams produced by extended sintering contained similar porous structures and exhibited comparable mechanical properties and shape recovery effects to those made by HIP processing. However, microporosity in the NiTi struts was observed due to insufficient densification.

To overcome the slow solid-state diffusion in conventional sintering, an alternative, cost-effective, single-step technique was developed by combining NiTi-Nb transient liquid phase sintering with the NaCl space-holder method. Addition of Nb enhanced the densification of NiTi struts (eutectic NiTi-Nb improved sintering by penetrating through capillary paths between NiTi particles), without significant modification of the salt-replicated pore macrostructure. Only slight decreases in shape recovery effects were observed, and comparable mechanical properties, including high ductility, were maintained.

To study the possibility of modifying foams toward structures more optimized for bone implant applications, acid treatments were used to widen fenestration sizes. Attempts to understand structure-mechanical property relationships using tomography-based modeling were made. Additional detailed suggestion upon each finding was provided at the end of each chapter.

## **7.2 Anticipated benefits**

The most significant contribution of this work, from the standpoint of porous metals research, is its utilization of both solid (NaF) and, for the first time, molten (NaCl) space-holders. Molten space holders offer significantly greater flexibility in processing, relative to pre-existing solid-place-holder methods, by enabling cheaper and more soluble space-holder materials to be applied in foaming technologically-important high-melting materials. They may find particular use in foaming metals for which, in past work [124], insoluble refractory space-holders were used which required the use of time-consuming acid leaching.

From the standpoint of porous implant materials in particular, the major contribution of this work is its demonstration of precise control over foam geometrical parameters, such as pore fraction, size, and geometry, which are crucial to the performance of porous implants. None of these parameters, as they appear here, lay outside the ranges achieved by previous methods, and most previous methods show a degree of control over one or more important foam parameters. But unlike these methods, the methods developed here offer a high level of control over many parameters simultaneously. Given the restrictions in pore structure imposed by use of a material

for bone replacement, it is expected that this higher level of control will prove attractive in this particular application.

A third and final anticipated benefit, which applies both to porous materials in general and to porous implants in particular, arises from the transient liquid phase sintering work of Chapter 4. Although this work is essentially a combination of prior transient liquid phase sintering knowledge with the space-holder method, it established the (perhaps surprising) fact that transient liquid phase sintering can be performed on structures which contain a high fraction of large pores. In other words, it demonstrated that, at least in the case of Nb-NiTi, infiltration of a liquid phase between the particles of an undensified foam matrix is not accompanied by filling of the liquid into the larger pores left behind by an evaporated place-holder. This fact can presumably be exploited in other systems as well, allowing good densification of powders in a foam using low temperatures, and without destroying larger pores created earlier in the process (for instance, by an evaporated place-holder).

It is on these three points that the uniqueness and interest of the work described here rests. However, many new opportunities have arisen in the course of this work which can be fruitful areas for future study. Before concluding, therefore, it is appropriate to point some of these out.

## **7.3 Suggestions for future work**

This section consists of two parts; the first part suggests areas for future work which build directly on the techniques described here, and the second suggests potential future work in porous NiTi using techniques beyond the scope of this work.

### **7.3.1 Methods arising from this work**

The suggestions collected from earlier chapters and presented here are mainly based on optimization of current processing methods and finer tuning of the microstructure and properties of porous NiTi toward bone implant requirements. In general, producing porous NiTi with higher porosity (60-80%), higher interconnectivity/fenestration size, superelasticity at body temperature, and lower stiffness will be goals for the next generations of NiTi foam. To approach this goal, specific recommendations for each technique are given below.

#### **7.3.1.1 HIP processing using the space-holder method**

The HIP process used here is close to an upper limit of temperature (1065°C) at which reaction between NiTi and HIP steel canister can be expected. Coatings or interlayers (for instance, Mo foil) at the interface between the powder and canister could push this upper limit to higher HIP temperatures. This could be useful for single-step densification of NiTi with high salt content, and without the need of subsequent sintering.

High volume fractions of salt (50-70%) should also be used for this future work; however, a study of powder mixing and loading into the HIP canister must be done to ensure the

uniformity of the final structure, especially with larger products. Different salt particle shapes (such as spherical or elongated particles) should be studied as well, and acid treatment of the resulting foam should be optimized, in order to increase the interconnectivity between pores. Mercury porosimetry should be used to evaluate the permeability of the foams and correlated to 3D tomographic data, which is an important aspect to encouraging bone ingrowth.

In addition, a method for removing HIP canister from the consolidated composite (for instance, selective electrochemical dissolution) should be developed to minimize the time spent on multiple and lengthy diamond saw cuts. Finally, Ni-rich NiTi mixtures should be used to achieve superelastic properties, instead of shape memory properties, and appropriate post-consolidation heat treatments should be developed and optimized.

#### 7.3.1.2 Transient liquid phase sintering with space-holders

For near-equiatomic NiTi foam, Nb content and sintering time should be minimized (preferably to below 6 at% Nb, and 4 hours, respectively) to inhibit formation of unnecessary NiTi-Nb phases that dampen shape memory effects, while preserving high densification in the NiTi struts and without sacrificing open porosity. To achieve uniform and highly-porous foam structures, powder mixing (especially at salt volume fractions exceeding 50%) should be studied. Scale-up (e.g. to samples 25 mm in diameter and 10 mm thick) of this method should also be attempted.

Complex porous NiTi part geometries should be investigated, by compacting in the desired shape and without high pressure (e.g. by CIP), followed with transient liquid phase

sintering. As a further extension, metals similar to Nb, such as vanadium (V) or tantalum (Ta), could be used to generate the transient liquid with NiTi.

### **7.3.2 Potential methods beyond the scope of this work**

Beside these ideas, potential future approaches using techniques beyond the scope of this work can be discussed. These can be divided into four categories, separated by their main objectives: 1) microstructure manipulation; 2) material alteration; 3) in-depth understanding of mechanical behavior; and 4) correlating properties with biological response.

#### 7.3.2.1 Microstructure manipulation

##### *Elongated pores*

Optimal design of metallic biomaterials should take into account the anisotropy of bone structure [180, 181]. Besides controlling such characteristics as porosity, pore size, pore roughness, and connectivity, therefore, pore aspect ratios should be increased, and alignment of these elongated pores should be attempted. This has been achieved in titanium foams [182], but not yet in NiTi foams, except for one study where continuous zone melting under pressurized hydrogen created elongated pores in NiTi [82]. Aligned, elongated pores in NiTi could combine high strength along the necessary axes with toughness, while at the same time helping manipulate bone growth direction in the bone implant. They could be achieved by using elongated space-holders, which also provide higher connectivity after removal, or by extrusion of mixtures of NiTi powders and space-holders. In-depth study of the resulting anisotropic

mechanical properties would be needed, of course, as well as a detailed comparison with the corresponding properties in anisotropic bone.

#### *Complex porous structures and tailor-made interconnectivity*

Although the salt space-holder method could faithfully replicate the space-holder geometry in its porosity, the resulting interconnectivity still relied on particle arrangement upon mixing, which is poorly controlled. To resolve this difficulty, a tailor-made space-holder template could be created prior to densification with NiTi powders, and a reverse-templated porous structure could thereby be achieved after its removal. For example, NiTi powder could be packed around stacked bent steel wires (or fine meshes), followed by electrochemical removal of the steel. This novel approach is currently in trial stages in the Dunand group for making Ti-based foams with complex 3D geometries, and was reported to be promising for application in NiTi as well [183].

#### *Functionally graded porous structure and porosity*

A remarkable feature of bone is its use of a hierarchical structure which varies from a near-dense, stiff external structure (cortical bone) to a highly-porous internal structure (cancellous bone). This complex bone structure design implies biological adaptation towards functional gradation, i.e. a continuous change of complex functional tissues from one structure or composition to another. Moreover, the structure naturally optimizes the load bearing response to external loading. Therefore, an implant should offer similar gradation in porosity and pore characteristics; high porosity with large open pores (to maximize bone ingress and

osteoconduction) at the implant surface to low porosity with small closed pores (to maximize strength and toughness) at the implant core.

A controlled gradient change in space holder size and volume fraction of each layer, from the surface towards the interior, should be used to produce a graded foam structure. A continuous, gradual change in pore structure will be more advantageous for stress distributions in the implant, as compared to typical porous surface coatings [184] where low fatigue strength (due to high local stress concentration) is observed at the interface. In cases where bonding of two or more layers of porous NiTi (with different pore features) is needed, strong bonding interfaces could be achieved by brazing the layers with eutectic NiTi-Nb.

#### 7.3.2.2 Material alteration

Mixtures of elemental Ni and Ti powders could be used to replace pre-alloyed NiTi powder, and thereby lower preparation cost. However, undesirable intermetallic compound formation would become a serious challenge. To combat this, titanium hydride ( $\text{TiH}_2$ ) powder could replace the Ti powders, since they decompose into fine Ti with low oxygen contamination, and improve final NiTi homogeneity, as well as provide an in-situ reducing cover gas [185]. Calcium hydride ( $\text{CaH}_2$ ) powder could also be included, and the resulting Ca vapor used as a reducing agent for titanium or nickel oxides during the sintering process, as demonstrated for full-density NiTi materials [186].

In term of space-holder materials, calcium chloride ( $\text{CaCl}_2$ ) may be the next choice for future work.  $\text{CaCl}_2$  could function as well as NaCl in the space-holder process, but it has a higher water solubility, and residual  $\text{CaCl}_2$  (if any) after processing would be more biocompatible.

Another interesting space-holder is sodium aluminate, which has been demonstrated for Fe- and Ni-based foams [187].

### 7.3.2.3 Properties characterization

#### *Heat recovery behavior of shape memory porous NiTi*

The heat recovery effect (i.e., strain recovery as a function of temperature) and phase transformation behavior of shape memory NiTi foam could be determined through dilatometry experiments using deformed foam samples.

Upon heating to temperatures above  $A_f$ , the transformation of martensite to austenite occurs, and leads to changes in the dimensions of a NiTi sample. Dilatometry, normally used to measure thermal expansion coefficients, allows such changes to be measured very precisely and with well-controlled heating or cooling cycles. It does so by monitoring the movement of a push rod contacting the sample, while simultaneously controlling sample temperature with a closely-placed thermocouple. A further benefit to using high-precision dilatometry is that the small volume changes occurring during phase transformations could also be measured [188].

The following quantities should be highlighted in these experiments: 1) one-dimensional shape memory strain upon heating; 2) phase transformation temperatures such as  $A_s$  and  $A_f$ , with respect to the thermal cycle; and 3) transformation temperature intervals and transformation temperature hysteresis. Modeling of the type used in section 6.2 (tomography-based FE modeling) could be performed and compare with the experimental results.

*Load transfer in (artificial/real) bone-implant composite*

The biomechanical properties of an implant (such as load transfer at the bone-implant interface) greatly influence the likelihood of osseointegration, which allows the implant to function during the healing process, and immediately after placement. For this reason, load distribution at the interface must necessarily be taken into account in implant design. The details of the interactions between bone and any particular implant will vary, however, with factors affecting load transfer, including not only the mechanical and physical properties (geometry and surface structure) of the implant, but the nature of bone-implant interface, the quality and quantity of the surrounding bone, and even the type of loading. Therefore, mechanical behavior observed in the implant alone is not sufficient to simulate mechanical performance of the implant at use.

To simulate the *in-vivo* performance and reliability of porous NiTi implants, a composite of bone (artificial or real) and NiTi foam should be made. A simple compression test on the composite could elucidate some of the effects of ingrown bone on overall mechanical behavior. Synchrotron x-ray studies could be employed for a more detailed investigation of the stress/strain distribution in the NiTi matrix and the reinforcing bone, and could also probe the corresponding effects on phase transformation behavior in the NiTi matrix (by in-situ diffraction measurements), as well as monitor the actual NiTi-bone interface (by microtomography) upon compressive loading and unloading. The stress-concentration points in the porous structure could then be revealed, providing guidance for improving processing methods to minimize the peak bone stress upon loading and maximize the reliability of the implant.

Modeling (for instance, by FE) of the relationships between implant structure, bone-implant load transfer, and overall implant properties could also be very fruitful. Information from such models could be used to predict implant performance (e.g., by identifying factors responsible for damage occurring to the underlying bone, as well as the subsequent degradation of the implant in *in vivo* tests) and create biologically- and mechanically-optimal porous NiTi structures.

In the case that a real bone-NiTi composite (i.e., a cultivation of bone cells inside a porous NiTi implant) is not feasible for load-transfer studies, an artificial bone-NiTi composite could be made by infiltration of a second phase (having a stiffness close to bone) into porous NiTi. This second phase might be a polymer or a low-stiffness metal such as gallium (Ga, Young's modulus of 10 GPa). An attempt at the latter case was made in 2006, when near-equiatomic NiTi foam with <40% porosity was successfully infiltrated (using a gas pressure of 20 psi) with gallium. However, diffraction experiments were not performed on this composite, since grain refiners were needed to reduce the grain size of Ga in order to get complete, non-spotty diffraction rings. Also, it should be noted that Ga-NiTi foam composites could not be used for mechanical testing at body temperature, since the melting point of Ga is 30°C.

#### *Fatigue of shape memory effect and superelasticity*

In practice, porous NiTi implants are expected to be exposed to complex cyclic deformation situations extending over long periods of time, making prediction of the service life for any particular implant application quite complicated. The performance of porous NiTi under a range of relevant service or physiological conditions must therefore be evaluated using

prolonged load-unload-heat recovery cycling (for foams with shape memory behavior) or continuous load-unload cycling (for that with superelasticity) until failure. Specifically, porous NiTi bone implants must survive compressive load-unload cycling corresponding to the movements and activities of patients, approximately  $10^7$  cycles over 10 years of implantation [6]. For reliable implant performance, therefore, porous NiTi must show a fatigue endurance limit of  $10^8$  cycles or more.

During cyclical loading, a gradual increase in the residual strains and internal stresses in the NiTi struts, as well as a decrease in their transformation stresses, can be expected. This could result in a decrease in the hysteresis and energy dissipation of the strut material. In addition, microstructural changes associated with pore structure can develop, which could accelerate local fatigue fracture and failure. High plasticity could be expected, for example, at stress concentrators in implants with heterogeneous microstructure or pore structure. Crack initiation can be expected to occur at pores, especially those having large size and irregular shape, and then propagate through the interpore ligaments. Porous NiTi might therefore become less stiff over extended cycling due to microcracking in the NiTi struts, causing gradual changes that are not captured by monotonic testing. This may however be partially compensated by increase bone infiltration in the implant.

To simulate the biological-mechanical environment in service, compression fatigue testing should be done in simulated body fluid at body temperature (37-40 °C). For even greater predictive power, study of fatigue in porous NiTi filled with bone (or bone substitute) is recommended, since bone-NiTi interactions are expected to cause changes in long-term behavior which could not be captured using simulated body fluids.

#### 7.3.2.4 Creating favorable biological properties

In addition to mechanically-optimized materials, materials with biologically-optimized NiTi-bone interfaces are needed. To prevent Ni release from NiTi, finished porous NiTi surfaces without undesirable phases and with homogeneous distributions of surface stress are required. NiTi surfaces could be treated with bioactive materials (such as self-assembling peptide amphiphiles [170] or calcium phosphate (CA-P) coatings [189]) to encourage bone ingrowth and biocompatibility at the interface. In-vitro testing in simulated body fluid (SBF) could be used to investigate the Ni release rates and corrosion resistance of NiTi foam over time, and could be done in bioreactors for better simulation of the true biomechanical environment. In bioreactor experiments, the effects of cyclical changes in biophysical stimuli, for instance external compressive loading or hydrostatic loading of fluid flow (fluid shear stress), could be observed on cellular differentiation or functional adaptation. *In vitro* cell culture tests could be performed to evaluate proliferation and differentiation of cultured cells, before moving to the next step of *in-vivo* testing in animal models. Finally, the overall design of implants for each application should be considered, in order to facilitate insertion during implantation surgery and removal during revision surgery.

## References

1. Ratner BD, Allan S, Hoffman, Frederick J, Shoen, and Jack E. Lemons. *Biomaterials science: An introduction to materials in medicine*. New York: Elsevier Academic P; 2004.
2. Hing KA. Bone repair in the twenty-first century: Biology, chemistry or engineering. *Philosophical Transactions of the Royal Society of London Series A-Mathematical Physical and Engineering Sciences* 2004; 362: 2821-50.
3. Katti KS. Biomaterials in total joint replacement. *Colloids and Surfaces B-Biointerfaces* 2004; 39: 133-42.
4. Krishna BV, Bose S, Bandyopadhyay A. Laser processing of net-shape NiTi shape memory alloy. *Metallurgical and Materials Transactions A-Physical Metallurgy and Materials Science* 2007; 38A: 1096-103.
5. Levine BR, Sporer S, Poggie RA, Della Valle CJ, Jacobs JJ. Experimental and clinical performance of porous tantalum in orthopedic surgery. *Biomaterials* 2006; 27: 4671-81.
6. Black J. *Biological performance of materials: Fundamentals of biocompatibility*. New York: Marcel Dekker; 1992.
7. Clohisy JC, Calvert G, Tull F, McDonald D, Maloney WJ. Reasons for revision hip surgery. *Clinical Orthopaedics and Related Research* 2004; 429: 189-92.
8. Huiskes R, Weinans H, Vanrietbergen B. The relationship between stress shielding and bone-resorption around total hip stems and the effects of flexible materials. *Clinical Orthopaedics and Related Research* 1992; 124-34.
9. Yang CY, Chen CR, Chang E, Lee TM. Characteristics of hydroxyapatite coated titanium porous coatings on Ti-6Al-4V substrates by plasma sprayed method. *Journal of Biomedical Materials Research Part B-Applied Biomaterials* 2007; 82B: 450-59.
10. Robertson DM, Pierre LS, Chahal R. Preliminary-observations of bone ingrowth into porous materials. *Journal of Biomedical Materials Research* 1976; 10: 335-44.
11. Kienapfel H, Sprey C, Wilke A, Griss P. Implant fixation by bone ingrowth. *Journal of Arthroplasty* 1999; 14: 355-68.

12. Karageorgiou V, Kaplan D. Porosity of 3D biomaterial scaffolds and osteogenesis. *Biomaterials* 2005; 26: 5474-91.
13. Fabbri M, Celotti GC, Ravaglioli A. Hydroxyapatite-based porous aggregates - physicochemical nature, structure, texture and architecture. *Biomaterials* 1995; 16: 225-28.
14. Cook SD, Walsh KA, Haddad RJ. Interface mechanics and bone-growth into porous Co-Cr-Mo alloy implants. *Clinical Orthopaedics and Related Research* 1985; 271-80.
15. Lemberg E, Rostoker W, Galante J. Fixation of skeletal replacement by fiber metal composites. *Clinical Orthopaedics and Related Research* 1972; 303.
16. Bobyn JD, Pilliar RM, Cameron HU, Weatherly GC. Osteogenic phenomena across endosteal bone-implant spaces with porous surfaced intra-medullary implants. *Acta Orthopaedica Scandinavica* 1981; 52: 145-53.
17. Clemow AJT, Weinstein AM, Klawitter JJ, Koeneman J, Anderson J. Interface mechanics of porous titanium implants. *Journal of Biomedical Materials Research* 1981; 15: 73-82.
18. Welsh RP, Pilliar RM, Macnab I. Surgical implants - role of surface porosity in fixation to bone and acrylic. *Journal of Bone and Joint Surgery-American Volume* 1971; A 53: 963.
19. Itala AI, Ylanen HO, Ekholm C, Karlsson KH, Aro HT. Pore diameter of more than 100  $\mu\text{m}$  is not requisite for bone ingrowth in rabbits. *Journal of Biomedical Materials Research* 2001; 58: 679-83.
20. Lu JX, Flautre B, Anselme K, Hardouin P, Gallur A, Descamps M, Thierry B. Role of interconnections in porous bioceramics on bone recolonization *in vitro* and *in vivo*. *Journal of Materials Science-Materials in Medicine* 1999; 10: 111-20.
21. Otsuki B, Takemoto M, Fujibayashi S, Neo M, Kokubo T, Nakamura T. Pore throat size and connectivity determine bone and tissue ingrowth into porous implants: Three-dimensional micro-CT based structural analyses of porous bioactive titanium implants. *Biomaterials* 2006; 27: 5892-900.
22. Flautre B, Descamps M, Delecourt C, Blary MC, Hardouin P. Porous HA ceramic for bone replacement: Role of the pores and interconnections - experimental study in the rabbit. *Journal of Materials Science-Materials in Medicine* 2001; 12: 679-82.
23. Sargeant T, Guler M, Oppenheimer S, Mata A, Satcher R, Dunand D, Stupp S. Hybrid bone implants: Self-assembly of peptide amphiphile nanofibers within porous titanium. *Biomaterials* 2008; 29: 161-71.

24. Takemoto M, Fujibayashi S, Neo M, Suzuki J, Kokubo T, Nakamura T. Mechanical properties and osteoconductivity of porous bioactive titanium. *Biomaterials* 2005; 26: 6014-23.
25. Gibson LJ. Biomechanics of cellular solids. *Journal of Biomechanics* 2005; 38: 377-99.
26. Bakan HI. A novel water leaching and sintering process for manufacturing highly porous stainless steel. *Scripta Materialia* 2006; 55: 203-06.
27. Andersen O, Waag U, Schneider L, Stephani G, Kieback B. Novel metallic hollow sphere structures. *Advanced Engineering Materials* 2000; 2: 192-95.
28. Greiner C, Oppenheimer SM, Dunand DC. High strength, low stiffness, porous NiTi with superelastic properties. *Acta Biomaterialia* 2005; 1: 705-16.
29. Gibson LJ, Ashby MF. *Cellular solids*. Cambridge: Cambridge University Press; 1997.
30. Bonnet JP, Topin F, Tadrist L. Flow laws in metal foams: Compressibility and pore size effects. *Transport in Porous Media* 2008; 73: 233-54.
31. Moore MJ, Jabbari E, Ritman EL, Lu LC, Currier BL, Windebank AJ, Yaszemski MJ. Quantitative analysis of interconnectivity of porous biodegradable scaffolds with micro-computed tomography. *Journal of Biomedical Materials Research Part A* 2004; 71A: 258-67.
32. Chawla N, Deng X. Microstructure and mechanical behavior of porous sintered steels. *Materials Science and Engineering A- Structural Materials Properties Microstructure and Processing* 2005; 390: 98-112.
33. Lagoudas DC, Vandygriff EL. Processing and characterization of NiTi porous SMA by elevated pressure sintering. *Journal of Intelligent Materials Systems and Structure* 2002; 13: 837-50.
34. Vandygriff EL. Fabrication and characterization of porous NiTi shape memory alloy by elevated pressure sintering. *Doctoral Thesis (Texas A&M University)* 2002;
35. Otsuka K, Wayman CM. *Shape memory materials*. Cambridge ; New York: Cambridge University Press; 1998.
36. Khalil-Allafi J, Dlouhy A, Eggeler G. Ni<sub>4</sub>Ti<sub>3</sub>-precipitation during aging of NiTi shape memory alloys and its influence on martensitic phase transformations. *Acta Materialia* 2002; 50: 4255-74.
37. Frenzel J, Zhang Z, Somsen C, Neuking K, Eggeler G. Influence of carbon on martensitic phase transformations in NiTi shape memory alloys. *Acta Materialia* 2007; 55: 1331-41.

38. Mentz J, Frenzel J, F.-X.; WM, Neuking K, Eggeler G, Buchkremer HP, Stover D. Powder metallurgical processing of NiTi shape memory alloys with elevated transformation temperatures. *Materials Science and Engineering A-Structural Materials Properties Microstructure and Processing* 2008 (Article in press);
39. Abkowitz S, Siergiej JM, Regan RR. Titanium-nickel alloy manufacturing methods. United States Patent Office Patent. 1969. 3,700,434
40. Kang SB, Yoon KS, Kim JS, Nam TH, Gjunter VE. In vivo result of porous TiNi shape memory alloy: Bone response and growth. *Materials Transaction* 2002; 43: 1045-48.
41. Rhalmi S, Odin M, Assad M, Tabrizian M, Rivard CH, Yahia LH. Hard, soft tissue and *in vitro* cell response to porous nickel-titanium: A biocompatibility evaluation. *Bio-Medical Materials and Engineering* 1999; 9: 151-62.
42. Ayers RA, Simske SJ, Bateman TA, Petkus A, Sachdeva RLC, Gyunter VE. Effect of nitinol implant porosity on cranial bone ingrowth and apposition after 6 weeks. *Journal of Biomedical Material Research* 1999; 45: 42-47.
43. Simske SJ, Ayers RA, Bateman TA. Porous materials for bone engineering. *Materials Science Forum* 1997; 250: 151-82.
44. Zhao Y, Taya M, Izui H. Study on energy absorbing composite structure made of concentric NiTi spring and porous NiTi. *International Journal of Solids Structure* 2006; 43: 2497-512.
45. Qidwai MA, DeGiorgi VG. Numerical assessment of the dynamic behavior of hybrid shape memory alloy composite. *Smart Materials and Structures* 2004; 13: 134-45.
46. Elzey DM, Sofla AYN, Wadley HNG. A shape memory-based multifunctional structural actuator panel. *International Journal of Solids and Structures* 2005; 42: 1943-55.
47. Zhou JB, Gao LP, Wang KS. Preparation of Ti-Ni porous alloys and its hydrogen isotope effects. *Journal of Rare Earths* 2005; 23: 449-51.
48. Thierry B, Merhi Y, Bilodeau L, Trepanier C, Tabrizian M. Nitinol versus stainless steel stents: Acute thrombogenicity study in an *ex vivo* porcine model. *Biomaterials* 2002; 23: 2997-3005.
49. Gil FJ, Planell JA. Properties and clinical applications of shape memory alloys. *Biomaterials and bioengineering handbook*. Wise DL, editor; 2000.
50. Ryhanen J, Kallioinen M, Tuukkanen J, Junila J, Niemela E, Sandvik P, Serlo W. *In vivo* biocompatibility evaluation of nickel-titanium shape memory metal alloy: Muscle and perineural tissue responses and capsule membrane thickness. *Journal of Biomedical Material Research* 1998; 41: 481-88.

51. Yahai L. Shape memory implants Yahia L, editors. Berlin; New York: Springer; 2000.
52. Li BY, Rong LJ, Gjunter VE, Li YY. Porous Ni-Ti shape memory alloys produced by two different methods. *Zeitschrift Fur Metallkunde* 2000; 91: 291-95.
53. Li BY, Rong LJ, Li YY. Porous NiTi alloy prepared from elemental powder sintering. *Journal of Materials Research* 1998; 13: 2847-51.
54. Yuan B, Zhu M, Gao Y, Li X, Chung CY. Forming and control of pores by capsule-free hot isostatic pressing in NiTi shape memory alloys. *Smart Materials and Structures* 2008; 17.
55. Panigrahi BB, Karabi D, Godkhindi MM. Synthesis of porous nickel titanide. *Transactions of the Indian Institute of Metals* 2003; 56: 565-69.
56. Yuan B, Zhang XP, Chung CY, Zhu M. The effect of porosity on phase transformation behavior of porous Ti-50.8 at.% Ni shape memory alloys prepared by capsule-free hot isostatic pressing. *Materials Science and Engineering A-Structural Materials Properties Microstructure and Processing* 2006; 438: 585-88.
57. Zhu SL, Yang XJ, Hu F, Deng SH, Cui ZD. Processing of porous TiNi shape memory alloy from elemental powders by Ar-sintering. *Materials Letters* 2004; 58: 2369-73.
58. Li BY, Rong LJ, Li YY. Stress-strain behavior of porous Ni-Ti shape memory intermetallics synthesized from powder sintering. *Intermetallics* 2000; 8: 643-46.
59. Bertheville B. Porous single-phase NiTi processed under Ca reducing vapor for use as a bone graft substitute. *Biomaterials* 2006; 27: 1246-50.
60. Zhang YP, Li DS, Zhang XP. Gradient porosity and large pore size NiTi shape memory alloys. *Scripta Materialia* 2007; 57: 1020-23.
61. Zhang YP, Yuan B, Zeng MQ, Chung CY, Zhang XP. High porosity and large pore size shape memory alloys fabricated by using pore-forming agent ( $\text{NH}_4\text{HCO}_3$ ) and capsule-free hot isostatic pressing. *Journal of Materials Processing Technology* 2007; 192: 439-42.
62. Wu SL et al. Pore formation mechanism and characterization of porous NiTi shape memory alloys synthesized by capsule-free hot isostatic pressing. *Acta Materialia* 2007; 55: 3437-51.
63. Tay BY, Goh CW, Gu YW, Lim CS, Yong MS, Ho MK, Myint MH. Porous NiTi fabricated by self-propagating high-temperature synthesis of elemental powders. *Journal of Materials Processing Technology* 2008; 202: 359-64.
64. Yeh CL, Sung WY. Synthesis of NiTi intermetallics by self-propagating combustion. *Journal of Alloys and Compounds* 2004; 376: 79-88.

65. Kim JS, Song JH, Chang MG, Yum YJ, Lee JK, Kwon YS. The effect of heating schedule and the size of the powder compact on the pore structure, mechanical and fatigue properties of porous TiNi produced by a self-propagating high-temperature synthesis method. *Journal of Ceramic Processing Research* 2007; 8: 70-73.
66. Zanotti C, Tacca A, Monagheddu M, Bertolino N, Giuliani P. Thermal explosion of powder mixtures: Numerical approach. *Propellants Explosives Pyrotechnics* 2004; 29: 112-17.
67. Li BY, Rong LJ, Li YY, Gjunter VE. Fabrication of cellular NiTi intermetallic compounds. *Journal of Materials Research* 2000; 15: 10-13.
68. Chu CL, Chung CY, Lin PH, Wang SD. Fabrication of porous NiTi shape memory alloy for hard tissue implants by combustion synthesis. *Materials Science and Engineering A-Structural Materials Properties Microstructure and Processing* 2004; 366: 114-19.
69. Li YH, Rong LJ, Li YY, Gunther VE. Influence of Ti powder characteristics on combustion synthesis of porous NiTi alloy. *Journal of Materials Science and Technology* 2002; 18: 248-50.
70. Li BY, Rong LJ, Li YY, Gjunter VE. Synthesis of porous Ni-Ti shape-memory alloys by self-propagating high-temperature synthesis: Reaction mechanism and anisotropy in pore structure. *Acta Materialia* 2000; 48: 3895-904.
71. Chu CL, Chung JCY, Chu PK. Effects of heat treatment on characteristics of porous Ni-rich NiTiSMA prepared by SHS technique. *Transaction of Nonferrous Metals Society of China* 2006; 16: 49-53.
72. Arciniegas M, Aparicio C, Manero JM, Gil FJ. Low elastic modulus metals for joint prosthesis: Tantalum and nickel-titanium foams. *Journal of the European Ceramic Society* 2007; 27: 3391-98.
73. Jarfors AEW, Sim C, San TE. Influence of process parameters on reaction products during self-propagating high-temperature synthesis of porous NiTi. *Advanced Materials Processing* 2003; 475-78
74. Chu CL, Chung CY, Lin PH, Wang SD. Fabrication and properties of porous NiTi shape memory alloys for heavy load-bearing medical applications. *Journal of Materials Processing Technology* 2005; 169: 103-07.
75. Yuan B, Chung CY, Zhu M. Microstructure and martensitic transformation behavior of porous NiTi shape memory alloy prepared by hot isostatic pressing processing. *Materials Science and Engineering A-Structural Materials Properties Microstructure and Processing* 2004; 382: 181-87.

76. Li YH, Rong LJ, Li YY. Superelasticity of porous NiTi alloy fabricated by combustion synthesis. *Shape memory materials and its applications*; 2001. 511-14
77. Biswas A. Porous NiTi by thermal explosion mode of SHS: Processing, mechanism and generation of single phase microstructure. *Acta Materialia* 2005; 53: 1415-25.
78. Grummon DS, Shaw JA, Gremillet A. Low-density open-cell foams in the NiTi system. *Applied Physics Letters* 2003; 82: 2727-29.
79. Sakurai N, Takekawa J. Shape recovery characteristics of NiTi foams fabricated by a vacuum process applied to a slurry. *Materials Transaction* 2006; 47: 558-63.
80. Kohl M, Bram M, Buchkremer P, Stover D, Habijan T, Koller M. Production of highly porous near-net-shape NiTi components for biomedical applications. *Metfoam Conference (Montreal, QC, Canada)* 2007.
81. Zhao Y, Taya M, Kang YS, Kawasaki A. Compression behavior of porous NiTi shape memory alloy. *Acta Materialia* 2005; 53: 337-43.
82. Sugiyama M, Hyun SK, Tane M, Nakajima H. Fabrication of lotus-type porous NiTi shape memory alloys using the continuous zone melting method and tensile property. *High Temperature Materials and Processes* 2007; 26: 297-301.
83. Odgaard A, Linde F. The underestimation of young modulus in compressive testing of cancellous bone specimens. *Journal of Biomechanics* 1991; 24: 691-98.
84. Bansiddhi A, Dunand DC. Porous NiTi for bone implants: A review. *Acta Biomaterialia* 2008 (Article in press).
85. Shabalovskaya SA. On the nature of the biocompatibility and on medical applications of NiTi shape memory and superelastic alloys. *Bio-Medical Materials and Engineering* 1996; 6: 267-89.
86. Itin VI, Gyunter VE, Shabalovskaya SA, Sachdeva RLC. Mechanical-properties and shape-memory of porous nitinol. *Materials Characterization* 1994; 32: 179-87.
87. Silbersteinm BM, Gyunter VE. *Shape-memory implants in spinal surgery*. Berlin: Springer; 2000.
88. Jarzem P, Leroux M, Assad M, Simonovich A, Fomichev N, Baykylov A. Porous TiNi device for degenerative disc diseases : Pre-clinical study. 48th Annual Meeting of the Orthopedic Research Society (Dallas, TX, USA) 2002.
89. Fischer H, Vogel B, Welle A. Applications of shape memory alloys in medical instruments. *Minimally Invasive Therapy and Allied Technologies* 2004; 13: 248-53.

90. Ayers R, Burkes D, Gottoli G, Yi HC, Moore JJ. The application of self-propagating high-temperature synthesis of engineered porous composite biomedical materials. *Materials and Manufacturing Processes* 2007; 22: 481-88.
91. Ponsonnet L, Treheux D, Lissac M, Jaffrezic N, Grosgeat B. Review of *in vitro* studies on the biocompatibility of NiTi alloys. *International Journal of Applied Electromagnetics and Mechanics* 2006; 23: 147-51.
92. Es-Souni M, Es-Souni M, Fischer-Brandies H. Assessing the biocompatibility of NiTi shape memory alloys used for medical applications. *Analytical and Bioanalytical Chemistry* 2005; 381: 557-67.
93. Prokoshkin SD, Pushin VG, Ryklina EP, Khmelevskaya IY. Application of titanium nickelide-based alloys in medicine. *Physics of Metals and Metallurgy* 2004; 97: S56-S96.
94. Martynova I, Skorohod V, Solonin S, Goncharuk S. Shape memory and superelasticity behavior of porous Ti-Ni material. *Journal De Physique IV* 1991; 1: 421-26.
95. Goncharuk NV, Martynova IF, Naidenova OR, Skorokhod VV, Solonin SM, Fridman GR. Characteristics of hyperelasticity and of shape memory of sintered porous titanium nickelide. *Soviet Powder Metallurgy of Metal and Ceramics* 1992; 31: 330-33.
96. Kujala S, Ryhanen J, Danilov A, Tuukkanen J. Effect of porosity on the osteointegration and bone ingrowth of a weight-bearing nickel-titanium bone graft substitute. *Biomaterials* 2003; 24: 4691-97.
97. Simske SJ, Sachdeva R. Cranial bone apposition and ingrowth in a porous nickel-titanium implant. *Journal of Biomedical Materials Research* 1995; 29: 527-33.
98. Assad M, Jarzem P, Leroux MA, Coillard C, Chernyshov AV, Charette S, Rivard CH. Porous titanium-nickel for intervertebral fusion in a sheep model: Part 1. Histomorphometric and radiological analysis. *Journal of Biomedical Materials Research Part B - Applied Biomater* 2003; 64B: 107-20.
99. Shabalovskaya SA. Surface, corrosion and biocompatibility aspects of nitinol as an implant material. *Bio-Medical Materials and Engineering* 2002; 12: 69-109.
100. Shabalovskaya S, Ryhanen J, Yahia LH. Bioperformance of nitinol: Surface tendencies. *Shape Memory Materials and Its Applications* 2001; 394-3: 131-38.
101. Gu YW, Li H, Tay BY, Lim CS, Yong MS, Khor KA. *In vitro* bioactivity and osteoblast response of porous NiTi synthesized by SHS using nanocrystalline Ni-Ti reaction agent. *Journal of Biomedical Materials Research - Part A* 2006; 78A: 316-23.

102. Kim JS, Kang JH, Kang SB, Yoon KS, Kwon YS. Porous TiNi biomaterial by self-propagating high-temperature synthesis. *Advanced Engineering Materials* 2004; 6: 403-06.
103. Zhang YM, Tan SB, Wang LX, Wang XP, Wang XC. Damping of porous TiNi alloy prepared by combustion synthesis method. *Rare Metal Materials and Engineering* 2004; 33: 63-65.
104. Li Q, Yu JY, Mu BC, Sun XD. BP neural network prediction of the mechanical properties of porous NiTi shape memory alloy prepared by thermal explosion reaction. *Materials Science and Engineering A –Structure, Materials, Properties Microstructure Processing* 2006; 419: 214-17.
105. Nemat-Nasser S, Su Y, Guo WG, Isaacs J. Experimental characterization and micromechanical modeling of superelastic response of a porous NiTi shape-memory alloy. *Journal of Mechanic Physics Solids* 2005; 53: 2320-46.
106. Entchev PB, Lagoudas DC. Modeling of transformation-induced plasticity and its effect on the behavior of porous shape memory alloys. Part II: Porous SMA response. *Mechanical Materials* 2004; 36: 893-913.
107. Flyvholm MA, Nielsen GD, Andersen A. Nickel content of food and estimation of dietary-intake. *Zeitschrift Fur Lebensmittel-Untersuchung Und-Forschung* 1984; 179: 427-37.
108. Patnaik P. *Handbook of inorganic chemicals*. New York, McGraw-Hill; 2003.
109. *Annual book of ASTM standards: Metals test methods and analytical procedures. Metals-mechanical testing; elevated and low-temperature tests; metallography*. Philadelphia ASTM; 2004. p. 267-92
110. *Water: Density at atmosphere pressure and temperatures from 0 to 100°C. Table of standard handbook data*. Moscow: Standartov; 1978.
111. Jackson CM, Wagner HJ, Wasilewski RJ, 55-nitinol - the alloy with a memory: Its physical metallurgy, properties, and applications, 1972.
112. Hakamada M, Kuromura T, Chen YQ, Kusuda H, Mabuchi M. Sound absorption characteristics of porous aluminum fabricated by spacer method. *Journal of Applied Physics* 2006; 100.
113. Jiang B, Zhao NQ, Shi CS, Du XW, Li JJ, Man HC. A novel method for making open cell aluminum foams by powder sintering process. *Materials Letters* 2005; 59: 3333-36.
114. Bram M, Stiller C, Buchkremer HP, Stover D, Baur H. High-porosity titanium, stainless steel, and superalloy parts. *Advanced Engineering Materials* 2000; 2: 196-99.

115. Zhang EL, Wang B. On the compressive behaviour of sintered porous coppers with low to medium porosities - part I: Experimental study. *International Journal of Mechanical Science* 2005; 47: 744-56.
116. Zhao YY, Fung T, Zhang LP, Zhang FL. Lost carbonate sintering process for manufacturing metal foams. *Scripta Materialia* 2005; 52: 295-98.
117. Li M, Liu Y, Ye JW, Zhang LF, Li J, Tu MJ. Process and compressive properties of porous nickel materials. *Powder Metallurgy* 2006; 49: 114-17.
118. Laptev A, Bram M, Buchkremer HP, Stover D. Study of production route for titanium parts combining very high porosity and complex shape. *Powder Metallurgy* 2004; 47: 85-92.
119. Esen Z, Bora Ş. Processing of titanium foams using magnesium spacer particles *Scripta Materialia* 2007; 56: 341-44
120. Fukami-Ushiro KL, Dunand DC. NiTi and NiTi-TiC composites III: Shape-memory recovery. *Metallurgical and Materials Transactions A-Physical Metallurgy and Materials Science* 1996; 27: 193-203.
121. Mari D, Dunand DC. NiTi and NiTi-TiC composites I: Transformation and thermal cycling behavior. *Metallurgical and Materials Transactions A* 1995; 26: 2833-47.
122. Vaidyanathan R, Bourke MAM, Dunand DC. An in situ neutron diffraction mechanical study of superelastic NiTi and NiTi-TiC composites. *Journal De Physique IV* 2003; 112: 823-26.
123. Gaillard C, Despois U, Mortensen A. Processing of NaCl powders of controlled size and shape for the microstructural tailoring of aluminium foams. *Materials Science and Engineering A-Structural Materials Properties Microstructure and Processing* 2004; 374: 250-62.
124. Brothers AH, Scheunemann R, DeFouw JD, Dunand DC. Processing and structure of open-celled amorphous metal foams. *Scripta Materialia* 2005; 52: 335-39.
125. Brothers AH, Prine DW, Dunand DC. Acoustic emissions analysis of damage in amorphous and crystalline metal foams. *Intermetallics* 2006; 14: 857-65.
126. Toshio S. Shape memory alloys. Funakubo H, editors. *Precision machinery and robotics*. Gordon and Breach Science Publishers; 1984.
127. Yuan B, Zhang XP, Chung CY, Zeng MQ, Zhu M. A comparative study of the porous TiNi shape-memory alloys fabricated by three different processes. *Metallurgical and Materials Transactions A* 2006; 37A: 755-61.

128. Dunand DC, Mari D, Bourke MAM, Roberts JA. NiTi and NiTi-TiC composites IV: Neutron diffraction study of twinning and shape-memory recovery. *Metallurgical and Materials Transactions A* 1996; 27: 2820-36.
129. Fukami Ushiro KL, Dunand DC. NiTi and NiTi-TiC composites III. Shape-memory recovery. *Metallurgical and Materials Transaction A* 1996; 27: 193-203.
130. Despois JF, Marmottant A, Salvo L, Mortensen A. Influence of the infiltration pressure on the structure and properties of replicated aluminium foams. *Materials Science and Engineering A-Structural Materials Properties Microstructure and Processing* 2007; 462: 68-75.
131. Zhao YY, Han FS, Fung T. Optimisation of compaction and liquid-state sintering in sintering and dissolution process for manufacturing al foams. *Materials Science and Engineering A-Structural Materials Properties Microstructure and Processing* 2004; 364: 117-25.
132. Hakamada M, Yamada Y, Nomura T, Kusuda H, Chen YQ, Mabuchi M. Effect of sintering temperature on compressive properties of porous aluminum produced by spark plasma sintering. *Materials Transactions* 2005; 46: 186-88.
133. Reed TB. Free energy of formation of binary compounds; an Atlas of charts for high-temperature chemical calculations. Cambridge, Massachusetts; London: The MIT Press; 1971. p 81.
134. Zhao JL, Cui LS, Gao WF, Zheng YJ. Synthesis of NiTi particles by chemical reaction in molten salts. *Intermetallics* 2005; 13: 301-03.
135. Kaufmann DW. Sodium chloride; the production and properties of salt and brine. New York: Reinhold Publisher; 1960. p 743.
136. Zhang N, Khosrovabadi PB, Lindenhovius JH, Kolster BH. TiNi shape memory alloys prepared by normal sintering. *Materials Science and Engineering A -Structural Materials Properties Microstructure and Processing* 1992; 150: 263-70.
137. Bertheville B. PM processing of single-phase NiTi shape memory alloys by VPCR process. *Materials Transactions* 2006; 47: 698-703.
138. Majkic G, Chennoufi N, Chen YC, Salama K. Synthesis of NiTi by low electrothermal loss spark plasma sintering. *Metallurgical and Materials Transaction A-Physical Metallurgy and Materials Science* 2007; 38A: 2523-30.
139. Locci AM, Orru R, Cao G, Munir ZA. Field-activated pressure-assisted synthesis of NiTi. *Intermetallics* 2003; 11: 555-71.

140. Whitney M, Corbin SF, Gorbet RB. Investigation of the mechanisms of reactive sintering and combustion synthesis of NiTi using differential scanning calorimetry and microstructural analysis. *Acta Materialia* 2008; 56: 559-70.
141. Queheillalt DT, Katsumura Y, Wadley HNG. Synthesis of stochastic open cell Ni-based foams. *Scripta Materialia* 2004; 50: 313-17.
142. Queheillalt DT, Hass DD, Sypeck DJ, Wadley HNG. Synthesis of open-cell metal foams by templated directed vapor deposition. *Journal of Materials Research* 2001; 16: 1028-36.
143. Quadbeck P, Kaschta J, Singer RF. Superalloy IN625 with cellular microstructure - fabrication route and mechanical properties. *Advanced Engineering Materials* 2004; 6: 635-39.
144. Yang TY, Shiue RK, Wu SK. Infrared brazing of Ti<sub>50</sub>Ni<sub>50</sub> shape memory alloy using pure Cu and Ti-15Cu-15Ni foils. *Intermetallics* 2004; 12: 1285-92.
145. Eijk C, Sallom ZK, Akselsen OM. Microwave brazing of NiTi shape with Ag-Ti and Ag-Cu-Ti memory alloy alloys. *Scripta Materialia* 2008; 58: 779-81.
146. Grummon DS, Shaw JA, Foltz J. Fabrication of cellular shape memory alloy materials by reactive eutectic brazing using niobium. *Materials Science and Engineering A-Structural Materials Properties Microstructure and Processing* 2006; 438: 1113-18.
147. Yang HB, Ying WH, Yang ZP, Lin JY, Zhang XM, Guo JH. Product microstructure of Ti-Ni-Nb shape memory alloy (SMA) by high-temperature synthesis (SHS) of self-propagating. *Rare Metal Materials and Engineering* 2002; 31: 152-55.
148. Li C, Zheng YF, Zhao LC. Electrochemical corrosion behaviour of Ti<sub>44</sub>Ni<sub>47</sub>Nb<sub>9</sub> alloy in simulated body fluids. *Materials Science and Engineering A-Structural Materials Properties Microstructure and Processing* 2006; 438: 504-08.
149. Hashi K, Ishikawa K, Matsuda T, Aoki K. Microstructures and hydrogen permeability of Nb-Ti-Ni alloys with high resistance to hydrogen embrittlement. *Materials Transaction* 2005; 46: 1026-31.
150. Luo W, Ishikawa K, Aoki K. High hydrogen permeability in the Nb-rich Nb-Ti-Ni alloy. *Journal of Alloys and Compounds* 2006; 407: 115-17.
151. Kishida K, Yamaguchi Y, Tanaka K, Inui H, Tokui S, Ishikawa K, Aoki K. Microstructures and hydrogen permeability of directionally solidified Nb-Ni-Ti alloys with the Nb-NiTi eutectic microstructure. *Intermetallics* 2008; 16: 88-95.
152. Siegert W, Neuking K, Mertmann M, Eggeler G. First cycle shape memory effect in the ternary NiTiNb system. *Journal De Physique Iv* 2003; 112: 739-42.

153. Zhang CS, Wang YQ, Chai W, Zhao LC. The study of constitutional phases in a  $\text{Ni}_{47}\text{Ti}_{44}\text{Nb}_9$  shape memory alloy. *Materials Chemistry and Physics* 1991; 28: 43-50.
154. Zhao LC, Duerig TW, Justi S, Melton KN, Proft JL, Yu W, Wayman CM. The study of niobium-rich precipitates in a Ni-Ti-Nb shape memory alloy. *Scripta Metallurgical Materialia* 1990; 24: 221-26.
155. Uchida K, Shigenaka N, Sakuma T, Sutou Y, Yamauchi K. Effect of Nb content on martensitic transformation temperatures and mechanical properties of Ti-Ni-Nb shape memory alloys for pipe joint applications. *Materials Transaction* 2007; 48: 445-50.
156. Funakubo H. Shape memory alloys. Precision machinery and robotics. New York: Gordon and Breach Science Publishers; 1984.
157. Rajagopalan S, Little AL, Bourke MAM, Vaidyanathan R. Elastic modulus of shape-memory NiTi from in situ neutron diffraction during macroscopic loading, instrumented indentation, and extensometry. *Applied Physics Letters* 2005; 86.
158. Mehta A, Gong XY, Imbeni V, Pelton AR, Ritchie RO. Understanding the deformation and fracture of Nitinol endovascular stents using in situ synchrotron x-ray microdiffraction. *Advanced Materials* 2007; 19: 1183.
159. Kulkov SN, Mironov YP. Martensitic-transformation in NiTi investigated by synchrotron x-ray-diffraction. *Nuclear Instruments & Methods in Physics Research Section A-Accelerators Spectrometers Detectors and Associated Equipment* 1995; 359: 165-69.
160. Miyamoto H, Taniwaki T, Ohba T, Otsuka K, Nishigori S, Kato K. Two-stage B2-B19-B19' martensitic transformation in a  $\text{Ti}_{50}\text{Ni}_{30}\text{Cu}_{20}$  alloy observed by synchrotron radiation. *Scripta Materialia* 2005; 53: 171-75.
161. Schmahl WW, Khalil-Allafi J, Hasse B, Wagner M, Heckmann A, Somsen C. Investigation of the phase evolution in a super-elastic NiTi shape memory alloy (50.7 at.%Ni) under extensional load with synchrotron radiation. *Materials Science and Engineering A-Structural Materials Properties Microstructure and Processing* 2004; 378: 81-85.
162. Schuster A, Voggenreiter HF, Dunand DC, Eggeler G. A new type of intrinsic two-way shape-memory effect in hooks of NiTi-wires. *Journal De Physique IV* 2003; 112: 1177-80.
163. Hasan M et al. Hard x-ray studies of stress-induced phase transformations of superelastic NiTi shape memory alloys under uniaxial load. *Materials Science and Engineering A* 2007 (Article in press);

164. Daymond MR, Young ML, Almer JD, Dunand DC. Strain and texture evolution during mechanical loading of a crack tip in martensitic shape-memory NiTi. *Acta Materialia* 2007; 55: 3929-42.
165. Rathod CR, Rajagopalan S, Vaidyanathan R. Mechanical characterization of shape-memory alloys using diffraction and instrumented indentation. *Shape Memory and Superelastic Technology* 2003; 331.
166. Chang BS, Lee CK, Hong KS, Youn HJ, Ryu HS, Chung SS, Park KW. Osteoconduction at porous hydroxyapatite with various pore configurations. *Biomaterials* 2000; 21: 1291-98.
167. Matsumoto Y, Brothers AH, Stock SR, Dunand DC. Uniform and graded chemical milling of aluminum foams. *Materials Science and Engineering A-Structural Materials Properties Microstructure and Processing* 2007; 447: 150-57.
168. Boonyongmaneerat Y, Chmielus M, Dunand DC, Mullner P. Increasing magnetoplasticity in polycrystalline Ni-Mn-Ga by reducing internal constraints through porosity. *Physical Review Letters* 2007; 99.
169. Petzow G. *Metallographic etching*. Ohio: ASM international; 2001.
170. Sargeant TD, Rao MS, Koh CY, Stupp SI. Covalent functionalization of NiTi surfaces with bioactive peptide amphiphile nanofibers. *Biomaterials* 2008; 29: 1085-98.
171. Zhao H, Van Humbeeck J, De Scheerder I. Surface conditioning of nickel-titanium alloy stents for improving biocompatibility. *Surface Engineering* 2001; 17: 451-58.
172. Zhao H, Stalmans R, van Humbeeck J, de Scheerder I. Pickling of laser-cut NiTi slotted tube stents: Effect on surface morphology, dimension changes and mechanical behaviour. *Journal De Physique IV* 2003; 112: 1125-28.
173. Man HC, Zhao NQ. Enhancing the adhesive bonding strength of NiTi shape memory alloys by laser gas nitriding and selective etching. *Applied Surface Science* 2006; 253: 1595-600.
174. Imwinkelried T. Mechanical properties of open-pore titanium foam. *Journal of Biomedical Materials Research Part A* 2007; 81A: 964-70.
175. Huiskes R, Hollister SJ. From structure to process, from organ to cell - recent developments of FE-analysis in orthopedic biomechanics. *Journal of Biomechanical Engineering-Transactions of the ASME* 1993; 115: 520-27.
176. Kujime T, Tane M, Hyun SK, Nakajima H. Three-dimensional image-based modeling of lotus-type porous carbon steel and simulation of its mechanical behavior by finite

- element method. *Materials Science and Engineering A -Structural Materials Properties Microstructure and Processing* 2007; 460: 220-26.
177. Prymak O et al. Morphological characterization and in vitro biocompatibility of a porous nickel-titanium alloy. *Biomaterials* 2005; 26: 5801-07.
  178. Schrooten J, Assad M, Van Humbeeck J, Leroux MA. *In vitro* corrosion resistance of porous NiTi intervertebral fusion devices. *Smart Materials & Structures* 2007; 16: S145-S54.
  179. Assad M, Likibi F, Jarzem P, Leroux MA, Coillard C, Rivard CH. Porous Nitinol vs. Titanium intervertebral fusion implants: Computer tomography, radiological and histological study of osseointegration capacity. *Materialwissenschaft Und Werkstofftechnik* 2004; 35: 219-23.
  180. Ishimoto T et al. Evaluation of bone quality near metallic implants with and without lotus-type pores for optimal biomaterial design. *Journal of the Japan Institute of Metals* 2007; 71: 432-38.
  181. Spoerke ED, Murray NGD, Li H, Brinson LC, Dunand DC, Stupp SI. Titanium with aligned, elongated pores for orthopedic tissue engineering applications. *Journal of Biomedical Materials Research Part A* 2008; 84A: 402-12.
  182. Chino Y, Dunand DC. Directionally freeze-cast titanium foam with aligned, elongated pores. *Acta Materialia* 2008; 56: 105-13.
  183. Kwok PJ, Oppenheimer SM, Dunand DC. Porous titanium by electro-chemical dissolution of steel space-holders. *Advanced Engineering Materials*, submitted 2008.
  184. Pilliar RM. Porous-surfaced metallic implants for orthopedic applications. *Journal of Biomedical Materials Research-Applied Biomaterials* 1987; 21: 1-33.
  185. Bertheville B, Neudenberger A, Bidaux JE. Powder sintering and shape-memory behaviour of NiTi compacts synthesized from Ni and TiH<sub>2</sub>. *Materials Science and Engineering A-Structural Materials Properties Microstructure and Processing* 2004; 384: 143-50.
  186. Bertheville B, Bidaux JE. Enhanced powder sintering of near-equiatomic NiTi shape-memory alloys using CA reductant vapor. *Journal of Alloys and Compounds* 2005; 387: 211-16.
  187. Boonyongmaneerat Y, Dunand DC. Ni-Mo-Cr foams processed by casting replication of sodium aluminate preforms. *Advanced Engineering Materials* 2008; 10: 379-83.

188. Paula AS, Mahesh KK, dos Santos CML, Canejo J, Fernandes FMB. One- and two-step phase transformation in Ti-rich NiTi shape memory alloy. *International Journal of Applied Electromagnetics and Mechanics* 2006; 23: 25-32.
189. Zhao J, Lu X, Weng J. Macroporous Ti-based composite scaffold prepared by polymer impregnating method with calcium phosphate coatings. *Materials Letters* 2008; 62: 2921-24.
190. Rhalmi S, Charette S, Assad M, Coillard C, Rivard CH. The spinal cord dura mater reaction to Nitinol and titanium alloy particles: A 1-year study in rabbits. *European Spine Journal* 2007; 16: 1063-72.
200. McNeese MD, Lagoudas DC, Pollock TC. Processing of TiNi from elemental powders by hot isostatic pressing. *Materials Science and Engineering A-Structural Materials Properties Microstructure and Processing* 2000; 280: 334-48.
201. Krone L, Schuller E, Bram M, Hamed O, Buchkremer HP, Stover D. Mechanical behaviour of NiTi parts prepared by powder metallurgical methods. *Materials Science and Engineering A-Structural Materials Properties Microstructure and Processing* 2004; 378:185-90.
202. Piao M, Miyazaki S, Otsuka K, Nishida N. Effects of Nb addition on the microstructure of Ti-Ni alloys. *Materials Transaction JIM* 1992; 33: 337-45.
203. Viadyanathan R, Bourke MAM, Dunand DC. Phase fraction, texture and strain evolution in superelastic NiTi and NiTi-TiC composites investigated by neutron diffraction. *Acta Materialia* 1999; 47: 3353-66.